



TECHNISCHE  
UNIVERSITÄT  
WIEN  
Vienna University of Technology

# Interfacing Trapped Ions and Plasmonic Particles with Optical Nanofibers

DISSERTATION

zur Erlangung des akademischen Grades

**Doktor der Naturwissenschaften**

eingereicht von

**Jan Petersen**

Matrikelnummer 1029718

Castellezgasse 16 / 7, 1020 Wien

an der  
Fakultät für Physik der Technischen Universität Wien

Betreuung: Prof. Dr. Arno Rauschenbeutel, E141 – Atominstitut

Diese Dissertation haben begutachtet:

---

(Prof. Dr. Arno  
Rauschenbeutel)

---

(Prof. Dr. Joachim Krenn)

Wien, 09.02.2015

---

(Jan Petersen)





TECHNISCHE  
UNIVERSITÄT  
WIEN  
Vienna University of Technology

# Interfacing Trapped Ions and Plasmonic Particles with Optical Nanofibers

DISSERTATION

submitted in partial fulfillment of the requirements for the degree of

**Doktor der Naturwissenschaften**

by

**Jan Petersen**

Registration Number 1029718

Castellezgasse 16 / 7, 1020 Wien

to the Faculty of Physics  
at the Vienna University of Technology

Advisor: Prof. Dr. Arno Rauschenbeutel, E141 – Atominstitut

The dissertation has been reviewed by:

---

(Prof. Dr. Arno  
Rauschenbeutel)

---

(Prof. Dr. Joachim Krenn)

Wien, 09.02.2015

---

(Jan Petersen)



# Abstract

The technological progress in the last decades is well described by an observation Gordon E. Moore, co-founder of Intel Corporation, made about 50 years ago, where he stated that the number of transistors on integrated circuits doubles approximately every two years. Until 2014, Moore's Law still proves to be accurate; however, the size of transistors is already close to atomic dimensions and growth in conventional information processing, where speed is concerned, will soon come to a halt. Thus, to ensure an ongoing progress, fundamentally new concepts for information processing are indispensable.

One prominent idea is to make use of quantum-mechanical phenomena to store and process data. Such a quantum computer promises to solve certain problems much quicker than its classical counterpart. An interesting approach towards the realization of quantum information processing is based on chains of individually trapped ions, where long term quantum information storage and high fidelity quantum gates have been demonstrated. However, ion state read-out and the scalability to larger ion numbers remains problematic. The integration of a sub-wavelength diameter optical nanofiber as part of a tapered optical fiber could overcome these obstacles because the strong light-matter coupling near the nanofiber surface would allow for efficient transfer of quantum information between distant ions. In order to realize such an ion-nanofiber interface, ions have to be trapped in close vicinity (i.e. sub-wavelength distance) of the nanofiber. Unfortunately, in this case, the ions are subject to coulomb forces from parasitic charges on the fiber, which renders stable trapping impossible. As a consequence, one requires the nanofiber to exhibit a sufficient conductivity, while maintaining its excellent optical properties (i.e. high transmission and strong evanescent field). The thesis at hand investigates experimental approaches towards this goal. While, with the techniques available, sufficiently conductive nanofibers could only be realized in conjunction with a small transmission, this work provides a clear course of actions to reach this regime.

Another novel concept to advance information processing is optical computing. By using light to compute and to transfer information, as opposed to traditional electron-based computation, higher data rates and lower heating rates can be reached. A key ingredient in this approach is an optical switch that controls the direction of propagation of light in nanophotonic waveguides. In this work, the implementation of a nanoscale optical switch is demonstrated. The underlying mechanism that is exploited is called spin-orbit interaction of light. Due to the strong confinement of nanofiber guided light, its electromagnetic field can no longer be described as a transverse wave because strong longitudinal polarization components occur. By positioning a gold nanoparticle on an optical nanofiber this effect is utilized to demonstrate that the polarization of an external excitation light field controls the propagation direction of the light that

is scattered into the waveguide by the nanoparticle. This method has great potential for integrated optical information processing and – using a quantum emitter (e.g. an atom) instead of a nanoparticle – it can be directly extended to quantum mechanical routing and quantum information processing.

# Kurzfassung

Der technische Fortschritt in den letzten Jahrzehnten lässt sich gut durch eine Beobachtung von Gordon E. Moore, Mitgründer der Intel Corporation, beschreiben. Vor etwa 50 Jahren konstatierte er, dass sich die Anzahl der Transistoren in integrierten Schaltungen alle zwei Jahre in etwa verdoppelt und noch heute bestätigen sich diese Vorhersagen des sogenannten Moore'schen Gesetzes. Da jedoch die Größe der heutigen Transistoren mittlerweile in atomare Dimensionen vorstößt, droht die rasante Entwicklung der Informationsverarbeitung an ihre Grenzen zu stoßen. Um die Geschwindigkeiten mit der Informationen verarbeitet werden können weiter zu steigern, sind fundamental neue Konzepte in der Informationstechnologie unabdingbar.

Eine herausragende Idee ist es, quantenmechanische Phänomene zu nutzen um Daten zu speichern und zu verarbeiten. Ein solcher Quantencomputer könnte gewisse Probleme deutlich schneller lösen als sein klassisches Gegenstück. Eines der vielversprechendsten Konzepte hierbei basiert auf dem Fangen von aneinandergereihten einzelnen Ionen, mit Hilfe derer Langzeitspeicherung von Quanteninformationen sowie Quantengatter hoher Genauigkeit bereits realisiert werden konnten. Sowohl das Auslesen der Ionenzustände, als auch die Skalierbarkeit hin zu größeren Ionenzahlen, sind jedoch ein Problem. Die Integration von optischen Nanofasern mit Durchmessern im Subwellenlängenbereich, die wiederum Teil einer verjüngten konventionellen optischen Faser sind, könnte diese Hindernisse bewältigen. Da, in unmittelbarer Nähe zur Nanofaseroberfläche die Licht-Materie Wechselwirkungen sehr stark sind, sollte es möglich sein, Nanofasern für eine effiziente Übertragung der Quanteninformationen zwischen entfernten Ionen zu nutzen. Um eine solche Ionen-Nanofaser Schnittstelle zu realisieren müssen die Ionen allerdings wenige hundert Nanometer entfernt von der Faseroberfläche gefangen werden. Unglücklicherweise führt dies dazu, dass parasitäre elektrische Ladungen auf der Nanofaseroberfläche eine Speicherung aufgrund der resultierenden Coulombkräfte unmöglich machen. Die Nanofaser muss folgerichtig eine ausreichende elektrische Leitfähigkeit aufweisen, ohne jedoch ihre exzellenten optischen Eigenschaften (d.h. hohe Transmission und starkes evaneszentes Feld) zu verlieren. Die vorliegende Doktorarbeit untersucht mehrere experimentelle Herangehensweisen um eine solche Faser herzustellen. Obwohl mit den verfügbaren Techniken eine hohe Leitfähigkeit in Verbindung mit der Erhaltung der optischen Eigenschaften der Nanofaser nicht realisiert werden konnten, präsentiert diese Arbeit klare Handlungsmöglichkeiten um dieses Regime zu erreichen.

Ein weiteres neuartiges Konzept um die Informationsverarbeitung voranzutreiben ist der optische Computer, der größtenteils mit optischen Elementen arbeitet. Auf diese Weise könnte es möglich sein sowohl höhere Datenraten als auch geringere Heizraten, im Vergleich zu den

heutzutage gängigen elektrischen Komponenten, zu erreichen. Ein wichtiges Element einer optischen Informationsverarbeitung ist ein Router, mit dem sich die Propagationsrichtung des Lichts in nanophotonischen Wellenleitern kontrollieren lässt. In dieser Arbeit wird die Umsetzung eines solchen Elements präsentiert. Dieser Nanorouter nutzt dabei den Effekt aus, dass das geführte Licht in einer Nanofaser stark komprimiert ist und aufgrund von starker longitudinaler Polarisationskomponenten nicht mehr als transversales elektromagnetisches Feld beschrieben werden kann. Durch das Positionieren eines einzelnen Gold-Nanoteilchens auf einer optischen Nanofaser, lässt sich dieser Effekt nutzen, und es wird gezeigt, dass sich, mit Hilfe der Polarisierung eines externen Anregungslichts, die Richtung kontrollieren lässt in die das Licht vom Nanoteilchen in die Faser gestreut wird. Diese Methode hat großes Potential für die künftige Entwicklung integrierter, optischer Schaltungen und – unter Verwendung eines Quantenemitters (z.B. eines Atoms) anstelle des Nanoteilchens – kann es direkt erweitert werden auf quantenmechanische Schaltungen und quantenmechanische Informationsverarbeitung.



# List of Publications

In the process of working on this thesis, the following article has been published in a peer-reviewed journal:

J. Petersen, J. Volz, and A. Rauschenbeutel.  
Chiral nanophotonic waveguide interface based on spin-orbit coupling of light.  
*Science*, 346(6205):67–71, 2014.



# Contents

<b>1</b>	<b>Introduction</b>	<b>1</b>
<b>2</b>	<b>Optical Nanofibers</b>	<b>5</b>
2.1	The electromagnetic wave equation . . . . .	6
2.2	Guided modes of the optical fiber . . . . .	8
2.2.1	The hybrid fundamental modes of an optical nanofiber . . . . .	16
2.3	Radiation modes of the optical fiber . . . . .	19
2.4	Tapered optical fibers . . . . .	20
2.4.1	TOF fabrication using a flame brushing technique . . . . .	21
<b>3</b>	<b>Metal Nanoparticles</b>	<b>23</b>
3.1	Optical properties of materials . . . . .	24
3.1.1	Lorentz model for dielectric media . . . . .	25
3.1.2	Drude model for metals . . . . .	28
3.1.3	Phenomenological Drude-Lorentz model for real metals . . . . .	29
3.1.4	Optical properties of gold . . . . .	30
3.2	Absorption and scattering by a nanosphere . . . . .	32
3.2.1	Extinction, absorption and scattering of light . . . . .	33
3.2.2	Quasi-static approximation . . . . .	33
3.2.3	Mie theory . . . . .	39
<b>4</b>	<b>Interfacing Optical Nanofibers with Ions</b>	<b>43</b>
4.1	Preface . . . . .	44
4.2	An optical nanofiber as an electrical conductor: Considerations . . . . .	45
4.2.1	Heating mechanisms and charge sensitivity in ion traps . . . . .	45
4.2.2	Desired conductivity of a quasi-charge free nanofiber . . . . .	45
4.2.3	Required properties of nanofibers in the framework of calcium ion experiments . . . . .	49
4.3	Coating of nanofibers by physical vapor deposition . . . . .	52
4.3.1	Properties of thin film growth . . . . .	52
4.3.2	Experimental setup for physical vapor deposition . . . . .	54
4.3.3	Coating nanofibers with silver: experimental results . . . . .	57
4.3.4	Coating nanofibers with chromium: Experimental Results . . . . .	60

4.4	Conclusion and other possible realizations . . . . .	63
<b>5</b>	<b>Interfacing Optical Nanofibers with Single Nanoparticles</b>	<b>67</b>
5.1	Spin-Orbit interaction of light in optical nanofibers . . . . .	68
5.2	Scattering characteristics of an emitter on a nanofiber . . . . .	71
5.3	Preparation of a single scatterer on an optical nanofiber . . . . .	78
5.3.1	Selection of a precise experimental system . . . . .	79
5.3.2	Nanofiber-based spectroscopy of a metal nanosphere . . . . .	80
5.3.3	Single nanoparticle deposition via a dipping technique . . . . .	86
5.4	A chiral nanophotic waveguide coupler . . . . .	90
5.4.1	Optical setup . . . . .	90
5.4.2	Experimental results . . . . .	92
5.4.3	Conclusion . . . . .	100
5.5	Towards nanophotonic devices . . . . .	101
5.5.1	Chiral Coupler: Optimizing waveguide coupling and directionality . . .	101
5.5.2	Polarization dependent backscattering and unidirectional waveguides .	103
5.5.3	Sensing applications . . . . .	105
<b>6</b>	<b>Summary and Outlook</b>	<b>107</b>
<b>A</b>	<b>Appendix</b>	<b>111</b>
A.1	A nanofiber-based ion trap using a metal nanoparticle and difference frequency generation . . . . .	111
A.2	Blue print of the PVD vacuum chamber . . . . .	115
A.3	A chiral nanophotonic waveguide coupler - Full set of measured datapoints . .	116
	<b>Bibliography</b>	<b>123</b>

# Introduction

The Internet has lastingly changed modern society and a life without it is already difficult to imagine. As a consequence of its extraordinary growth in the last 50 years, it is nowadays used by billions of people. An integral part of this global system of interconnected computer networks are optical fibers: Optical fibers provide an almost lossless transmission channel for light which in turn is well suited as an information carrier. Together, they reach data transfer rates which outclass electrical or wireless communication models. Even though today's information transfer between computers is, therefore, almost purely optical, the processing of data inside the computer is still carried out by electronic devices. The reason for this is that there are no competitive optical counterparts to devices like transistors, switch and diodes. Thanks to them, computers are able to process informations much faster than any human being can which in turn led to an improved efficiency and productivity of our society. Its concomitant technological progress in the last decades is well described by an observation Gordon E. Moore, co-founder of Intel Corporation, made about 50 years ago, where he stated that the number of transistors on a computer chip doubles approximately every two years [1]. Until 2014, Moore's Law still proves to be accurate; however, the size of transistors is already close to atomic dimensions and growth of computing power will soon come to a halt. Thus, to ensure an ongoing progress, fundamentally new concepts for information processing are indispensable.

In classical computers, information is quantified in form of electronic bits. If these bits approach nanometer-scale dimensions quantum effects come into play that limit the ability to confine them. One prominent idea, that was pioneered by R. Feynman and P. Benioff, is to make use of these properties and to store and process data quantum mechanically [2–4]. Such a quantum computer uses quantum bits, or qubits [5], as its fundamental unit of information and promises to solve certain problems much quicker than its classical counterpart [6, 7]. A promising approach towards the realization of quantum information processing is based on chains of individually trapped ionized atoms [8, 9]. In this approach, information is stored in their atomic states [10, 11]. While long term quantum information storage and high fidelity quantum gates have been demonstrated [12, 13], the main limitation of ions is that they are 'stationary qubits', i.e. unable to transmit the information they carry over any significant distance. This poses se-

were problems for the scalability of ion trap quantum processing towards more than a few tens of ions. Similar to the classical case, light is an obvious candidate to take on that role. Photons can act as 'flying qubits' and transmit quantum information over very long distances, particularly when using optical fibers. As a consequence, a light-matter interface that allows one to transfer quantum information efficiently between to systems is of great importance [14].

A promising candidate that could provide this property are nanophotonic waveguides such as sub-wavelength diameter optical nanofibers [15–17]. Nanofibers are typically realized as the waist of a tapered standard optical fiber. They tightly confine light over long distances with a significant power fraction of the light propagating outside of the fiber in the evanescent field [18]. As a result, any emitter in close proximity (i.e. sub-wavelength distance) to the nanofiber surface can strongly interact with the evanescent field. Coupling has already been demonstrated for uncharged emitters such as atoms [19], molecules [20], NV centers [21] and quantum dots [22]. However, in contrast to them, ions are subject to coulomb forces and parasitic charges on the nanofiber will render stable trapping of them impossible [23]. As a consequence, one requires the nanofiber to exhibit a sufficient conductivity, while maintaining its excellent optical properties (i.e. high transmission and strong evanescent field). In this case, parasitic charges generated on the fiber surface could be removed and stable ion-fiber coupling could possibly be achieved.

In chapter 4 of this thesis two approaches towards this goal using physical vapor deposition of silver (Ag) and chromium (Cr) are presented. In the case of silver, a strongly pronounced island growth on the nanofiber prevented acceptable electrical conductivities before transmission was lost. In the case of chromium, however, a conductive and minimally transmissive nanofiber could be realized. The results obtained in this thesis seem promising such that with future improvements in the fiber production and thin film deposition processes, a coated nanofiber with the ability to act as a light-matter interface in ion traps might be within reach.

Another possibility to advance information processing is to give up the current hybrid computing approach where electricity and light are used to process and transmit information respectively, and to pursue an all-optical architecture. The reason why light has not yet replaced electricity as the information carrier when it comes to information processing is that there are no integrated circuits yet which are able to control the flow of light at the same level as for electronics. In addition to the fact that an all-optical approach would make interfacing issues irrelevant, it provides two additional advantages compared to a conventional computer. Firstly, processing power as well as miniaturization result in critical heat generation in conventional computers that could be significantly reduced if optical devices were introduced. Secondly and in contrast to electric information carriers, individual light beams do not cross talk when being sent down the same channel at the same time. Because of that, they can be processed by a single optical element simultaneously (i.e. in one clock cycle) rendering possible a massive gain in net speed of the computing system. Around 2012, IBM and other companies have reported the development of commercial applications using optical links to connect chips [24,25]. Also, Optical signal processors already exist for very specific applications like fast fourier transformations [26]. Moreover, in 2013, researchers at MIT, Harvard University and the Vienna University of Technology demonstrated an optical analog of a transistor, in a proof-of-principle experiment

---

where a single photon was used to control the transmission of light through a cloud of cold cesium atoms [27]. Optical computing is still on the verge of breakthrough and a multitude of questions still have to be answered.

In particular, when building miniaturized circuits for light, novel physical phenomena occur. Light fields are usually considered to be paraxial [28], meaning that they are purely transversally polarized. However, this approximation no longer holds true and longitudinal polarization components arise when the light field is transversally confined (e.g. in strongly focused beams or in the evanescent field of prisms and nanophotonic waveguides). The occurrence of the longitudinal components gives rise to phenomena such as spin-orbit interaction of light: For a plane wave that is circularly polarized the spin angular momentum can point parallel or anti-parallel to its propagation direction. On the other hand, in nanophotonic waveguides, the local spin of the guided light depends on its propagation direction due to large field gradients of the strongly confined light. Thus, in this strongly non-paraxial regime, spin and orbital angular momentum of light are no longer independent physical quantities but are coupled [29–32]. Spin-orbit interaction of light has been observed for freely propagating light fields [33, 34], in the case of total internal reflection [35, 36], in plasmonic systems [37–40], for radio frequency waves in metamaterials [41] and at whispering gallery mode resonators [42]. In particular, it changes the physical nature of light-matter coupling and enables new functionalities of nanophotonic devices. When, for example, an emitter is placed in the evanescent field of a nanophotonic waveguide, this spin-orbit interaction leads to a directional scattering into the waveguide.

Exploiting this effect, chapter 5 demonstrates the implementation of a nanoscale optical switch. By positioning a gold nanoparticle on an optical nanofiber, it is demonstrated that the polarization of an external excitation light field controls the propagation direction of the light that is scattered into the waveguide by the nanoparticle. This method has the potential to advance integrated optical information processing and – using a quantum emitter (e.g. atom) instead of a nanoparticle – it can be directly extended to quantum mechanical routing and quantum information processing [43–46].





## Optical Nanofibers

Silica glass fibers are the backbone of our modern communication society. Over a billion kilometers are wound around the globe to transmit information. Thanks to the availability of extremely clean silica glasses, light that is confined in such a standard optical fiber is shielded from the environment and in combination isolated from almost any absorbing source (see Fig. 2.1). The Internet as such would probably not exist in its present form without the existence of optical fibers. Consequently, 2009 the Nobel Prize Committee awarded Charles Kuen Kao for its pioneering work in this field [47].

Nowadays it is possible to transmit 100 000 books in 1 second through a glass fiber of the size of a human hair over several thousand kilometers. This low loss, high bandwidth transport of information together with a comparably low weight and cheap production cost makes glass fibers a highly superior long-distance transmission medium with respect to wire cables. The small diameters and their ability to guide light to almost any location also lead to a multitude of applications in biology and medicine.

When the fiber diameter is decreased to diameters below the wavelength of the guided light a significant part of its optical power propagates outside of the optical fiber in form of an evanescent wave. In this way light can be strongly confined and, in contrast to a highly focused free-

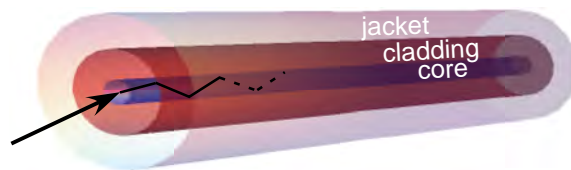


**Figure 2.1: Standard optical fiber.** *Nomenclature for describing a standard optical fiber. A light ray (black line) is totally internally reflected inside the core (blue) due to its higher refractive index with respect to the cladding (red). To protect the waveguide from its surrounding environment it is usually coated with a jacket layer.*

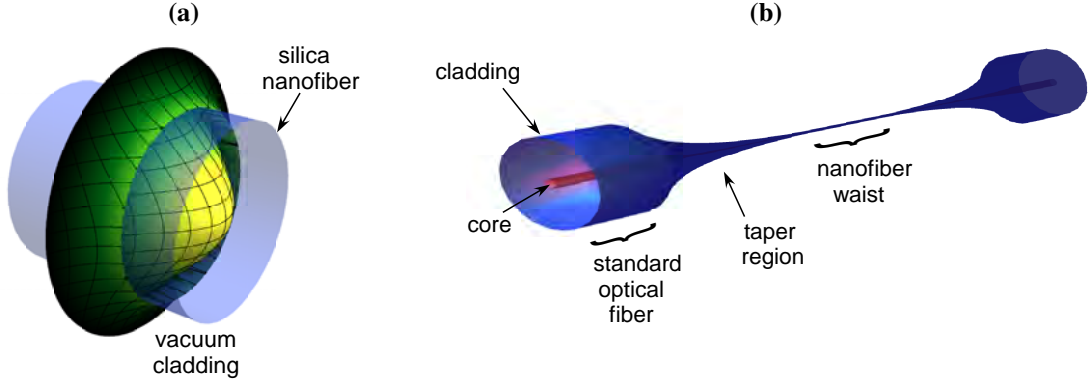


**Figure 2.2: Tapered optical fiber.** (a) Intensity profile (yellow green) of the circularly polarized fundamental mode in- and outside of a nanofiber (red). (b) Schematic of a tapered optical fiber. The standard optical fiber, consisting of a cladding and core region, is tapered down to a subwavelength-diameter nanofiber waist region. The intensity in the outer vicinity of the fiber surface is only slightly smaller than the maximum intensity at the center of the fiber. The ratios between cladding, core and waist are not true to scale.

space beam, this confinement can be maintained over very long distances and matter in close vicinity of the fiber surface can interact efficiently with the guided light (see Fig. 2.2a). Such a so called optical nanofiber can be realized at the waist of a biconical tapered standard optical fiber and is typically realized in a heat and pull process (see Fig. 2.2b).

In this chapter the theory of light propagation in optical fibers is discussed and important characteristics of optical nanofibers are presented. Starting with the electromagnetic wave equation in section 2.1 the guided and radiation modes of a step-index optical fiber are introduced (Sect. 2.2 and 2.3). Section 2.2.1 considers the case where the diameter of the optical fiber is well below the wavelength of the guided light and only supports the hybrid fundamental modes  $HE_{11}$ . The theoretical descriptions in the first three sections will closely follow the treatment presented in the books by A. Yariv [48] and D. Marcuse [49] as well as the paper by Fam Le Kien [50]. Section 2.4 explains how such an optical nanofiber can be realized as the waist of a tapered standard optical fiber using a flame brushing technique. The last section discusses the electrical properties of silica nanofibers.

## 2.1 The electromagnetic wave equation

An electromagnetic wave, such as an optical beam, must be a solution to Maxwell's electromagnetic wave equation. As optical fibers are cylindrically symmetric dielectrics, first we solve this equation for an isotropic, charge-free medium in cylindrical coordinates. In a second step, the solution will then be applied to the boundary conditions of a step-index optical fiber.

The electromagnetic response of a medium is summarized in Maxwell's equations [51]:

$$\nabla \cdot \mathbf{D} = \rho \quad (2.1a) \quad \nabla \times \mathbf{H} = \mathbf{J} + \partial_t \mathbf{D} \quad (2.1c)$$

$$\nabla \cdot \mathbf{B} = 0 \quad (2.1b) \quad \nabla \times \mathbf{E} = -\partial_t \mathbf{B}, \quad (2.1d)$$

where the notation  $\partial_\alpha = \partial/\partial\alpha$ , with  $\alpha = (r, \phi, z)$  is used. Moreover,  $\mathbf{E}$  is the electric,  $\mathbf{H}$  the magnetic field,  $\mathbf{J}$  the current density and  $\rho$  the charge density. The electric displacement field  $\mathbf{D}$  and the magnetic flux density  $\mathbf{B}$  are defined as  $\mathbf{D} = \overset{\leftrightarrow}{\epsilon} \cdot \mathbf{E}$  and  $\mathbf{B} = \overset{\leftrightarrow}{\mu} \cdot \mathbf{H}$ , respectively, with  $\overset{\leftrightarrow}{\mu} = \mu_0 \overset{\leftrightarrow}{\mu_r}$  and  $\overset{\leftrightarrow}{\epsilon} = \epsilon_0 \overset{\leftrightarrow}{\epsilon_r}$ . Here,  $\overset{\leftrightarrow}{\mu_r}$  ( $\overset{\leftrightarrow}{\epsilon_r}$ ) is the relative permeability (permittivity) of the material and  $\mu_0$  ( $\epsilon_0$ ) is the vacuum permeability (permittivity), respectively.

In an isotropic, charge-free medium ( $\rho = 0$ ,  $\mathbf{J} = 0$  and  $\nabla \cdot \mathbf{E} = 0$ ), both,  $\overset{\leftrightarrow}{\mu}$  and  $\overset{\leftrightarrow}{\epsilon}$  are scalars<sup>1</sup> and if we take the curl of Eq. (2.1d) and eliminate  $\nabla \times \mathbf{B}$  using Eq. (2.1c) we get the electromagnetic wave equation for the electric field  $\mathbf{E}$ :

$$\Delta \mathbf{E}(\mathbf{r}, t) - \mu(\mathbf{r}) \epsilon(\mathbf{r}) \frac{\partial^2 \mathbf{E}(\mathbf{r}, t)}{\partial t^2} = 0. \quad (2.2)$$

Here,  $\Delta$  is the Laplace operator and  $t$  denotes the time variable. Equation (2.2) describes waves with a speed  $v(\mathbf{r}) = c/n(\mathbf{r})$ , where  $c = 1/\sqrt{\mu_0 \epsilon_0} = 2.998 \times 10^8$  m/s is the speed of light in vacuum and  $n(\mathbf{r}) = \sqrt{\mu_r(\mathbf{r}) \epsilon_r(\mathbf{r})}$  the refractive index of the isotropic dielectric medium. In order to obtain the wave equation of the magnetic field, one can simply replace  $\mathbf{E}$  with  $\mathbf{H}$  in Eq. (2.2).

If we express Eq. (2.2) in cylindrical coordinates  $(r, \phi, z)$ , we can solve it for the core and cladding of a cylindrically symmetric optical fiber, whose axis points along  $z$ . By satisfying the boundary conditions, a complete description of the optical fiber modes can be obtained. The Laplace operator in cylindrical coordinates is of the form

$$\Delta = \partial_r^2 + \frac{1}{r} \partial_r + \frac{1}{r^2} \partial_\phi^2 + \partial_z^2. \quad (2.3)$$

For an optical wave of frequency  $\omega/(2\pi)$  that propagates along the fiber, we can write

$$\begin{bmatrix} \mathbf{E}(\mathbf{r}, t) \\ \mathbf{H}(\mathbf{r}, t) \end{bmatrix} = \begin{bmatrix} \mathbf{E}(r, \phi) \\ \mathbf{H}(r, \phi) \end{bmatrix} \exp(i[-\omega t + \beta z]), \quad (2.4)$$

where  $\beta$  is the propagation constant in a medium with an arbitrary refractive index profile. Both fields are linked with each other via Eq. (2.1c) and Eq. (2.1d) and the transversal components can be expressed in terms of the axial components  $E_z$  and  $H_z$ :

$$\begin{aligned} E_r &= \frac{i\beta}{\omega^2 \mu \epsilon - \beta^2} \left( \partial_r E_z + \frac{\omega \mu}{\beta} \frac{\partial_\phi}{r} H_z \right) & E_\phi &= \frac{i\beta}{\omega^2 \mu \epsilon - \beta^2} \left( \frac{1}{r} \partial_\phi E_z - \frac{\omega \mu}{\beta} \partial_r H_z \right) \\ H_r &= \frac{i\beta}{\omega^2 \mu \epsilon - \beta^2} \left( \partial_r H_z - \frac{\omega \epsilon}{\beta} \frac{\partial_\phi}{r} E_z \right) & H_\phi &= \frac{i\beta}{\omega^2 \mu \epsilon - \beta^2} \left( \frac{1}{r} \partial_\phi H_z + \frac{\omega \epsilon}{\beta} \partial_r E_z \right). \end{aligned} \quad (2.5)$$

<sup>1</sup>In general, both  $\overset{\leftrightarrow}{\mu}$  and  $\overset{\leftrightarrow}{\epsilon}$  are second rank tensors.

So by solving the wave equation (2.2) for the axial components, the transversal ones can be deduced. Thus, it is enough to solve the wave equation for  $E_z$  and  $H_z$  and by substituting Eq. (2.4) into Eq. (2.2), we can write

$$\left( \partial_r^2 + \frac{1}{r} \partial_r + \frac{1}{r^2} \partial_\phi^2 + (k^2 - \beta^2) \right) \begin{bmatrix} E_z \\ H_z \end{bmatrix} = 0, \quad (2.6)$$

where  $k = n\omega/c$  is the propagation constant in a medium with refractive index  $n$ . This equation is separable into a radial and azimuthal part and the solution takes the form

$$\begin{bmatrix} E_z \\ H_z \end{bmatrix} = \begin{bmatrix} E_0 e_z(r) \\ H_0 h_z(r) \end{bmatrix} \exp(\pm i l \phi), \quad (2.7)$$

with  $l \in \mathbb{N}_0$  being a positive integer number and  $e(r)$  ( $h(r)$ ) the electric (magnetic) profile functions, respectively. With this ansatz Eq. (2.6) becomes

$$\left[ \partial_r^2 + \frac{1}{r} \partial_r + (k^2 - \beta^2 - \frac{l^2}{r^2}) \right] \begin{bmatrix} e_z(r) \\ h_z(r) \end{bmatrix} = 0. \quad (2.8)$$

This differential equation is known and its solutions are called (modified) Bessel functions of order  $l$ . In the case where  $h^2 = k^2 - \beta^2 > 0$ , it is

$$\begin{bmatrix} e_z(r) \\ h_z(r) \end{bmatrix} = \begin{bmatrix} c_1 \\ \tilde{c}_1 \end{bmatrix} J_l(hr) + \begin{bmatrix} c_2 \\ \tilde{c}_2 \end{bmatrix} Y_l(hr), \quad (2.9)$$

whereas in the case of  $q^2 = \beta^2 - k^2 > 0$ , we get

$$\begin{bmatrix} e_z(r) \\ h_z(r) \end{bmatrix} = \begin{bmatrix} c_1 \\ \tilde{c}_1 \end{bmatrix} I_l(qr) + \begin{bmatrix} c_2 \\ \tilde{c}_2 \end{bmatrix} K_l(qr). \quad (2.10)$$

where  $c_1, \tilde{c}_1, c_2$  and  $\tilde{c}_2$  are complex constants that are determined by the boundary conditions and ( $I_l$  and  $K_l$ )  $J_l$  and  $Y_l$  are the (modified) Bessel functions of order  $l$  of the first and second kind, respectively. The Bessel functions  $J_l$  and  $Y_l$  are oscillating functions where  $Y_l$  is singular at the origin. The modified Bessel functions  $I_l$  ( $K_l$ ), on the other hand, are monotonically increasing (decreasing), respectively. In Fig. 2.3 all of them are plotted for parameters that will be relevant in the course of this work.

## 2.2 Guided modes of the optical fiber

In most cases the optical fiber has a distinct core region of radius  $a$  with a refractive index  $n_1$  and a cladding region of radius  $b$  with a refractive index  $n_2$ , that is smaller than  $n_1$  (see Fig. 2.4a). As a consequence, due to Snell's law, a light ray that is propagating in the core region is totally internally reflected in all cases where the angle between the core-cladding interface and the ray's propagation direction lies within  $0 \leq \theta < \theta_c$ , where  $\theta_c = \arccos n_2/n_1$  (see Fig. 2.4b). This type of fiber is called a step-index optical fiber and in the case of standard optical silica fibers the cladding is usually made of pure silica, whereas the core is made of doped silica to slightly

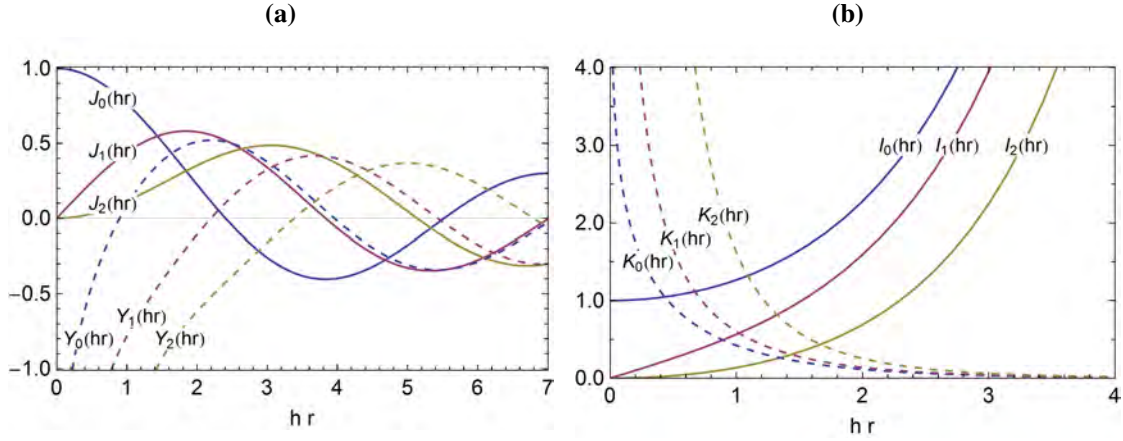


**Figure 2.3: Bessel functions.** (a) Plot of the Bessel functions of the first ( $J_l$ ) and second ( $Y_l$ ) kind. (b) Plot of the modified Bessel functions of the first ( $I_l$ ) and second ( $K_l$ ) kind.

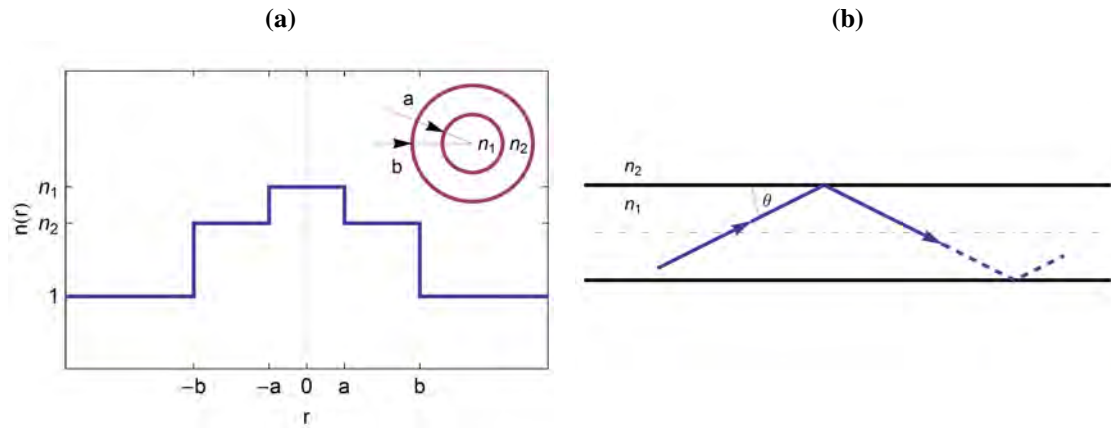


**Figure 2.4: Refractive index profile and total internal reflection.** (a) Standard refractive index profile of a step-index optical fiber in vacuum ( $n = 1$ ) where the fiber axis is located at  $r = 0$ . The inset shows a transversal cut through the fiber. (b) Total internal reflection inside the core of a fiber.

increase its refractive index with respect to the cladding<sup>2</sup>. For standard optical fibers the cladding radius  $b$  is usually much larger than the core radius  $a$ . That is why for deducing the transversally confined modes, we can assume  $b = \infty$  as the field is already effectively zero at  $r = b$ . It is apparent that the propagation constant  $\beta$  of a confined mode in this core-cladding system has to lie within the propagation constants of a wave propagating exclusively in a medium with a refractive index of the cladding and a wave propagating exclusively in a medium with a refractive index of the core, i.e.

$$n_2 \frac{\omega}{c} < \beta < n_1 \frac{\omega}{c} . \quad (2.11)$$

For the fields in the core ( $r < a$ ) this means that  $k^2 - \beta^2 > 0$  and solution Eq. (2.9) has to be applied. In Fig. 2.3a we can see that the Bessel function of the second kind diverges  $Y_l$  for  $r \rightarrow 0$ . Since the fields must remain finite at  $r = 0$ , we set  $c_2 = \tilde{c}_2 = 0$  and get

$$\begin{bmatrix} e_z(r) \\ h_z(r) \end{bmatrix} = \begin{bmatrix} A \\ B \end{bmatrix} J_l(hr) , \quad r < a , \quad (2.12)$$

where  $A, B \in \mathbb{C}$  are complex constants,  $h^2 = n_1^2 k_0^2 - \beta^2$  a field-characterizing parameter inside the core and  $k_0 = \omega/c$  the angular wavenumber in vacuum.

For the cladding ( $r > a$ ) it is  $\beta^2 - k^2 > 0$  and solution Eq. (2.10) has to be applied. To ensure that the field vanishes for  $r = \infty$  we set  $c_1 = \tilde{c}_1 = 0$ . The radial characteristics of the guided field part in the cladding are therefore governed by the modified Bessel functions of the second kind  $K_l$ , leading to a radially decaying evanescent field (see Fig. 2.3b). We note that this also means that no radial power flow exists for the guided modes of a step-index optical fiber. The fields of confined modes in the cladding are given by

$$\begin{bmatrix} e_z(r) \\ h_z(r) \end{bmatrix} = \begin{bmatrix} C \\ D \end{bmatrix} K_l(qr) , \quad r > a , \quad (2.13)$$

where  $C, D \in \mathbb{C}$  are complex constants and  $q^2 = \beta^2 - n_2^2 k_0^2$  a field-characterizing parameter in the cladding. In order to obtain the full solution, the amplitudes  $A, B, C, D$  will be used to satisfy the boundary condition at the cladding-core interface demanding that  $E_\phi, E_z, H_\phi$  and  $H_z$  be continuous at the core-cladding boundary. So, by substituting Eq. (2.12) and Eq. (2.13) into Eq. (2.5) the system of equations can be reduced to the following condition:

$$\left[ \frac{J'_l(ha)}{ha J_l(ha)} + \frac{K'_l(qa)}{qa K_l(qa)} \right] \left[ \frac{n_1^2 J'_l(ha)}{ha J_l(ha)} + \frac{n_2^2 K'_l(qa)}{qa K_l(qa)} \right] = \left[ \frac{1}{(qa)^2} + \frac{1}{(ha)^2} \right]^2 \left[ \frac{l\beta}{k_0} \right]^2 . \quad (2.14)$$

---

<sup>2</sup>In the case where the refractive indices of core and cladding differ only very slightly the fiber is called 'weakly guiding'.

Together with the condition Eq. (2.11) this leads to a finite number of eigenvalues of  $\beta$  for a given  $l$  and  $\omega$  and the following relations for the amplitudes:

$$\begin{aligned} B &= \mathfrak{i} \frac{\beta s l}{\mu \omega} A \\ C &= v A \\ D &= v B, \end{aligned} \quad (2.15)$$

where

$$s = \left[ \frac{1}{(q a)^2} + \frac{1}{(h a)^2} \right] \left[ \frac{J'_l(h a)}{h a J_l(h a)} + \frac{K'_l(q a)}{q a K_l(q a)} \right]^{-1}, \quad v = \frac{J_l(h a)}{K_l(q a)}.$$

The amplitudes can now all be expressed for the case of counterclockwise quasi-circularly<sup>3</sup> polarized light by the complex constant  $A$ , which in turn can be extracted from the profile functions. Then, the cylindrical-coordinate vector components of the profile functions  $e(r)$  ( $h(r)$ ) of the guided modes are given, inside the fiber core  $r < a$ , by

$$\begin{aligned} e_r(r) &= \mathfrak{i} \frac{q}{h v} [(1 - s l) J_{l-1}(h r) - (1 + s l) J_{l+1}(h r)] \\ e_\phi(r) &= -\frac{q}{h v} [(1 - s l) J_{l-1}(h r) + (1 + s l) J_{l+1}(h r)] \\ e_z(r) &= \frac{2 q}{\beta v} J_l(h r) \\ h_r(r) &= \frac{\omega \epsilon_0 n_1^2 q}{h \beta v} [(1 - s_1 l) J_{l-1}(h r) + (1 + s_1 l) J_{l+1}(h r)] \\ h_\phi(r) &= \mathfrak{i} \frac{\omega \epsilon_0 n_1^2 q}{h \beta v} [(1 - s_1 l) J_{l-1}(h r) - (1 + s_1 l) J_{l+1}(h r)] \\ h_z(r) &= \mathfrak{i} \frac{2 q s}{\omega \mu v} l J_l(h r), \end{aligned} \quad (2.16)$$

and in the cladding region  $r > a$ , by

$$\begin{aligned} e_r(r) &= \mathfrak{i} [(1 - s l) K_{l-1}(q r) + (1 + s l) K_{l+1}(q r)] \\ e_\phi(r) &= -[(1 - s l) K_{l-1}(q r) - (1 + s l) K_{l+1}(q r)] \\ e_z(r) &= \frac{2 q}{\beta} K_l(q r) \\ h_r(r) &= \frac{\omega \epsilon_0 n_2^2}{\beta} [(1 - s_2 l) K_{l-1}(q r) - (1 + s_2 l) K_{l+1}(q r)] \\ h_\phi(r) &= \mathfrak{i} \frac{\omega \epsilon_0 n_2^2}{\beta} [(1 - s_2 l) K_{l-1}(q r) + (1 + s_2 l) K_{l+1}(q r)] \\ h_z(r) &= \mathfrak{i} \frac{2 q s}{\omega \mu} l K_l(q r), \end{aligned} \quad (2.17)$$

<sup>3</sup>The prefix 'quasi' is used to indicate that in general a non-vanishing longitudinal field component is present in addition to the transversal polarization state present in paraxial light fields.

where

$$s_1 = \frac{\beta^2}{k_0^2 n_1^2} s, \quad s_2 = \frac{\beta^2}{k_0^2 n_2^2} s.$$

Here,  $J'(x) = \partial J(x)/\partial x$  and  $K'(x) = \partial K(x)/\partial x$  denote the derivative with respect to the argument. Note that the  $z$ -components along the fiber axis are in general non-zero. So in contrast to a purely transversal – also known as paraxial – light field, the guided modes exhibit a longitudinal component, which can be referred to as the so called spin-orbit interaction of the light. The implications of this phenomenon will be discussed in more detail in chapter 5.

In conclusion, the electromagnetic fields of the full set of quasi-circularly polarized guided fiber modes, labeled by the mode index  $\mu = (\omega, \mathfrak{c}, l, \mathfrak{d})$ , read

$$\begin{bmatrix} \mathbf{E}_{\text{circ}}^{(\mu)}(\mathbf{r}, t) \\ \mathbf{H}_{\text{circ}}^{(\mu)}(\mathbf{r}, t) \end{bmatrix} = A \left( \hat{\mathbf{r}} \begin{bmatrix} e_r(r) \\ h_r(r) \end{bmatrix} + \mathfrak{c} l \hat{\boldsymbol{\phi}} \begin{bmatrix} e_\phi(r) \\ h_\phi(r) \end{bmatrix} + \mathfrak{d} \hat{\mathbf{z}} \begin{bmatrix} e_z(r) \\ h_z(r) \end{bmatrix} \right) \exp(i[-\omega t + \mathfrak{c} l \phi + \mathfrak{d} \beta z]), \quad (2.18)$$

and in the case of quasi-linearly polarized guided fiber modes, labeled by the mode index  $\mu = (\omega, \varphi_0, l, \mathfrak{d})$ ,

$$\begin{aligned} \begin{bmatrix} \mathbf{E}_{\text{lin}}^{(\mu)}(\mathbf{r}, t) \\ \mathbf{H}_{\text{lin}}^{(\mu)}(\mathbf{r}, t) \end{bmatrix} = \sqrt{2} A \left( \hat{\mathbf{r}} \begin{bmatrix} e_r(r) \\ h_r(r) \end{bmatrix} \cos(l(\phi - \varphi_0)) \right. \\ \left. + i \hat{\boldsymbol{\phi}} \begin{bmatrix} e_\phi(r) \\ h_\phi(r) \end{bmatrix} \sin(l(\phi - \varphi_0)) \right. \\ \left. + \mathfrak{d} \hat{\mathbf{z}} \begin{bmatrix} e_z(r) \\ h_z(r) \end{bmatrix} \cos(l(\phi - \varphi_0)) \right) \exp(i[-\omega t + \mathfrak{d} \beta z]). \quad (2.19) \end{aligned}$$

Here,  $\hat{\mathbf{r}} = \hat{\mathbf{x}} \cos(\phi) + \hat{\mathbf{y}} \sin(\phi)$ ,  $\hat{\boldsymbol{\phi}} = -\hat{\mathbf{x}} \sin(\phi) + \hat{\mathbf{y}} \cos(\phi)$ , and  $\hat{\mathbf{z}}$  stand for the unit basis vectors of the cylindrical coordinate system, whereas  $\hat{\mathbf{x}}$  and  $\hat{\mathbf{y}}$  are the unit basis vectors of the Cartesian coordinate system for the fiber transverse plane  $xy$ .  $\beta = |\beta|$  is taken to be positive and, accordingly, the parameter  $\mathfrak{d} = +1$  or  $-1$  stands for forward ( $+\hat{\mathbf{z}}$ ) or backward ( $-\hat{\mathbf{z}}$ ) propagation direction, respectively.  $\mathfrak{c} = +1$  or  $-1$  refers to counterclockwise or clockwise circulation of the transverse component of the field with respect to the positive direction of the fiber axis  $z$ , respectively.  $\varphi_0$  is the angle of the quasi-linearly polarized mode in the transverse plane. The quasi-linearly polarized guided modes are a linear superposition of the quasi-circular polarized modes. We replace the parameter  $\varphi_0$  with  $\xi$  for the special cases  $\varphi_0 = 0$  ( $\varphi_0 = \pi/2$ ) where the guided modes  $\mu = (\omega, \xi, l, \mathfrak{d})$  are quasi-linear polarized along the principal axis  $\hat{\mathbf{x}}$  ( $\hat{\mathbf{y}}$ ).

Sometimes it is useful to include the mode parameters into the profile function. This leads to the following nomenclature for circular and linear polarization

$$\begin{aligned} \mathbf{e}^{(\mu)} = \begin{bmatrix} \mathbf{e}_{\text{circ}} \\ \mathbf{e}_{\text{lin}} \end{bmatrix} = \begin{bmatrix} \mathbf{e}^{(\omega, \mathfrak{c}, l, \mathfrak{d})} \\ \mathbf{e}^{(\omega, \varphi_0, l, \mathfrak{d})} \end{bmatrix} \\ = \begin{bmatrix} \hat{\mathbf{r}} e_r + \mathfrak{c} l \hat{\boldsymbol{\phi}} + \mathfrak{d} \hat{\mathbf{z}} e_z \\ \sqrt{2} \left( \hat{\mathbf{r}} e_r \cos(l(\phi - \varphi_0)) + i \hat{\boldsymbol{\phi}} \sin(l(\phi - \varphi_0)) + \mathfrak{d} \hat{\mathbf{z}} e_z \cos(l(\phi - \varphi_0)) \right) \end{bmatrix}, \quad (2.20) \end{aligned}$$



Also note that  $\mathbf{E}$  is related to the real value of the electric field by  $\mathcal{E} = 1/2 (\mathbf{E} + \mathbf{E}^*)$ .

The coefficient  $A$  can be determined from the axial component  $S_z$  of the time averaged Poynting vector, which describes the intensity of a mode

$$S_z(\mathbf{r}) = \frac{1}{2} \operatorname{Re} [\mathbf{E}(\mathbf{r}) \times \mathbf{H}^*(\mathbf{r})] \cdot \hat{\mathbf{z}}, \quad (2.21)$$

The power  $P_z$  that is stored in the optical mode follows from integration of  $S_z$  over a cross-section perpendicular to the  $z$ -axis of the fiber, leading to a relation of  $A$  to  $P$ .<sup>4</sup>

In some books the derivation for the guided modes is done in Cartesian coordinates, which might be convenient for several situations. The cylindrical coordinate components in Eq. (2.16) and Eq. (2.17) can be transformed to their Cartesian counterparts with the well known transformation relation for vector fields

$$\begin{pmatrix} e_x \\ e_y \\ e_z \end{pmatrix} = \begin{pmatrix} \cos(\phi) & -\sin(\phi) & 0 \\ \sin(\phi) & \cos(\phi) & 0 \\ 0 & 0 & 1 \end{pmatrix} \begin{pmatrix} e_r \\ e_\phi \\ e_z \end{pmatrix}. \quad (2.22)$$

The same transformation holds true for the magnetic field components.

After having discussed the shape of the guided modes, we turn our attention to the determination of the propagation constant  $\beta$  of each guided mode for a given frequency  $\omega$ . Equation (2.14) expresses the boundary conditions, any mode has to meet in order to be guided by the fiber. The condition is quadratic in  $J'_l(ha)/ha J_l(ha)$ , so by separating it, two classes of solutions can be found. By convention they are called the EH-modes

$$\frac{J_{l+1}(ha)}{ha J_l(ha)} = \frac{n_1^2 + n_2^2}{2n_1^2} \frac{K'_l(qa)}{qa K_l(qa)} + \left( \frac{l}{(ha)^2} - R \right), \quad (\text{EH}) \quad (2.23)$$

and HE modes

$$\frac{J_{l-1}(ha)}{ha J_l(ha)} = -\frac{n_1^2 + n_2^2}{2n_1^2} \frac{K'_l(qa)}{qa K_l(qa)} + \left( \frac{l}{(ha)^2} - R \right), \quad (\text{HE}) \quad (2.24)$$

where

$$R = \sqrt{\left[ \frac{n_1^2 - n_2^2}{2n_1^2} \right]^2 \left[ \frac{K'_l(qa)}{qa K_l(qa)} \right]^2 + \left[ \frac{l\beta}{n_1 k_0} \right]^2 \left[ \frac{1}{(qa)^2} + \frac{1}{(ha)^2} \right]^2}.$$

Here, the following Bessel function relations were used

$$\begin{aligned} J'_l(z) &= -J_{l+1}(z) + \frac{l}{z} J_l(z), \\ J'_l(z) &= +J_{l-1}(z) - \frac{l}{z} J_l(z). \end{aligned}$$

The convention to name the modes  $\text{EH}_{lm}$  and  $\text{HE}_{lm}$ , where  $l$  denotes the mode number and  $m$  counts the solution number with increasing  $ha$  values, indicates whether the  $z$ -component of the

<sup>4</sup>In section 2.2.1 an analytic expression of  $A$  is given for the case of a single-mode fiber.

electric or magnetic field is larger. For the EH mode  $e_z$  contributes more to the mode than  $h_z$  and vice versa. Equation (2.23) and (2.24) are transcendental and can only be solved numerically or graphically by plotting each side as a function of  $h a$  using

$$(q a)^2 = V^2 - (h a)^2, \quad \text{where} \quad V = 2\pi \frac{a}{\lambda} \sqrt{n_1^2 - n_2^2}. \quad (2.25)$$

The normalized frequency, also called the  $V$ -parameter, determines how many modes can propagate in a fiber as a function of the fiber radius  $a$  divided by the optical wavelength  $\lambda = 2\pi c/\omega$ . For a given  $V$ -parameter one can find intersection points that mark the solutions for existing guided modes. The graphical solutions to both types of modes are shown in Fig. 2.5a and b for  $l = 1$ . It can be seen, that the right hand sides diverge at  $h a = V$  (in the plots  $V$  is set to 8).

It can be shown that, in the case where  $l = 0$  (i.e.  $\partial/\partial\phi = 0$ ), the characteristic mode equations simplifies to

$$\frac{J_1(h a)}{h a J_0(h a)} = -\frac{n_2^2}{n_1^2} \frac{K_1(q a)}{q a K_0(q a)}, \quad (\text{TM}) \quad (2.26)$$

and

$$\frac{J_1(h a)}{h a J_0(h a)} = -\frac{K_1(q a)}{q a K_0(q a)}, \quad (\text{TE}) \quad (2.27)$$

where the relations  $K_0(z) = -K_1(z)$  and  $J_{-1}(z) = -J_1(z)$  were used. Under the second condition Eq. (2.27) the amplitudes  $A$  and  $C$  are equal to zero and one finds that the only non-vanishing field components are  $h_r$ ,  $h_z$  and  $e_\phi$ . In addition, as the electric field is fully transversal, these modes are referred to as transversal electric modes (TE-modes). The first mode class (Eq. (2.26)) is called transversal magnetic modes (TM-modes) as the only remaining components are  $e_r$ ,  $e_z$  and  $h_\phi$  (because  $B = D = 0$ ) and the magnetic field fully transversal. Note that this indeed means, that all other guided modes are explicitly not fully transversal. The graphical solutions to both modes are shown in Fig. 2.5c and d. Note that the right hand side of the TE and TM-modes' characteristic equation is always negative, which in turn leads to a range of the  $V$ -parameter below 2.405, where there is no intersection and therefore no guided mode with  $l = 0$ . However, as can be seen in Fig. 2.5b this is not the case for the  $\text{HE}_{1m}$ -modes, where always at least one solution exists, the  $\text{HE}_{11}$ -mode. This is the fundamental mode of a guided fiber and an optical fiber is called a single-mode fiber, when only this mode is a solution to the characteristic equations. The corresponding single-mode condition is set by the maximum size of the  $V$ -parameter:  $V < 2.405$ .<sup>5</sup> Thus, for a given  $V$ -parameter all propagation constants  $\beta$  can be calculated via Eq. (2.23) and Eq. (2.24). In Fig. 2.6 the refractive index  $\beta/k_0$  of the mode is plotted for the seven lowest order modes as a function of the  $V$ -parameter for  $\lambda = 532$  nm,  $n_1 = 1.46$  (core) and  $n_2 = 1$  (cladding). As can be seen, in order for the modes to propagate inside the fiber, the effective mode index has to lie between these two refractive indices. At its cutoff, each mode has a refractive index that is equal to  $n_2$ . This can be understood, when we consider a fixed wavelength  $\lambda$  for the light field. In this case at cutoff the core radius  $a$  is the

<sup>5</sup>From an experimental point of view the single-mode condition is fulfilled when, for a fixed laser wavelength, the radius of the fiber core is below a certain size. A single-mode waveguide at one wavelength does not guarantee a single-mode waveguide at a shorter wavelength.

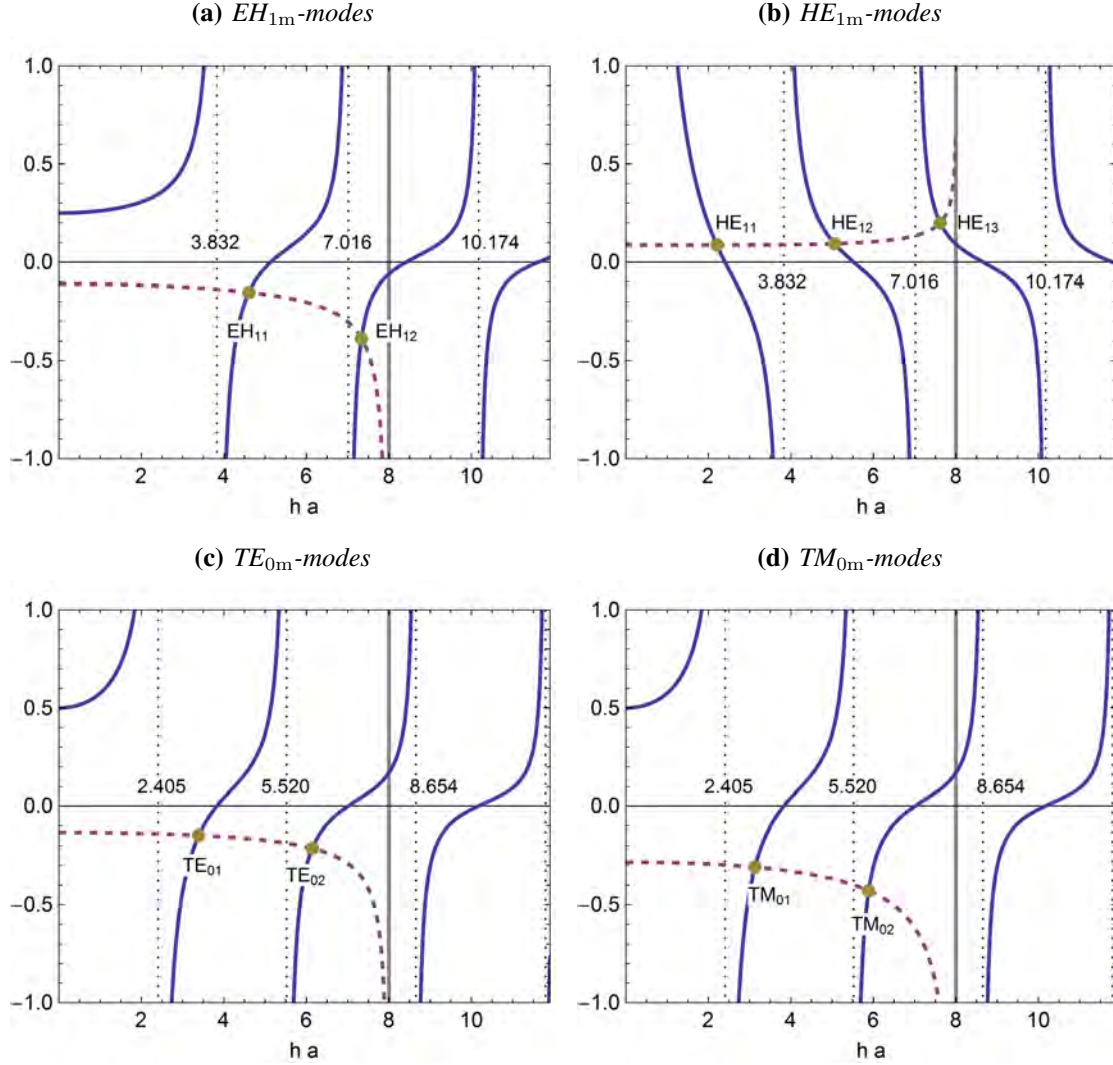


**Figure 2.5: Graphical determination of the propagation constants.** (a) Plot of the left (blue) and right hand side (dashed red) of the characteristic equation Eq. (2.23) for  $EH_{1m}$ -modes, where the  $V$ -parameter is set to 8 (gray). The left hand side diverges at  $ha = 3.832, 7.016, \dots$  (dotted gray). The intersections (yellow dots) mark the two existing modes for the corresponding  $V$ -parameter. (b) Same as in (a) but for the characteristic equation Eq. (2.24) for  $HE_{1m}$ -modes. (c) Same as in (a) but for the characteristic equation Eq. (2.26) for  $TM$ -modes, where the left hand side diverges at  $ha = 2.405, 5.520, \dots$ . (d) Same as in (c) but for the characteristic equation Eq. (2.26) for  $TM$ -modes.

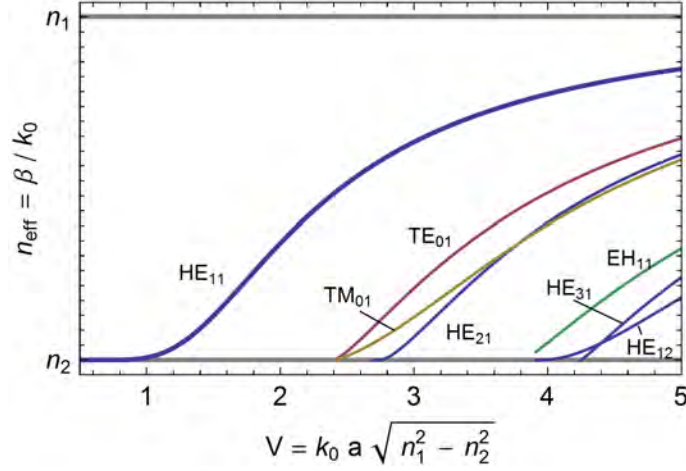


**Figure 2.6: Normalized propagation constants.** Normalized propagation constants as a function of the  $V$ -parameter for the first seven lowest order modes of a step-index circular waveguide with  $\lambda = 532$  nm,  $n_1 = 1.46$  and  $n_2 = 1$ . Note that only the  $HE_{11}$ -mode has no cutoff.

smallest possible for the mode to survive and most of its energy propagates in medium 2. The opposite holds true for very large core radii, where most of the modes' energy propagates in medium 1. To summarize, any fiber supports at least one guided mode, where the exact number is determined by the refractive indices of core and cladding, the optical wavelength and the core radius.

### 2.2.1 The hybrid fundamental modes of an optical nanofiber

For many applications it is necessary that the guided light does not change its properties and does not exhibit e.g. modal dispersion, when the fiber is bent or ambient conditions change. The easiest way to accomplish this requirement is to use a single mode optical fiber. Such a fiber is designed such that its  $V$ -parameter is smaller than 2.405, which means that the fiber only supports the fundamental  $HE_{11}$ -modes. The electric and magnetic field of the fundamental modes can be described with Eq. (2.18) and Eq. (2.19) for the case where  $l = 1$ . It is relevant to note, that the set of modes with quasi-circular polarizations  $\mathbf{c} = +1, -1$  (Eq. (2.18)) and quasi-linear polarizations along  $\hat{x}$  and  $\hat{y}$ , i.e.  $\varphi_0 = 0^\circ, 90^\circ$  (Eq. (2.19)), can both be used to define an orthogonal mode basis for the fundamental guided  $HE_{11}$ -modes. Therefore, in total, a single mode fiber is fully described by four guided modes, that is two orthogonally polarized modes for both propagation directions  $\mathbf{d} = +1$  and  $-1$ , respectively.

In addition, for a guided single-mode light field, an analytical expression can be given that relate

the coefficient  $A$  to the optical power  $P_z$  of that mode. It is

$$\begin{aligned}
 P_z &= P_z^{(in)} + P_z^{(out)}, \\
 P_z^{(in)} &= A^2 \frac{\pi a^2 \omega \epsilon_0}{\beta} \frac{n_1^2 q^2}{v^2 h^2} \left\{ (1-s)(1-s_1) [J_0^2(ha) + J_1^2(ha)] \right. \\
 &\quad \left. + (1+s)(1+s_1) [J_2^2(ha) - J_1(ha) J_3(ha)] \right\}, \\
 P_z^{(out)} &= A^2 \frac{\pi a^2 \omega \epsilon_0}{\beta} n_2^2 \left\{ (1-s)(1-s_2) [K_1^2(qa) - K_0^2(qa)] \right. \\
 &\quad \left. + (1+s)(1+s_2) [K_1(qa) K_3(qa) - K_2^2(qa)] \right\},
 \end{aligned} \tag{2.28}$$

where  $P_z^{(in)}$  ( $P_z^{(out)}$ ) is the part of the total optical power that propagates inside (outside) the core, respectively.

A special case of such single mode fibers are subwavelength-diameter fibers where the role of the cladding is usually played by the vacuum ( $n_2 = 1$ ). Such a so called optical nanofiber can be realized as the waist of a tapered standard optical fiber and is typically produced in a heat and pull process (see Fig. 2.2b). At the waist, the radius of the former core of the standard optical fiber is much smaller than the optical wavelength and therefore does not contribute to guiding the light. Hence, the former cladding takes on the role of the core and the vacuum plays the role of the new cladding. Now, the old cladding radius can be associated with the core radius  $a$  in the previous formulas and for all radii, where  $V < 2.405$  the nanofiber can again be considered to be single-mode. However, in contrast to standard optical fibers, its evanescent field is no longer protected by the cladding medium and can be accessed in the vicinity of the nanofiber surface. In a certain range below the cutoff radius  $a$  the light field is strongly confined and a significant part of the optical power propagates outside of the fiber. Such a situation is depicted in Fig. 2.7a, where the radial intensity profile of the fundamental mode quasi-linearly polarized along  $x$  ( $\varphi_0 = 0$ ) is plotted for experimental parameters oftentimes used in the course of the thesis (nanofiber radius,  $a = 160$  nm; wavelength,  $\lambda = 532$  nm). Inside the fiber the profile resembles that of a Gaussian beam. The discontinuity at the fiber vacuum interface, stems from the boundary condition of the radial component of the electric field and is consequently most pronounced along the polarization axis. The evanescent field intensity extends into the vacuum over several hundred nanometer and is on the order of the intensity in the fiber center, for appropriately chosen fiber radii. As a consequence, matter that is situated in close proximity of the nanofiber surface interacts strongly with the guided light field. Fig. 2.7b shows the intensity at the fiber surface ( $x = a, y = 0$ ) for a fundamental mode quasi-linearly polarized along  $x$  ( $\varphi_0 = 0$ ) as a function of the normalized radius  $a/\lambda$  for two optical wavelengths. The fundamental mode can be confined to an area of approximately  $\lambda^2$ . As can be seen, the intensity on the fiber surface becomes maximal for a certain normalized radius of around  $a/\lambda \simeq 0.23$  and drops for larger and smaller normalized radii. Note that the intensity decays much quicker when decreasing the radius than it does when the radius is increased. This is why, when producing optical nanofibers, one usually chooses slightly larger radii than  $a/\lambda \simeq 0.23$  to avoid optical nanofibers with diameters that are too small, due to variations in

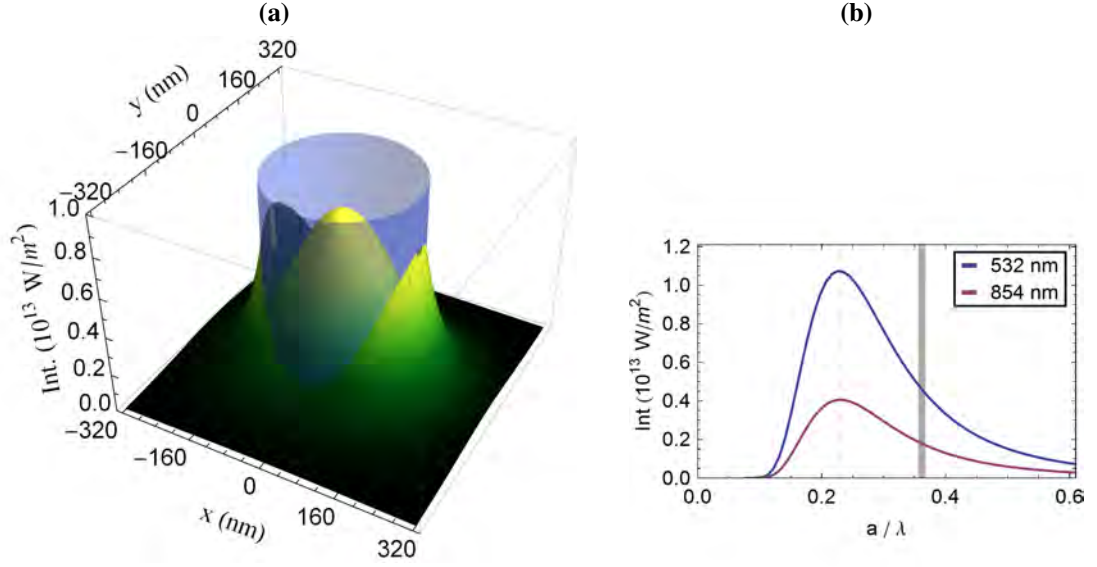


**Figure 2.7: Tapered optical fiber.** (a) Intensity profile of the quasi-linearly polarized fundamental mode with an optical power of  $P_z = 1$  mW in- and outside of a nanofiber (red). The plot parameters used were  $a = 160$  nm,  $\lambda = 532$  nm and  $n_1 = 1.46$ . (b) Intensity of the fundamental mode at the position  $x = a, y = 0$  for the same parameters as in (a) in the case of the blue curve. For the red all parameters are left unchanged apart from the optical wavelength which is  $\lambda = 854$  nm. The dashed line highlights the point  $a/\lambda \simeq 0.23$ , for which the intensity on the fiber surface is approximately maximized. The gray line marks the normalized cutoff radius of the fiber in order to be single mode. Note that they are not exactly the same for both plots.

the production. The intensities in the vicinity of the nanofiber surface are on the order of those in a strongly focused free-space Gaussian beam of equal power and diameter. However, in a free-space beam the focal region is localized in all three dimensions (i.e. in the transversal plane as well as in the axial direction). An optical fiber mode, on the other hand, can in principle be transversally confined over arbitrarily long distances. While this is a clear advantage for many experimental applications, such as surface-adsorbed spectroscopy, it can also present an obstacle, as every particle on or in close proximity of the fiber surface – even unwanted particles, such as dust – can absorb a significant part of the energy stored in the light field.<sup>6</sup>

<sup>6</sup>The exact amount of absorption mainly depends on the medium the particle is made of and the particle size and its distance to the fiber surface.

## 2.3 Radiation modes of the optical fiber

In section 2.2 we found out that the number of guided modes a waveguide can support is larger or equal to one and always finite, so to provide a complete orthogonal set of modes, radiation modes must exist that satisfy the boundary conditions. As a consequence, any electromagnetic field in the presence of the optical fiber can be expressed as the sum over the guided modes plus integrals over the radiation modes. As the derivation of the radiation modes is rather complex, we present only the final results for the electric field components for a step-index optical fiber. A more rigorous approach can be found in various articles [50, 52] and books [49].

In addition to the guided mode solutions in the previous chapter, additional solutions to Equation (2.8) can be found – the radiation modes. For these modes the longitudinal propagation constant  $\beta$  is continuous for a given  $\omega$  and, in contrast to Eq. (2.11), varies as

$$-n_2 \frac{\omega}{c} < \beta < n_2 \frac{\omega}{c} . \quad (2.29)$$

For an optical fiber with a cladding radius that is extended to infinity, the mode functions  $\tilde{e}^{(\nu)}(\mathbf{r})$  of the electric field  $\tilde{\mathbf{E}}_{\text{rad}}^{(\nu)}(\mathbf{r}, t)$  of the radiation modes are labeled by the mode index  $\nu = (\omega, \beta, \mathbf{c}, l)$  and are given by

$$\begin{aligned} \tilde{e}_r^{(\nu)}(r) &= \mathfrak{i} \frac{1}{h^2} \left[ \beta h \tilde{A} J_l'(hr) + \mathfrak{i} l \frac{\omega \mu_0}{r} \tilde{B} J_l(hr) \right] \\ \tilde{e}_\phi^{(\nu)}(r) &= \mathfrak{i} \frac{1}{h^2} \left[ \mathfrak{i} l \frac{\beta}{r} \tilde{A} J_l(hr) - h \omega \mu_0 \tilde{B} J_l'(hr) \right] \\ \tilde{e}_z^{(\nu)}(r) &= \tilde{A} J_l(hr) , \end{aligned} \quad (2.30)$$

inside the fiber core  $r < a$  and

$$\begin{aligned} \tilde{e}_r^{(\nu)}(r) &= \mathfrak{i} \frac{1}{q^2} \sum_{j=1,2} \left[ \beta q \tilde{C}_j H_l^{(j)'}(qr) + \mathfrak{i} l \frac{\omega \mu_0}{r} \tilde{D}_j H_l^{(j)}(qr) \right] \\ \tilde{e}_\phi^{(\nu)}(r) &= \mathfrak{i} \frac{1}{q^2} \sum_{j=1,2} \left[ \mathfrak{i} l \frac{\beta}{r} \tilde{C}_j H_l^{(j)}(qr) - q \omega \mu_0 \tilde{D}_j H_l^{(j)'}(qr) \right] \\ \tilde{e}_z^{(\nu)}(r) &= \sum_{j=1,2} \tilde{C}_j H_l^{(j)}(qr) , \end{aligned} \quad (2.31)$$

in the cladding region  $r > a$ . Here,  $H_l^{(j)}$  are the Hankel functions of the  $j$ -th kind of order  $l$ . The amplitudes  $\tilde{C}_j$  and  $\tilde{D}_j$ , with  $j = 1, 2$ , can be related to  $\tilde{A}$  and  $\tilde{B}$  such that only those two coefficients are linearly independent, where the polarization index  $\mathbf{c} = +1, -1$  labels two such choices of  $\tilde{A}$  and  $\tilde{B}$ .<sup>7</sup> It is

$$\begin{aligned} \tilde{C}_j &= \mathfrak{i} (-1)^j \frac{\pi q^2 a}{4 n_2^2} \left( \tilde{A} L_j + \mathfrak{i} \mu_0 c \tilde{B} V_j \right) \\ \tilde{D}_j &= \mathfrak{i} (-1)^{j-1} \frac{\pi q^2 a}{4} \left( \mathfrak{i} \epsilon_0 c \tilde{A} V_j - \tilde{B} M_j \right) , \end{aligned} \quad (2.32)$$

<sup>7</sup>  $\mathbf{c}$  is used to distinguish between two degenerate polarization modes

where

$$\begin{aligned} V_j &= \frac{l k \beta}{a h^2 q^2} (n_2^2 - n_1^2) J_l(h a) H_l^{(j)*}(q a) \\ M_j &= \frac{1}{h} J'_l(h a) H_l^{(j)*}(q a) - \frac{1}{q} J_l(h a) H_l^{(j)*'}(q a) \\ L_j &= \frac{n_1^2}{h} J'_l(h a) H_l^{(j)*}(q a) - \frac{n_2^2}{q} J_l(h a) H_l^{(j)*'}(q a) . \end{aligned} \quad (2.33)$$

The magnetic field components can be derived from the electric components via Eq. (2.1d). Orthogonality of the radiation modes requires

$$\int_0^{2\pi} d\phi \int_0^\infty n^2(r) [\tilde{e}^{(\nu)} \tilde{e}^{(\nu')*}]_{\beta=\beta', l=l'} r dr = N_\nu \delta_{\nu\nu'} \delta(\omega - \omega') , \quad (2.34)$$

where  $n(r)$  is  $n_2$  for  $r < a$  and  $n_1$  for  $r > a$ . A convenient choice for two polarizations is to define  $A$  as a real number and  $\tilde{B} = i \eta \tilde{A}$  and  $\tilde{B} = -i \eta \tilde{A}$  for  $\nu = -1$  and  $+1$ , respectively, which leads to

$$\eta = \epsilon_0 c \sqrt{\frac{n_2^2 |V_j|^2 + |L_j|^2}{|V_j|^2 + n_2^2 |M_j|^2}} . \quad (2.35)$$

The normalization constant  $N_\nu$  that is usually set to 1 can be expressed as

$$N_\nu = \frac{8 \pi \omega}{q^2} \left( n_2^2 |C_j|^2 + \frac{\mu_0}{\epsilon_0} |D_j|^2 \right) . \quad (2.36)$$

Together with the guided modes this complete orthogonal set of modes can be used to calculate the spontaneous emission of a scatterer in the vicinity of the fiber.

## 2.4 Tapered optical fibers

In the previous sections optical properties of fibers and nanofibers have been discussed. Nanofibers are typically realized at the waist of a biconical tapered standard optical fiber that is usually made of a pure silica cladding and a doped silica glass core [53]. So, in order to realize a nanofiber, the glass of the standard optical fiber has to be heated up to a temperature where it undergoes a so-called glass transition. In this regime the glass starts to melt and behaves somewhat rubber-like. At that point one can literally stretch the fiber, thereby pulling material out of the molten region. This leads to a reduction of the volume/radius and with a reproducible method of this concept one can in principle realize arbitrary nanofiber radii in the center of the molten area. The transition area between the fiber waist and the cold and unprocessed part is called the taper region (see Fig. 2.8). In principle, the radius profile in the taper region can be designed such that the core guided mode transfers adiabatically into a cladding guided mode and back again to the core guided case. In this case close to unit transmission from one unprocessed fiber end to the other can be achieved. A detailed analysis of the adiabatic transfer and the coupling to higher order modes can be found in [54]. In a very clean production environment it is possible to achieve transmission values of  $\geq 98\%$  through the tapered optical fiber. The fabrication method with which all tapered optical fibers for this thesis have been produced is a carefully designed flame pulling process. It is presented in section 2.4.1.



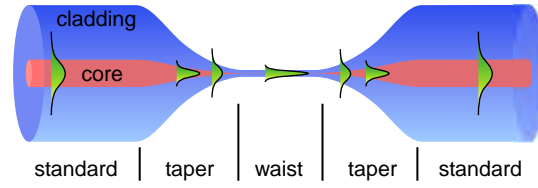


**Figure 2.8: Tapered optical fiber.** Schematic of a tapered optical fiber indicating the mode conversion from (i) the unprocessed standard optical fiber via (ii) the taper region to the (iii) nanofiber waist with a sub-wavelength diameter  $a$  and back. The intensity distribution of the guided mode is schematically represented by the green curves.

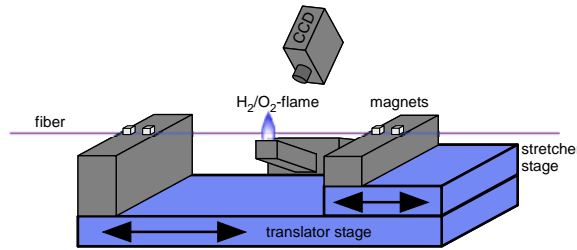


**Figure 2.9: Pulling rig.** Schematic of the pulling rig used in this group. The fiber is fixed onto the two translation stages by magnets and a CCD camera is used to guarantee that the fiber is clean. Once the fiber is heated up by the flame, the translator stage moves the fiber through the flame while the stretcher stage stretches the fiber.

### 2.4.1 TOF fabrication using a flame brushing technique

In this section we discuss the production technique for tapered optical fibers that is used in our group, the flame-brushing technique. All tapered optical fibers used in this thesis were fabricated in a pulling rig, that was designed by F. Warken, which used this technique [55]. Figure 2.9 shows a schematic of it. The working steps to fabricate a tapered optical fiber are described in the following.

The pulling rig is situated in a clean box with high-efficiency particle (HEPA) filters to ensure a dust-free environment. A standard optical fiber has a polymer protection layer (jacket) around its cladding and core. Before such a fiber can be heated up, this layer has to be removed and subsequently cleaned thoroughly with lens tissues and highly purified acetone. After the cleaning process the fiber is placed into two v-groove fiber holders and fixed with magnets. The fiber holders themselves are fixed onto translation stages as it is sketched in Fig. 2.9. To be sure the fiber is indeed clean the fiber can be monitored with a CCD camera using a microscope objective.<sup>8</sup> After the fiber is fixed and confirmed to be clean, a software controlled program can be started for the final production of a tapered optical fiber. The translator stage constantly

<sup>8</sup>The working step to inspect the fiber after it has been placed on the fiber holders has only recently been included into the pulling routine leading to less transmission losses in average and, as a consequence, more deterministic results.

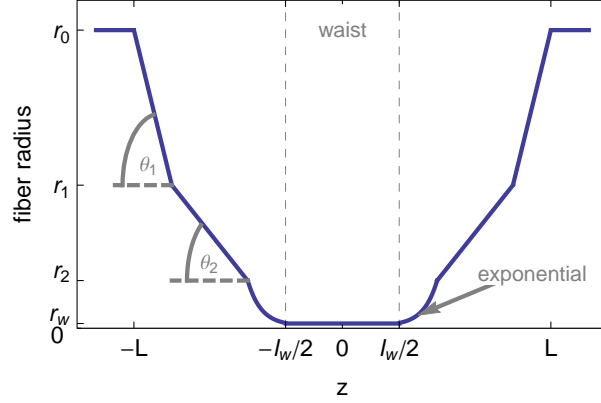


**Figure 2.10: Radial fiber taper profile.** The fiber taper profile used in the course of this work consists of two linear and one exponential decreasing radius section and is defined by the angles  $\theta_1$ ,  $\theta_2$ , the radii  $r_0$ ,  $r_1$ ,  $r_2$ ,  $r_w$  and the waistlength  $l_w$ . The section labeled as waist is the part of the tapered optical fiber, what will be referred to as the optical nanofiber.

moves a part of the fiber back and forth through the  $\text{H}_2/\text{O}_2$ -flame that keeps this part in a molten-like state. Meanwhile the other translation stage moves one fiber holder away from the other, thereby stretching the fiber. After the fabrication process the tapered optical fiber is fixed on a fiber mount using UV-curing glue to transport it to the experimental setup.

The physical mechanisms behind this flame brushing technique are understood and it is therefore possible to fabricate nearly arbitrary radius profiles by computing the translation stage trajectories during the tapering process in advance. The typical profile used in this work can be seen in Fig. 2.10. With this profile it is possible to transfer the core-guided mode (unprocessed fiber) adiabatically into a cladding guided mode (fiber waist). The most critical region for standard optical fibers ( $r_0 = 62.5 \mu\text{m}$ ) is typically in the region around  $20 \mu\text{m}$ , where a small gradient of about 1 mrad ensures an adiabatic mode transfer. Together with (i) the purities of the  $\text{H}_2/\text{O}_2$ -flame, (ii) the cleanliness of the unprocessed fiber, (iii) the dust-free environment, (iv) the smooth tapered optical fiber surface, due to the high surface tension during the fabrication process, it is possible to optimize tapered optical fibers for any wavelength that is to be used in the experiment. In our group, we reach transmission values of  $\geq 98\%$  compared to the unprocessed fiber. The variation of the most important parameter, the waist radius  $r_w$ , is empirically found to be  $\pm 5\%$  of the desired value that is an input parameter of the pulling software.

## Metal Nanoparticles

From everyday experience we know that metals reflect light in the visible regime. However, when the dimensions of the metal are on the order of or even below the wavelength of the incident light field, distinct and somewhat unexpected phenomena can occur. Such sub-wavelength metal nanoparticles are formed by 1 to 100 million metal atoms and exhibit unique physical properties due to their high surface to volume ratio and their ability to strongly confine electromagnetic waves that impinge on them. Additionally, because of the characteristic optical response of metals in general and the nanoparticle's boundary constraints, so called localized plasmon resonances arise in the visible regime that can lead to extraordinary high field enhancements and surprising spectral features. The optical properties of nanoparticles have been used in ancient times as coloring matter, where e.g. nanoparticles have been embedded in glass. The most prominent example for this is probably the Lycurgus cup [56] (see Fig. 3.1). When illuminated from behind with white light, due to the spectral features of the metal nanoparticles in the glass, it shows a very rich shading of colors ranging from green to red. In the last



**Figure 3.1: Lycurgus cup.** Roman glass cage cup from the 4th-century. The glass is enriched with gold nanoparticles. Left panel: Illumination from the front leads to green reflected light. Right panel: Illumination from behind shows ruby red colors. The exact mechanism behind it was discovered by the Viennese Richard Zsigmondy, who received the Nobel Prize for Chemistry in 1925 for his research in this field [57]. The Lycurgus cup is exhibited in the British Museum, London.

decades, plasmonics research field lead to a vast amount of exciting applications and proposals [58]: Metal nanoparticles or nanofilms were used for optical sensing of DNA [59, 60], cancer treatment [61–63], single molecule detection [64–66], near-field optical microscopy [67], making objects invisible through negative refractive indices [68–71] and many more applications. Plasmonics also promises to give a major impetus to the field of quantum optics [72–75] and optical computing [76–78] as well as to applications such as data storage [79], optoelectronics [80–82] and photovoltaics [83, 84]. Consequently, plasmonic nanostructures have the potential to significantly influence modern society.

How small particles absorb and scatter light can only be described when we have knowledge on (i) how a material reacts to an electromagnetic field with respect to its wavelength and (ii) how the field reacts when material boundaries are imposed on it. In this chapter the theoretical background for the interaction of light with matter is presented in section 3.1. It turns out that, by approximating the electrons inside the material as harmonic oscillators, dielectric materials and – as a special case of this situation – metals can be well described. The respective model is called Lorentz model for dielectrics (Sect. 3.1.1) and Drude model in case of metals (Sect. 3.1.2). In reality however, the Drude model struggles to explain the optical response of metals for the visible regime, which is why phenomenological models like the Drude-Lorentz model (Sect. 3.1.3) are typically used in its place. This thesis mostly deals with gold nanoparticles in its course, which is why the optical response of gold is explicitly given in section 3.1.4.

Section 3.2 is devoted to the situation when the size of a metal structure, e.g. a sphere, is on the order of the wavelength of the light that impinges upon the sphere’s surface. In these circumstances the light field will be scattered or absorbed by the sphere (Sect. 3.2.1), exerting a restoring force on to the electron gas which leads to a collective oscillation, the so-called localized plasmon surface resonance. This phenomenon and corresponding consequences, such as a field amplification in the vicinity of the metal nanoparticle, will be explained with a quasi-static model (Rayleigh theory) in section 3.2.2 and, for the case where the particle size becomes larger, with a fully analytical approach (Mie theory) in section 3.2.3.

The theoretical descriptions in the above mentioned sections will summarize the excellent treatments presented in the books by Jackson [51], Bohren and Huffman [85], Novotny and Hecht [28], and Maier [86].

## 3.1 Optical properties of materials

The interaction between an electromagnetic field and a material is mainly influenced by the frequency dependence of the complex dielectric function of the material. While, in general, a correct treatment of the properties of solids requires a quantum mechanical approach, many interesting features are well explained on the basis of classical physics.

It turns out that the electromagnetic response of a dielectric is well described by approximating the electron cloud around a nucleus by a damped, driven harmonic oscillator where the restoring and driving force are associated with the natural frequency of the electron cloud oscillation and the electromagnetic field, respectively. This classical model was developed by Hendrik Antoon Lorentz (1906).

In the case of metals, Paul Drude (1900) assumed that the valence electrons are completely un-

bound and constantly collide with the heavy and immobile nuclei. The dielectric function for a Drude-metal can then be directly deduced from the Lorentz theory by omitting the restoring force that is present in the case of a dielectric. The Drude-model was later on extended by Arnold Sommerfeld by expanding it to quantum mechanical observations. In the case of noble metals damping mechanisms occur in the visible regime, which are well described by a phenomenological model called the Drude-Lorentz model, which basically combines the two simple models from above by adding bound-electron contributions to the dielectric function of the free-electron model.

### 3.1.1 Lorentz model for dielectric media

The electromagnetic response of a material is described by its complex relative permittivity<sup>1</sup>  $\epsilon_r = \epsilon'_r + i\epsilon''_r$  and its complex relative permeability  $\mu_r = \mu'_r + i\mu''_r$ , both of which are linked to the complex refractive index  $n = n' + i n'' = \sqrt{\epsilon_r \mu_r}$ . Here, the real (imaginary) part of the physical quantities is denoted by one (two) prime(s), respectively.

A classical explanation for the optical response of a dielectric polarizable medium can be found when we treat the material as a group of identical, independent harmonic oscillators. To distinguish the Lorentz and Drude Model, that will be discussed in the following section, some Lorentz model-symbols will have a  $\sim$  attached to them. If, for simplicity, we assume that the material is non-magnetic ( $\mu_r = 1$ ), the corresponding equation of motion for a single electron of charge  $-e$  can be written as:

$$\tilde{m}_e \partial_t^2 \mathbf{r} + \tilde{m}_e \tilde{\gamma} \partial_t \mathbf{r} + \tilde{m}_e \omega_0^2 \mathbf{r} = -e \mathbf{E}(\mathbf{r}, t), \quad (3.1)$$

with the effective electron mass  $\tilde{m}_e$  of the bound electron, the damping rate  $\tilde{\gamma}$  and the natural frequency  $\omega_0$ . Furthermore, the notation  $\partial_t = \partial/\partial t$  is used. We can Fourier-transform Eq. (3.1) to describe the amplitude of the electron oscillation  $\mathbf{r}$  in terms of the driving field  $\mathbf{E} \propto e^{-i\omega t}$  and its frequency  $\omega$ .<sup>2</sup> The corresponding microscopic electric dipole moment  $\mathbf{d}$  reads

$$\begin{aligned} \mathbf{d}(\omega) &= e \mathbf{r}(\omega) \\ &= \frac{e^2}{\tilde{m}_e (\omega_0^2 - \omega^2) - i\omega \tilde{\gamma}} \mathbf{E}(\omega). \end{aligned} \quad (3.2)$$

The dipole moment can also be written in terms of its complex polarizability  $\alpha$ ,<sup>3</sup> which gives

$$\mathbf{d} = \alpha \mathbf{E}. \quad (3.3)$$

Now, if we assume the material to consist of  $N$  oscillators per unit volume a macroscopic polarization  $\mathbf{P}$  can be derived:

$$\begin{aligned} \mathbf{P}(\omega) &= N \mathbf{d}(\omega) \\ &= \epsilon_0 \chi_e(\omega) \mathbf{E}(\omega), \end{aligned} \quad (3.4)$$

<sup>1</sup>The permittivity is often also referred to as the dielectric function or, misleadingly, the dielectric constant of a material.

<sup>2</sup>Note that  $\mathbf{E}$  is related to the real value of the electric field by  $\mathcal{E} = 1/2 (\mathbf{E} + \mathbf{E}^*)$ .

<sup>3</sup>Here, the polarizability is defined as a scalar. However, in general, the polarizability  $\vec{\alpha}$  is a tensor.

where  $\epsilon_0$  is the vacuum permittivity and

$$\chi_e = \frac{\check{\Omega}_p^2}{(\omega_0^2 - \omega^2) - \mathfrak{i} \omega \check{\gamma}}, \quad (3.5)$$

$$\check{\Omega}_p = \sqrt{\frac{N e^2}{\check{m}_e \epsilon_0}}, \quad (3.6)$$

are the electric susceptibility and plasma frequency of the material. With the relations  $\mathbf{D} = \epsilon_0 \epsilon_r \mathbf{E}$  and  $\mathbf{D} = \epsilon_0 \mathbf{E} + \mathbf{P}$  for the macroscopic dielectric displacement  $\mathbf{D}$ , we arrive at the desired result for the complex relative electric permittivity  $\epsilon_r = \epsilon'_r + \mathfrak{i} \epsilon''_r$  of a material with a single resonance  $\omega_0$ :

$$\begin{aligned} \check{\epsilon}_r(\omega) &= 1 + \chi_e(\omega) = 1 + \frac{\check{\Omega}_p^2}{(\omega_0^2 - \omega^2) - \mathfrak{i} \check{\gamma} \omega}, \\ \check{\epsilon}'_r(\omega) &= 1 + \frac{\check{\Omega}_p^2 (\omega_0^2 - \omega^2)}{(\omega_0^2 - \omega^2)^2 + \check{\gamma}^2 \omega^2}, \\ \check{\epsilon}''_r(\omega) &= \frac{\check{\gamma} \check{\Omega}_p^2 \omega}{(\omega_0^2 - \omega^2)^2 + \check{\gamma}^2 \omega^2}. \end{aligned} \quad (3.7)$$

This way of describing atomic scale resonances is extremely general. Regardless of what is actually causing the resonance, one can always fit the parameters above to the problem under consideration to describe that resonance.

In Fig. 3.2a,c,e, the optical response of a material described with the Lorentz model is plotted in terms of different physical quantities, for some typical parameter values ( $\omega_0 = 2 \text{ eV}$ ,  $\check{\Omega}_p = 4 \text{ eV}$ ,  $\check{\gamma} = 0.5 \times 10^{15} \text{ s}$ ). For a beam of light incident from air that hits the material at normal incidence, the reflectance of a material is defined as  $R(\omega) = \mathfrak{r} \mathfrak{r}^*$ , with  $\mathfrak{r}(\omega) = (1 - n)/(1 + n)$  being the reflection coefficient. The plots depict four regions, where the material reacts differently:

( $\omega \ll \omega_0$ ) At energies well below the resonance frequency, both, the permittivity and the refractive index are purely real as the electrons are able to oscillate in phase with the driving force. The permittivity is non-zero, which is called the dc-offset, and slowly increasing with  $\omega$ , also known as normal dispersion. Panel (e) shows that in this regime, the material's reflection is rather small. Such a feature corresponds to a transparent material such as glass. As we will see in the next section, such a small reflectance does not occur in the case of metals.

( $\omega \simeq \omega_0$ ) On resonance the oscillation is out of phase with the electromagnetic field and the properties of the material become very different. This can for example be seen by the strong decrease of the real part of the permittivity, labeled as anomalous dispersion, down to negative values. Also the imaginary part of the refractive index, i.e. the extinction coefficient, that describes how a wave decays when propagating in the material, becomes maximal. The decay rate determines the width of the resonance.

( $\omega_0 < \omega < \check{\Omega}_p$ ) In between resonance and the plasma frequency the imaginary part of the refractive index is larger than the real part and the material is reflective.

( $\omega \gg \check{\Omega}_p$ ) Well above the plasma frequency normal dispersion is observed again, the losses are very low and the material becomes transmissive once more.

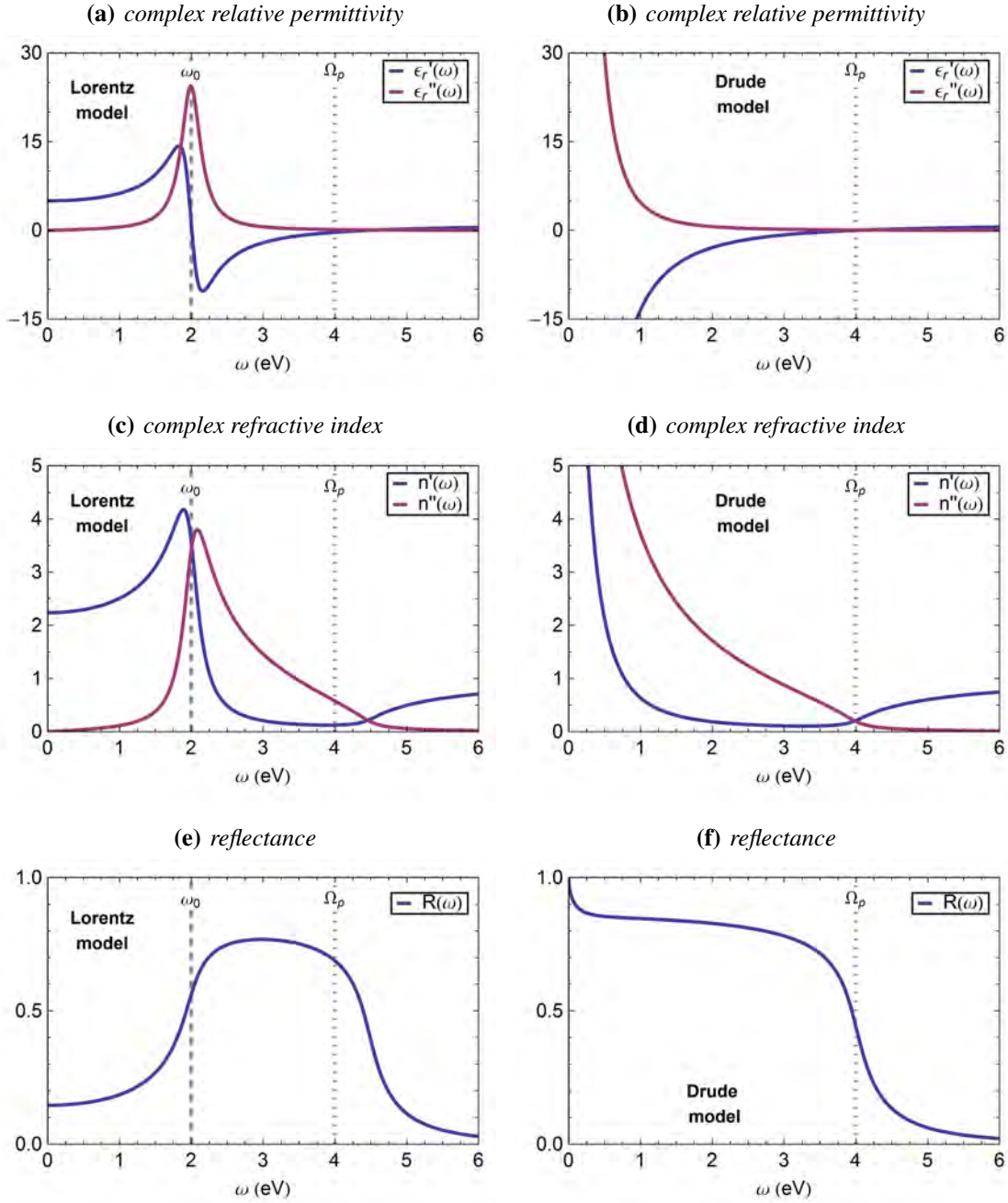


**Figure 3.2: Optical response of the Lorentz and Drude model.** (a) Plot of the real (blue) and imaginary (red) part of the relative permittivity. (c) Same as in (a) but for the complex refractive index. (e) Plot of the reflectance of the material for a beam of light at normal incidence in air. In all plots the parameters  $\omega_0 = 2$  eV,  $\tilde{\Omega}_p = \tilde{\Omega}_p = 4$  eV and  $\tilde{\gamma} = \tilde{\gamma} = 0.5 \times 10^{15}$ /s were used. (b,d,f) Same as (a,c,e) for the Drude model presented in section 3.1.2 where a restoring force, i.e. a natural frequency  $\omega_0$ , does not exist.

### 3.1.2 Drude model for metals

In contrast to dielectric media, metals exhibit conduction electrons that are unbound and able to move freely within the bulk of the metal. The corresponding equation of motion can be easily deduced from the case of a dielectric medium (Eq. (3.1)) by removing the restoring force term. This yields

$$\tilde{m}_e \partial_t^2 \mathbf{r} + \tilde{m}_e \tilde{\gamma} \partial_t \mathbf{r} = -e \mathbf{E}(\mathbf{r}, t), \quad (3.8)$$

where  $\tilde{m}_e$  is the effective mass of the free electrons,<sup>4</sup> and  $\tilde{\gamma}$  is the relaxation time of the free electron gas. In contrast to the previous chapter, some symbols will have a  $\sim$  attached to them. If perform on Eq. (3.8) the same operations like in the case of the Lorentz model (Sect. 3.1.1) we end up with a formula for the complex relative dielectric permittivity  $\tilde{\epsilon}_r = \tilde{\epsilon}'_r + i \tilde{\epsilon}''_r$ , that reads

$$\begin{aligned} \tilde{\epsilon}_r(\omega) &= 1 - \frac{\tilde{\Omega}_p^2}{\omega^2 + i \omega \tilde{\gamma}}, \\ \tilde{\epsilon}'_r(\omega) &= 1 - \frac{\tilde{\Omega}_p^2}{\omega^2 + \tilde{\gamma}^2}, \\ \tilde{\epsilon}''_r(\omega) &= \frac{\tilde{\gamma} \tilde{\Omega}_p^2}{\omega(\omega^2 + \tilde{\gamma}^2)}. \end{aligned} \quad (3.9)$$

Note that

$$\tilde{\Omega}_p = \sqrt{\frac{\tilde{N} e^2}{\tilde{m}_e \epsilon_0}}, \quad (3.10)$$

is the plasma frequency for the Drude model, with  $\tilde{N}$  being the free electron density. In this equation the resonance frequency term is removed compared to Eq. (3.7). In Fig. 3.2**b,d,f**, the optical response of a Drude material is plotted for the same parameters used in the Lorentz model plots in Fig. 3.2**a,c,e**. As a Drude metal excludes restoring forces and thus a resonance frequency  $\omega_0$ , the plots can be divided into three regions :

( $\omega \ll \tilde{\Omega}_p$ ) Below the plasma frequency, in comparison with a dielectric medium described by the Lorentz model, the imaginary part of the permittivity and refractive index is very large, leading to the well known feature of metals being reflective. While the imaginary part of the permittivity diverges, the real part actually saturates at a large negative value of  $\tilde{\epsilon}_r(0) = 1 - \tilde{\Omega}_p^2/\tilde{\gamma}^2$  compared to the Lorentz model counterpart.

( $\omega \simeq \tilde{\Omega}_p$ ) In the small damping regime, i.e.  $\tilde{\gamma} \ll \omega$ , the permittivity  $\tilde{\epsilon}_r$  approximately zero for  $\omega = \tilde{\Omega}_p$ . From Maxwell's equations it can be deduced that this excitation can be associated with a longitudinal collective oscillation of the electron gas, known as a plasma oscillation. As such, it can not be excited by transverse electromagnetic fields. In quantum mechanics, the quanta of these longitudinal charge oscillations are called (volume) plasmons.<sup>5</sup>

( $\omega \gg \tilde{\Omega}_p$ ) Above the plasma frequency, the real part of the permittivity becomes positive while the imaginary part tends towards zero. This results in a metal being weakly absorbing well

---

<sup>4</sup>The effective mass of free electrons are in general not the same as the mass of bound electrons for the case of the Lorentz model in section 3.1.1.

<sup>5</sup>The term 'volume' is given to distinguish it with the localized surface plasmons discussed later in this chapter.



above the plasma frequency which is exactly the same for a dielectric material. As the plasma frequency for metals tends to lie in the ultraviolet regime, this phenomenon is known as the ultraviolet transparency and can be used to filter high frequency radiation.

Another way of describing such a Drude metal is to rewrite the imaginary part in Eq. (3.9) such that  $\tilde{\epsilon}_r'' = \sigma/(\epsilon_0 \omega)$ , where the conductivity  $\sigma$  is defined as

$$\sigma = \frac{\tilde{\gamma}^2}{\omega^2 + \tilde{\gamma}^2} \sigma_0 . \quad (3.11)$$

In the limit of  $\omega \rightarrow 0$  the conductivity becomes the DC-conductivity

$$\sigma_0 = \frac{\epsilon_0 \tilde{\Omega}_p^2}{\tilde{\gamma}} , \quad (3.12)$$

which is the proportionality factor in Ohm's law for Drude metals ( $\mathbf{J} = \sigma_0 \mathbf{E}$ ). For realistic estimates of the values  $\tilde{\Omega}_p$  and  $\tilde{\gamma}$  one derives DC-conductivities around  $10^6/(\Omega \text{ m})$ , which is indeed about the right order of magnitude for typical metals (Chromium:  $5 \times 10^6/(\Omega \text{ m})$ , Gold:  $5 \times 10^7/(\Omega \text{ m})$ ). It is important to note that electric conductivity of a material should be discussed in the framework of quantum mechanics rather than in a classical Drude model. However, this discussion should give a qualitative idea about how a metal that is electrically conductive at low frequencies behaves surprisingly different at frequencies around its plasma frequency and above and paves the way for describing the phenomena discussed in the second part of this chapter (see Sect. 3.2).

Although the association of a realistic metal with an electron gas is a strong approximation, the Drude model can successfully describe many properties of metals. It is possible to modify the Drude model slightly to include a contribution of the bound electrons to the polarizability of the material by replacing the '1' in Eq. (3.9) with a phenomenological dielectric constant  $\epsilon_\infty$ . Yet again, the model breaks down in the visible regime for many metals due to the occurrence of interband transitions, that will be introduced in the following section (Sect. 3.1.4). For an accurate prediction of the optical response of metals, usually, extended phenomenological models that combine the Lorentz and the Drude model are fitted to experimentally measured datasets.

### 3.1.3 Phenomenological Drude-Lorentz model for real metals

In reality a metal does not only consist of oscillating conduction electrons, of course. It also exhibits electrons that are bound to lower bands and that can be excited if the energies are high enough. While for alkali metals the Drude model describes the optical response of a metal adequately up to energies of ultra violet light, for noble metals it does not reproduce their permittivity already in the visible regime.

The absorption of light by a material can be divided into two processes – intraband and interband transitions. An excitation of an electron within the conduction or valence band of the crystal is called intraband transition. As long as the Pauli principle<sup>6</sup> is obeyed the excitation

<sup>6</sup>The Pauli principle is a quantum mechanical term which demands that two fermions, e.g. electrons, cannot occupy the same quantum mechanical state.

energies are continuous within the band and can be arbitrarily small. However, in an insulator all bands are completely filled or empty which is why such intraband transitions occur essentially in metals only. Thus, due to the conduction electrons, low electromagnetic energies can be absorbed in case of a metal, while in a dielectric interband excitations dominate the absorption characteristics. Simply speaking, the intraband absorption is the reason why conductors are usually highly absorbing and reflective in the visible and infrared regime, while insulators tend to be transparent and weakly reflecting. In the Drude model, the intraband transitions are quantified with the imaginary part  $\tilde{\epsilon}''$  of the permittivity (3.9). Above a certain energy, interband transitions set in and photons can excite electrons from lower bands very efficiently to the conduction band. In this case only distinct energies or energy intervals are absorbed. Interband effects are the main reason why the Drude model fails to describe metals in the visible/UV-regime.

As it happens, interband transitions can be well described with the Lorentz model discussed in section 3.1.1. So by combining both, intraband effects expressed by the Drude model and interband effects described by the Lorentz model, a phenomenological Drude-Lorentz model of the complex permittivity  $\epsilon_r$  of a material can be constructed:

$$\begin{aligned}\epsilon_r(\omega) &= \tilde{\epsilon}_{r,0}(\omega) + \sum_{j=1}^k f_j \tilde{\epsilon}_{r,j}(\omega) , \\ \tilde{\epsilon}_{r,0}(\omega) &= 1 - \frac{\tilde{\Omega}_p^2}{\omega^2 + \mathfrak{i} \omega \tilde{\gamma}_0} , \\ \tilde{\epsilon}_{r,j}(\omega) &= \frac{\tilde{\Omega}_p^2}{(\omega_{0,j}^2 - \omega^2) - \mathfrak{i} \tilde{\gamma}_j \omega} .\end{aligned}\tag{3.13}$$

The model uses empirically found values for a Drude-material with  $k$  Lorentz oscillators with resonance frequency  $\omega_{0,j}$ , strength  $f_j$  and lifetime  $\tilde{\gamma}_j$  that are fitted to measured datapoints of the material to be described.

#### 3.1.4 Optical properties of gold

In the course of this work a lot of experiments have been carried out with gold. Thus, we discuss the above acquired formulations in this context. Gold (Au) is a group 11 element together with copper, silver and roentgenium. It is very inert, so exposing it to air for example is not causing it to degrade. This makes it an ideal candidate for applications or research where metallic features are required without the ability to shield the metal from its environment. As a noble metal, its 5d-shell is completely filled, so the metallic properties originate from its half filled 6s-shell. The electrons form a metallic bond that leads to a free electron density of  $\tilde{n}_e \simeq 5.98 \times 10^{28}/\text{m}^3$ . The bandstructure exhibits five relatively flat d-bands and an sp-hybridized conduction band, that is filled with electrons up to the Fermi level  $E_{\text{Fermi}}$ . In Fig. 3.3 we can see that the conduction band is almost parabolic, which is what we would expect for a free electron gas (energy  $\propto k^2$ , see e.g. [87]). The optical excitation of a 5d-electron into the sp-band can be associated with an interband transition. In the case of gold, the most pronounced interband absorption sets in at 2.38 eV i.e. 520 nm [88], which is the reason for a constantly increasing absorption for higher

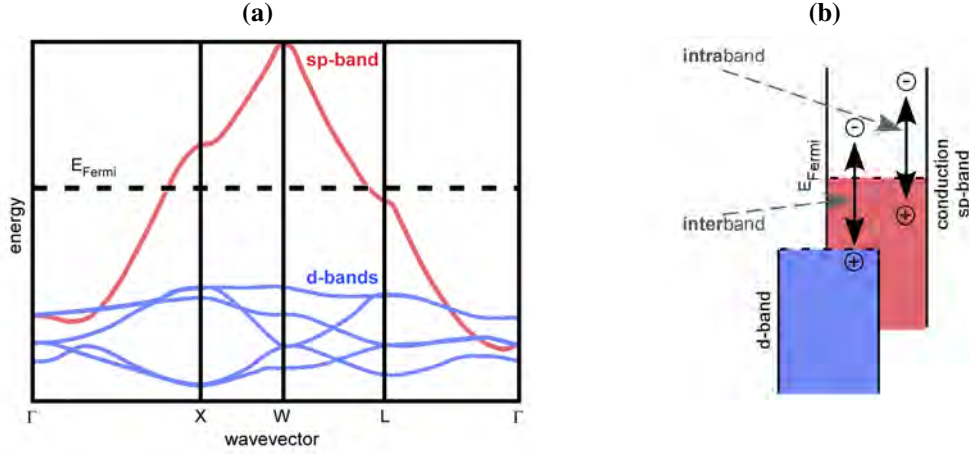


**Figure 3.3: Band structure gold.** (a) Band structure of gold. While the d-bands (blue), and its highest member the 5d-band, are rather flat the sp-band (red) is more or less parabolic in shape. The wavevectors  $\Gamma$ , X, W and L denote high-symmetry points inside the Brillouin zone of gold. The calculated data is taken out of [89]. (b) Sketch of the two important non-radiative decay channels: intra- and interband transitions.

<b>Gold</b>	$j = 0$	$j = 1$	$j = 2$	$j = 3$	$j = 4$	$j = 5$
$f_j$	0.760	0.024	0.010	0.071	0.601	4.384
$\tilde{\gamma}_j$	0.053	0.241	0.345	0.870	2.494	2.214
$\hbar\omega_{0,j}$		0.415	0.830	2.969	4.304	13.32

**Table 3.1: Drude-Lorentz fit parameters for gold.** Fit parameters from [90] for semitransparent gold films. Note that for the Drude term  $\tilde{\epsilon}_{r,0}$  the analogies  $\tilde{\Omega}_p = \sqrt{f_0} \tilde{\Omega}_p$  and  $\tilde{\gamma} = \tilde{\gamma}_0$  were used to include it into the fit.  $\tilde{\gamma}_j$  and  $\omega_{0,j}$  are given in eV. The fit parameters are valid in the regime from 0.5 eV to 6 eV.

(shorter) energies (wavelengths).<sup>7</sup> The interband transition is, in the case of gold, an excitation within the sp-band.

Rakic et al. calculated the Drude-Lorentz fit parameters (for  $k = 5$ ) for gold films [90], which are shown in Tab. 3.1. While these are phenomenological values, the first remarkable onset of interband transitions at 2.38 eV seems to be replicated by the  $j = 3$  resonance in table 3.1. In Fig. 3.4a the complex relative permittivity is shown for these parameters. For comparison the Drude-model permittivity is also shown as dotted lines for typical values of gold. In the limit of very small frequencies, i.e. where no significant interband transitions are present, the two models resemble each other quite well. However, in the visible regime especially the imaginary parts that mainly characterize the absorption characteristics of a material differs quite significantly for wavelengths smaller than 600 nm (see Fig. 3.4b). This is why, in the course of this thesis the phenomenological relative complex permittivity for gold will always be used,

<sup>7</sup>The first interband resonance sets in close to the X-point at around 1.8 eV) but it is much less pronounced than the one mentioned above.

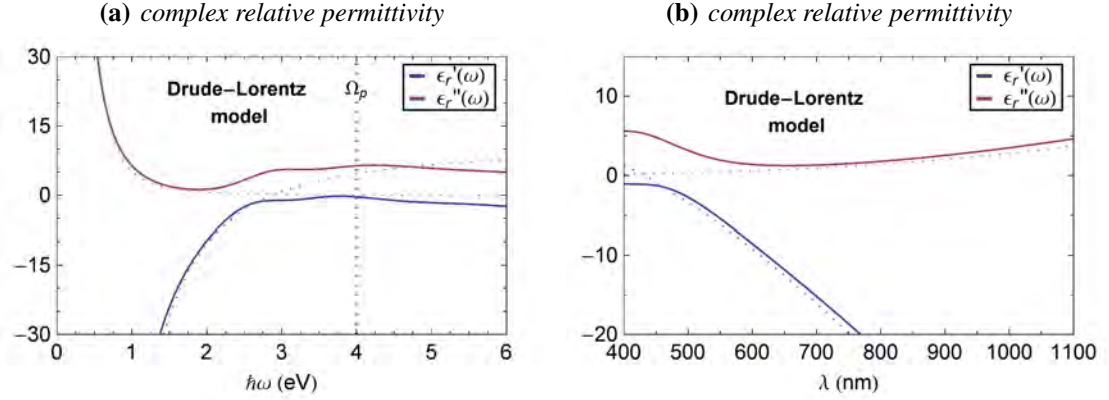


**Figure 3.4: Relative complex permittivity of gold.** (a) Plot of the real (blue) and imaginary (red) relative permittivity of a Drude-Lorentz material matched to the case of gold. The dotted lines are the equivalent graphs for a pure Drude metal. The fit parameters are taken from [90]. (b) Same as in (a) plotted as a function of wavelength in the visible and infrared regime (1.12 eV to 3.09 eV).

when the optical response of gold is to be evaluated.

## 3.2 Absorption and scattering by a nanosphere

In the previous section we have seen, that electron oscillations can be excited when illuminating a material (especially a metal) with light. Until now we covered the situation where the material can be considered as bulk material and how it reacts to an electromagnetic field. However, when the material's size is on the order of the optical wavelength the surface of the material will induce a back-action on the electron oscillation leading to additional absorption and scattering effects. A common case of a nanostructure is the nanosphere, where its curvature of the surface leads to a restoring force of the light-driven conduction electrons. The resulting resonances are called localized surface plasmons. These tightly confined electron oscillations lead to high local charge accumulations at the interface between the particle's surface and the surrounding medium, thereby causing strongly enhanced optical near fields close to the metal surface.

The whole concept of absorption and scattering of a sphere was solved analytically by Gustav Mie in 1908 [91]. The so called Mie theory can be deduced by solving Maxwell's equations for the boundary conditions of a sphere leading to the absorption and scattering cross section of a sphere and its shape-, media- and wavelength-dependent features, like the localized surface plasmon resonance (Sect. 3.2.3). Albeit being analytically fully correct, in a mathematical sense the Mie formulations are rather complicated and obscure some underlying concepts. When the electromagnetic field across the nanoparticle can be treated as homogeneous, the particle can be considered as quasi point-like. In this case, electrostatics can be used to calculate the response of a nanosphere to a light field. This quasi-static approximation illustrates several aspects that are important for this work (Sect. 3.2.2).

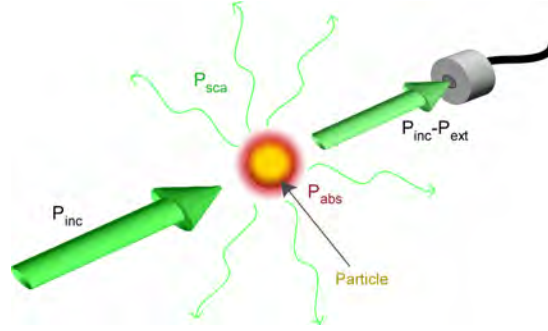


**Figure 3.5: Optical extinction spectroscopy.** Schematic for spectroscopy calculations. An incident light beam is partly absorbed and scattered by a particle. The energy removed from the incident beam by both processes is called extinction.

### 3.2.1 Extinction, absorption and scattering of light

Oftentimes, to examine matter, physicists measure its influence on an electromagnetic field and thereby rely on observables after the interaction took place. The main physical quantity to be derived via this concept is the cross section of the object under observation. It associates an effective area with the object for the interaction that is to be described.

Consider a light beam that is directed at a photo detector, that detects a light power  $P_{inc}$ . Now, when a particle is placed inside this beam, part of the light's power will be absorbed by the particle from which again some part will be re-emitted in form of an electromagnetic wave. Nevertheless the presence of the particle has led to a so called extinction of the incident beam which manifests itself in a reduction of the measured power by the photo detector. Extinction is therefore a result of the absorbed and scattered power of the particle (see Fig. 3.5). This way of characterizing the optical response of a particle is called optical extinction spectroscopy.

A convenient way of describing scattering and absorption processes is to formulate absorption (scattering) cross sections  $\sigma_{abs}$  ( $\sigma_{sca}$ ), to relate incident light intensities  $I_{inc}$  to the absorbed (scattered) Power  $P_{abs}$  ( $P_{sca}$ ) by the nanoparticle, respectively, via:

$$\sigma_{abs}(\lambda) = \frac{P_{abs}(\lambda)}{I_{inc}(\lambda)}, \quad (3.14)$$

$$\sigma_{sca}(\lambda) = \frac{P_{sca}(\lambda)}{I_{inc}(\lambda)}. \quad (3.15)$$

Thus, the particle can effectively be understood as as a fully absorbing (scattering) disc with an area of  $A = \sigma_{abs(sca)}$  for light with a wavelength of  $\lambda$ . The extinction cross section is the sum of the other two cross sections, i.e.

$$\sigma_{ext} = \sigma_{abs} + \sigma_{sca}. \quad (3.16)$$

### 3.2.2 Quasi-static approximation

When a metal nanosphere is sufficiently small compared to the wavelength of an incident light field, the particle can be treated as microscopically large but macroscopically small. This case

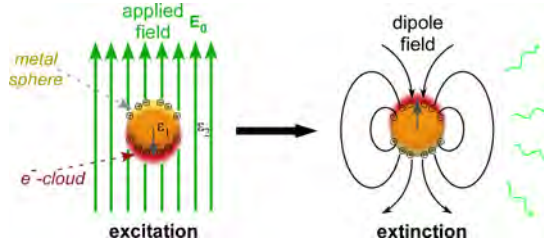


**Figure 3.6: Quasi-static approximation.** Schematic of the situation in cases where the metal nanosphere is much smaller than the wavelength. The excitation field  $\mathbf{E}_0$  is constant across the particle and drives an electron cloud inside the particle, that leads to extinction, i.e. absorption and scattering, by the nanosphere. In the quasi-static regime, the scattered field is equivalent to the field of an oscillating dipole. The complex relative permittivities are denoted with  $\epsilon_1$  ( $\epsilon_2$ ) for the nanosphere (surrounding medium), respectively.

assumes that the nanosphere consists of many particles itself but, nevertheless, that the phase of the electric field across the particle volume stays approximately constant, only varying as  $e^{-i\omega t}$  over time. That is why this regime is referred to as 'quasi-static' and electrostatics can be used to calculate the response of a metal nanosphere to an electric field (Fig. 3.6). The harmonic time dependence can be added to the solution later on. The quasi-static approximation adequately describes the optical properties of particles with radii  $R$  that are smaller than about a tenth of the wavelength  $\lambda$  of the electromagnetic field. Furthermore, its simplicity also leads to an intuitive understanding of the underlying, most dominant processes.

In electrostatics we can find the potential  $\Phi$  via the Laplace equation  $\nabla^2 \Phi = 0$ .<sup>8</sup> In the described case we can assume azimuthal symmetry which, after some calculations, leads to an electric field in- and outside the nanosphere via  $\mathbf{E} = -\nabla \Phi$  that reads [51]

$$\begin{aligned} E_{\text{in}} &= \frac{3\epsilon_2}{\epsilon_1 + 2\epsilon_2} \mathbf{E}_0, \\ E_{\text{out}} &= \mathbf{E}_0 + \frac{3\hat{\mathbf{n}}(\mathbf{d} \cdot \hat{\mathbf{n}}) - \mathbf{d}}{4\pi\epsilon_0\epsilon_2} \frac{1}{r^3}, \end{aligned} \quad (3.17)$$

where  $\mathbf{E}_0$  is the applied field,  $\mathbf{r} = r\hat{\mathbf{n}}$  is the vector from the nanoparticle to the position where the resulting field should be evaluated and  $\epsilon_1$  ( $\epsilon_2$ ) is the complex relative permittivity of the particle (surrounding medium). The resulting field outside the nanosphere is a superposition of the applied field and the electrostatic field of an ideal, microscopic, point-like dipole with a dipole moment of

$$\mathbf{d} = \epsilon_2 \alpha \mathbf{E}_0. \quad (3.18)$$

It is proportional to the complex polarizability  $\alpha$  of a nanosphere<sup>9</sup>

$$\alpha(\lambda, R) = 4\pi\epsilon_0 R^3 \frac{\epsilon_1(\lambda) - \epsilon_2}{\epsilon_1(\lambda) + 2\epsilon_2}, \quad (3.19)$$

<sup>8</sup>In electrodynamics the Helmholtz equation has to be solved instead of the Laplace equation.

<sup>9</sup>In general, i.e. when the particle is non-spherical,  $\alpha$  is a second rank tensor, denoted as  $\vec{\alpha}$ , and depends on the polarization of the electric field.

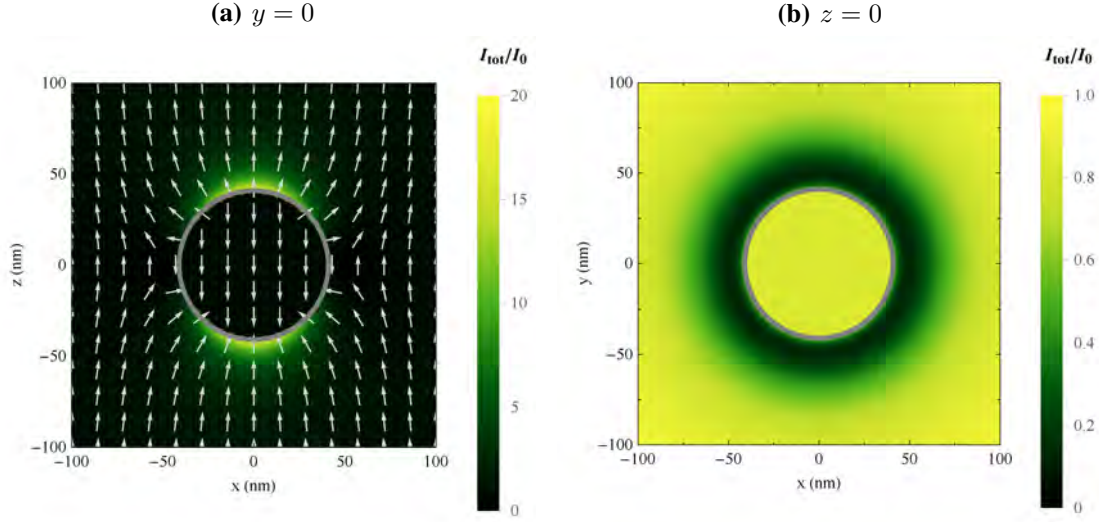


**Figure 3.7: Near-field intensity distribution.** Intensity distribution for a gold nanoparticle ( $R = 40$  nm) that is excited by a plane wave ( $\lambda = 532$  nm) linearly polarized along the  $z$  axis for a plane (a) that contains the dipole axis (b) that is perpendicular to the dipole axis. In panel (a) also the unit vectors of the electric field are shown. They are not shown in panel (b) as they exclusively point along  $z$  in this case. Also notice the different color scales in the two panels. In both cases a ratio of 1 indicates that the field is mainly given by the incident light field.

which incorporates all particle specific parameters and shows the same functional form as the Clausius-Mossotti relation [51]. In many cases the surrounding medium is approximately independent of the wavelength of the applied field, which is why this dependency was neglected. The dipole moment always points along the direction of the applied field, which means that, within the quasi-static regime, the nanosphere is a polarization maintaining dipole scatterer [92, 93]. The field outside the nanosphere is cylindrically symmetric along the dipole axis. Figure 3.7 shows the normalized intensity distribution  $(I_{\text{in}} + I_{\text{out}})/I_0$  in the plane containing the dipole axis and the one perpendicular to it, with  $I_i = \mathbf{E}_i \cdot \mathbf{E}_i^*$  ( $i = \text{in, out, 0}$ ), for a gold nanoparticle that is excited by linearly polarized plane wave for typical parameters ( $\lambda = 532$  nm,  $R = 40$  nm) used in the course of this thesis. As one can see, the light field is strongly localized and the intensity around the nanosphere can actually be about twenty times stronger than that of the applied field.<sup>10</sup>

Interestingly, the field inside the particle does not depend on  $r$  and is thus constant. However, Beer's law tells us that the field should decay exponentially inside the metal as  $e^{l/\delta}$ , where  $l$  is the penetration depth and  $\delta$  the skin depth. At low frequencies the skin depth is given by  $\delta = \sqrt{2/(\sigma_0 \omega \mu_0)}$  depending on the DC-conductivity introduced in Sect. 3.1.2. Consequently, the skin depth is a good measure to determine the validity of the quasi-static approximation. If

<sup>10</sup>Although this will not be part of this work, it is worth mentioning that even higher intensities can be realized when two or more such nanoparticles are brought very close together. The field in between them can be increased by about another order of magnitude.

the particle is smaller than the skin depth, it is certainly correct to use the formulas presented above. For typical metals at room temperature it is  $\delta \simeq 100$  nm. In the following section (Sect. 3.2.3) an additional method will be introduced to determine when it is valid to use the quasi-static picture.

With the above acquired dipole formulation at hand, one can also derive the scattering ( $\sigma_{\text{sca}}$ ) and absorption ( $\sigma_{\text{abs}}$ ) cross sections of a nanosphere in the quasi-static regime. By dividing the dissipated ( $P_{\text{abs}} = (\omega/2)\text{Im}[\mathbf{d} \cdot \mathbf{E}_0^*]$ ) and radiated power ( $P_{\text{sca}} = \omega^4 |\mathbf{d}|^2 / (12\pi\epsilon' v_2^3)$ ) of the sphere's dipole [28, 94],<sup>11</sup> by the intensity of the incident plane wave, we find

$$\sigma_{\text{abs}}(\lambda, R) = \frac{2\pi}{\lambda} \text{Im}[\alpha(\lambda, R)] , \quad (3.20)$$

$$\sigma_{\text{sca}}(\lambda, R) = \frac{8\pi^3}{3\epsilon_0^2 \lambda^4} |\alpha(\lambda, R)|^2 . \quad (3.21)$$

Here,  $v_2$  is the speed of light in the surrounding medium (see Sect. 2.1). It is noteworthy to point out that all formulas presented above in this section are actually independent of any distinct permittivity, so the sphere does not have to be a metal. Thus, if the polarizability is weakly dependent on the wavelength of the applied field, the amount of light any particle scatters scales with  $1/\lambda^4$  if the particle is sufficiently small. Scattering in this sub-wavelength particle regime is often referred to as Rayleigh scattering. It is the reason why the sky is blue and why long wavelength, infrared light is usually used in fiber optics for data transfer.

However, this general trend can be overlain, if the polarizability of the particle exhibits drastic changes. This is the case where the Clausius-Mossotti functional  $(\epsilon_1 - \epsilon_2)/(\epsilon_1 + 2\epsilon_2)$  is at its maximum value. In the case, where  $\epsilon_2$  is real and  $\epsilon_1''$  is small or slowly-varying around the maximum value region, the resonance condition can be simplified to  $\epsilon_1' = -2\epsilon_2$ .<sup>12</sup> At this point, the electrons in the metal oscillate collectively and the mode is called the (localized) dipole surface plasmon of the metal nanosphere. In contrast to a plasmon in bulk, a localized surface plasmon in a nanosphere can be excited by a transverse electric light field. The corresponding cross sections are shown in 3.8a for a gold nanosphere ( $R = 40$  nm) surrounded by air in the visible regime. For an excitation wavelength of  $\lambda = 532$  nm we find a ratio of  $\sigma_{\text{sca}}/\sigma_{\text{abs}} \simeq 0.35$ .

It is important to note however, that this value does not only depend on the wavelength, it also changes strongly with the particle radius as depicted in 3.8b. While the absorption cross section scales with the particle's volume as  $\alpha \propto R^3$ , the scattering cross section is even proportional to the volume squared. Necessarily, given a large enough radius, the energy that is scattered by the particle will be larger than the amount of energy that is absorbed.<sup>13</sup> This leads to interesting optical phenomena. When illuminating for example small gold nanoparticles with white light, the absorption of green light dominates over its scattering thereby rendering a reddish color. On the other hand, for larger gold nanoparticles the absorption is smaller than the scattering which consequently leads to a blueish or greenish color. This effect is shown in figure Fig. 3.9 for monodispersed gold nanoparticles in deionized water.

Based on the formulas derived above, we understand that also the permittivities of the nanopar-

<sup>11</sup>The formula for  $P_{\text{sca}}$  is only correct for a nonconducting medium, i.e.  $\sigma = 0$  (see Eq. (3.11))

<sup>12</sup>This condition is also known as the Fröhlich condition.

<sup>13</sup>Note that at one point the quasi-static picture is not valid any longer. The volume effect holds true however, even in an exact formulation of this problem.



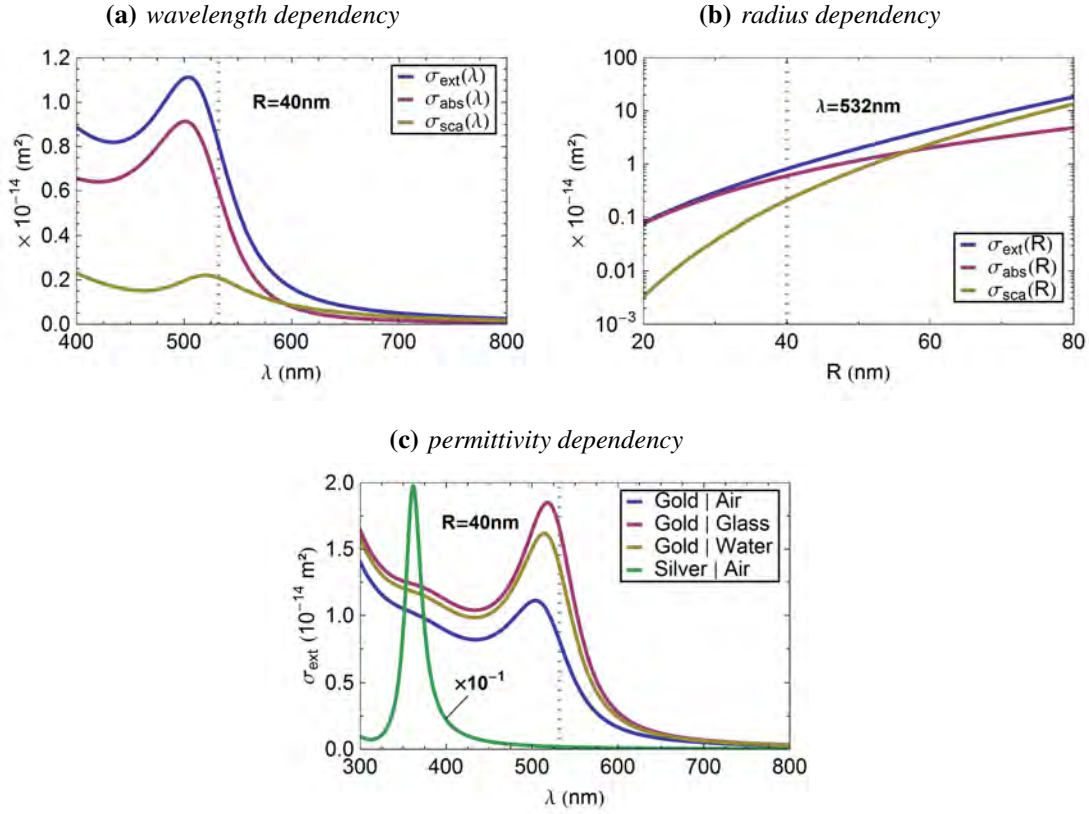


**Figure 3.8: Cross-sections - Quasi-static regime.** Extinction (blue), absorption (red) and scattering (yellow) cross section in air for a (a) fixed nanoparticle radius of  $R = 40$  nm as a function of  $\lambda$  and (b) fixed excitation wavelength  $\lambda = 532$  nm as a function of  $R$ . Note that the cross sections in panel (b) are plotted on a logarithmic scale. (c) Extinction cross sections for a gold nanoparticle in air (blue), water (red) and glass (yellow) as well as for a silver nanoparticle in air (green). For the permittivity of silver we also used the parameters elaborated in [90]. The cross section of the silver nanoparticle is scaled down by a factor of ten. The dotted vertical lines mark the values  $\lambda = 532$  nm and  $R = 40$  nm.



**Figure 3.9: Monodispersed gold nanoparticles.** Photograph of monodispersed gold nanoparticles in deionized water. The color of the colloid depends on the size of the nanoparticles. By decreasing the nanoparticle size from left to right, the color changes from blue to red. The photograph was made by A. Bellew [95].

ticle material and its surrounding medium play a crucial role for the optical response of a nanosphere. This is shown in Fig. 3.8c for different nanoparticle materials (gold, silver) and surrounding media (air, glass, water). When the refractive index  $n'_2$  of the surrounding medium is increased, the height of the localized plasmon resonance peak becomes larger and its position shifts to higher wavelengths by more than 10 nm. The high sensitivity of such nanoantennas to surrounding media is a result of the strongly localized field, i.e. the large intensities in the vicinity of the nanoparticle surface, as depicted in Fig. 3.7. In conjunction with the small size of the nanoparticle, this sensitivity is the reason why nanoparticles are or promise to be a great tool for sensing applications, such as the detection of single base pair mismatches in DNA [60], cancer treatment [63], single molecule detection [65], near-field optical microscopy in general [67] and many more. Figure 3.7c shows that the position of the localized plasmon resonance can be shifted up to a certain extent, by changing the material of the nanoparticle. For example, compared to a gold nanoparticle, the resonance of the silver nanoparticle, is shifted towards smaller wavelengths and about a factor of ten larger in size, because of a different plasma frequency and other interband transitions.

As can be seen in the following section, in addition to the dipole mode derived above, a nanoparticle supports in fact an infinite number of higher order modes and the general terminology is therefore 'localized surface plasmon'.<sup>14</sup> However, the qualitative features presented in this section remain to be valid. The term localized is used to distinguish the collective electron oscillation in a nanoparticle from the volume plasma of a bulk metal and the surface plasmon of a metal layer, both of which have different geometry dependent resonance conditions. The localized surface plasmon resonance arises due to the curved surface of the particle that exerts an effective restoring force on the driven electrons. For a nanosphere surrounded by air, it is for example found at  $\omega_0 = \tilde{\Omega}_p/\sqrt{3}$ .

As a summary, a metal nanosphere has a unique spectral feature due to its sub-wavelength

---

<sup>14</sup>Other common designations are particle plasmon or particle plasmon polariton.

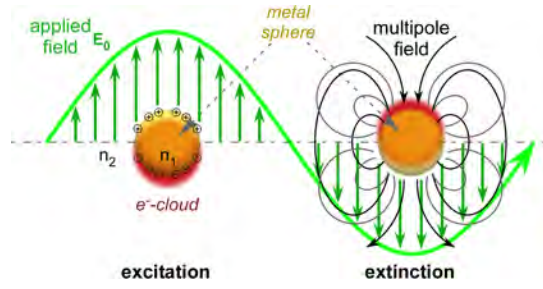


**Figure 3.10: Mie theory.** Schematic of the situation where an optical light field illuminates a spherical nanoparticle. The excitation field  $E_0$  varies across the particle and drives an electron cloud inside the particle, that leads to extinction, i.e. absorption and scattering, by the nanosphere. In the full model Mie theory, the scattered field is equivalent to a multipole field. The complex refractive indices are denoted with  $n_1$  ( $n_2$ ) for the nanosphere (surrounding medium), respectively.

size, called the localized surface plasmon resonance. When resonantly excited by an electromagnetic field, the nanosphere can be described by an elementary resonant, polarization maintaining dipole antenna. The near field around it is significantly enhanced with respect to the applied field leading to a strong interaction with everything that is situated in close vicinity of the nanoparticle.

### 3.2.3 Mie theory

Thanks to Mie's theory it is possible to calculate the scattering and absorption cross section as well as the electromagnetic field distribution in- and outside of an uncharged sphere of arbitrary size analytically for the case of a homogeneous surrounding medium. To do this, Maxwell's equations have to be solved in spherical coordinates for the case of a particle that is illuminated by a plane wave. The required parameters are the bulk complex refractive indices for particle and surrounding medium and the particle's radius. Indeed, even for nanoscale spherical particles, the problem can be solved analytically with the macroscopic complex refractive index of the bulk material – no adaptations have to be made. The experimental situation is sketched in Fig. 3.10 for the case of a nanosphere. In contrast to the quasi-static approximation (Sect. 3.2.2) it is not assumed that the phase of the electromagnetic field is constant across the particle's volume. As the general idea is actually quite similar to the concepts presented in chapter 2, in the following, the steps towards the final formulas will only be sketched.<sup>15</sup> A complete derivation can for example be found in [96].

Under the assumption that the media are linear and isotropic the electromagnetic fields, that have to fulfill the wave equation (Eq. (2.2)), will be expressed in terms of the spherical harmonics, i.e. multipole expanded. Doing this, four expansion coefficients  $a_L$ ,  $b_L$ ,  $c_L$  and  $d_L$  (with  $L$  being the order of the multipole expansion) for the external and internal field arise which

<sup>15</sup>The main difference is that the optical fiber is cylindrically symmetric instead of spherically. This leads to an additional requirement the fields have to fulfill, leading to a contribution by associated Legendre functions. In combination with the in chapter 2 presented Bessel functions they lead to the so called spherical harmonics.

can be determined from the boundary conditions:<sup>16</sup>

$$\begin{aligned} a_L(\lambda, R) &= \frac{m \psi_L(m x) \psi'_L(x) - \psi_L(x) \psi'_L(m x)}{m \psi_L(m x) \xi'_L(x) - \xi_L(x) \psi'_L(m x)} , \\ b_L(\lambda, R) &= \frac{\psi_L(m x) \psi'_L(x) - m \psi_L(x) \psi'_L(m x)}{\psi_L(m x) \xi'_L(x) - m \xi_L(x) \psi'_L(m x)} , \end{aligned} \quad (3.22)$$

where  $m = n_1/n_2$  is the ratio of the complex refractive indices of the particle ( $n_1$ ) and the surrounding medium ( $n_2$ ). The size parameter  $x = |\mathbf{k}| R = 2\pi R/\lambda$  relates the particle radius  $R$  to the wavevector  $\mathbf{k}$  or wavelength  $\lambda$  of the incident light field propagating in the surrounding medium. Additionally,  $(\psi'_L, \xi'_L)$   $\psi_L, \xi_L$  are the (derivatives of) the Riccati-Bessel functions, respectively. The coefficients  $c_L$  and  $d_L$  for the internal fields were omitted, as they will not be relevant throughout this thesis.

In terms of these expressions the Mie cross sections read:

$$\sigma_{\text{ext}}(\lambda, R) = \frac{2\pi}{|\mathbf{k}|^2} \sum_{L=1}^{\infty} (2L+1) \text{Re}[a_L + b_L] , \quad (3.23)$$

$$\sigma_{\text{sca}}(\lambda, R) = \frac{2\pi}{|\mathbf{k}|^2} \sum_{L=1}^{\infty} (2L+1) [a_L + b_L] , \quad (3.24)$$

while  $\sigma_{\text{abs}}$  can be calculated via Eq. (3.16). If we only examine the dipole term  $\sigma_{\text{ext}, L=1}$  of the scattering cross section and Taylor expand the coefficients  $a_{L=1}$  and  $b_{L=1}$  up to the order of  $x^3$ , the quasi-static dipole cross section (Eq. (3.20)) is reproduced if we claim that  $x \ll 1$ . Now, to determine whether the quasi-static approximation is valid, one can simply compare the size of the different Mie terms  $L = 1, 2, 3, \dots$ . Figure 3.11 shows the ratio of the extinction cross-section summands  $\sigma_{\text{ext}, L=2}$  and  $\sigma_{\text{ext}, L=1}$ , for air ( $n \simeq 1$ ) and glass ( $n \simeq 1.46$ ) as the surrounding medium. While the surrounding medium has a significant effect on these ratios, one can roughly say that, in the case of air and glass, for particle radii  $R$  that are about ten times smaller than the exciting wavelength  $\lambda$  it is sufficient to consider the first order dipole term ( $L = 1$ ), rather than a sum of several orders. In this regime the curves presented in the previous section (Sect. 3.2.2) can be associated with the Mie picture with only marginal differences. The quasistatic approximation is expected to lead to a slight overestimation of the plasmon peak resonance and a slight underestimation of the peak cross section. So, to understand the physical process behind optically excited nanospheres it is often sufficient to consult the quasi-static formulations. Nevertheless, all through this dissertation, the analytical Mie cross sections will be used to calculate light-particle interactions.

---

<sup>16</sup>Maxwell's equations demand the transverse components of the electromagnetic field to be continuous across the boundary separating two media.

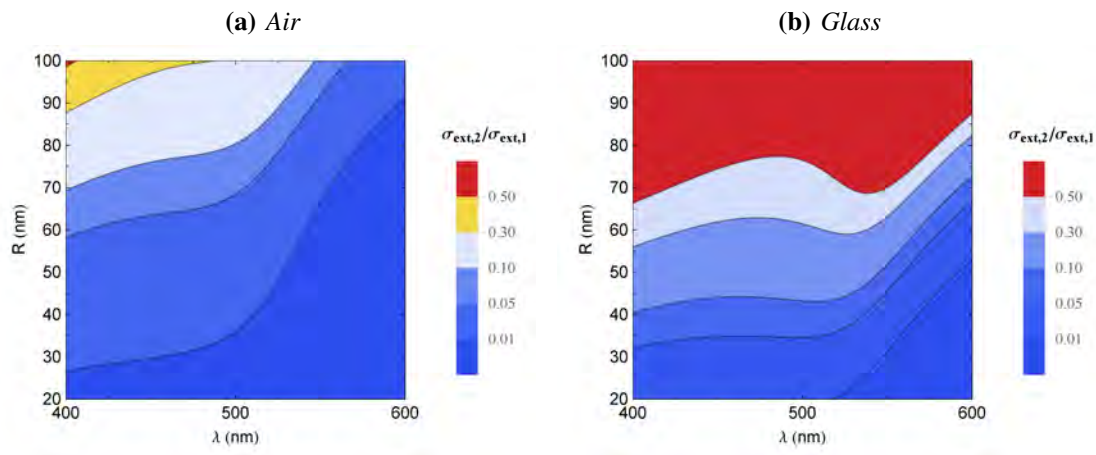


**Figure 3.11: Mie theory multipoles.** Ratio  $\sigma_{ext,L=2}/\sigma_{ext,L=1}$  of the extinction cross sections of a gold nanoparticle for the surrounding medium being air (a) and glass (b). Notice the different legend scales. The ratio between the  $L = 3$ -term and the dipole term is about 1 order of magnitude smaller than the presented plots.



# Interfacing Optical Nanofibers with Ions

Trapped ions offer an excellent control over their external and internal degree of freedom and can be strongly confined for long durations. By tuning the electric trapping potential it is possible to adjust their position very accurately which can be used to enable strong interactions with other objects and between themselves. For these reasons, they are an important quantum system in research on quantum information processing [10] and all the necessary building blocks for a scalable quantum computer have been demonstrated using chains of trapped ions [5, 97, 98]. In many of the current implementations, quantum information between ions can only be transmitted via their motional degree of freedom. This limits the maximum distance of quantum information transfer to a few micrometers. By contrast, photons are quantum systems with which quantum informations can be carried over very large distances when using, e.g., optical fibers.

It has been shown that atoms [99], molecules [54] and nanoparticles (see chapter 5) can be efficiently coupled to the guided field modes of optical nanofibers. Accordingly, nanofibers seem to be a natural candidate to transfer the information from ions to photons (and vice versa) and thereby mediate long distance ion interactions. In this way, one could profit from the advantageous properties of both systems, i.e. the well-controlled, strong interactions of ions for quantum computation, and the capability of photons to transport information for quantum communication.

In order to do this, however, the ions have to be placed in close vicinity of the nanofiber surface. However, the presence of only a few elementary charges on the fiber destabilizes the trapping potential such that the ions can no longer be trapped [23]. A critical issue that has to be addressed and investigated when a nanofiber is to be integrated into an ion trap. Nanofibers are electric insulators. In order to remove surface charges from them, they have to be made electrically conductive up to a certain extent. Moreover, heating due to electric field noise in the proximity of close by objects is a general concern in the ion trapping community. The exceptionally small and well controlled diameter of the nanofiber, thus, makes it an ideal object to study these heating effects in ion trap experiments in a new regime.

After an introduction about the status of this project in Sect. 4.1, optical nanofibers are discussed in the context of the electrical as well as optical requirements for integrating them into ion traps (Sect. 4.2). The two most promising approaches which have been implemented in the course of this thesis are physical vapor deposition of silver and chromium. Section 4.3 discusses the results of these approaches and in Sect. 4.4 possible improvements and other approaches will be discussed.

### 4.1 Preface

The project to combine optical nanofibers with ion traps was carried out by a collaboration, using the expertise in ion trapping of the research group of Prof. Dr. Rainer Blatt at the University of Innsbruck and the expertise in nanofiber physics of the research group of Prof. Dr. Arno Rauschenbeutel at the Vienna University of Technology. While a PhD student (Benjamin Ames) in Innsbruck started designing and setting up an ion trap suitable for the implementation of optical nanofibers, this thesis focused on the fabrication of conductive optical nanofibers. As local charge accumulations, also known as patch potentials, on the surface of nanofibers will influence trapped ions considerably and would in particular render the trapping of ions close to the fiber impossible, achieving this would have a major impact on the capabilities of this combined system.

To remove charges of the nanofiber, its conductivity will have to be increased by more than 10 orders of magnitude without significantly reducing the strength of the guided field mode.<sup>1</sup> In the course of this thesis, it turned out that this task could not be realized within a reasonable timescale. Although we managed to fabricate a conductive and minimally transmissive nanofiber, in 2014, it was decided to fully concentrate on the second project within this thesis, which is presented in chapter 5. Shortly before that, Benjamin Ames confirmed the first ever demonstration of trapped ions close to a conventional, bare nanofiber, fabricated in Vienna. It was possible to trap ions about 26  $\mu\text{m}$  away from the fiber, which is one of the closest trapped ion-to-surface distances that has been achieved. As expected, the distance seems to be limited by charges on the nanofiber surface. Currently, the research focuses on understanding the origins that cause the fiber to become charged and on methods to discharge the nanofiber in order to decrease the ion-to-fiber distance even further.

As a side remark, thanks to the small dimensions of the nanofiber it could be an ideal candidate to probe heating mechanisms of ions due to electric field noise at surface distances below 30  $\mu\text{m}$  which have not been investigated until now.

---

<sup>1</sup> The exact reduction that can be tolerated depends on the application that is to be realized. For a large incoupling efficiency of an emitting ion into the guided nanofiber modes, the transmission of the nanofiber should probably not be reduced by more than a factor of 10. On the other hand, to use the nanofiber for exciting an ion via an evanescent light field this factor could be much larger.



## 4.2 An optical nanofiber as an electrical conductor: Considerations

### 4.2.1 Heating mechanisms and charge sensitivity in ion traps

In ion traps, ions are confined with electric (and sometimes magnetic) fields. Consequently, the ions are prone to fluctuations and static distortions of the electric trapping fields. A key feature of both distortions is that they scale strongly with the distance of the ion to the closest surface – the closer the ion approaches a surface the larger the distortion.<sup>2</sup> This limits further miniaturization of ion traps and, as a direct consequence, to date, the smallest demonstrated ion to surface distances are around  $d \simeq 30 \mu\text{m}$  [100].

Ion trap electrodes are per definition electrically conductive as they are used to provide a well defined voltage. If charges accumulate on their surfaces the voltage supply will quickly compensate for them. If other surfaces are moved far away from the trapping site, static distortions of the trapping potential are not an issue. Consequently, electric field noise will be the dominant perturbation. Sources of electric field noise include unwanted electromagnetic radiation, Johnson and technical noise and local charge variations (also known as patch potentials). The resulting motional heating of the ions is a limiting factor in many experiments and several of its origins are not yet well understood [101]. An extensive summary of this active research field can be found in [100].

If, in addition to the trap electrodes, a *dielectric* surface is brought close to trapped ions, the trapping potential will be deformed. The dielectric changes the effective refractive index of the surrounding medium and charge accumulations on it can not be removed and are therefore much larger than in the case of conductive materials. This leads to serious deformations of the trapping potential up to a point where the ions can no longer be confined.<sup>3</sup> In [23] it was found that in a typical ion trap setup, three ions are sensitive to an accumulation of 40 elementary charges in a coated glass plate 1.2 mm away from the ion chain.

In the context of approaching trapped ions with a nanofiber this means that static charging effects of the fiber surface are a serious issue. By increasing the electrical conductivity of the nanofiber one could counteract this effect by either discharging the nanofiber or applying a fixed electric potential to it.

### 4.2.2 Desired conductivity of a quasi-charge free nanofiber

In pursuance of integrating an optical nanofiber into an ion trap, the dielectric nanofiber has to be made electrically conductive up to a certain extent. As an estimation of its charging and discharging process we use the following rate equation for the charge on the fiber:

$$dQ = \left( -\frac{Q}{\tau} + \gamma \right) dt. \quad (4.1)$$

<sup>2</sup> The coulomb force for static distortions scales as  $d^{-2}$ , where  $d$  is the distance of the ion to the closest surface. Depending on the dominant mechanism, the electrical field noise is expected to scale as  $d^{-2}$  to  $d^{-6}$  [100].

<sup>3</sup> That is why the closest surface in ion traps is almost always an electrode. All other surfaces are moved as far away as possible from the trapped ions.

Here,  $Q$  is the charge on the fiber,  $\tau$  is the time constant of the discharging process and  $\gamma$  describes the charge production rate on the nanofiber. For the steady state,  $dQ/dt = 0$ , we find that

$$\gamma = \frac{Q_0}{\tau}, \quad (4.2)$$

with  $Q_0$  being the steady state charge. If we treat the nanofiber as an RC-element, the time constant,  $\tau = RC$ , can be expressed by the resistance ( $R$ ) and capacitance ( $C$ ) of the fiber. So, in order to estimate the maximum resistance, we must estimate the capacitance of the nanofiber inside an ion trap. An upper approximation for it can be obtained when considering the case where the nanofiber passes through a conductive co-axial cylinder that has the same radius as the nanofiber-electrode separation  $d$ . The corresponding capacitance is then

$$C_{\text{coax}} = 2\pi\epsilon_0 \frac{L}{\ln(d/a)}, \quad (4.3)$$

where  $L$  is the length of the nanofiber and  $a$  the nanofiber radius. Additionally, the capacitance of a nanofiber in an ion trap should not be smaller than that of a nanofiber in free space:

$$C_{\text{free-space}} = 2\pi\epsilon_0 \frac{L}{\ln(L/a)}. \quad (4.4)$$

In order to have a significant part of the optical power in the evanescent field of the guided mode, in the visible regime the nanofiber radius should be around  $a \approx 250$  nm. Together with a typical electrode separation of  $d \approx 500$   $\mu\text{m}$  and a nanofiber waistlength of  $L \approx 10$  mm we expect the capacitance  $C_{\text{trap}}$  of the nanofiber in the ion trap to be around 45 fF  $\lesssim C_{\text{trap}} \lesssim 75$  fF. If the tapered and unprocessed part of the tapered optical fiber is included in the considerations, the maximum value can be about an order of magnitude larger. Thus, depending on the actual realization, a reasonable estimate of the capacitance of a nanofiber within an ion trap is some hundred femtofarads.

Figure 4.1 shows the resistance of the nanofiber that is needed to keep the total electric charge on the fiber at a number of elementary charges  $Q_0/e$  for realistic cases where 1 (25) elementary charges per second are being created on its surface.<sup>4</sup> To realize an essentially uncharged fiber ( $Q_0 \leq 1$ ), this means that its resistance should be below  $R_0 \lesssim 10^{12} \Omega$ .

The electrical resistance of an object

$$R = \frac{l}{A}\rho, \quad (4.5)$$

strongly depends on its shape (length,  $l$ ; cross sectional area  $A$ ) and can be derived via the electrical resistivity  $\rho$  of the material. In the case of glass, for temperatures  $T$  below the transformation

---

<sup>4</sup> These charge production rates assume that the main fraction of charges will be produced due to illumination of the fiber with ultraviolet light of  $\lambda = 397$  nm with which  $^{40}\text{Ca}^+$ -ions are typically cooled. At this wavelength, Harlander et al. illuminated an antireflection-coated glass plate and found a charge production efficiency of  $\eta = 0.4 \times 10^{-10}$  electrons per photon [23]. Under the assumption that the ions will be cooled at typical intensities around the saturation intensity [102], we find a production rate of  $\gamma = 25/\text{s}$  when the laser beam illuminates an effective area of the nanofiber of  $A_{\text{eff}} = 1 \text{ cm} \times 500 \text{ nm}$ . A production rate of  $\gamma = 1/\text{s}$  assumes that the laser beam is essentially directed *past* the nanofiber and that it is only illuminated by a small fraction of the beam.

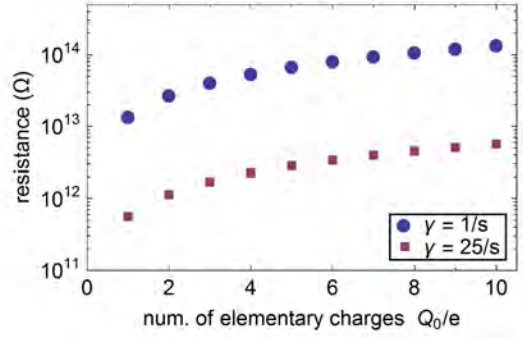


**Figure 4.1: Uncharged nanofiber.** Maximum resistance  $R$  of an optical nanofiber in order to keep it at a number of elementary charges,  $Q_0/e$ , for a charge production rate  $\gamma = 1/s$  (blue circles) and  $\gamma = 25/s$  (red squares).

range where glass softens, the electric properties can be described via the Rasch-Hinrichsen law

$$\lg \rho = \tilde{A} - \tilde{B}/T, \quad (4.6)$$

with  $\tilde{A}$  and  $\tilde{B}$  being specific glass constants. For fused silica ( $\text{SiO}_2$ ) the volume resistivity at room temperature is  $\rho_{\text{SiO}_2} \approx 10^{19} \Omega \text{ m}$  ( $\tilde{A}_{\text{SiO}_2} = -0.394$ ,  $\tilde{B}_{\text{SiO}_2} = -6222.4 \text{ K}$ ).<sup>5</sup> Using this value, we find a resistance for an optical nanofiber of typical dimensions (radius,  $a = 250 \text{ nm}$ ; length,  $l_w = 1 \text{ cm}$ ) of  $R_{\text{bare}} \approx 10^{29} \Omega$ . Clearly, this is much larger than  $R_0$  and keeping the bare nanofiber uncharged or at a fixed electric potential will not be possible.<sup>6</sup> Consequently, the nanofiber has to be made electrically conductive up to a certain extent.

One solution to this issue is to deposit a thin conductive layer onto the nanofiber as it is, for example, common practice for touch-screens and solar cells.<sup>7</sup> However, there is a crucial difference between coating nanofibers and coating flat substrates as sketched in Fig. 4.2. For a flat substrate, e.g. a conventional microscope glass plate, the length across which the resistance is measured is roughly of the same size as the length of the electrode. In the case of an optical nanofiber the length of the electrode is given by the nanofiber's circumference, which is about four orders smaller than typical nanofiber lengths of  $l_w \approx 1 \text{ cm}$ . Consequently, for the same layer thickness,  $t$ , the resistance across the nanofiber is four orders of magnitude larger than in the case of a glass plate ( $R_{\text{fiber}} \approx 10^4 R$ ).

Moreover, for the case of the glass plate, incident light propagates *through* the coating and its initial power  $P_0$  reduces to  $P = P_0 \exp(-\alpha t)$ , where  $\alpha = -4\pi n''/\lambda$  is the absorption

<sup>5</sup> Note that, resistivities above  $10^{13} \Omega \text{ m}$  are usually very hard to measure.

<sup>6</sup> The extraordinary high volume resistivity of glass is the reason why it is commonly used as an electric insulator for high voltage power transmission etc.

<sup>7</sup> A common quantity in this context is the so called sheet resistance  $\mathcal{R}_s = \frac{\rho}{t}$ , that assumes a layer of uniform thickness  $t$  across the coated sample. In this case, the resistance can be written as  $R = \frac{l}{h} \mathcal{R}_s$ , where  $l$  is the length over which the resistance is to be measured,  $h$  is the length along which the object is contacted at both sides. The aspect ratio  $\frac{l}{h}$  is often referred to as the number of squares of the layer and  $\mathcal{R}_s$  is often given in units of 'ohms per square' ( $\Omega/\text{sq}$ ) to differentiate it from the bulk resistance  $R$ .

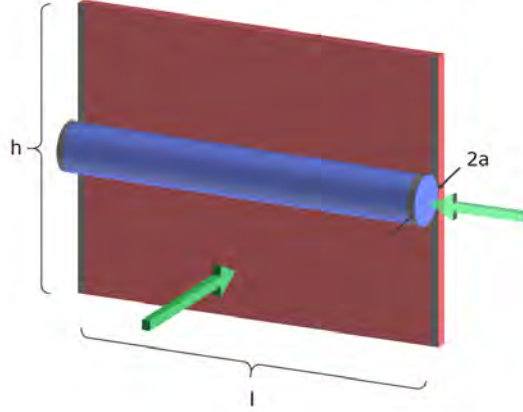


**Figure 4.2: Resistance of different objects.** Geometrical aspects of the electrical resistance in the case of a coated glass plate (red) and coated fiber (blue). The resistance will be measured across two electrodes (gray) on the sides of the objects. For the same coating thickness, the resistance across both objects scales with the ratio  $l/h$  of the length of the object  $l$  across which the resistance is to be measured and the length  $h$  of the electrodes. For a cylindrical object,  $h$  is given by its circumference  $2\pi a$ . Thus, in case of a typical nanofiber, this leads to a much smaller electrode length compared to a square glass plate and therefore to a much higher resistance. The green arrows indicate the propagation direction of light through the fiber and through the glass plate.

coefficient and  $n''$  is the imaginary part of the complex refractive index of the coating (see Sect. 3.1.1 - 3.1.3). This attenuation is connected to the transmittance,  $\mathcal{T}$ , and absorbance,  $\mathcal{A}$ , via

$$\mathcal{T} = P/P_0 = e^{-\alpha \ell} = 10^{-\mathcal{A}}, \quad (4.7)$$

$$\mathcal{A} = \frac{\alpha \ell}{\ln 10}, \quad (4.8)$$

with  $\ell$  being the traveled distance. In the case of optical nanofibers, light has to travel *along* the film over the total length  $l_w$  of the nanofiber. However, only a fraction  $P_{\text{coat}}/P_0$  of the power of the guided light propagates inside the coating. If we assume the coating to be a weakly absorbing, homogeneous layer with bulk properties, we can estimate the transmittance,  $\mathcal{T}_{\text{fiber}}$ , of the nanofiber to be

$$\mathcal{T}_{\text{fiber}} = \exp(-(P_{\text{coat}}/P_0) \alpha l_w). \quad (4.9)$$

Figure 4.3 illustrates this interplay between transmittance and resistance for the glass plate and the nanofiber for two different coating materials (i.e. silver and chromium). As expected, for a given transmittance, the resistance across the glass plate is several orders of magnitude lower than the resistance across the nanofiber. In all cases, an increase in transmittance goes along with an increase in resistance. According to these estimations, it might be possible to realize optical nanofibers with resistances around  $R_0 \lesssim 10^{12} \Omega$  with a transmittance close to one. However, these estimations assume that the electric and optical properties of the bulk material are still

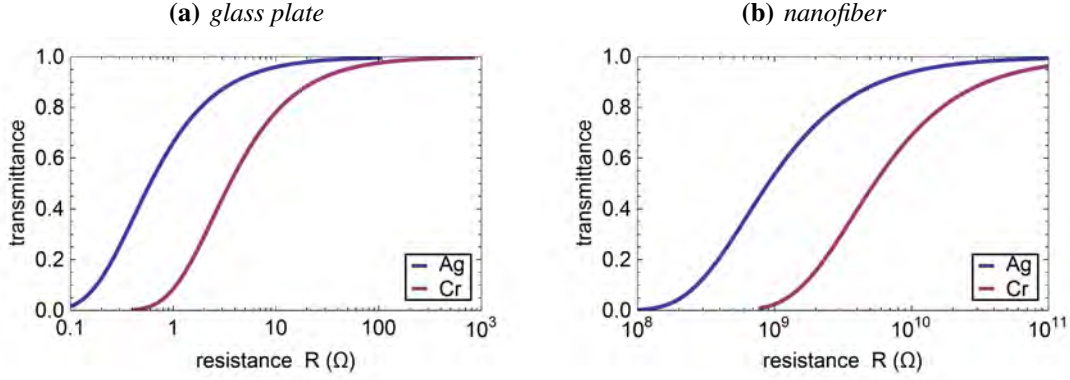


**Figure 4.3: Optical and electrical properties of coated objects.** Transmittance as a function of resistance of a (a) glass plate and (b) nanofiber that are coated with silver (blue) and chromium (red). The wavelength of the light that is propagation through glass plate and nanofiber (as indicated in Fig. 4.2) is  $\lambda = 866$  nm. We used literature values for the bulk resistivity of silver (chromium) of  $\rho_{Ag} = 1.59 \times 10^{-8} \Omega \text{ m}$  ( $\rho_{Cr} = 1.25 \times 10^{-7} \Omega \text{ m}$ ) and an imaginary part of the complex refractive index of  $n''_{Ag} = 5.45$  ( $n''_{Cr} = 4.13$ ) [90]. The glass plate has a length of  $l_g = 1.2$  cm and an electrode width of  $w_g = 3.7$  cm. The dimensions for the nanofiber are: radius,  $a = 250$  nm and length,  $l_w = 1$  cm. Notice, that the resistance is plotted on a logarithmic scale. In the case of chromium, a resistance of  $R = 10 \Omega$  ( $R = 10^{10} \Omega$ ) corresponds to a layer thicknesses of  $t \simeq 4$  nm ( $t \simeq 0.8 \times 10^{-4}$  nm) on the glass plate (nanofiber). The latter case would correspond to a sub-atomic layer.

valid for layer thicknesses below a few tens of nanometer. As we will see later in this chapter, due to the nature of the growth process of films, it is not correct to assume the resistivity and complex refractive index of the bulk material in order to calculate the effects of a thin film.

### 4.2.3 Required properties of nanofibers in the framework of calcium ion experiments

Atomic ions can be confined in Paul traps, where the trapping potential is realized by a combination of static and time dependent electric fields [103]. In a conventional linear Paul trap (see Fig. 4.4), these fields are supplied by four blade electrodes (radio frequency) and two endcap electrodes (static). In order to carry out precision experiments in such a setup, it is necessary to laser cool the ions to lower motional energies [104]. The concept of laser cooling is shown in Fig. 4.5 for the case of  $^{40}\text{Ca}^+$ -ions. Here, only the laser wavelengths are labeled/sketched that are needed to cool the ions down to the Doppler limit.<sup>8</sup> Accordingly, the nanofiber – which should be very close to the ion (sub  $\mu\text{m}$  distance) – will to a certain extent be exposed to light with a wavelength of 397 nm and 866 nm.

An optical nanofiber that is integrated in an ion trap (for a sketch of the realization in Innsbruck see Fig. 4.4) could be used as a tool to excite ions via the fiber, to capture light emitted by the ions or simply as a dielectric surface. A proof of principle experiment could be, to

<sup>8</sup> In order to perform, e.g. quantum logic operations, the ions have to be cooled down to their motional ground state via sideband cooling [104].

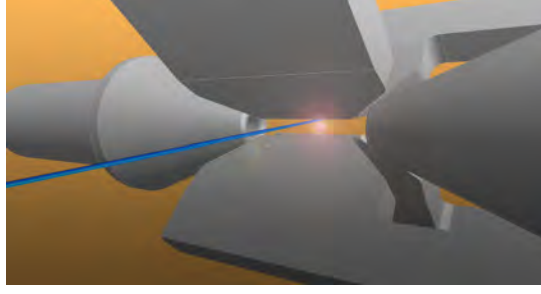


**Figure 4.4: Linear Paul trap and optical nanofiber.** Illustration of a conventional linear Paul trap, with an optical nanofiber (blue) oriented perpendicular to the trapping axis. The arrow-like structures on the left and right are the two endcap electrodes of the ion trap and the other four structures are commonly referred to as the blade electrodes.

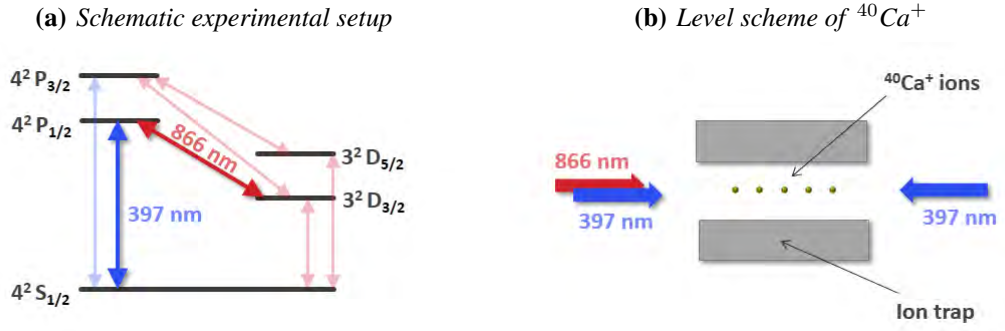


**Figure 4.5: Doppler cooling of  $^{40}\text{Ca}^+$ -ions.** (a) Energy-level scheme of  $^{40}\text{Ca}^+$ . The labeled transitions are the ones needed for Doppler cooling. The other ones that are depicted are mostly used for sideband cooling. The  $^{40}\text{Ca}^+$ -ion has a single valence electron and no hyperfine structure. (b) For Doppler cooling of  $^{40}\text{Ca}^+$ -ions, the  $S_{1/2}$  to  $P_{1/2}$  transition near 397 nm is employed. To prevent pumping into the  $D_{3/2}$  state, an additional repump laser at 866 nm has to be used. Resolved-sideband cooling [104] would be performed on the  $S_{1/2}$  to  $D_{5/2}$  transition near 729 nm.

demonstrate coupling between the nanofiber guided mode and trapped ions. By sending light through the fiber one could guide it to individual atoms. Figure 4.6 illustrates the achievable Rabi frequencies for the case of guided light with a power of  $P = 1 \text{ mW}$ <sup>9</sup> and a wavelength of  $\lambda = 866 \text{ nm}$  (i.e. the  $D_{3/2}$  to  $P_{1/2}$  transition).<sup>10</sup> As can be seen, by changing the nanofiber radius

<sup>9</sup> This power was chosen due to unpublished measurements during this thesis where nanofibers that were covered with dust broke in ultra high vacuum ( $p \approx 10^{-8} \text{ mbar}$ ) when light above this value was sent through the fiber. The rupture was attributed to individual dust particles on the fiber that absorb a significant amount of the guided light and transform it to heat. As a very rough estimation this power was used as the maximum power that can be sent through coated nanofibers. In the case of uncoated fibers, transmitted powers of a few hundred mW were already measured [105].

<sup>10</sup> In general, the higher the energy of the photons, the larger is the probability for the photons to create charges on a surface they hit. Therefore, photons at a wavelength of 866 nm are a better choice than photons at a wavelength

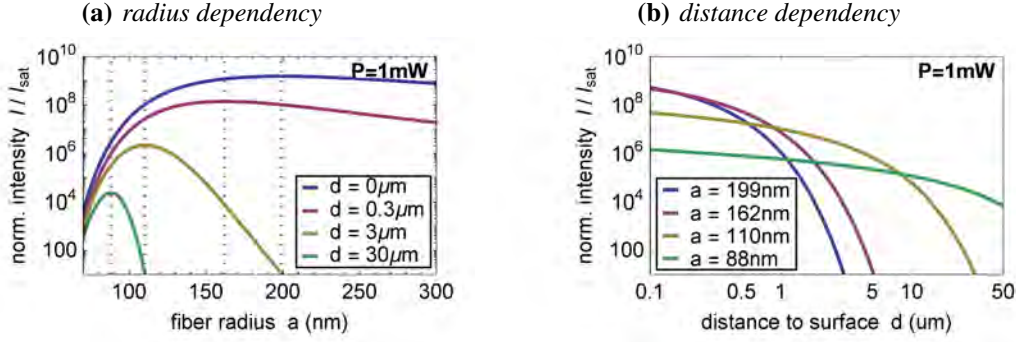


**Figure 4.6: Excitation intensity around nanofibers.** Intensity of the fundamental mode normalized to the saturation intensity of the  $D_{3/2}$  to  $P_{1/2}$  transition ( $\lambda = 866 \text{ nm}$ ) as a function of (a) the fiber radius,  $a$ , and (b) the distance,  $d$ , above the fiber surface. The mode is quasi-linearly polarized along  $\hat{y}$  and the power that is sent through the nanofiber is set to be  $1 \text{ mW}$ . In panel (a) the inset shows the fixed distances to the fiber surface where the normalized intensity is evaluated and the dashed vertical lines denote the radii where the intensity is maximal for each case. Those positions are taken as the fixed radii that are used in panel (b) (see inset) to evaluate the normalized intensities. Typical excitation intensities in a  $^{40}\text{Ca}^+$ -ion trap, for example, lie around a few hundred  $I_{\text{sat}}$ . Notice that the x-axis in panel (a) is plotted on a linear and in panel (b) on a logarithmic scale. As a comparison, the peak intensity of a gaussian beam of  $1 \text{ mW}$  with a beam waist of  $1 \text{ mm}$  has a normalized intensity of about  $I_0/I_{\text{sat}} \approx 190$ .

it is possible to shape the region, inside which the ions are efficiently excited effectively acting as a region-selective light-ion coupling device. In the case of *coated* nanofibers, the guided light will be severely attenuated and the normalized intensities in Fig. 4.6 will probably decrease by several orders of magnitude resulting in a much smaller interaction area. Consequently, the metallic layer should be as transparent as possible around  $866 \text{ nm}$ . Moreover, as discussed in Sect. 4.2, the closer the ions get to the surface the stronger the forces acting upon them become, up to a minimum trapping distance below which they can no longer be confined. Hence, in order to have an interaction region around the fiber that is actually populated by ions, this minimum trapping distance should not be larger than the interaction region. If the nanofiber is to be used as an *efficient* tool to collect emitted photons in order to transfer information from the ion to the guided mode and vice versa, the ion will have to be within a few hundred nanometers from the surface of the nanofiber (for details see Sect. 5.2).

Another important aspect that might influence the ions is the mechanical oscillation of the optical nanofiber in vacuum. In [106], Junge et.al. reported that the root mean square of the fluctuating gap between a nanofiber and a whispering-gallery-mode resonator is  $\pm 9 \text{ nm}$  in the frequency range up to  $\pm 200 \text{ Hz}$ . For the trapping distances discussed here, which are a  $1 \mu\text{m}$ , an oscillation amplitude around  $10 \text{ nm}$  will have a small effect on the ions.

Ultimately, one can conclude that the electric and optic requirements of an integrated nanofiber depend on each other: For an effectively uncharged fiber, the ions could possibly be trapped very close to its surface ( $\sim 1 \mu\text{m}$ , or even less) thereby allowing for a stronger absorption due to a

larger thickness of the conductive layer. On the other hand, if a method can be found that allows for almost lossless transmission at the requested wavelengths, one could cope with higher resistances. The nanofiber resistance should not exceed  $R \simeq 10^{12} \Omega$  and in order to demonstrate the collection of light emitted by an ion, the transmittance should at least be about  $\mathcal{T} \simeq 0.01$ .

### 4.3 Coating of nanofibers by physical vapor deposition

There is a multitude of methods and techniques to make an object electrically conductive. However, no research has been published yet in the framework of electrically conductive and yet optically transmissive nanofibers. That is why, in this thesis, a study about possible realizations has been performed where the fabricated fibers were measured against the requirements that have been outlined in Sect. 4.2. Besides other factors, also economical aspects played an important role when deciding on which fabrication method should be implemented.<sup>11</sup>

Conventional physical vapor deposition (PVD) evaporates a material that is to be deposited via electrically resistive heating in vacuum.<sup>12</sup> As long as the material can be heated up to a high enough vapor pressure, in principle, any material can be deposited. This is very convenient when it comes to a material study of possible coating materials. Moreover, PVD is comparably easy and cheap to implement. It is for those reasons, that we decided to realize electrically conductive and optically transmissive nanofibers with this method.

There are many aspects in favor of one or the other material. In accordance to our estimations in Sect. 4.2.2 and due to reasons outlined in the respective sections, we decided to take silver and chromium as coating materials.

#### 4.3.1 Properties of thin film growth

When a material is heated up, its particles gain energy and the probability for them to be evaporated rises. At high vapor pressures  $p_v$  of the material, i.e. when the material is being evaporated into a gaseous form, thin film growth by vapor deposition can be carried out. Thin film growth can be divided into three stages: nucleation, coalescence and thickness growth. The initial atomic processes that are responsible for nucleation and coalescence are sketched in Fig. 4.7: When an evaporated atom comes close to a surface, attracting van-der-Waals forces act on it. If the forces are strong enough the atom sticks to the surface and is adsorbed. At this point it is also called an adatom. The remaining kinetic energy of the adatom can now lead to several processes. If the energy is still high enough the adatom can surmount the van-der-Waals potential again and be desorbed from the surface. Alternatively, it can migrate on the surface, which is called diffusion. The process, when two diffusing adatoms collide is called nucleation. If

---

<sup>11</sup> Very recently, Moore et.al. proposed another possible solution to realize an uncharged fiber [107]. In their setup levitated and positively charged single silica microspheres ( $Q \approx 100e$  to  $1000e$ ) that are optically cooled were discharged using UV flashes of a Xenon lamp. The number of elementary charges of the spheres could be inferred from their resulting motion. While this technique is not transferable to the nanofiber ion trap, here the ions could serve as charge sensitive probes in order to determine the charge of the fiber (similar to [23]).

<sup>12</sup> Other techniques that vaporize the material include Sputter deposition (via plasma discharge), electron beam deposition (via electron bombardment), pulsed laser deposition (via photon bombardment), cathodic arc deposition (via high power electric discharge).



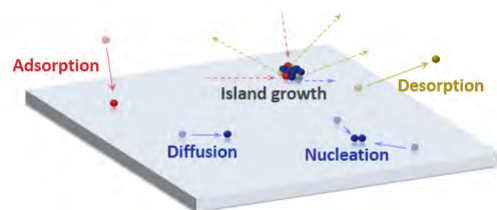


**Figure 4.7: Thin film growth processes.** Schematic illustration of initial atomic processes that take place during the nucleation and coalescence process. High energy atoms (red) of the evaporated material are adsorbed by the surface. Subsequently, the adatom can either be trapped on the surface – leading to diffusion and nucleation (blue) – or re-evaporated, which is called desorption (dark yellow). The combination of all these processes leads to island growth.

more and more adatoms aggregate a so called island is formed. For the cases where metals are deposited on oxides (e.g. fused silica), it is energetically favorable for the adatoms to nucleate and the formation of islands is the initial growth mode [108, 109].<sup>13</sup> At this state of the growth process the islands are isolated. A light field that is incident on the film interacts with these nanoscale absorbers and can excite a characteristic resonances, so-called the localized surface plasmon resonances. Strength and spectral position of the plasmon resonance depends on the material and the size of the islands (for details, see chapter 3). Over time these separated islands grow in size and number until they touch and coalesce. The percolation threshold is defined as the moment, where enough islands have grown together such that a continuous network over the substrate has been formed. For a large number of materials and substrates the percolation thickness lies between 1 nm and 20 nm. From this point on, metal films behave optically similar to the equivalent bulk material: While visible light that is incident on such a film will be transmitted, infrared light will be reflected (compare with Fig. 3.2f).

Above percolation thickness electrons, can migrate through the network and the electric resistance across the substrate drops heavily by several orders of magnitude. The resistivity of the film approaches the one for bulk, when the film thickness becomes larger than the mean free path length of the electrons in bulk.<sup>14</sup> At room temperature, the last stage of coalescence takes place on timescales of a day after deposition [113]. This process is referred to as 'self-diffusion' or 'self-thickening' in literature.

Due to the high kinetic energy of the evaporated atoms, thin film growth is a phenomenon far from thermodynamic equilibrium. Structure and characteristics of thin films strongly depend on the deposition conditions, i.e. physical properties of the substrate and the deposition material

<sup>13</sup> The growth mode where separated three-dimensional islands form on the substrate is called Volmer-Weber mode. The opposite mode where layer by layer is grown is called Frank-van-der-Merwe mode. A layer plus island growth mode is called Stranski-Krastanov mode.

<sup>14</sup> It is interesting to note that even when the islands are still separated, finite but significantly smaller conductivities can be measured [110–112].

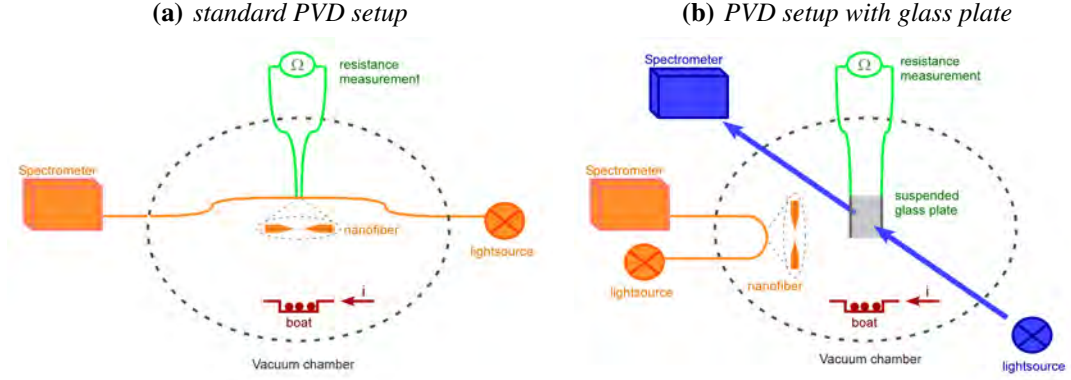


**Figure 4.8: PVD configurations.** (a) PVD on an optical nanofiber. An electric current  $i$  is sent through a boat that is loaded with the deposition material (red). Meanwhile, white light is sent through the fiber onto a spectrometer (orange) and the resistance across the tapered optical fiber is measured (green). (b) Due to expected high resistances and low transmissions across a coated tapered optical fiber, a second PVD configuration was set up which contains an additional suspended glass plate inside the chamber (blue). In this case, the resistance can be measured across the glass plate (green) instead of the tapered optical fiber. White light spectroscopy is performed for both of them.

as well as the residual vacuum. It is for that reason, that the theoretical reproduction of film performances remains to be a challenge [114].

#### 4.3.2 Experimental setup for physical vapor deposition

The basic evaporation setup that was used for the measurements in the following sections, consists of a 30 cm long Conflat (CF) 6-way cross that is used as the vacuum chamber (see Sect. A.2 in the appendix) and a tungsten boat which was heated up electrically by a modified welding supply via electrical feedthroughs. The two standard PVD configurations are shown in Fig. 4.8. Figure 4.8a sketches the standard PVD setup, where the white light extinction spectrum through the optical nanofiber as well as the electrical resistance across it can be measured simultaneously. Because of the strong optical absorption when the nanofiber is being coated and the high electrical resistance of the bare nanofiber, a second configuration, using a conventional microscope glass plate, was developed which is sketched in Figure 4.8b: For a glass plate with the same coating thickness, both, electrical resistance and optical absorption are significantly lower than compared to a tapered optical fiber (see Sect. 4.2.2). It is therefore possible to investigate the coating process at layer thicknesses where ohmmeter ( $R_{\max} = 2 \text{ G}\Omega$ ) and spectrometer ( $\mathcal{A}_{\max} = -\lg(I_{\min}/I_0) \simeq 4$ ) reach their limits in the case of the tapered optical fiber. As only one of both objects can be connected to the ohmmeter, for this configuration the glass plate's resistance is measured. In order to avoid measurement errors due to parasitic resistances, the glass plate was suspended on two UHV compatible, isolated Kapton wires which were soldered

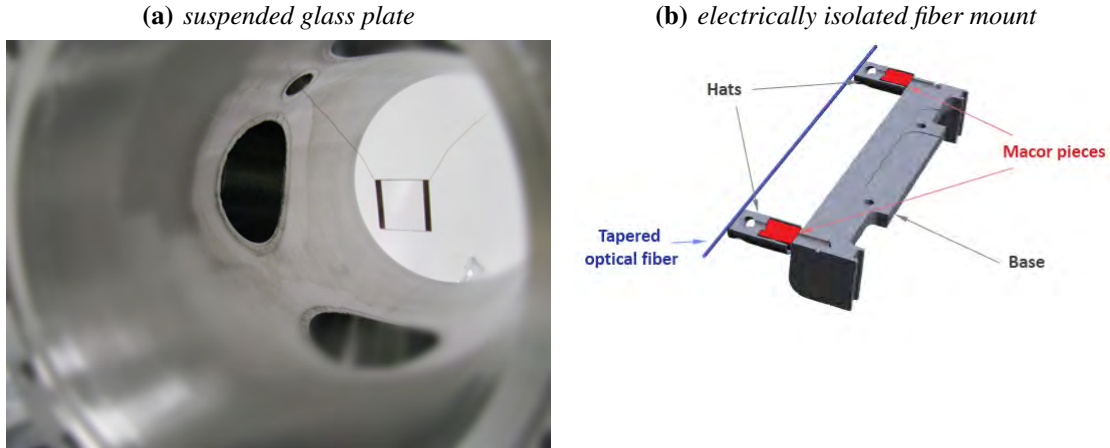


**Figure 4.9: Electrical isolation of deposition targets.** (a) Conventional microscope glass plate inside the vacuum chamber that is suspended on insulated wires. (b) Picture of a cut through the tapered optical fiber mount that was used for the PVD measurements. The tapered optical fiber (blue) is fixed on the hats of the mount. The hats serve as electrodes and are electrically isolated from (i.e. they do not directly touch) the base of the mount and each other thanks to two supporting Macor pieces (shown in red). Additionally, the hats cover the Macor supports without touching them at the sides in order to reduce the risk of short circuiting both hats via a conductive layer. Macor is a glass ceramic that is easy to machine and that has a volume resistivity which is equal to glass. The resistance of the Macor pieces is much larger ( $R > 10^{16} \Omega$ ) than the expected resistance across the coated tapered optical fiber. The fiber mount was made by the IQOQI workshop in Innsbruck and can be integrated into the ion trap setup in Innsbruck.

onto gold electrodes on the glass plate (see Fig. 4.9a).<sup>15</sup> For measuring the resistance of the nanofiber, a special fiber mount was used (see Fig. 4.9b). The fiber mount consists of two Macor pieces that isolate the hats (i.e. the two parts where the tapered optical fiber is fixed on) from each other. Similar as with the glass plate, insulated Kapton wires are attached to the hats of the mount to measure the resistance across the tapered optical fiber.<sup>16</sup> The Kapton wires and the tapered optical fiber are extracted from the vacuum chamber via standard Swagelok connectors where the metal ferrules are replaced by Teflon ferrules. Fibers and wires are lead to the outside via holes inside the ferrule [115].

Thanks to an optional frame inside the vacuum chamber, the mount can be fixed such that the fiber directly faces the evaporation source. This way there is no direct line of sight from the boat to the Macor pieces and the formation of a percolated film on them which would cause a significant parallel resistance is prevented. In case of the second configuration, the glass plate is positioned on top of the evaporation source and the fiber mount has to be positioned besides the direct line of sight to the evaporation source. In both PVD configurations, the whole tapered

<sup>15</sup> The gold electrodes of the glass plate were evaporated onto it in advance. The Kapton wires can be purchased at Accu-Glass Products, inc.

<sup>16</sup> Notice that, the positions where the tapered optical fiber is fixed onto the mount are in the unprocessed sections. As a consequence the resistance is measured across the nanofiber and taper section as well as a part of the unprocessed fiber.

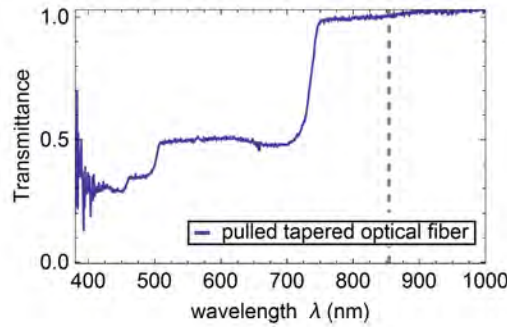


**Figure 4.10: Typical transmission spectrum of an uncoated nanofiber.** *Typical transmission spectrum for the tapered optical fiber profile that is used in the PVD measurements with respect to the unprocessed fiber. The nanofiber radius is  $a = 250$  nm making the nanofiber be single mode for all wavelengths above  $\lambda \simeq 450$  nm. The dashed lines indicate the calcium transitions at  $\lambda = 397$  nm and  $\lambda = 866$  nm. The unprocessed fiber is single mode for wavelengths above  $\lambda \simeq 670$  nm.*

optical fiber will be coated and not only the nanofiber section.

The evaporation source is a replaceable Teflon boat. It is directly connected to two high current feedthroughs. The boat is heated up by applying a high current to it via a welding source<sup>17</sup> whose electrode and work lead are directly connected to the electric feedthroughs. The source provides an alternating current in the range from about 20 A to 180 A, so in order to be able to tune the current down to zero a transformer is interposed. With this source, boat temperatures in the range of 920 °C to more than 1800 °C can be achieved.<sup>18</sup>

The vacuum chamber is attached to a pump system consisting of a two stage setup including a turbo pump (Pfeiffer HiCube 80) and a membrane pump (Pfeiffer MVP 015). A full-range pressure gauge (Pfeiffer PKR 251) measures the chamber pressure. The pump system reaches minimum chamber pressures of around  $10^{-9}$  mbar. This way, oxidization and contamination of the coating material will be strongly suppressed with respect to atmospheric pressure.

For the measurements, standard optical fibers<sup>19</sup> were tapered down to a nanofiber radius of  $a = 250$  nm.<sup>20</sup> After production, a transmission spectrum is recorded which typically looks like the one presented in Fig. 4.10. A high transmittance is important because it indicates that there are no contaminants on the nanofiber. The latter not only reduces the transmission characteristics of the nanofiber, but also leads to porous structures during film growth and could lead to rupture of the nanofiber, when the power of the guided light exceeds a certain threshold. The length of

<sup>17</sup> Elektra Beckum Elektroden-Schweissgerät SB 201 T. If long duty cycles and signal noise are not an issue, welding sources provide an remarkably cost-efficient solution as high-current power supplies.

<sup>18</sup> The temperatures were measured with a two color pyrometer through one of the view ports.

<sup>19</sup> SM800, manufactured from Fibercore

<sup>20</sup> The fiber radius of  $a = 250$  nm was chosen to achieve a large evanescent field for the wavelengths of 397 nm and 866 nm, because it was not clear which wavelength was going to be used. Notice that a nanofiber with a radius of 250 nm is no longer single mode for a wavelength of 397 nm. In case of the experiment outlined in Sect. 4.2.3, where the nanofiber provides a coupling field, a smaller radius would be better. Not only does it increase the intensity far away from the nanofiber surface (see 4.6), it also leads to less power of the guided light field inside the coating.

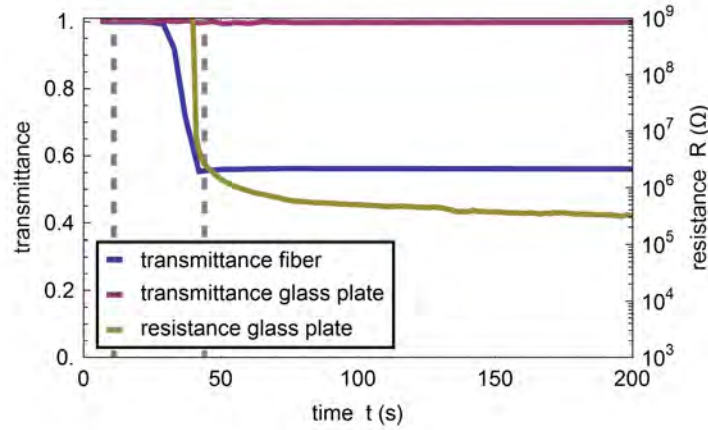


**Figure 4.11: Silver deposition on a glass plate and a tapered optical fiber - Experimental results.**

*Transmittance of a tapered optical fiber (blue) as well as transmittance (red) and resistance (dark yellow) of a glass plate during PVD of silver as a function of time. The transmittances are shown at a wavelength of 866 nm. The time,  $t = 0$  s, corresponds to the start of the heating of the evaporation source. The dashed vertical lines at  $t = 11$  s and  $t = 45$  s indicate the start and stop time of evaporation, respectively. Notice that the resistance of the glass plate is plotted on a logarithmic scale.  $2 \times 10^9 \Omega$  is the maximum resistance that could be measured by the ohmmeter.*

the nanofiber part of the tapered optical fiber is 1 cm. This value was a requirement for the ion trap integration in Innsbruck in order to align it properly to the ion chain and reduce distortions of the trapping potential by the taper region.

### 4.3.3 Coating nanofibers with silver: experimental results

In Sect. 4.2 it could be seen that integrating a nanofiber into an ion trap leads to strict requirements on the electrical conductivity of the fiber. Silver (Ag) is widely used as a deposition material in PVD setups. It has the lowest on resonance transmission loss of any natural noble metal at optical frequencies [116], a very low deposition temperature and the highest electrical conductivity of all elements reported [117]. It is for those reasons that it was decided to investigate silver as one possible coating material within the study of vapor deposition materials.

As a first approach, optical nanofibers and glass plates were coated with the PVD configuration shown in Fig. 4.8b. We evaporated silver (99.99 % pure silver pellets, Umicore) by heating the tungsten boat to around  $T \simeq 1200$  °C for 30 s. These settings corresponds to a calculated mass evaporation rate of  $10^{-3}$  g/s and deposition rates on the glass plate (tapered optical fiber) of  $10^{-6}$  g/(cm<sup>2</sup> s) ( $10^{-7}$  g/(cm<sup>2</sup> s)) [118]. The different values result from different distances and orientations to the boat.

Figure 4.11 shows the time evolution of the transmittance for the nanofiber and the glass plate as well as the resistance measured across the glass plate. While the transmittance (at 866 nm) of the tapered optical fiber drops down to a value of around  $\mathcal{T} = 0.56$ , the transmittance



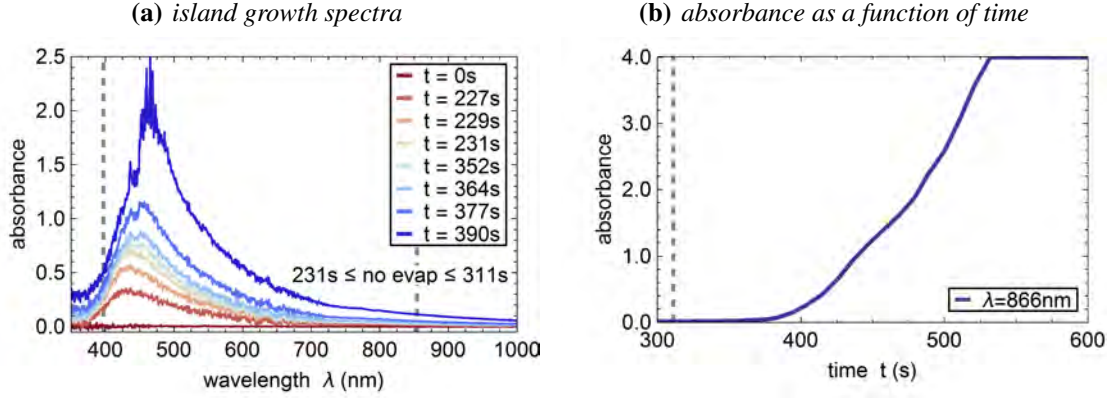


**Figure 4.12: Silver island growth on a tapered optical fiber - Experimental results.** (a) Absorbance spectra of silver islands on a tapered optical fiber. Over time (red to blue, see inset) more and more islands form on the surface of the nanofiber and grow in size. Both these effects lead to an increase of the absorbance. At  $t = 0$  s the current source that heats up the boat was switched on. It was temporarily switched off from  $t = 231$  s to  $t = 311$  s. The dashed vertical lines indicate the wavelengths  $\lambda = 397$  nm and  $\lambda = 866$  nm. (b) Absorbance at  $\lambda = 866$  nm as a function of time for the same deposition measurement as in panel (a). The dashed vertical line indicates the restart time of the evaporation at  $t = 311$  s. The spectrometer cannot detect higher absorbances than  $A = 4$ .

tance of the glass plate remains unchanged. At  $t = 40$  s we see the onset of conductivity of the glass plate as a very steep reduction of resistance down to  $10^6 \Omega$ . This regime corresponds to the percolation threshold, i.e. the transition from isolated islands to a connected network across the glass plate. The evaporation was intentionally stopped at the onset of conductivity, which is the reason for the high transmission and resistance values. The further change of the resistance after the end of the evaporation process is due to self-thickening as described in Sect. 4.3.1. In the above measurement, the resistance kept drifting over more than a day in conjunction with theoretical predictions (further details about self-thickening can for example be found in [113]). The first change in resistance across the glass plate is detected about 7 s later than the drop in fiber transmission.

To answer the question of whether there exists a measurable resistance across the tapered optical fiber, we repeated the measurement with the PVD configuration shown in Fig. 4.8a. Due to a different location of the nanofiber with respect to the evaporation source, the mass deposition rate was on the order of  $10^{-5} \text{ g}/(\text{cm}^2 \text{ s})$  [118]. Figure 4.12a shows the white light transmission spectra through the tapered optical fiber during deposition. The shape of the spectra exhibits distinct features of a surface plasmon resonance of single nanoparticles as introduced in chapter 3. This is a clear signature of an island growth-like behavior. Over time, the absorbance (see eq.4.7) grows in size and its maximum shifts to higher wavelengths. While the second effect is due to the fact that the islands grow in size, the first effect is also due to an increasing number of islands.

Figure 4.12b shows the absorbance at  $\lambda = 866$  nm as a function of time. At an absorbance

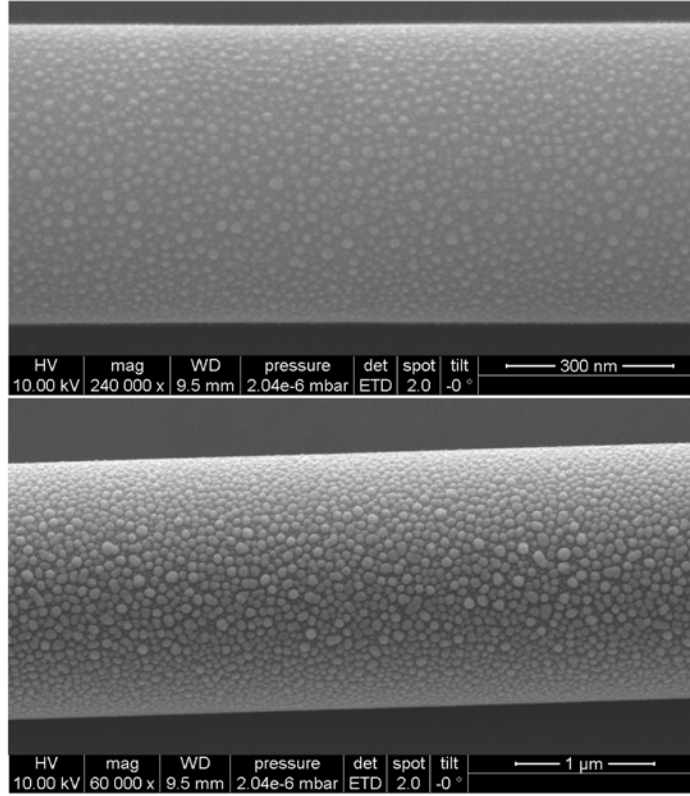


**Figure 4.13: Silver island growth on a tapered optical fiber - Experimental results.** SEM images for the silver deposition process in Fig. 4.12 of the waist region (upper image) and taper region (lower image). The fiber diameter is  $2a = (535 \pm 4) \text{ nm}$  [ $2a = (1.85 \pm 0.01) \mu\text{m}$ ] in the upper [lower] image. The average island diameter is about  $2\bar{R} = (21 \pm 4) \text{ nm}$  [ $2\bar{R} = (73 \pm 10) \mu\text{m}$ ] in the upper [lower] image. Notice the different magnifications in both pictures. The errorbars correspond to the resolution of the SEM.

of  $\mathcal{A}(866 \text{ nm}) = 4$ , which is the highest the spectrometer can detect, the resistance was above the measurement range of the device. The PVD was carried out for additional hours without changing this state. We attribute this effect to the deposition rate in our setup. At low deposition rates Sennett et.al. reported, that islands tend to growth in height rather than in width, which leads to a later (or no) coalescence with neighboring islands compared to higher deposition rates [119].<sup>21</sup>

This fact could be confirmed with scanning electron microscope (SEM) pictures taken after the experiment (see Fig. 4.13).<sup>22</sup> It can clearly be seen, that the islands have not coalesced yet.

<sup>21</sup> In fact, several more PVD measurements have been carried out with silver. Conductivity could not be detected in any of them.

<sup>22</sup> In order to carry out SEM measurements, the nanofiber is deposited on a 2-inch diameter Al-substrate and fixed onto it using UV-curing glue. In order not to break the tapered optical fiber, the deposition process is monitored with a microscope. A bare nanofiber can be seen in 5.12.

Moreover, a correlation between the diameter of the fiber and the mean size of the islands is visible. Several SEM images have been analyzed along the tapered optical fiber and the ratio between fiber diameter and island diameter seems to be constant. For a clear statement more data would have to be taken. To the authors knowledge island growth on high curvature substrates has not been investigated so far.

### 4.3.4 Coating nanofibers with chromium: Experimental Results

Due to the fact that a resistance across the tapered optical fiber could not be realized even hours after the absorbance was already very large. While this should in principle be possible for high enough evaporation rates, it seemed very unrealistic to reach conductivity in a regime where the optical transmission is still relevant. In this context, the percolation thickness plays a key role which is why chromium (Cr) attracted our attention. Chromium is reported to be the best coating material in high resolution scanning electron microscopy due to its negligible film thickness as well as small particle size during the growth process [119, 120] and is used for thin film resistors and photomasks [121].

Using the PVD configuration shown in Fig. 4.8a, we evaporated chromium by heating the tungsten boat to around  $T \simeq 2400^\circ\text{C}$  for about 120 s. This corresponds to a mass evaporation rate of  $10^{-1}$  g/s and deposition rates on the tapered optical fiber of  $10^{-4}$  g/(cm<sup>2</sup> s) [118]. Figure 4.14a shows the white light absorbance spectra through the tapered optical fiber for several times during evaporation. As can be seen, the absorbance grows over time. Chromium nanoparticles do not exhibit a localized surface plasmon resonance in the visible spectrum,<sup>23</sup> which is why no absorbance peaks are observed. In Fig. 4.14b the corresponding transmittance (at  $\lambda = 397$  nm and  $\lambda = 866$  nm) and electrical resistance are shown as a function of time. The transmittance decreased by two orders of magnitude in the first 20 s of the evaporation over the range from around  $\lambda = 400$  nm to  $\lambda = 1000$  nm. Approximately 60 s after the start of the evaporation, the tapered optical fiber becomes conductive.<sup>24</sup> The range from  $t \simeq 80$  s to  $t \simeq 120$  s, where the temperature of the tungsten boat was ramped down goes along with an increase in resistance to  $R \simeq 2 \times 10^8 \Omega$ . About  $t \simeq 480$  s later, the resistance had increased by about 7 %. As in the case of PVD with silver (Sect. 4.3.3), this can be explained with a self-thickening process of the chromium film (see Sect. 4.3.1 and [113]) and (extrapolating this increase) probably led to an unmeasurable resistance four days after the evaporation was performed. It was possible to recover conductivity by re-evaporation of chromium. In addition to the recorded white light transmission spectra through the tapered optical fiber, we also measured the transmitted power for laser light (wavelength,  $\lambda = 532$  nm) before and after the coating procedure in order to determine the final transmittance. The residual transmittance about fifteen minutes after the end of the evaporation process was  $\mathcal{T} \simeq 10^{-6}$ .

<sup>23</sup> Using Mie theory (see Sect.3.2.3) and the chromium values for the Drude-Lorentz model parameters published in [90], the first resonance can be found around  $\lambda = 300$  nm.

<sup>24</sup> By extrapolating the data points from the onset of conductivity to the start of the boat temperature ramp down process, one would obtain a resistance of  $R \approx 10^{11} \Omega$  at the start of the evaporation ( $t = 0$  s). The resistance of the bare fiber is, however, estimated to be around  $R \approx 10^{26} \Omega$ . Due to the abrupt change of electrical properties at the percolation threshold it is not possible to estimate the resistance that far away from the measured data.



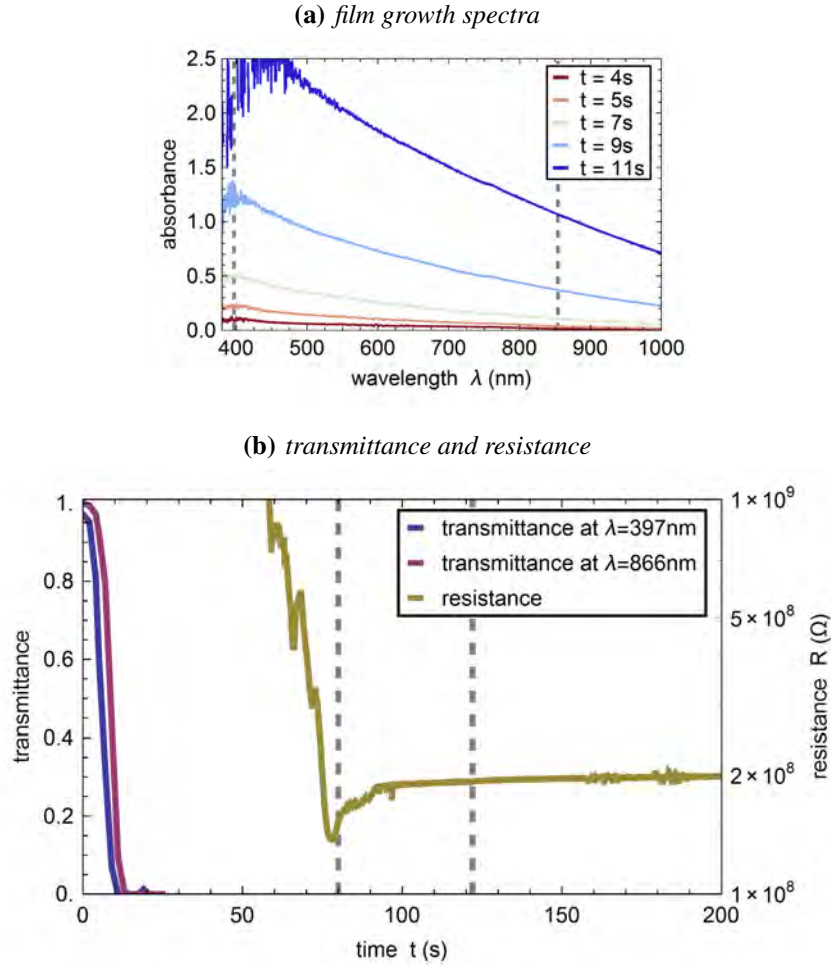


**Figure 4.14: Chromium film growth on a tapered optical fiber - Experimental results.** (a) Absorbance spectra of chromium film growth on a tapered optical fiber. Over time (red to blue, see inset) more and more chromium is deposited on the surface of the nanofiber leading to a rise in absorbance. The dashed vertical lines indicate the calcium transition wavelengths at  $\lambda = 397$  nm and  $\lambda = 866$  nm. (b) Transmittance (blue, red) and resistance (dark yellow) across a tapered optical fiber as a function of time. The transmittances are shown at a wavelength of 397 nm (blue) and 866 nm (red). The time,  $t = 0$  s, corresponds to the start of the heating of the evaporation source. In the range of the dashed vertical lines ( $80 \text{ s} \leq t \leq 122 \text{ s}$ ) the current source that heats the evaporation source was ramped down. Notice that the resistance of the glass plate is plotted on a logarithmic scale.  $2 \times 10^9 \Omega$  is the maximum resistance that could be measured by the ohmmeter.

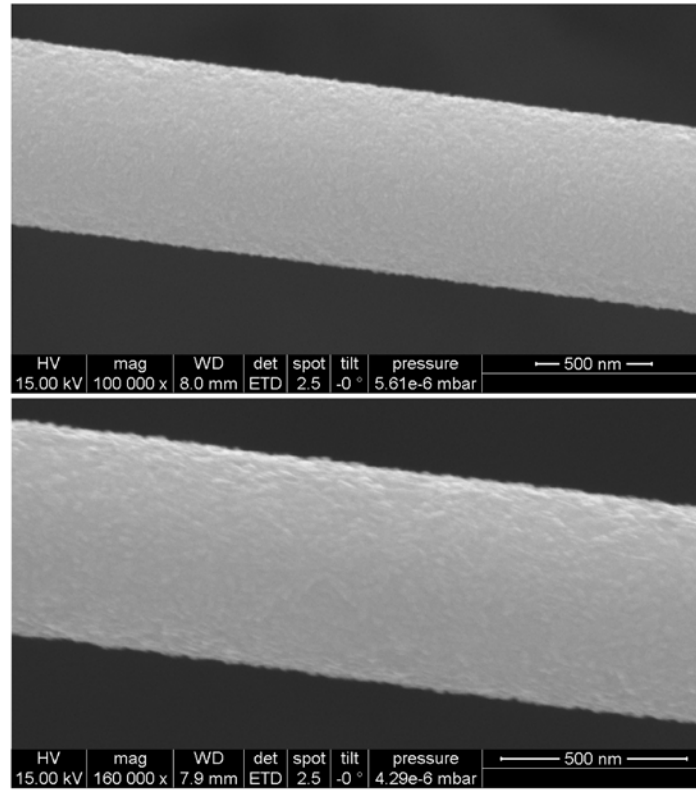


**Figure 4.15: Chromium film growth on a tapered optical fiber - Experimental results.** SEM images for the chromium deposition process in the taper region (upper image) and waist region (lower image). The fiber diameter is  $2a = (801 \pm 6) \text{ nm}$  [ $2a = (574 \pm 4) \text{ nm}$ ] in the upper [lower] image. Notice the different magnifications in both pictures. The errorbars correspond to the resolution of the SEM.

The values presented above are preliminary results. In future experiments two mechanisms should be investigated more thoroughly: (i) The stability of the deposited film under the influence of strong guided fields in order to rule out a potential re-evaporation of the chromium from the surface of the tapered optical fiber. (ii) The order of magnitude of the parallel resistance across the shielded Macor pieces of the fiber mount. Both effects could lead to an underestimation of the actual nanofiber resistance.

The SEM images in Fig. 4.15 were taken after several more evaporation runs in addition to the one presented in Fig. 4.14. A clear coalesced film structure is visible on the nanofiber.<sup>25</sup> The variation of the nanofiber diameter after fabrication is empirically found to be  $\pm 5\%$  of the desired value, which leads to the estimation that the film thickness is on the order of 50 nm.

<sup>25</sup> A bare nanofiber can be seen in 5.12.

## 4.4 Conclusion and other possible realizations

In this chapter, tapered optical fibers and, as additional test objects, microscope glass plates were coated using physical vapor deposition in order to investigate changes of their electric and optical properties.

With silver as the deposition material, electrically conductive glass plates with almost loss-less transmission were realized. However, this was not the case for tapered optical fibers. The reason for this was a strongly pronounced island growth on the surface of the nanofiber that seemed to have never coalesced. At low deposition rates it was shown that islands tend to grow in height rather than in width leading to a much later coalescence with neighboring islands [119]. Evaporated chromium on the other hand reached percolation thickness on tapered optical fibers. While the transmittance was severely reduced a region was found where the fiber was electrically conductive ( $R \simeq 2 \times 10^8 \Omega$ ) and yet optically transmissive ( $\mathcal{T} \simeq 10^{-6}$ ). With these values, it might be possible to generate intensities close to the fiber surface that are on the order of the saturation intensity for high enough optical input powers (see Sect.4.2.3). However, using the nanofiber as an interface to collect the photons emitted from the ions and thus to transfer quantum information from ions to photons would not be possible.

However, there might be a directly accessible parameter regime where one could simultaneously obtain high transmission and high conductivity: From Eq. (4.5) and Eq. (4.9) we know that  $R_{\text{fiber}} \propto l_w$  and  $\mathcal{T}_{\text{fiber}} \propto \exp(-\alpha l_w)$ . For the same coating thickness, a reduction of the nanofiber length from  $l_w = 1 \text{ cm}$  to  $l_w = 1 \text{ mm}$  would therefore lead to a reduced resistance of  $R \simeq 2 \times 10^7 \Omega$  and an increased transmittance of  $\mathcal{T} \simeq 0.25$ , which are suitable values in order to efficiently collect fluorescence from the ions.

So far we have considered only the waist region of the tapered optical nanofiber. Unfortunately, in a realistic scenario the tapered region can not be neglected in the transmittance calculations because the evanescent field is still significant for small taper radii. In the case of a waist length of 1 mm, a large fraction of the optical losses (about 80 %) would result from the taper transition. This leads to a maximally achievable transmittance of  $\mathcal{T} \simeq 10^{-4}$ .<sup>26</sup> To reduce the influence of the taper on the transmittance, the gradient of the radius profile of the taper regions has to be increased for small fiber radii. Due to the fabrication process, this gradient is limited by the width of the flame, which in our pulling rig is equal to 1 mm. To reduce this width, the fiber pulling rig would have to be modified. Moreover, the ion trap setup would have to be changed in order to compensate for the reduced waist length of the nanofiber.

In addition to changing the fiber geometry, further options are available to increase the transmittance through the tapered optical fiber:

(i) Reducing the coating thickness down to higher resistances leads to a concomitant increase of the transmittance. However, because of the rapid decay of the resistance in Fig. 4.14 until the evaporation was stopped, it is very likely that the chromium film thickness is slightly above percolation threshold. Consequently, even a small reduction in film thickness might lead to a situation where the film is below percolation resulting in a large increase in resistance with almost

<sup>26</sup> In order to calculate the corrected transmittance, the absorption coefficient  $\alpha_{\text{Cr}}$  for the chromium coated fiber was calculated. The transmittance through the tapered optical fiber was then calculated via  $\mathcal{T} = \exp(-\int_{\text{TOF}} (P_{\text{coat}}(z)/P_0) \alpha_{\text{Cr}} dz)$ , where  $P_{\text{coat}}(z)/P_0$  is the power fraction inside the coating at the position  $z$  along the tapered optical fiber.

no gain in transmission.<sup>27</sup> (ii) Point (i) directly leads to the question of achieving percolation at smaller film thicknesses. The percolation thickness is closely related to the smoothness (also referred to as 'wetting') of the film [122]. In this setup, improved wetting could be realized by increasing the deposition rate and decreasing the temperature of the nanofiber [114].

(iii) A third option would be to improve the evaporation system. A precise PVD apparatus allows one to stop the deposition precisely at / shortly before percolation. Also, film deposition techniques like e.g. atomic layer deposition [123], sputtering, electron beam deposition [121] or cathodic arc deposition [124], could probably realize smoother films. In a first approach, chromium films have been sputtered onto nanofibers during this thesis with an external system.<sup>28</sup> The coated fibers had resistances of  $3 \times 10^5 \Omega$  and  $3 \times 10^6 \Omega$  depending on the evaporation time but had no measurable transmittance. Other possibilities to improve wetting are plasma pretreatment and ion beam milling. The main problems with using external device are the pollution of the nanofiber before and after the deposition process, an oxidation of the deposited film and the difficulty to monitor the transmittance and resistance during the deposition process.

An central part of this project was to track down and to evaluate possible materials, methods or techniques in order to fabricate conductive and yet transmissive nanofibers. While the metals silver and chromium seemed or seem to be good candidates, it is possible, that better materials exist to achieve this goal. A selection of them shall be discussed in the following:

**Transparent conductive oxides:** Transparent conductive oxides (TCO's) are doped metal oxides and form the largest group of coating materials for touch screens and solar cells. Their most prominent member, Indium tin oxide (ITO,  $\text{In}_2\text{O}_3:\text{Sn}$ ), is probably one of the first coating materials that comes into mind when thinking about fabricating conductive and yet transmissive nanofibers. ITO could be directly used in the setup of this thesis. When seen in bulk form (Fig. 4.16) ITO is, like metals, not transmissive at all. Its sheet resistance is about one order larger than silver and the percolation thickness is one order larger than chromium [125–128]. The big advantage of TCO's in general is that the metal oxide characteristics can be changed up to a certain extent by the doping material and the amount of dopants. That is why TCO's remain to be a class of materials that would be interesting to investigate. Because indium is rare and expensive other TCO's get more and more attention. One interesting member among them is fluorine-doped zinc oxide ( $\text{ZnO:F}$ ) which is reported to have a better conductivity as well as a higher transparency than ITO [129].

**Alkali metals:** Alkali metals are broadly used as glass coatings in photomultiplier tubes and, due to the existence of alkali metal dispensers, a comparably easy-to-build-up deposition setup can be realized. For this reason, rubidium (Rb) and cesium (Cs) were actually the first materials that were investigated as deposition materials in this thesis in order to realize con-

---

<sup>27</sup> It would be interesting to get a grasp on the electrical properties of deposited films whose resistances are too high to be investigated by the ohmmeter used in this thesis. Reducing the length of the nanofiber, increasing the fiber radius (and simultaneously reducing the evanescent field intensity) or using a more sensitive (and more expensive) measurement device, such as an electrometer or a pico-ammeter would allow one to measure the nanofiber resistance over a much larger range. Indeed, elements were already being built to measure the resistance across the tapered optical fiber at an external patch clamp platform, which is normally used to determine the properties of ion channels of cells.

<sup>28</sup> Quorum Q150T S Sputter Coater



**Figure 4.16: Indium tin oxide (ITO) pieces for physical vapor deposition.** *Indium tin oxide (ITO) pieces as they are used in physical vapor deposition or electron beam deposition. In bulk form, they are entirely opaque. (The image is taken from [www.lesker.com](http://www.lesker.com).)*

ductive nanofibers. In both cases, however, experiments remained unsuccessful. After several possible reasons had been ruled out, two possible explanations remain: The white light that was used to measure the optical transmission led to what is called light induced atomic desorption (LIAD) [130, 131].<sup>29</sup> In this context it is interesting to notice that the opposite process of light induced atomic *adsorption* also exists [132]. The second explanation is that the evaporation rate of the dispensers was too small. Evaporation runs for durations of more than a week neither led to a permanent change in transmission of the glass plate nor to a measurable resistance.

**Other metals:** Aluminum (Al) is reported to have the highest opacity of all metals across the visible spectrum. Like chromium, it has a very small grain size and provides smooth films. Unfortunately, it is challenging to evaporate Aluminum and it also oxidizes. In contrast to all metals mentioned so far, gold (Au) is chemically inert and therefore an interesting candidate. At second sight, however, gold has a percolation threshold that is comparable to the one of silver and in addition a worse conductivity.

**Graphene:** Graphene is a zero-gap semiconductor made out of a monolayer of carbon atoms. It has a very high electron mobility and can provide conductivities on the same order as copper or silver. To date, however, typical conductivities are about two orders of magnitude smaller. The transmittance of a free standing monolayer is frequency independent and about  $\mathcal{T} \simeq 0.977$  [133]. Bao et al provided a technique (including vapor deposition) to attach graphene along the core of a standard optical fiber whose cladding was partially carved away and demonstrated that light propagating through the fiber core along a graphene sheet is only weakly damped if polarized correctly [134, 135]. The insertion loss due to a graphene layer with a length of a few millimeter was 5 dB. Commercial devices exhibit insertion losses of about 1.5 dB. While technically challenging, it might also be possible to attach graphene onto a *tapered* optical fiber.

**Conductive nanostructures:** A different approach than coating the tapered optical nanofiber with a material would be to attach nanostructures like a thin wire to the fiber surface. Compared to a homogeneous coating all around the fiber, an attached co-propagating nanowire should al-

<sup>29</sup> Small correlations of the transmittance with switching the light source on and off during deposition could be recorded but a measurable resistance could not even be obtained when the light source was switched off for many hours.

low for better transmissions [136,137] and still exhibit comparable conductivities. Alternatively, connected wires, i.e a metallic nanothrough network, would also be thinkable. The deposition or fabrication of such devices could possibly be realized with e.g. AFM-deposition [21, 138], electrospinning metal deposition [139] or laser printing [140].

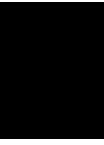
It is interesting to note, that a hybrid film consisting of a percolated silver nanowire network and a monolayer graphene was recently realized [141]. Combining the advantageous properties of both techniques, its sheet resistance and transmittance were among those of the best materials to date.

**Tapered optical fiber fabrication from coated standard optical fibers:** An intuitive solution for the realization of conductive nanofibers is to fabricate coated tapered optical fibers by applying the heat and pull process explained in Sect. 2.4.1 to already metal coated standard optical fibers. This method was investigated in the course of this thesis as part of a Bachelor thesis [142].<sup>30</sup> Because in this group the heating is performed by a  $H_2/O_2$ -flame, we limited our investigations to gold (Au) and palladium-gold (Pd:Au) coatings which are not prone to being incinerated by the flame. However, due to large temperature gradients along the fiber, the coating agglomerated at the unprocessed part of the nanofiber after being molten. In order to circumvent this problem, a much more educated heating profile along the whole tapered optical fiber during the heat and pull process would have to be developed.

In conclusion, by combining all the proposed optimizations, i.e. modification of the fiber profile, improvements of the coating process and possibly better coating materials, a tapered optical fiber with sufficient transmittance reaching orders of 10 % should be within range.

---

<sup>30</sup> In this context, we determined the temperature of the molten region of the tapered optical fiber to be in between  $(1907 \pm 27)$  K and  $(2047 \pm 47)$  K during fabrication with the pulling rig of this group. This temperature is important in order to determine which coating materials can be processed.



# Interfacing Optical Nanofibers with Single Nanoparticles

The development of integrated electronic circuits laid the foundations for the information age which fundamentally changed modern society. During the last decades, a transition from electronic to photonic information transfer took place and, nowadays, nanophotonic circuits and waveguides promise to partially replace their electronic counterparts and to enable new functionalities [143–145].

For a plane wave that is circular polarized the spin angular momentum points parallel or anti-parallel to its propagation direction, depending only on the sense of circulation. The strong confinement of light provided by waveguides, however, leads to large intensity gradients on the wavelength scale, where this is no longer the case. In contrast to paraxial light fields, the local spin of the guided light depends on its propagation direction. Thus, in this strongly non-paraxial regime, spin and orbital angular momentum of light are not independent physical quantities any more but are coupled [29, 30]. In particular, the spin depends on the position in the transverse plane and on the propagation direction of light in the waveguide – an effect referred to as spin-orbit interaction of light (SOI).

As discussed in chapter 2, for vacuum-clad dielectric waveguides, evanescent fields arise in the vicinity of the surface and allow one to locally interface the guided fields with micro- and nanoscopic emitters [146], which leads to an asymmetry of the scattering properties of the emitter into the left and right direction of the waveguide. Due to SOI the evanescent fields exhibit a locally varying longitudinal polarization component that points in the direction of propagation of the light. It oscillates in quadrature with respect to the transversal components and together they lead to elliptic polarization in the plane containing the waveguide axis [18]. Surprisingly and in contrast to paraxial light fields, the corresponding photon spin is in general not parallel or antiparallel to the propagation direction of the guided light. In special cases it can even be perpendicular to the propagation direction and antiparallel to the orbital angular momentum [31, 32].

In this chapter, first, light is shed on the concept of SOI at nanofibers (Sect. 5.1) and the consequences for point-like dipole emitters that couple to their evanescent fields (Sect. 5.2). Section 5.3 discusses the preparation of a nanofiber-emitter system. It is shown that the nanofiber is a great tool for detecting single nanoparticles via white light extinction spectroscopy (Sect. 5.3.2). This fact can be exploited to prepare single nanoparticles onto the nanofiber. In this thesis, an experimental technique was developed that is able to identify a single nanoparticle on the nanofiber with a success probability of close to one (Sect. 5.3.3). With this technique at hand, in section 5.4, we experimentally demonstrate that SOI at an optical nanofiber drastically changes the scattering characteristics of a nanoscale particle located in the nanofiber's evanescent field. In free space, point-like scatterers exhibit a dipolar emission pattern (see Sect. 3.2.2 and [51]) where, for the emission of both, linearly and circularly polarized light, the intensity distribution of the scattered light is cylindrically symmetric with respect to the dipole axis. Here, we illustrate that SOI breaks this symmetry and drive this effect up to the point where the amount of light that is scattered into the nanofiber modes by a gold nanosphere, can significantly exceed the power that propagates in the opposite direction. The strength of the directionality depends on the polarization of the applied light field with respect to the position of the nanoparticle on the fiber surface. Parts of the results presented in this chapter have been published in [147].

## 5.1 Spin-Orbit interaction of light in optical nanofibers

In contrast to the standard description of light as a purely transverse wave, longitudinal field components are often significant in cases where the electric field changes significantly on a length scale comparable to  $\lambda/(2\pi)$  [32]. This can directly be derived from Gauss's law. For an electric field  $\mathbf{E} = \mathbf{E}_0 \exp(i[-\omega t + kz])$ , with  $\mathbf{E}_0 = (E_{0,x}, E_{0,y}, E_{0,z})$  and  $k = 2\pi/\lambda$ , it reads

$$\partial_x E_x + \partial_y E_y + \partial_z E_z = 0. \quad (5.1)$$

For beams that slowly vary along  $z$ , the vector amplitude  $\mathcal{E}_0$  reads

$$E_{0,z} = \frac{i}{k} (\partial_x E_{0,x} + \partial_y E_{0,y}). \quad (5.2)$$

If we assume, without loss of generality, linearly polarized light along  $y$ , it is  $\partial_y E_{0,y} = 0$  and

$$E_{0,z} = \frac{i}{k} \partial_x E_{0,x}. \quad (5.3)$$

Here, it can clearly be seen, that the longitudinal component  $E_z$  of the light field becomes significant for  $\partial_x E_{0,x} \simeq k$  and that it oscillates  $\pi/2$  out of phase, i.e. in quadrature, with respect to the transversal components.

In particular, such a situation occurs in the case of total internal reflection in the evanescent field. For the case of a nanofiber mode  $\mu_y^{\mathfrak{d}}$  quasi-linearly polarized along  $\hat{\mathbf{y}}$  and propagating along  $\mathfrak{d} \hat{\mathbf{z}}$  (see Eq. (2.19)),<sup>1</sup> we find a ratio between the longitudinal and transversal field component

---

<sup>1</sup>As discussed in chapter 2, one can decompose the guided modes into quasi-linearly polarized orthogonal modes along  $\varphi_0$  and  $\varphi_0 + 90^\circ$ . In the following, we will use as orthogonal mode basis the quasi-linearly polarized  $\text{HE}_{11}$ -modes along  $\hat{\mathbf{x}}$  and  $\hat{\mathbf{y}}$ , i.e.  $\mu_x^\pm = (\omega, \varphi_0 = 0^\circ, 1, \pm)$  and  $\mu_y^\pm = (\omega, \varphi_0' = 90^\circ, 1, \pm)$ . The  $\pm$  sign is an abbreviation for  $\mathfrak{d} = +1, -1$ , that indicates the propagation direction of the guided light in the fiber along  $\pm \hat{\mathbf{z}}$  and  $\hat{\mathbf{x}}, \hat{\mathbf{y}}, \hat{\mathbf{z}}$  are the unit vectors along the corresponding axes.



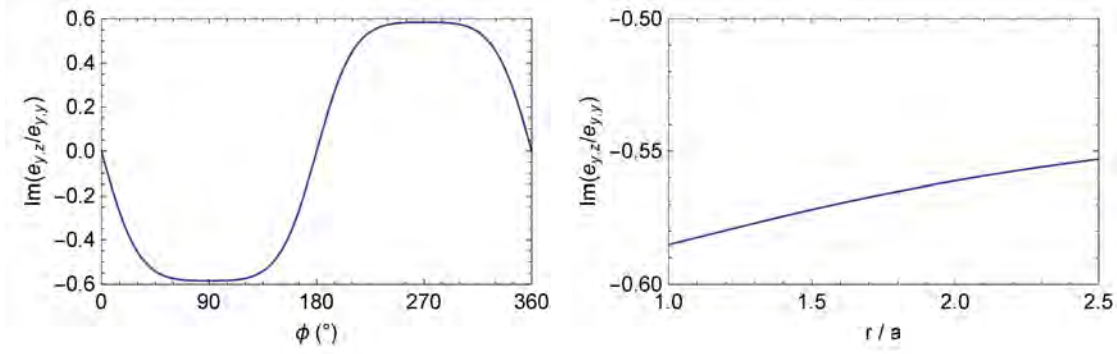


**Figure 5.1: Longitudinal field component of the fundamental guided mode.** Imaginary part of the ratio of the longitudinal field component  $e_{y,z}$  and the  $y$ -component  $e_{y,y}$  for the guided mode  $e_y$ , which is quasi-linearly polarized along  $\hat{y}$  and propagating along  $+\hat{z}$ . Panel (a) shows the ratio on the fiber surface as a function of the azimuthal dependency and panel (b) as a function of the radial distance  $(x, y) = (0, r)$ . The ratio is calculated for a wavelength of  $\lambda = 532$  nm and a fiber radius of  $a = 160$  nm. The real part of the ratio is zero.

of

$$\frac{e_{y,z}}{e_{y,y}} = -i \frac{2q}{\beta} \frac{|\sin(\phi)| K_1(qr)}{(1-s)K_0(qr) + (1+s)K_2(qr) \cos(2\phi)}, \quad (5.4)$$

where  $e_{y,k}$  is the  $k$ -component ( $k = x, y, z$ ) of the  $\text{HE}_{11}$ -mode that is quasi-linearly polarized along  $y$ . As expected, the longitudinal component  $e_{y,z}$  is  $\pi/2$  out of phase like in the case shown above (see Eq. (5.3)). The maximum ratio is obtained on the top and on the bottom of the nanofiber (i.e.  $\phi = 90^\circ$  and  $\phi = 270^\circ$ ). For small radii fibers it increases with the radius  $a$ . For large fiber radii ( $a \gg \lambda$ ) it approaches  $(1 - (n_2/n_1)^2)^{1/2}$ , which is about 0.729 in the case of glass surrounded by air or vacuum. This expression can also be directly derived for the evanescent field of a plane wave that undergoes total internal reflection at a planar dielectric interface at grazing incidence [148, 149]. In Fig. 5.1 the dependency of Eq. (5.4) with respect to the azimuthal position  $\phi$  and the radial position  $r$  is shown for a wavelength of  $\lambda = 532$  nm and nanofiber radius of  $a = 160$  nm. According to Eq. (5.4), we find a maximum ratio of 0.578 (panel (a)) on the fiber surface. As can be seen in panel (b), it does not change by a lot when moving away from the fiber surface.

Because it is  $\pi/2$  out of phase with the transversal components, a significant longitudinal component leads to almost circular polarizations  $\sigma^\pm = (i\hat{z} \pm \hat{y})/\sqrt{2}$  in the plane containing the fiber axis. As a consequence, on top of the fiber, the local spin angular momentum of the guided mode field is perpendicular to the propagation direction and antiparallel to the local orbital angular momentum [31, 32]. The local orbital angular momentum is proportional to the cross product of propagation direction and the its radial position  $\mathbf{r}$ . Moreover, looking at Fig. 5.2, the orientation of both these quantities flips around on the bottom of the fiber or when the propagation direction is changed. This phenomenon is named spin-orbit interaction of light and the light propagation is *chiral*.<sup>2</sup> Its characteristics are in sharp contrast to paraxial

<sup>2</sup> In literature, the term 'chiral' is often used in this context to indicate asymmetric properties of a system: A

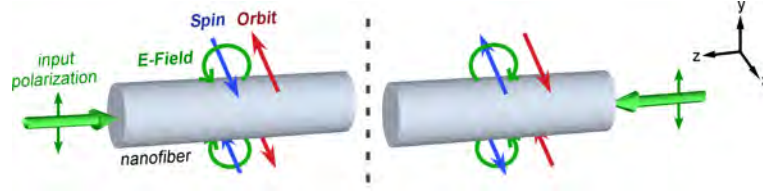


**Figure 5.2: Spin-orbit interaction of light in optical nanofibers.** When the nanofiber-guided light is quasi-linearly polarized along the  $y$ -axis, longitudinal polarization components occur. For guided light traveling in  $+z$ -direction, this leads to nearly circular  $\sigma^-$  ( $\sigma^+$ ) polarization on the top (bottom) of the fiber, see circular green arrows. For light propagating in  $-z$  direction,  $\sigma^- = (\hat{z} \pm \hat{y})/\sqrt{2}$  and  $\sigma^+ = (\hat{z} \pm \hat{y})/\sqrt{2}$  are interchanged. At these positions, the spin angular momentum of the light (blue arrows) is oriented perpendicular to the propagation direction and anti-parallel to the orbital angular momentum (red arrows), defined with respect to the  $z$  axis [32].

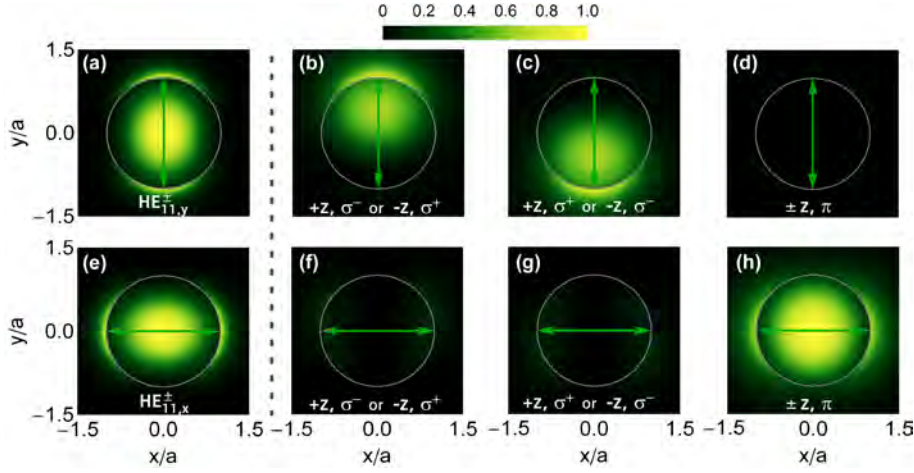
light fields, where the spin is parallel or antiparallel to the propagation direction. Spin-orbit interaction of light has been observed for freely propagating light fields [33, 34], in the case of total internal reflection [35, 36], in plasmonic systems [37–40], for radio frequency waves in metamaterials [41] and at whispering gallery mode resonators [42].

Figure 5.3 shows the overlaps  $|\hat{e}_{x,y}^\pm \cdot \sigma^\pm|^2$  and  $|\hat{e}_{x,y}^\pm \cdot \pi|^2$  of these modes with a circularly  $\sigma^\pm = (\hat{z} \pm \hat{y})/\sqrt{2}$  and linearly  $\pi = \hat{x}$  polarized light field as a function of its position in the fiber transverse plane.<sup>3</sup> The calculations were performed for a wavelength of  $\lambda = 532$  nm and a fiber radius of  $a = 160$  nm). A strong asymmetry can be seen in panels Fig. 5.3b and Fig. 5.3c. Depending on the propagation direction of the light field and the position  $(x, y)$  in the fiber transverse plane, the overlap is large with the  $\mu_y^+$  or  $\mu_y^-$  mode. In particular, the asymmetry reverses when the light field is  $\sigma^+$  instead of  $\sigma^-$  polarized or when the position of the dipole particle is changed from  $(x, y)$  to  $(x, -y)$ . The reason for this is that the local guided mode profile function  $e^{(\mu)}(x, y)$  depends both on the position in the fiber transverse plane and on the propagation direction of the mode — a consequence of spin-orbit interaction of the nanofiber guided light. Later in this chapter it will be shown, that the overlap of guided mode and polarized light field is directly proportional to the emission rate of a particle which emits equivalently polarized light. This fact can be used to realize directional scattering into the waveguide.<sup>4</sup>

chiral system can not be matched with its mirror image solely via rotation. Regarding Fig. 5.2, three axis can be defined: (i) The axis  $\hat{r}$  from the nanofiber axis to a ‘probe’ position  $\mathbf{r}$  on the nanofiber where the guided mode exhibits elliptical polarization locally (e.g. on top), (ii) the nanofiber axis  $\hat{z}$  and (iii) the axis of the local spin orbital angular momentum  $\hat{x}$  at position  $\mathbf{r}$ . In this case, due to the fact that the spin orbital angular momentum depends on the propagation direction of the guided mode, the case where the guided mode travels along  $+\hat{z}$  is distinguishable from the one where it travels along  $-\hat{z}$ . In these two cases it is not possible to rotate the system such that it matches its mirror image.

<sup>3</sup> Note that this overlap is different from the *polarization* overlaps  $|\hat{e}_{x,y}^\pm \cdot \sigma^\pm|^2$  and  $|\hat{e}_{x,y}^\pm \cdot \pi|^2$  of the *unit* vectors  $\hat{e}$  of the guided modes  $e$ .

<sup>4</sup> In the following, the difference between the terminologies scattering and emission is that scattering describes the process where the particle scatters an incident light field while in the case of emission the process of how the emitter was excited is omitted.



**Figure 5.3: Guided modes of a nanofiber.** (a) Intensity,  $|e_y^{\pm}|^2$ , of the  $\mu_y^{\pm}$  modes, normalized to its peak value on the fiber axis. (b) Position dependent overlap,  $|e_y^+ \cdot \sigma^-|^2$ , of the  $HE_{11,y}^+$  mode with a  $\sigma^- = (\hat{z} - \hat{y})/\sqrt{2}$  polarized light field and overlap,  $|e_y^- \cdot \sigma^+|^2$ , of the  $HE_{11,y}^-$  mode with a  $\sigma^+ = (\hat{z} + \hat{y})/\sqrt{2}$  polarized light field. (c) Overlap of the  $HE_{11,y}^+$  mode with a  $\sigma^+$  polarized dipole and overlap of the  $HE_{11,y}^-$  mode with a  $\sigma^-$  polarized dipole. (d) Overlap of the  $HE_{11,y}^{\pm}$  modes with a  $\pi = \hat{x}$  polarized light field. (e-h) Same as (a) to (d) but for the fiber modes  $HE_{11,x}^{\pm}$ . The calculations assume a wavelength of  $\lambda = 532$  nm and a fiber radius of  $a = 160$  nm. The overlaps are normalized to the peak value on the fiber axis in panel (h). On top of the fiber ( $x = 0, y = a$ ), we find a normalized overlap of 0.88, 0.06, and 0 in panels (b) to (d), respectively.

## 5.2 Scattering characteristics of an emitter on a nanofiber

The emission properties of a particle change, when it is placed in close vicinity to a waveguide. In the presence of a nanofiber the mode density of the electromagnetic field is modified which changes the intensity distribution of the emitted light.<sup>5</sup> The electromagnetic field modes can be expressed as the sum over guided and radiation modes [49] (see Eq. (2.16) - Eq. (2.20) and Eq. (2.30) - 2.31). The emission rate  $\gamma^{(\text{gui}, \mu)}$  ( $\gamma^{(\text{rad}, \nu)}$ ) of a point-like particle into a given guided nanofiber eigenmode  $\mu = (\omega, \xi, 1, \mathfrak{d})$  (radiation mode  $\nu = (\omega, \beta, \mathfrak{c}, l)$ ) is proportional to the square of the absolute value of the induced electric dipole moment  $\mathbf{d}$  of the particle and to the profile function  $e^{(\mu)}$  ( $\tilde{e}^{(\nu)}$ ) of the respective mode. Here,  $\xi = (x, y)$  denotes the direction along which the  $HE_{11}$ -mode  $\mu = (\omega, \xi, l = 1, \mathfrak{d})$  is quasi-linearly polarized (see Sect. 2.2). In detail, for a single-mode nanofiber, the equations for the total emission rates into the guided orthogonal

<sup>5</sup>The general effect was first described by E. M. Purcell in 1946 [150].

HE<sub>11</sub>-modes and into the radiation modes read [151]:

$$\gamma_{\text{tot}}^{(\text{gui})}(\omega, r, \phi) = \sum_{\xi \mathfrak{d}} \gamma^{(\mu)}(\omega, r, \phi) = \frac{\omega \beta'}{2 \epsilon_0 \hbar} \sum_{\xi \mathfrak{d}} \left| \mathbf{d}^* \cdot \mathbf{e}^{(\mu)}(\omega, r, \phi) \right|^2, \quad (5.5)$$

$$\gamma_{\text{tot}}^{(\text{rad})}(\omega, r, \phi) = \frac{\omega}{2 \epsilon_0 \hbar} \sum_{\epsilon l} \int_{-n_2 k_0}^{n_2 k_0} d\beta \left| \mathbf{d}^* \cdot \tilde{\mathbf{e}}^{(\nu)}(\omega, r, \phi) \right|^2, \quad (5.6)$$

where  $\beta'$  is the derivative of the longitudinal propagation constant  $\beta$  with respect to the oscillation frequency  $\omega$  of the electric dipole. In contrast to the case of guided modes, for radiation modes  $\beta$  can vary continuously from  $-n_2 k_0$  to  $n_2 k_0$  for each value of  $\omega$  ( $k_0 = \omega/c$ ). Note that, in addition to the mode parameters  $\mu$  and  $\nu$ , the emission rates also depend on the fiber radius  $a$  and the position  $(r, \phi)$  of the emitter, where  $(r, \phi)$  are the cylindrical coordinates in the nanofiber transverse plane.

Consider a dipole emitter located in the fiber transverse plane. The emission rate into the nanofiber (see Eq. (5.5)) is proportional to the overlap,  $\left| \mathbf{d}^* \cdot \mathbf{e}^{(\mu)}(\omega, r, \phi) \right|^2$ , of the dipole moment  $\mathbf{d}$  of the emitter with the guided modes  $\mathbf{e}^{(\mu)}$ . If we assume a circularly  $\sigma^\pm = (\hat{\mathbf{z}} \pm \hat{\mathbf{y}})/\sqrt{2}$  or linearly  $\pi = \hat{\mathbf{x}}$  oscillating dipole, the overlaps illustrated in Fig. 5.3 are directly proportional to the expected normalized emission rates into the fiber. Here, it can clearly be seen that, due to spin-orbit interaction, the emission rates into the forward ( $\mathfrak{d} = +1$ ) and backward ( $\mathfrak{d} = -1$ ) guided modes are not necessarily equal but can in general be asymmetric. It is instructive to quantify the asymmetry of the emission process into a single-mode nanofiber in terms of a directionality  $\mathcal{D}$ , defined as

$$\begin{aligned} \mathcal{D} &= \frac{\gamma^+ - \gamma^-}{\gamma^+ + \gamma^-}, \\ \gamma^+ &= \gamma_x^{(\mathfrak{d}=+1)} + \gamma_y^{(\mathfrak{d}=+1)}, \\ \gamma^- &= \gamma_x^{(\mathfrak{d}=-1)} + \gamma_y^{(\mathfrak{d}=-1)}, \end{aligned} \quad (5.7)$$

where the main linear polarization component  $\xi = (x, y)$  of the respective HE<sub>11</sub>-mode into which the emission rate is to be calculated is given as an index. The directionality is +1 (−1) when all the light emitted into the nanofiber is propagating along  $+\hat{\mathbf{z}}$  ( $-\hat{\mathbf{z}}$ ) and 0 for an equal amount of light sent into both directions. For the three situations depicted in Fig. 5.3, i.e.  $\mathbf{d} = \sigma^\pm$  and  $\pi$ , Fig. 5.4 shows the equivalent directionalities,  $\mathcal{D}(x, y)$ , across the fiber transverse plane. Both, Figure 5.4a and b can be divided into an upper and lower part: In the case of panel (a), i.e. for a  $\sigma^+$  polarized dipole moment, the directionality is positive for all points where  $y > 0$  and negative for  $y < 0$ . This dependency flips sides in the case of panel (b), i.e. for a  $\sigma^-$  polarized dipole moment. So, either by changing the circulation sense of the dipole moment or by changing the emitter's position from  $(x_0, y_0)$  to  $(x_0, -y_0)$ , the direction into which the majority of the light is emitted can be changed. For the parameters used in the plots (wavelength,  $\lambda = 532$  nm) and fiber radius,  $a = 160$  nm), we find perfect directionalities of  $\mathcal{D} = \pm 1$  at the positions  $(x_0, y_0) = (0, \pm 0.915a)$ , close to the fiber surface. For a linear  $\pi$  polarized dipole moment on the other hand, as can be seen in panel (c), the emission into both directions is always the same, i.e. the directionality is zero. To summarize, the existence

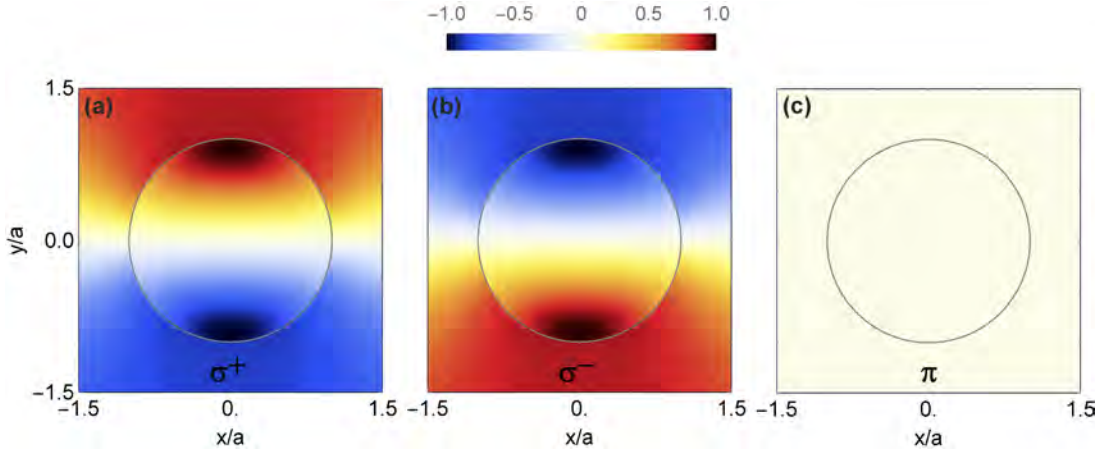


**Figure 5.4: Directionality of dipole emitters at a nanofiber.** (a) Position dependent directionality,  $\mathcal{D}$ , of a  $\sigma^+$  polarized dipole moment  $\mathbf{d}$  across the transverse plane of a nanofiber. (b) Directionality of a  $\sigma^-$  polarized dipole moment. (c) Directionality of a  $\pi$  polarized dipole moment. The calculations assume a wavelength of  $\lambda = 532$  nm) and a fiber radius of  $a = 160$  nm. We find a maximum absolute directionality of  $|\mathcal{D}| = 1$  at  $(x_0, y_0) = (0, \pm 0.915a)$  in panels (a) and (b). In panel (c) no directionality is observed ( $\mathcal{D} = 0$ ).

of the longitudinal polarization component  $e_z^{(\mu)}$  of the guided modes leads to local elliptical polarizations in a plane containing the fiber axis. If the dipole moment of the point-like particle is also elliptically polarized in this plane, an asymmetric emission into the nanofiber occurs.

It is instructive to note, that in contrast to the overlap in Fig. 5.3 which is proportional to  $|\mathbf{d}^* \cdot \mathbf{e}|^2$ , the directionality barely decays when moving further away from the fiber. While overlap and emission rate  $\gamma^{(\text{gui})}$  become smaller and smaller further away from the fiber, the directionality, as it is defined in Eq. (5.7), is almost invariant to the distance of the emitter to the fiber. In fact, the only thing that matters for a strong asymmetry in the emission is that the overlap,  $|\hat{\mathbf{d}}^* \cdot \hat{\mathbf{e}}|^2$ , of the *unit* vectors  $\hat{\mathbf{e}}$  and  $\hat{\mathbf{d}}$  of the guided modes and the dipole moment, respectively, is large. Here, only the relative orientation of the polarizations matters, which is why we can speak of a *polarization* overlap, in this context.

Until now, the emission into the radiation modes has been omitted from the discussion. By including this process into the model, interesting phenomena unfold and it is possible to quantify how efficient a particle emits into the fiber depending on the distance to the fiber surface or the fiber radius. Figure 5.5 illustrates the amount of light that is emitted into the guided and radiation modes for the cases where the particle, situated on top of the nanofiber ( $\phi = 90^\circ$ ), is excited by a circularly  $\sigma^+$  and linearly polarized excitation light field (Fig. 5.7).<sup>6</sup> Far away from the fiber, the situation resembles that of an emitter in free space. Accordingly, its emission rate into

<sup>6</sup> The code used to calculate the emission rates into guided and radiation modes (and all quantities that result from them) is based on a FORTRAN code by F. Le Kien (private communication). It was modified to the case of an emitter with arbitrary dipole moment  $\mathbf{d}$  that can be excited via an external or guided light field.

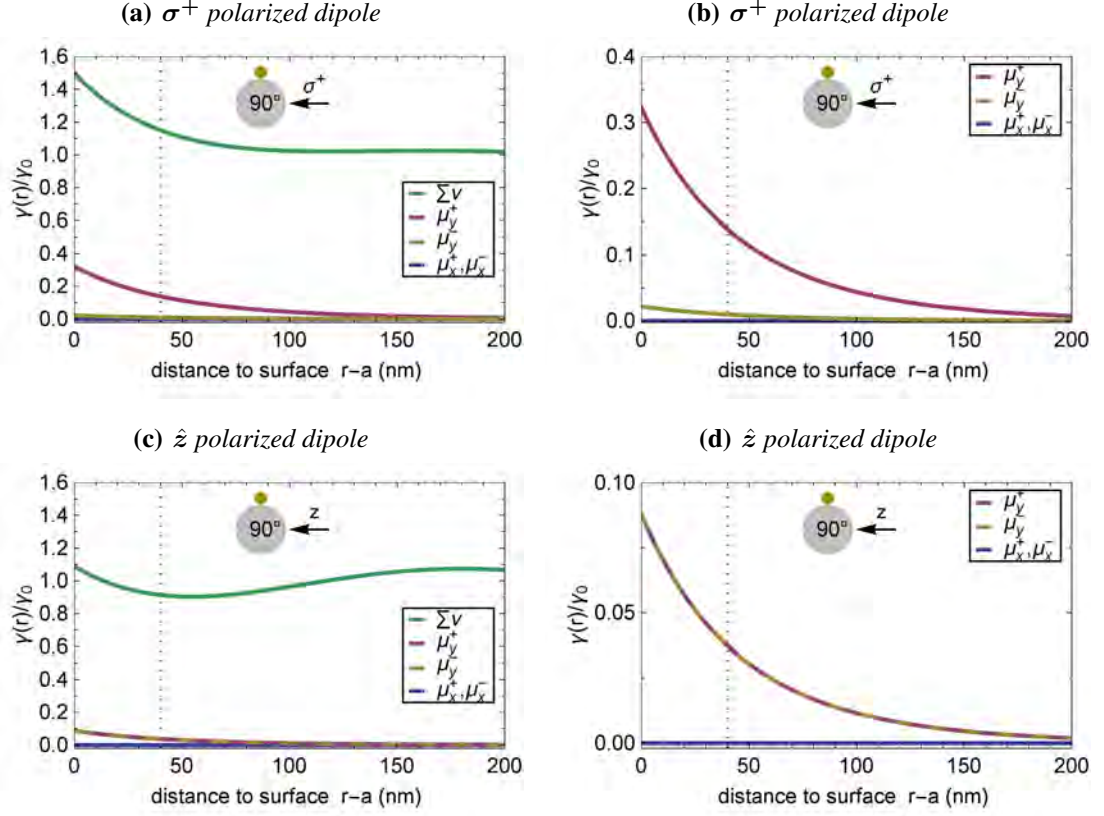


**Figure 5.5: Emission rates of a dipole emitter near a nanofiber.** Emission rates of an emitter, situated on top ( $\phi = 90^\circ$ ) of a nanofiber, into the radiation and guided modes of a nanofiber ( $a = 160$  nm). The rates depend on the oscillation of the dipole moment of the emitter and its radial distance to the nanofiber surface. The situation is sketched in an inset of each plot where yellow and gray disk stand for emitter and nanofiber, respectively. Next to them, the polarization of the dipole moment of the emitter is denoted. **(a)** Normalized emission rate of a circular polarized  $\sigma^+ = (\hat{i}\hat{z} + \hat{y})/\sqrt{2}$  dipole moment into the four fundamental guided modes  $\mu_{(x,y)}^\pm$  (red, dark yellow, blue) and into the radiation modes  $\nu$  (green). The emission rate into  $\mu_y^\pm$  strongly depends on the propagation direction of the mode and the emission rate into the  $\mu_x^\pm$  modes is always zero for  $\sigma^+$  and  $\phi = 90^\circ$ . **(b)** Same as (a), but zoomed into the guided modes emission rates. **(c,d)** Same situation as in (a,b) for a linearly ( $\hat{z}$ ) polarized dipole moment. While the emission rates  $\mu_x^\pm$  (blue) are always zero, the emission rates  $\mu_y^\pm$  (dashed red, dark yellow) are equal for both propagation directions. The emission rates are normalized to the free-space emission rate  $\gamma_0$ , i.e. the case where no nanofiber is present. The dashed gray vertical lines denote a distance of 40 nm away from the fiber surface, which is the distance to the center of a spherical emitter that has a radius of  $R = 40$  nm and that is situated on the fiber surface.



the guided modes approaches zero and the total emission rate  $\gamma_{\text{tot}}^{(\text{rad})}$  into all radiation modes  $\nu$  eventually reproduces the free-space emission rate

$$\gamma_0 = \gamma_{\text{tot}}^{(\text{rad})}(\omega, r \rightarrow \infty, \phi). \quad (5.8)$$

When approaching the nanofiber, the emission rates into the guided modes increase as the guided mode intensities become larger. Surprisingly, not only the emission into guided modes increases but also the emission into radiation modes can become larger and even exceed the unperturbed free-space emission rate  $\gamma_0$ . While the physical process behind this is more complicated a qualitative explanation is that the light emitted by the particle can be reflected back by the nanofiber which leads to enhanced emission – the light that is reflected by the nanofiber surface interferes constructively with the emitted light by the dipole. This interference also leads to oscillations of the emission rate into the radiation modes (see Fig. 5.5c). As expected, we only observe a directional behavior of the system if the excitation light field is circularly polarized like in Fig. 5.5a,b, where the emission rate into the  $\mu_y^+$  mode is significantly higher than into the counter-propagating mode  $\mu_y^-$ . For linear polarization (Fig. 5.5c,d) there is no asymmetry as the emission rates into the  $\mu_y^+$  and  $\mu_y^-$  mode are equally large and always zero into the  $\mu_x^\pm$  modes for the discussed situation.

It was shown, that the emission characteristics of a particle drastically change in the proximity of an optical nanofiber. Besides its distance to the fiber surface, the emission rates strongly depend on the radius of the nanofiber. Changing the radius, the mode intensity,  $|e^{(\mu)}(r > a)|^2$ , outside the nanofiber, i.e. in the evanescent field, can be changed significantly. In the extreme case of an infinitely large nanofiber radius, for example, the evanescent field is basically zero. For possible applications, the fraction of light emitted into the nanofiber is a crucial parameter. For this purpose, we define the efficiency  $\eta^{(\mu)}$  for a particle to emit into one of the four orthogonal guided fundamental modes  $\mu$  with respect to all other modes as

$$\eta^{(\mu)}(\omega, r, \phi; a) = \frac{\gamma^{(\mu)}(\omega, r, \phi; a)}{\gamma_{\text{tot}}^{(\text{gui})}(\omega, r, \phi; a) + \gamma_{\text{tot}}^{(\text{rad})}(\omega, r, \phi; a)}, \quad (5.9)$$

where  $\gamma_{\text{tot}}^{(\text{gui})}$  is the sum over all decay rates into the  $\text{HE}_{11}$ -modes  $\mu_{(x,y)}^\pm$  and  $\gamma_{\text{tot}}^{(\text{rad})}$  the total decay rate into all radiation modes  $\nu$ . For a point-like dipole situated on the surface of the nanofiber, the efficiency becomes  $\sum_\mu \eta^{(\mu)} \simeq 0.25$ , which is quite an impressive fraction of the total emitted power. Figure 5.6a and Figure 5.6b illustrate the efficiency  $\eta^{(\mu)}$  for two different induced dipole orientations as a function of the fiber radius. In the case of a  $\sigma^+$  polarized excitation light field, more than 15% of the total emitted power will be emitted into the  $\mu^+$ -direction for a fiber radius of  $a \simeq 120$  nm.

Figure 5.6c and d show the directional behavior for the case of a varying fiber radius and the particle situated on top of the fiber ( $\phi = 90^\circ$ ). While the directionality (see Eq. (5.7)) is zero for a  $\hat{z}$  polarized excitation light field, it exceeds 90 % in the case a  $\sigma^+$  polarized field for radii above  $a \simeq 190$  nm. Note that efficiency and directionality can not be simultaneously maximized. While the fraction of emitted light that is coupled into the guided modes increases up to a certain extent when the fiber radius is decreased, it is the other way around for the directional

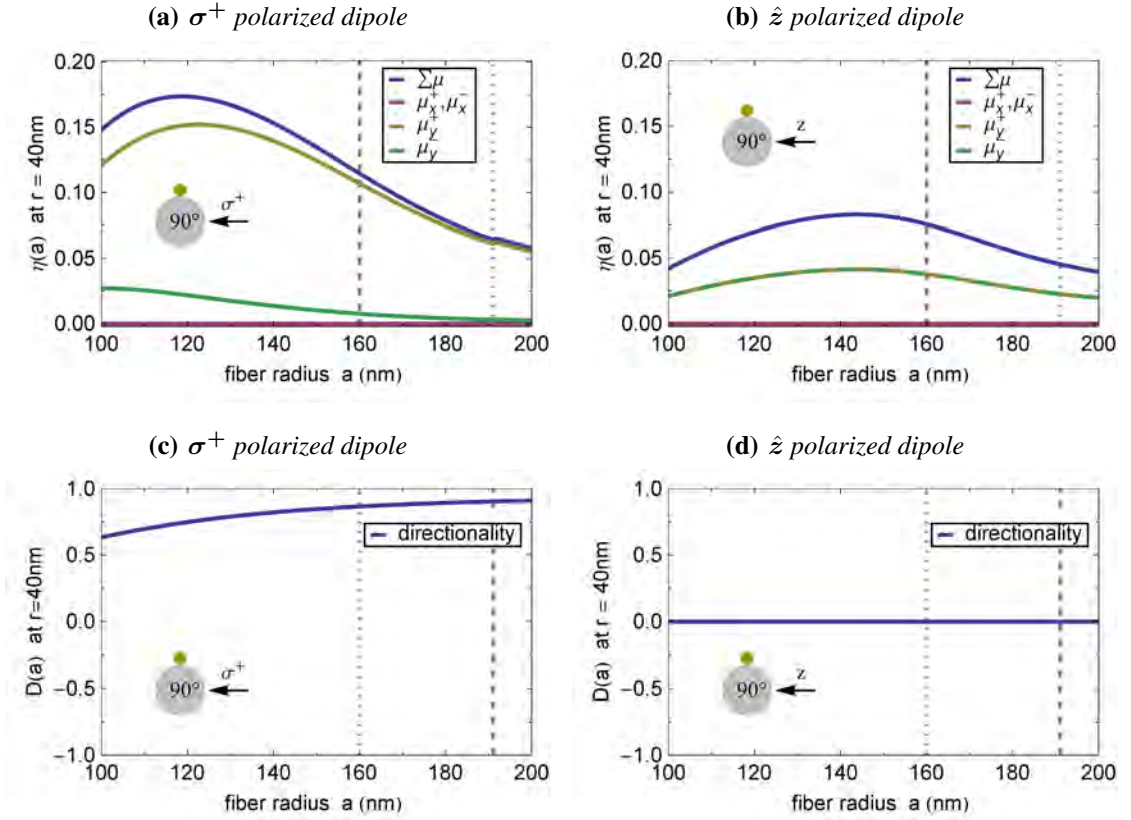


**Figure 5.6: Efficiency and directionality of a dipole emitter near a nanofiber.** Efficiency for a particle to emit into the respective guided mode(s) when its dipole moment is (a)  $\sigma^+$  polarized or (b)  $\hat{z}$  polarized. (c,d) Same situation as in (a,b) but for the directionality. Here, the emitter is 40 nm away from the fiber surface. The dashed line indicates a fiber radius of  $a = 160$  nm and the dotted line indicates the radius  $a_{sm} = 191$  nm above which the nanofiber no longer supports only the four  $HE_{11}$ -modes.

behavior of the emission process.

So far, we considered the emission characteristics of an excited dipole without taking into account *how* the dipole is actually excited. For typical applications this is realized with a light field as depicted in Figure 5.7. Here, a nanoscopic particle positioned on a nanofiber is illuminated by a paraxial excitation light field  $\mathbf{E}_0$ . Depending on its polarization and the position of the particle, directional scattering will be observed by the two detectors at the right and left port of the nanofiber. In this scenario, the term *scattering* will be used in the context of Eq. (5.10) instead of emission. For a point-like scatterer (see e.g. Sect. 3.2.3), its optical response is sufficiently described by its dipole moment  $\mathbf{d}$  via Eq. (3.18). As a consequence, the scattering rate  $\gamma^{(\mu)}$  ( $\gamma^{(\nu)}$ ) into a guided mode  $\mu$  (radiation mode  $\nu$ ) is directly proportional to the overlap between the vector amplitude  $\mathbf{E}_0$  of the excitation light and the guided (radiation) mode of the



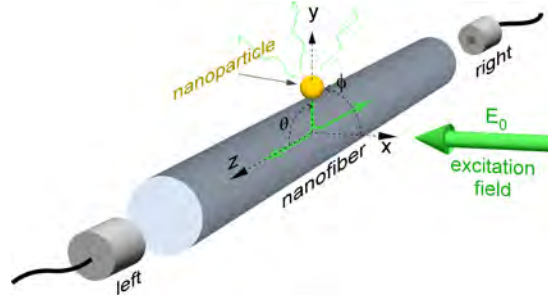


**Figure 5.7: Directional scattering into a nanofiber.** An emitter (e.g. a single nanoparticle) on a nanofiber is illuminated using a laser beam propagating in the negative  $x$ -direction. Due to the presence of the fiber, the spontaneous emission profile of the particle changes compared to the free-space case. The light can either be scattered into guided modes, i.e. to the left ( $+\hat{z}$ ) or right ( $-\hat{z}$ ), or into radiation modes.

fiber at the particle's position  $(r, \phi)$ . This yields

$$\gamma^{(\varrho)}(\omega, r, \phi) \propto \left| \vec{\alpha}^{(\varrho)}(\omega)^* \mathbf{E}_0^* \cdot \mathbf{e}^{(\varrho)}(\omega, r, \phi) \right|^2, \quad (5.10)$$

where  $\varrho = \mu, \nu$ . If, additionally, the scatterer is spherically symmetric (e.g. a spherical nanoparticle), the polarizability tensor can be associated with the complex scalar polarizability (see Eq. (3.19)) and its dipole moment points along the polarization direction of the excitation light field  $\mathbf{E}_0$ . Such an emitter is then a polarization maintaining scatterer [92, 93]. As long as the polarization of the excitation light field can be realized at the location of the nanoparticle, any dipole moment can be experimentally implemented and the asymmetry of the scattering can be tuned by the polarization of the incident light field and the position of the emitter. A polarization maintaining emitter is therefore an ideal candidate to shed light on the effect of spin-orbit interaction of light in nanophotonic waveguides and their resulting directional properties.

It is important to note that the light field  $\mathbf{E}_0$  that is incident onto a nanofiber is not only scattered by the nanoparticle but also scattered by the nanofiber. In particular, the modification of the intensity distribution as well as changes of the local polarizations depend on the polarization of the incident light field. As a consequence, in a realistic situation, the nanofiber-modified excitation light field  $\mathbf{E}_{\text{mod}}$  has to be considered as the real excitation light field of the nanoparticle. Figure 5.8 illustrates the situation of an incident plane wave, propagating along  $-\hat{x}$ , that is linearly polarized along  $y$  (panel (a)) and  $z$  (panel (b)). For both polarizations, the nanofiber acts as a lens and leads to a focusing effect and much higher intensities with respect to the incident light field  $\mathbf{E}_0$  behind the nanofiber at  $\phi \simeq 180^\circ$ . In addition, shadow regions with low intensities evolve, whose positions depend on the incident wavelength and the fiber radius. In the presented case, they can be found around  $\phi \simeq 180^\circ \pm 70^\circ$ . The resulting local *polarization* is only modified for the case where the field is polarized transversally to the fiber axis: An incident light field, linearly polarized along  $\hat{y}$  leads to field components along  $\hat{x}$  and  $\hat{y}$  when scattered by a fiber (panel (a)); an incident field linearly polarized along  $\hat{z}$  is not coupled to  $x$  or  $y$  (panel (b)). As can be seen in the left plot in panel (a), the contribution of the  $x$ -component of the

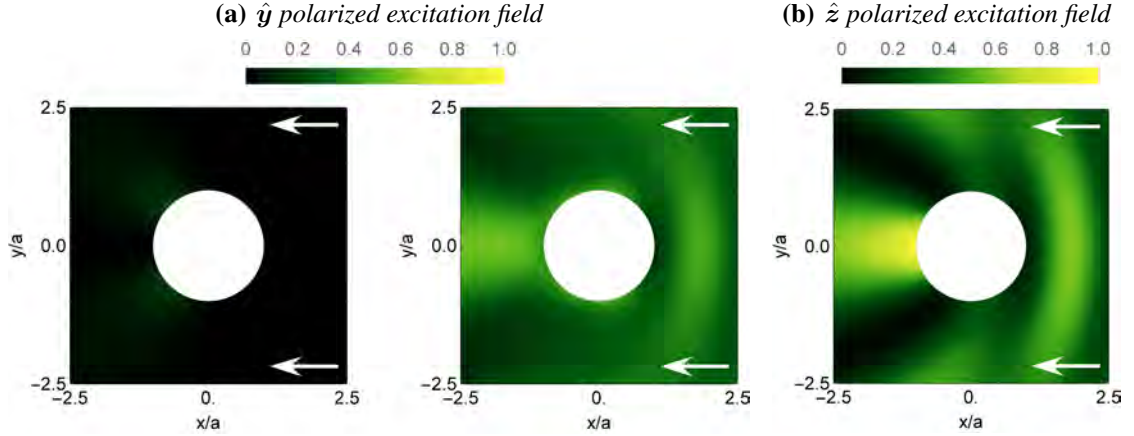


**Figure 5.8: Light scattering by a nanofiber.** Modification of the intensity distributions for an excitation light field  $\mathbf{E}_0$  polarized along (a) the  $\hat{y}$  axis and (b) the  $\hat{z}$  axis, owing to the presence of the nanofiber. Here, the normalized intensity,  $I_{mod, norm} = |\mathbf{E}_{mod}|^2 / I_{max}$ , is shown for an incident plane wave that propagates along  $-\hat{x}$  (indicated by the white arrows).  $\mathbf{E}_{mod}$  is the superposition of the incident light field  $\mathbf{E}_0$  and the field that is scattered by the nanofiber and  $I_{max}$  is the maximum intensity in panel (b). The wavelength is chosen to be  $\lambda = 532$  nm and the fiber radius is  $a = 160$  nm. In the case where the excitation light field is polarized perpendicular to the fiber axis ( $\mathbf{E}_0 = E_0 \hat{y}$ ), electric field components along  $\hat{x}$  arise, as shown in the left plot of panel (a). This is not the case in panel (b) where the light is polarized along the fiber axis ( $\mathbf{E}_0 = E_0 \hat{z}$ ).

$\hat{y}$ -polarized incident field is quite small.<sup>7</sup> A detailed discussion of the modifications, including formulas, and a ready-to-use FORTRAN code which was employed in thesis can be found in the book of Barber and Hill [152].

### 5.3 Preparation of a single scatterer on an optical nanofiber

Now, that the theoretical background has been outlined in the two sections above, we would like to explore spin-orbit interaction at nanofibers by measuring the directionality of the scattering process. For this, a metallic nanosphere is the ideal candidate, as it is a polarization-maintaining scatterer [92, 93] whose dipole moment can be set via the polarization of the exciting light field. Moreover, a metallic nanosphere exhibits high scattering cross sections around the localized plasmon resonance and is thereby able to couple a significant power fraction of the incident light field into the nanofiber. Before the directional behavior can be studied in detail, however, the question of which precise experimental system should be used as well as how to actually deposit a nanoparticle on a nanofiber will be discussed in this section.

The tapered optical fiber has a waist diameter of a few hundred nanometers at its waist and has to be handled very carefully. Not only can it be broken by very small mechanical forces, it is also highly susceptible to pollution which causes the fiber to lose its optical properties.

<sup>7</sup> The only region, where the  $x$ -component is considerable – but still only about half the size of the corresponding  $y$ -component – is around  $\phi \simeq 180^\circ \pm 70^\circ$ .

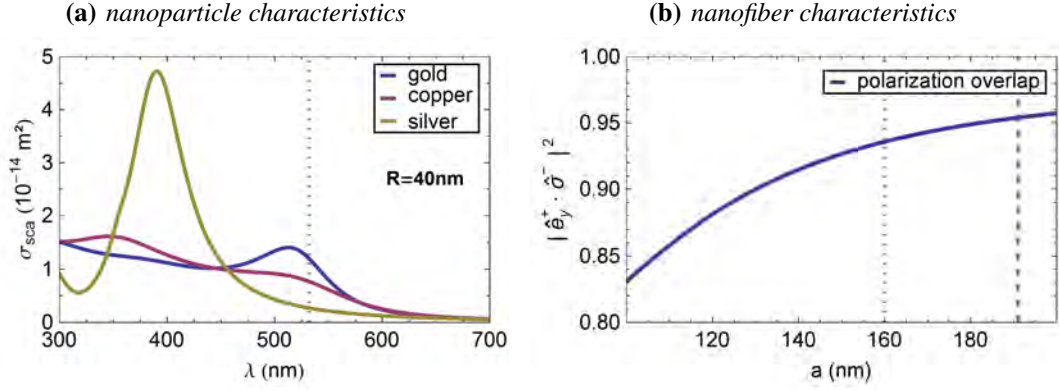


**Figure 5.9: Experimental considerations.** (a) Plot of the Mie scattering cross section of a nanosphere ( $R = 40 \text{ nm}$ ) surrounded by air made out of gold (blue), copper (red) and silver (dark yellow). The dotted vertical line denotes the wavelength used in the following experiments. (b) Polarization overlap of the  $HE_{11}$ -mode  $\mu_y^+$  with  $\sigma^-$  polarized light on the fiber surface at  $\phi = 90^\circ$ . For glass-air interfaces the maximum value possible is about 0.97. The dotted vertical line indicates a fiber radius of  $a = 160 \text{ nm}$  as used in our experiment and the dashed line indicates the radius  $a_{sm} = 191 \text{ nm}$  above which the nanofiber no longer supports only the four  $HE_{11}$ -modes.

This renders the deposition of a nanoparticle on it a critical part of the experiment. In this thesis, a technique has been developed where this deposition process can be carried out with surprising ease. Thanks to a dipping technique – using a pipette and nanoparticles dispersed in deionized water – that is carried out while simultaneously performing a white light nanofiber-based spectroscopy, the probability of successfully depositing exactly one nanoparticle on the nanofiber is empirically found to be close to one.

### 5.3.1 Selection of a precise experimental system

To explore the directional scattering in an experimental realization, an interplay between several effects has to be taken into account:

Let us first answer the question about which characteristics the nanosphere should exhibit. Above all, to maximize the coupling between nanofiber mode and nanoparticle the scattering cross section of the nanosphere should be as large as possible. We shall limit our discussion to gold, silver and copper as nanosphere materials, because these are the materials that are most readily available. Figure 5.9a shows the calculated scattering cross section as a function of the wavelength. One sees that the maximum scattering cross sections – which are defined by the localized surface plasmon resonances – lie all between 300 nm to 600 nm. In this figure the scattering cross sections are plotted for a nanosphere radius of  $R = 40 \text{ nm}$ . However, the result for the plasmon resonance range holds true for all radii in the range from about 20 nm to 80 nm.

<sup>8</sup> Consequently, the excitation laser should work in the above presented wavelength range. The

<sup>8</sup>If localized surface plasmon resonances at longer wavelengths are desired, it is advisable to look into hybrid nanoparticles consisting of a dielectric core and a metal shell, which are also known as nanoshells.

most obvious choice is a solid-state diode-pumped, frequency-doubled Nd:YVO<sub>4</sub> Verdi laser – available in our group – that provides a single-frequency output light at  $\lambda = 532$  nm.

In order for the sphere to be a polarization maintaining dipole scatterer, it has to be much smaller than the optical wavelength, which sets an upper boundary to the size of the particle. If we refer to Fig. 3.11 we see that in the case of gold the dipole term accounts for over 90% of the overall response of the nanosphere for radii below 40 nm. This is also valid for the other two materials, which is why – comparing the scattering cross sections in Fig. 5.9a and the scattering cross sections at  $\lambda = 532$  nm – a gold nanosphere with a radius of  $R = 40$  nm is the particle of choice. In addition to the fact that it has the highest scattering cross section at 532 nm the chemical inertness of gold makes it an even more viable candidate.

The design of the tapered optical fiber, and especially the choice of the nanofiber radius  $a$  is not straight forward. With the laser wavelength set to  $\lambda = 532$  nm the maximal fiber radius at which the nanofiber is still single mode is  $a_{\text{sm}} = 191$  nm (see Sect. 2.2.1). Therefore, a nanofiber radius smaller or equal to  $a_{\text{sm}}$  is required. As we have seen in the previous section, the decay rates  $\gamma^{(\mu)}$  into the guided modes scale with  $|\mathbf{d}^* \cdot \mathbf{e}^{(\mu)}|^2$ . Consequently, a strong electric field  $|\mathbf{e}|$  at the position of the nanoparticle is in general favorable. For each wavelength, there exists a certain radius  $a_{\text{Imax}}$  for which the evanescent field has maximum intensity on the fiber surface. This radius can be found at approximately  $a_{\text{Imax}}/\lambda \simeq 0.23$ , which yields an optimum radius of  $a_{\text{Imax}} \simeq 120$  nm for  $\lambda = 532$  nm.

Figure 5.9b shows the directionality as a function of  $a$ . We can see that with larger fiber radii one obtains stronger longitudinal polarization components and thereby more overlap of the guided field modes  $\mu_y^\pm$  with circular polarization. In the case of glass-air interfaces it can reach a polarization overlap with circular polarization of 97 %. In order to obtain high coupling efficiencies as well as a strong directional scattering, we choose a fiber diameter of  $a = 160$  nm between  $a_{\text{Imax}}$  and  $a_{\text{sm}}$ .

All chosen experimental parameters, i.e. the nanoparticle and fiber radius  $R = 40$  nm and  $a = 120$  nm as well as the operating laser wavelength of  $\lambda = 532$  nm are highlighted as dashed vertical lines in the plots in the previous section (5.2).

### 5.3.2 Nanofiber-based spectroscopy of a metal nanosphere

Nanoparticles are smaller than the wavelength of visible light and therefore hard to observe via far-field extinction spectroscopy as introduced in Section 3.2.1. Even in case of diffraction-limited illumination, several nanoparticles of equal shape should be excited at the same time to achieve acceptable signal-to-noise ratios [153]. One way to overcome these limitations is near-field extinction spectroscopy which exploits sub-wavelength optical coupling from one element to another [154–156]. While the most prominent member in this field is the near-field scanning optical microscope (NSOM), a single tapered optical fiber is already an efficient tool to perform near-field extinction spectroscopy [20]. Due to the strong confinement of the guided modes, the large light-matter coupling strength on the nanofiber surface enables one to detect a single nanoparticle.

In Sect. 5.2 the scattering rates of a polarization maintaining dipole scatterer (e.g. a nanosphere) close to a nanofiber have been examined as a function of the position of the nanoparticle  $(r, \phi)$

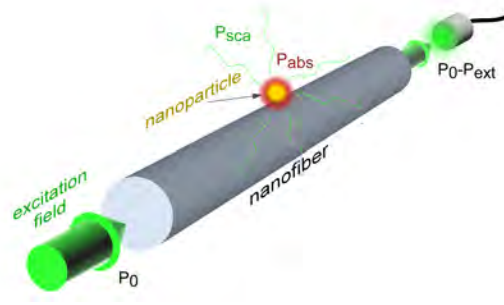


**Figure 5.10: Nanofiber based nanoparticle spectroscopy.** Light that is sent through the nanofiber is partly scattered and absorbed by the nanoparticle. The initially transmitted power  $P_0(\lambda)$  is therefore reduced by the extincted power  $P_{\text{ext}}(\lambda)$  due to the presence of the nanoparticle.

and the nanofiber radius  $a$ . In this section, we use these results to determine how a white light transmission spectrum through a tapered optical fiber is changed when a single nanoparticle is placed on the waist of the tapered optical fiber (i.e. the nanofiber). We consider the situation illustrated in Fig. 5.10 where the nanofiber guided light acts as the excitation light field. A common physical quantity to describe the change in transmission due to the nanoparticle is the absorbance

$$\mathcal{A}(\lambda, r, \phi) = -\log_{10} \left( \frac{P_0(\lambda) - P_{\text{ext}}(\lambda)}{P_0(\lambda)} \right), \quad (5.11)$$

that relates the transmitted power distribution  $P_0(\lambda)$  before the nanosphere is placed on the nanofiber surface with the power distribution  $P_0(\lambda) - P_{\text{ext}}(\lambda)$  after it has been placed. Here,  $P_{\text{ext}}$  is the extincted power due to the presence of the nanoparticle (i.e. the sum of the scattered and absorbed power).

We can find an analytical expression for the absorbance  $\mathcal{A}_{\text{sca}}$  due to scattering if we express the excitation field  $\mathbf{E}_0$  in Eq. (5.10) with the guided field modes  $e^{(\mu)}$ . For an unpolarized white light source the excitation field can be approximated as an incoherent equal superposition of the two  $\text{HE}_{11}$ -modes  $\mu_x^0$  and  $\mu_y^0$  propagating along one direction. The resulting scattering rates can be used to calculate a power distribution for the light that remains in the two  $\text{HE}_{11}$ -modes  $\mu_x^0$  and  $\mu_y^0$ . The absorbance due to scattering then reads

$$\begin{aligned} \mathcal{A}_{\text{sca}}(\lambda, r, \phi) &= -\log_{10} \left( \frac{P_0(\lambda) - P_{\text{sca}}(\lambda, r, \phi)}{P_0(\lambda)} \right) \\ &= -\log_{10} \left( 1 - \frac{(2\pi\hbar c/\lambda) \gamma_{\text{loss}}(\lambda, r, \phi)}{P_0(\lambda)} \right), \end{aligned} \quad (5.12)$$

where

$$\gamma_{\text{loss}}(\lambda, r, \phi) = \gamma_x^{(\text{gui}, -0)}(\lambda, r, \phi) + \gamma_y^{(\text{gui}, -0)}(\lambda, r, \phi) + \gamma_{\text{tot}}^{(\text{rad})}(\lambda, r, \phi), \quad (5.13)$$

is the sum of the scattering rates into the opposite fiber direction and into all radiation modes. As before,  $(r, \phi)$  denotes the position of the nanoparticle. As  $\gamma_{\text{loss}}$  is proportional to  $P_0(\lambda)$ , the absorbance is actually independent of the power  $P_0(\lambda)$ .

In the previous section, we were only interested in the part of the optical power that is *scattered* by the nanoparticle. However, as it was shown in chapter 3, a large part of the excitation energy is *absorbed* by the nanosphere. For a nanosphere radius of  $R = 40$  nm the free-space absorption cross section is about three times as large as the scattering cross section at  $\lambda = 532$  nm. This is why for the total extinction  $P_{\text{ext}} = P_{\text{sca}} + P_{\text{abs}}$  of the guided light field both processes have to be taken into account when determining the absorbance  $\mathcal{A} = \mathcal{A}_{\text{sca}} + \mathcal{A}_{\text{abs}}$ . Using the free-space absorption cross section,  $\sigma_{\text{abs}}$ , an analytical expression can be found for the absorbance:

$$\begin{aligned}\mathcal{A}_{\text{abs}}(\lambda, r, \phi) &= -\log_{10} \left( \frac{P_0(\lambda) - P_{\text{abs}}(\lambda, r, \phi)}{P_0(\lambda)} \right) \\ &= -\log_{10} \left( 1 - \frac{\sigma_{\text{abs}}(\lambda, R)}{A_{\text{eff}}(\lambda, r, \phi)} \right),\end{aligned}\quad (5.14)$$

where

$$A_{\text{eff}}(\lambda, r, \phi) = \frac{P_0(\lambda)}{I(\lambda, r, \phi)}, \quad (5.15)$$

is the effective area which relates the transmitted power  $P_0(\lambda)$  in the absence of the nanoparticle with the intensity  $I(\lambda, r, \phi)$  at the position  $(r, \phi)$  of the nanoparticle [157]. In 3.8 we have seen that the cross sections depend on the permittivity of the surrounding medium. The free-space absorption cross section is only an approximation to the real case. However, the broken symmetry due to the presence of the nanofiber leads to a more complicated analysis. In principle, the oscillation of the electron cloud inside the nanoparticle leads to a polarization of the nanofiber. As a simplification it is possible to explain this process in the quasi-static approximation via effective permittivity that accounts for the influence of the nanofiber [158].<sup>9</sup> For this reason, Eq. (5.14) is an underestimation of the real absorbance due to absorption.

Figure 5.11 shows  $\mathcal{A}_{\text{sca}}(\lambda)$ ,  $\mathcal{A}_{\text{abs}}(\lambda)$  and  $\mathcal{A}(\lambda)$  for a gold nanoparticle with a radius of  $R = 40$  nm and a fiber radius of  $a = 160$  nm, when unpolarized white light is sent through the fiber (panel **a**) and the expected variations of  $\mathcal{A}$  when nanofiber and nanoparticle are slightly larger or smaller (panel **b**). In order to predict experimentally measured values, both processes, scattering and absorption, were calculated for the Mie model (see Sect. 3.2.3).<sup>10</sup> Around the plasmon resonance at  $\lambda \simeq 520$  nm the absorbance is about 0.017 for the case of a nanoparticle and nanofiber radius of  $R = 40$  nm and  $a = 160$  nm.

Another term that is commonly used in the context of extinction spectroscopy is the transmittance

$$\mathcal{T} = (P_0 - P_{\text{ext}})/P_0 = 10^{-\mathcal{A}}. \quad (5.16)$$

For the situation in Fig. 5.11**a** it drops down to less than 0.96, i.e. more than 4 % of the power around the plasmon resonance are lost when a single nanoparticle is deposited on a nanofiber. This value is much higher than in the case of conventional far-field extinction spectroscopy and makes optical nanofibers an attractive tool for the efficient detection of single emitters

<sup>9</sup> In fact, the effective permittivity is often used as a fit parameter to determine the influence of a substrate [113].

<sup>10</sup> The theory for a nanoparticle close to a nanofiber is approximated with the Rayleigh model. Therefore, the scattering cross section is scaled to match the prediction of the more exact Mie theory far away from the fiber.

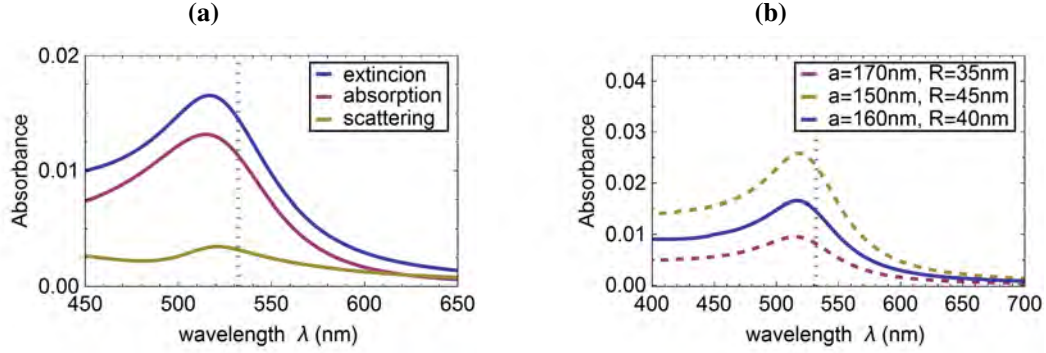


**Figure 5.11: Absorbance of nanofiber guided light due to a single nanosphere.** (a) Nanofiber guided light absorbance spectrum for a gold nanosphere due to scattering, absorption and extinction. For the nanoparticle radius considered here, with a radius of  $R = 40$  nm, the absorbance due to nonradiative losses (absorption) is larger than due to radiative losses (scattering). The nonradiative losses are assumed to be the same as for a nanosphere in free space. The nanofiber radius was taken to be  $a = 160$  nm. (b) Absorbances due to extinction for realistic radius variations of the nanoparticle ( $\pm 5$  nm) and the nanofiber ( $\pm 10$  nm). The largest (smallest) absorbance is expected for the largest (smallest) particle radius and the smallest (largest) fiber radius. For the maxima of each individual absorbance spectrum we find  $\mathcal{A}_{\min} = 0.010$ ,  $\mathcal{A}_{\text{mean}} = 0.017$  and  $\mathcal{A}_{\max} = 0.026$ . Both radius variations contribute significantly to the absorbance. If the fiber radius is fixed at  $a = 160$  nm and only the nanoparticle radius is varied the absorbance spread reduces to  $0.011 \leq \mathcal{A} \leq 0.024$ .

like nanoparticles [157]. It is therefore possible to resolve a successful deposition of a single nanoparticle on the nanofiber.

Moreover, for a small number of nanoparticles the total absorbance is just the sum of the single particle absorbances as long as the particle distance is larger than about 200 nm. Above this distance the interaction between the particles can be neglected because of the  $1/r^3$ -dependence of the near-field scattered by a nanosphere (see Eq. (3.17)). Below this distance the particles start to get coupled and show different spectral features than isolated nanoparticles, which in turn makes it relatively simple to distinguish them from isolated and especially single nanoparticles. To underline this fact, experimental results of a multiple nanoparticle deposition will be shown without yet explaining the details of their realizations. A detailed description about the deposition process and the scanning electron microscope imaging will be given in Sect. 5.3.3.

Figure 5.12 and Fig. 5.13 illustrate experimental extinction spectra (panels (a)) and SEM images (panel (b)) of a deposition of a single and three nanoparticles, respectively. The shape of the measured absorbance spectrum of a single spherical nanoparticle fits really well to the theory from above. As expected, it is also slightly larger due to the theoretical simplifications.

As can be seen in Fig. 5.13b the three nanoparticles were deposited such that two of them touch each other and form a so called *dimer*. As an approximation dimers can be treated like a new single nanoparticle of ellipsoidal shape where the three principal axes (two of them are of equal length) determine the positions of its two plasmon resonances. While the two short principal axes lead to the same resonance position as in the case of a single nanosphere, the long principal



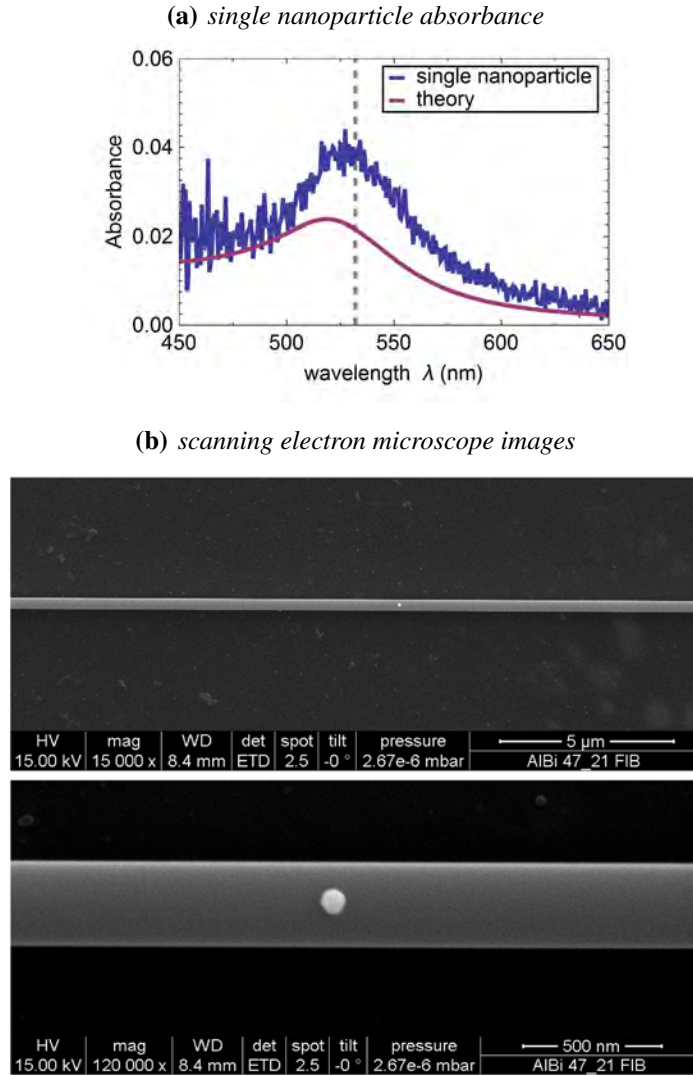


**Figure 5.12: Single particle extinction spectrum - experimental realization.** (a) Experimental (blue) and theoretically expected (red) single nanoparticle absorbance spectrum after a successful deposition. The theoretical spectrum is not fitted to the experimental data. It is calculated according to Sect. 5.3.2 for the nanofiber and nanoparticle radii deduced from (b). The discrepancy between experiment and theory is mainly due to the assumption that the presence of the nanofiber does not modify the absorption cross section of the nanoparticle. (b) Scanning electron microscope images for the above prepared single nanoparticle-nanofiber system for two different resolutions. It can be seen that no other particles distort the scattering characteristics of the nanoparticle. The particle's diameter is found to be  $2R = (90 \pm 3) \text{ nm}$  and the one of the nanofiber is  $2a = (315 \pm 3) \text{ nm}$ . The errorbars correspond to the resolution of the SEM.



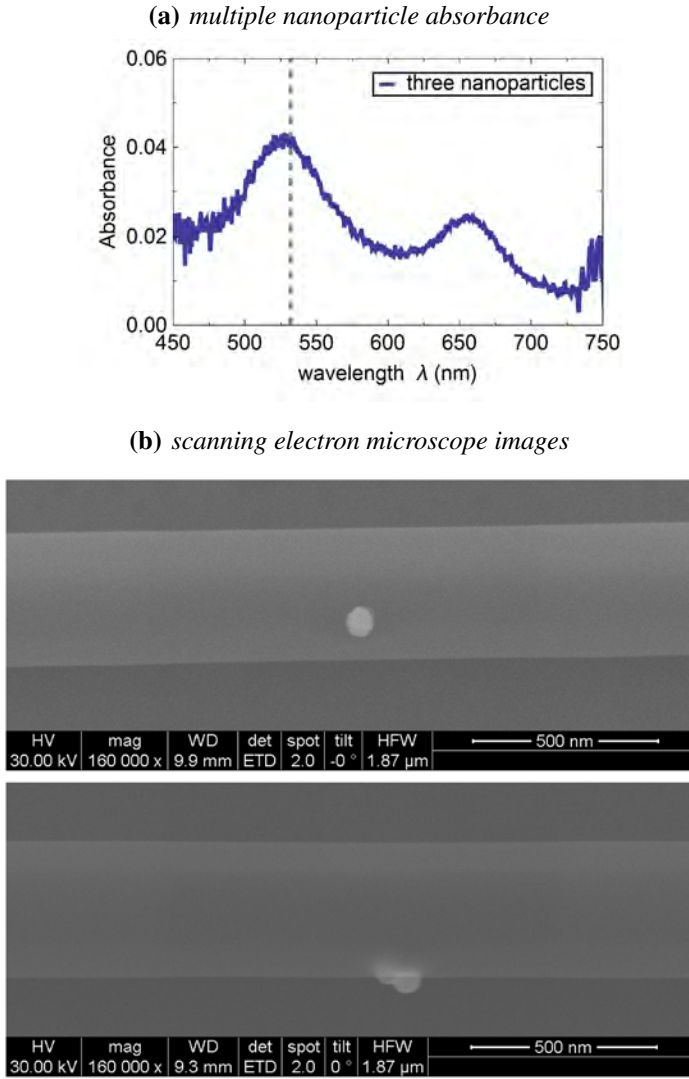


**Figure 5.13: Multiple particle extinction spectrum - experimental realization.** (a) *Experimental multiple nanoparticle absorbance spectrum. The resonance peak at a wavelength of about  $\lambda \approx 660$  nm evolves because of two nanospheres that touch each other (see panel (b)).* (b) *Scanning electron microscope images for the extinction spectrum in panel (a). The distance between the isolated particle (upper image) and the dimer (lower image) was too large to be resolved by a single SEM picture. The upper picture shows an isolated nanoparticle. The lower picture shows a so called dimer. The diameters were found to be: isolated particle,  $2R_{\text{single}} = (84 \pm 2)$  nm, left dimer particle,  $2R_{\text{dimer},l} = (58 \pm 4)$  nm, right dimer particle,  $2R_{\text{dimer},r} = (64 \pm 4)$  nm and nanofiber,  $2a = (365 \pm 4)$  nm. The errorbars correspond to the resolution of the SEM.*

axis gives rise to a slower collective electron oscillation frequency – its resonance is shifted to larger wavelengths.

To conclude, if the nanofiber and nanoparticle size are known, the exact number of deposited nanoparticles can in principle be determined solely via white light extinction spectroscopy. Moreover, if more than one nanoparticle is deposited the extinction spectrum reveals if the particles are interacting with each other or if they can be considered independent.

### 5.3.3 Single nanoparticle deposition via a dipping technique

With the knowledge of how to detect a single nanoparticle on a nanofiber we can address the question of how to deposit a single nanoparticle on an optical nanofiber:

After a tapered optical fiber has been fabricated and fixed on a fiber mount (see chapter 2.4) it is transported in a closed dust-free Tupperware box to the experimental setup. The setup for the deposition of single nanoparticles is built up on a thoroughly cleaned optical table. The site must be as dust-free as possible to maintain the optical properties of the nanofiber. Therefore, the air is filtered not only with the high efficiency particle filters (HEPA) above the table but also, as a second purifying step, with an additional HEPA filter on a superstructure which was built-up over the main part of the experiment.<sup>11</sup> Inside this superstructure, the tapered optical fiber is carefully taken out of the box and integrated into the deposition setup.

Starting with gold nanoparticles dispersed in deionized water (BBI Solutions) the nanofiber is approached with a droplet of this dispersion using an Eppendorf pipette mounted on a three-axis translation stage. A sketch of the experimental situation is shown in Fig. 5.14. After the nanoparticle dispersion has been taken up with the pipette it is possible to create an adhering droplet on the outside of the tip of the pipette by cautiously expelling the dispersion. As an initial step, the droplet has to be roughly aligned with the waist region of the tapered optical fiber. Subsequently, we monitor the droplet approaching the nanofiber with the help of an optical microscope with a long working distance objective (magnification: 20x), as can be seen in Fig. 5.15, and simultaneously use a white light source (Avantes AvaLight-DH-S) to send light through the tapered optical fiber to record a real-time absorbance spectrum with a spectrometer (Avantes AvaSpec-2048).

At one point, the surface of the nanofiber touches the surface of the droplet, which results in a large jump in absorbance over the whole recorded wavelength range, until the droplet is moved away from the fiber again.<sup>12</sup> The nanoparticles float inside the droplet until at one point, one of them settles on the fiber surface. Over time, more and more nanoparticles follow. The deposition process is therefore of statistical nature: For a dispersion with a nanoparticle density of  $n_{np} \simeq 1 \times 10^{10}/\text{ml}$  the droplet has to touch the nanofiber surface for about a minute in order to deposit one or a few nanoparticles. However, in order to reduce the probability of depositing more than one nanoparticle on the fiber, the time that the droplet touches the fiber should be

---

<sup>11</sup> The superstructure has acrylic glass walls or movable dust-repellent curtains wherever it is possible without hindering the experimental procedures.

<sup>12</sup> Because of the surface tension of the purified water in which the nanoparticles are dispersed, it is possible to push – and thereby stretch – the nanofiber, by moving the droplet further down after they touched. It was not possible to push the nanofiber into the inside of the droplet. When the nanofiber is pushed further and further down, at one point, it will finally pass through the droplet and exit on the other side.

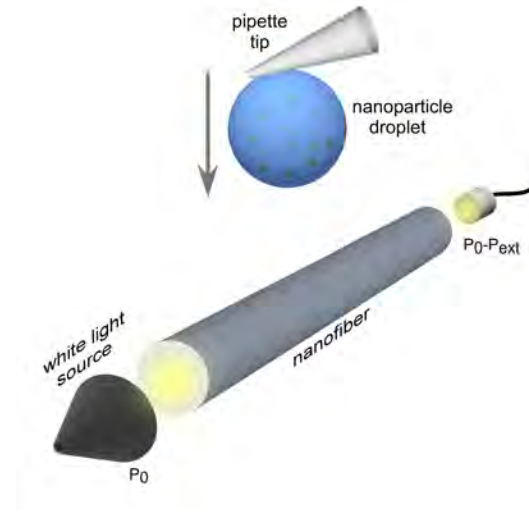


**Figure 5.14: Nanoparticle deposition via a dipping technique.** Schematic picture of the nanoparticle deposition process. The nanoparticle droplet is lowered onto the nanofiber while a white light absorbance spectrum is recorded.

reduced. If no particle was deposited, the deposition process can be simply repeated.<sup>13</sup>

After a successful deposition of one or a few nanoparticles, a characteristic absorbance spectrum (similar to Fig. 5.12 or 5.13) is observed after the droplet has been moved away from the nanofiber. From shape and height of the spectrum it is possible to determine the number of particles deposited on the fiber.

The method yields a positioning accuracy of around  $100\ \mu\text{m}$  along the nanofiber axis (i.e. longitudinally) which is limited by the minimum length over which the droplet touches the fiber. As the droplet is huge compared to the nanofiber and the nanofiber can not get inside the droplet, lowering the droplet from the top onto the nanofiber assures that the nanoparticle is deposited on the top of the nanofiber. The remaining angular uncertainty in azimuthal direction was experimentally obtained to be  $\Delta\phi \approx 20^\circ$ . The longitudinal position uncertainty can be further narrowed down by sending resonant light through the nanofiber and monitoring the waist region with the camera (see Fig. 5.15(c)). From the scattered light one can obtain the nanoparticle's position with the resolution accuracy of the microscope. In addition, this imaging yields a second estimate of the particle number and by combining both methods (absorbance and imaging) we can deposit and distinguish a single nanoparticle from more than one nanoparticle on the nanofiber with a success probability of close to one.<sup>14</sup>

<sup>13</sup> To decrease the time it takes for a successful deposition, one can increase the nanoparticle density by e.g. letting some of the deionized water of the droplet evaporate before approaching the fiber. However, this also increases the probability to deposit more than just one nanoparticle.

<sup>14</sup> The absorbance  $\mathcal{A}$  scales linearly with the number of nanospheres deposited on the nanofiber. Figure 5.11b shows that there is a chance to consider two small, isolated nanospheres as one large nanosphere. If, however nanoparticles agglomerate and form dimers or trimers, they can again be distinguished from the single nanosphere

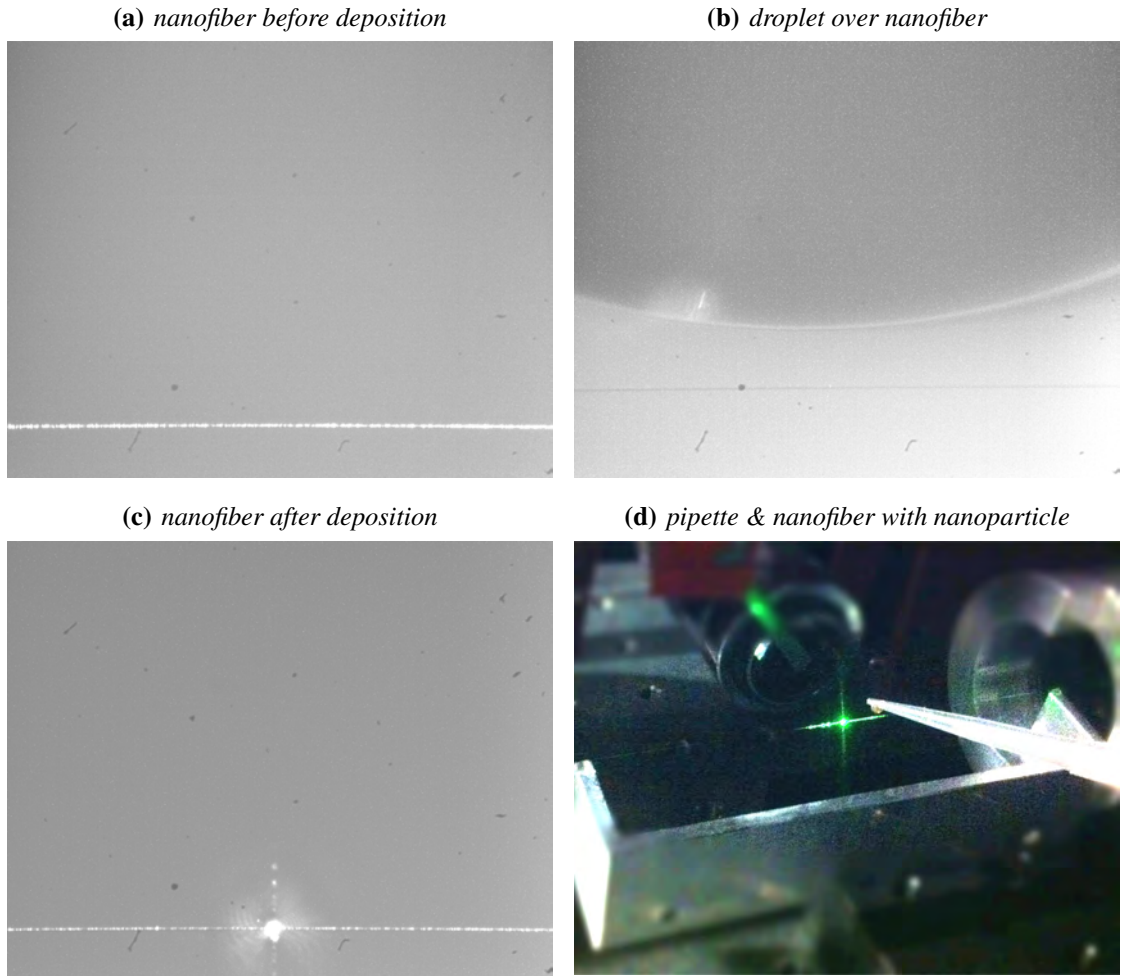


**Figure 5.15: Nanoparticle deposition - experimental methods.** (a-c) Microscope pictures (dimensions,  $380\ \mu\text{m} \times 330\ \mu\text{m}$ ) of a small part of the nanofiber section of a tapered optical fiber. The nanofiber can be seen as a thin horizontal line at the bottom part of the images. Pictures (a) and (c) are overexposed to highlight the nanofiber. (a) Light with a wavelength of  $\lambda = 532\ \text{nm}$  is sent through the fiber. On this nanofiber part, no scatterers can be seen. The residual light scattered from the nanofiber is possibly due to microscopic fiber cracks, surface adsorbates or defects in the silica nanofiber. (b) Nanoparticle droplet right on top of a part of the nanofiber illuminated by ambient white light. The droplet is much larger than the view-frame of the image. (c) Light with a wavelength of  $\lambda = 532\ \text{nm}$  is sent through the fiber. On this nanofiber part, the scattered light of a nanoparticle saturates the picture. (d) Photograph of a tapered optical fiber fixed to a mount on top of which the tip of the pipette is situated. Light with a wavelength of  $\lambda = 532\ \text{nm}$  is sent through the nanofiber and the light scattered by the deposited nanoparticle can be seen. The rest of the nanofiber also scatters green light due to the above mentioned processes. Behind the nanofiber, the objective can be recognised in the background.

It is also possible to clean the nanofiber from dust and deposited nanoparticles, which makes the dipping technique reversible: In the case of dust it is often successful to use a pipette and drop highly purified alcohol over the region where the dust particle is scattering light. To remove persisting dust and especially nanoparticles, the edge of a lense cleaning tissue is soaked with highly purified alcohol.<sup>15</sup> After that, the edge is carefully lowered onto and slowly pulled over location of the scatterer that is to be removed. This procedure is repeated until the scatterer is removed – the absorbance spectrum retrieves its shape before the dust/nanoparticle was on the nanofiber. While a non-negligible risk of breaking the fiber exists, this way of cleaning is still a much more attractive option than fabricating a new fiber right away.

In order to measure the nanofiber and nanoparticle diameters as well as to ensure that it is indeed the number of particles one aimed for, it is possible to measure the nanofiber waist region with a scanning electron microscope (SEM). Because the SEM that was used in this thesis is not in a clean room, the imaging procedure leaves the nanofiber covered with dust and therefore more or less unusable afterwards. Therefore, this procedure can only be used as a post-analysis method after all measurements have been carried out. For the SEM analysis, the nanofiber is deposited on a 2-inch diameter Al-substrate while preserving its initial azimuthal orientation when the nanoparticle was deposited. This allows one to measure the azimuthal position of the nanoparticle on the fiber. During deposition, it is helpful to use a microscope and send intense light (e.g. laser light) through the tapered optical fiber to see it being scattered from the nanoparticle(s) and the nanofiber. In this way, the distance between nanofiber and substrate can be monitored more easily and the moment when the nanofiber touches the substrate appears as a 'switching off' of the fiber coupled laser light because no more light is transmitted into the nanofiber section. Afterwards, the fiber is fixed on the substrate with an UV-curing glue and the protruding parts are cut away.<sup>16</sup> In order to transport the sample safely to the SEM we use thoroughly cleaned Tupperware boxes and fix the substrate to the box with double sided adhesive tape. Before the sample is introduced into the SEM, it is helpful to coat it with a 4 nm gold palladium layer to avoid charging effects that would deteriorate the quality of the images or even break the nanofiber.<sup>17</sup>

In order to find the nanoparticle with the SEM on the nanofiber waist (typical lengths:  $l = 1$  cm to 3 cm), we deposit – after the measurements and before the deposition of the nanofiber onto the substrate – groups of additional particles on the fiber at positions  $\pm 1, 2, 3$  mm away

---

by their resonance position and shape (see 5.3.2). So a confusion between one and two nanospheres happens only in the case, where the nanospheres are more than about two hundred nanometers away from each other and can not be distinguished by the camera (i.e less than a few micrometers). In addition to that, it is unlikely to deposit exactly two small nanospheres where there are mainly larger ones dispersed in the droplet. All in all this explains why such a high success probability can be reached.

<sup>15</sup>The use of a lens tissue is favorable because of two reasons: Firstly, it is very clean. Secondly, due to its very low mass and mechanical flexibility, it does not directly transfer forces (exerted onto it because of e.g. minor hand movements) to the nanofiber even when both touch each other.

<sup>16</sup> In principle it is possible to fix the fiber on the substrate mechanically such that it can be removed after the SEM imaging. For details see [105].

<sup>17</sup> Indeed, for nanofiber radii of around 160 nm long, high resolution imaging of one part of the fiber, can cause the fiber to degrade within seconds and eventually rip apart. This is probably due to electrostatic forces and happened occasionally even when the fiber was coated.

from the initial nanoparticle, which serve as markers for finding the correct fiber region.

In Fig. 5.12a an absorbance spectrum after a successful single nanoparticle deposition is presented. After the absorbance spectrum showed the expected single particle absorbance, the measurements shown in the following section 5.4 were carried out with this nanoparticle-nanofiber system. Post-analytic SEM measurements could verify that it was indeed one single nanoparticle (see Fig. 5.12b). From the images one obtains a diameter of  $(315 \pm 3)$  nm and  $(90 \pm 3)$  nm for the nanofiber and nanoparticle used in the experiment, respectively, which gives almost the absorbance spectrum we expect from our simplified model in Sect. 5.3.2. Residual deviations from the experimental absorbance spectrum are mainly due to approximations in the model (see Sect. 5.3.2 for details).

The presented dipping technique can be used at ambient conditions. The only requirement is a dust-free environment, if the optical properties of the tapered optical fibers are to be conserved. The dipping technique is consequently very easy to implement compared to other commonly used nanoparticle deposition techniques [159], out of which scanning probe assembly is the most accurate [21, 138, 160, 161].<sup>18</sup> In 2012, Yalla et. al. published an experiment with quantum dots on an optical nanofiber that essentially used a more elaborated version with better resolution of the technique presented in this thesis with a so-called sub-picoliter needle-dispenser that had a tip aperture of 17  $\mu$ m and a position accuracy of 5  $\mu$ m [22].

### 5.4 A chiral nanophotic waveguide coupler

With the technique presented above for depositing a single nanoparticle on the nanofiber we have a system at hand with which the directional scattering that was predicted in Sect. 5.2 can be investigated. To do this the nanoparticle-nanofiber system is illuminated from the side with a laser beam of variable polarization.

#### 5.4.1 Optical setup

According to the calculations in Sect. 5.2, the directionality of a nanoparticle-nanofiber system depends on the longitudinal polarization component of the guided modes, the particle's polarizability and position around the fiber as well as – in case of a polarization maintaining dipole scatterer – the exciting light field's polarization. While the first two parameters depend on material properties like the fiber and nanoparticle radii, the other two parameters can be adjusted in the experimental setup presented in this section.

In order not to expose the nanofiber to additional dust, the directionality setup is built up at the same location, as the deposition setup discussed in Sect. 5.3.3. After a single nanoparticle is successfully deposited on the nanofiber surface, its position along the fiber axis is determined with the microscope objective.<sup>19</sup> Subsequently, the excitation light field will then be centered

---

<sup>18</sup> Strictly speaking, not even the microscope objective would be needed for nanoparticle deposition as it is possible to observe the droplet touching the nanofiber by the naked eye.

<sup>19</sup> The single scattering center can per definition only be at a position, where the nanoparticle dispersion droplet touched the fiber.

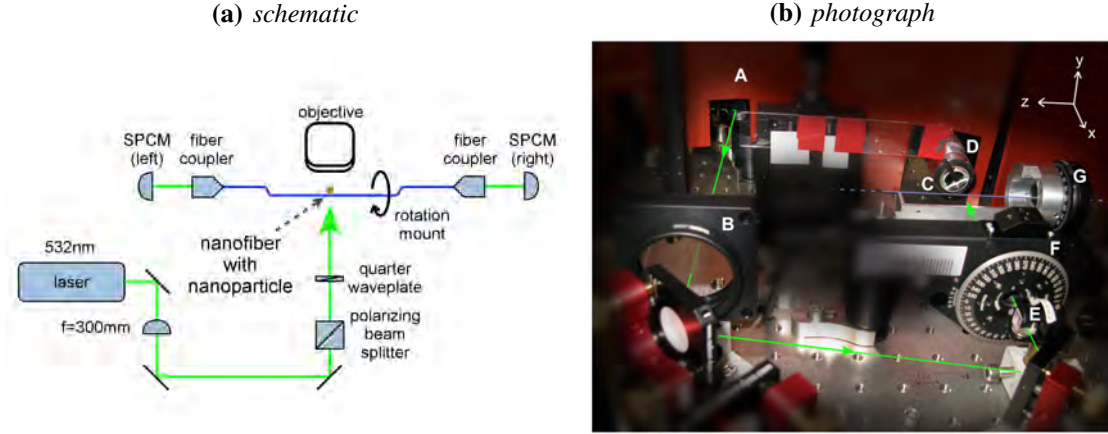


**Figure 5.16: Chiral waveguide coupling - optical setup.** (a) Schematic and (b) photograph of the experimental setup for the measurements of the asymmetric scattering of a gold nanosphere into an optical nanofiber. The labeled elements in the photograph are from left to right: (A) excitation beam with a wavelength of  $\lambda = 532 \text{ nm}$  (green line), (B) focussing lens with a focal length of  $f = 300 \text{ mm}$ , (C) optical nanofiber (light blue line) (D) microscope objective with a working distance of  $WD = 200 \text{ mm}$  that is shielded from the incident excitation light, (E) polarizing beam splitter, (F) quarter-wave plate in a motorized rotation mount, (G) mechanical rotation mount to rotate the tapered optical fiber around its axis. In order to measure the light scattered into the nanofiber, the fiber output ports are connected to SPCMs. The experimental parameters of the excitation beam used in the following measurements are: total power,  $P = (260 \pm 5) \mu\text{W}$  and waist radius at nanofiber,  $w = (150 \pm 10) \mu\text{m}$ .

on this point. Figure 5.16 shows the optical setup: An intensity stabilized laser beam with a wavelength of  $\lambda = 532 \text{ nm}$  (A) is focused (B) onto the nanoparticle on the nanofiber (C), which can be observed with a microscope objective (D). To guarantee a deterministic polarization of the excitation field at the nanoparticle, a polarizing beam splitter (E) is used as a polarization filter in front of a quarter-wave plate (F) that sets the ellipticity of the polarization. The fiber mount is fixed to a specially designed rotation mount (G) whose rotation axis can be well matched to the fiber axis. Depending on the measurements, the fiber ends can be connected to a white light source and a spectrometer for depositing single nanoparticles, to a 532 nm laser source to determine the position of the nanoparticle or to single photon counting modules (SPCMs) to determine the scattering rates into the guided modes.

The intensity stabilized excitation beam is a focused Gaussian beam with a waist radius of around  $w = 150 \mu\text{m}$  at the position of the nanoparticle, thereby assuring a homogeneous spatial intensity distribution with negligible longitudinal polarization components along  $\hat{x}$ . Accordingly, the excitation beam can be considered as paraxial. The part of the laser beam that is transmitted through the polarizing beam splitter is polarized along the fiber axis ( $\hat{z}$ ). This means that the polarization of the excitation field  $\mathbf{E}_0$  at the nanoparticle can be tuned between circularly  $\sigma^\pm = (i\hat{z} \pm \hat{y})/\sqrt{2}$  and linearly  $\hat{z}$ -polarized excitation light field depending on the orientation of the quarter-wave plate optical axis. For intermediate angles the polarization is elliptical with



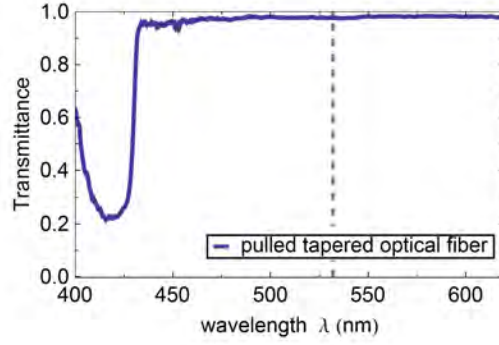


**Figure 5.17: Transmission profile of the tapered optical fiber.** *Transmittance of the tapered optical fiber used for the measurements in this section relative to the transmission of the unprocessed standard optical fiber. The onset of transmission to a transmittance value of almost 1.0 is around  $\lambda_{\text{cutoff}} = 430$  nm. This is the cutoff wavelength of the unprocessed fiber. The dashed vertical line indicates the laser wavelength of  $\lambda = 532$  nm where the transmittance is 0.977.*

the major axis along  $\hat{z}$ .

The fiber can be rotated around its axis. Because the bare nanofiber is cylindrically symmetric, this amounts effectively to a change of the nanoparticle's azimuthal position around the fiber by rotating the fiber. In this way, the overlap of the nanoparticle's dipole moment that points along the direction of the excitation field with the guided modes at the position of the nanoparticle can be changed.

The fiber rotation mount is fixed onto a translation stage that moves the fiber along its own axis ( $\hat{z}$ ). The stage ensures that the nanoparticle is deposited in the waist of the tapered optical fiber and it is used to reposition a successfully deposited nanoparticle in the center of the view frame of the microscope objective. In this way, the alignment routine of the excitation beam with the nanoparticle position is straightforward by simply matching the position of the nanoparticle with the center of the excitation beam.

#### 5.4.2 Experimental results

We investigate the directional scattering using a tapered optical fiber that is made out of a standard single-mode optical fiber for 532 nm (SM450, Fibercore). In Fig. 5.17 it can be seen that the transmission through the tapered optical fiber above 450 nm is almost lossless. The wavelength below which the transmittance falls down to nearly 0.2 indicates the cutoff wavelength  $\lambda_{\text{cutoff}}$  of the unprocessed fiber. Below this wavelength the standard optical fiber is no longer single mode and supports more than the  $\text{HE}_{11}$ -modes. When this multimode light now enters the taper region, the higher order modes, however, are not adiabatically transferred into the waist region and therefore lost. This process manifests as a reduction in transmission below the cutoff wavelength  $\lambda_{\text{cutoff}}$  of the unprocessed fiber. The nanoparticle-nanofiber system that is used for all the measurements presented in this section is the one presented in 5.12.

Figure 5.18 illustrates the schematic setup used to investigate directional incoupling. In



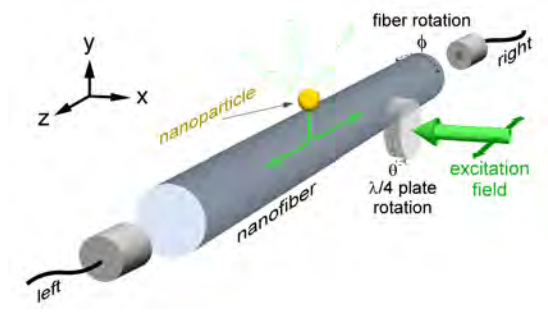


**Figure 5.18: Sketch of the experimental setup.** A single nanoparticle on a silica nanofiber surface is illuminated with light propagating in  $-\hat{x}$ -direction. The polarization of the light can be set via the rotation of a quarter-wave plate by the angle  $\theta$ . The azimuthal position of the nanoparticle can be changed by rotating the fiber around its axis by the angle  $\phi$ . The light scattered into the nanofiber is detected using single photon counting modules at the left ( $+\hat{z}$ ) and right ( $-\hat{z}$ ) fiber output port.

order to model the measured photon fluxes  $\Gamma^{(\text{gui},\pm)}$  detected by the left and right SPCM, we use the formulations of the scattering rates  $\gamma^{(\text{gui},\pm)}$  given in Eq. (5.5) and (5.10) and obtain:

$$\Gamma^{(\text{gui},\pm)} = \frac{1}{\mathcal{L}} \left( \kappa_f \left\{ |\mathbf{E}_0^* \cdot \mathbf{e}_x^\pm(r, \phi - \phi_0)|^2 + |\mathbf{E}_0^* \cdot \mathbf{e}_y^\pm(r, \phi - \phi_0)|^2 \right\} + c_0 \right), \quad (5.17)$$

with the two fit parameters  $\kappa_f$  and  $\phi_0$ , being the flux amplitude of the photons that are scattered into the fiber by the particle and the angular offset of the nanoparticle from the expected deposition position. The parameter  $c_0$  accounts for an offset incoupling rate due to effects such as parasitic scattering of dust particles. The optical losses  $\mathcal{L}$  incorporate (i) absorption due to possible dust on the fiber, (ii) optical losses in the taper regions of the fiber and (iii) photon flux reductions due to detection efficiencies of the SPCMs. The profile functions of the fundamental fiber modes  $\mathbf{e}_{x,y}^\pm$  are normalized to one on the fiber axis and  $\mathbf{E}_0$  is the vector amplitude of the excitation light field. It is normalized to one before it interacts with the nanoparticle-nanofiber system.  $\phi_0$  is the angular offset of the nanoparticle on the fiber from its expected deposition position at  $\phi = 90^\circ$ .

The measured photon fluxes at both fiber outputs are shown in Fig. 5.19a and b, as a function of the azimuthal position  $\phi$  of the nanoparticle and  $\theta$  that describes the polarization state of the excitation light field. Here,  $\theta$  is the rotation angle between the optical axis of the quarter-wave plate and the  $y$ -axis. Before passing through the waveplate, the polarization of the light is aligned along  $z$ . Thus, we can set the polarization to linear along  $\hat{z}$  ( $\theta = 0^\circ, 90^\circ$ ) and circular, i.e.,  $\sigma^-$  ( $\theta = 45^\circ$ ) or  $\sigma^+$  ( $\theta = 135^\circ$ ). For intermediate angles the polarization is elliptical with the major axis pointing along  $\hat{z}$ . The situation where the nanoparticle is located on the top of the fiber ( $x = 0, y = a$ ) corresponds to a rotation angle of  $\phi = 90^\circ$ . The figures show an interpolation of the measured photon fluxes (each data point time-averaged over 5 s, only corrected for the nonlinear response of the SPCMs) of a set of measurements along discrete values of  $\phi$ .

As expected from Sect. 5.2 a directional behavior can clearly be seen for most points  $(\theta, \phi)$ , when comparing the measured photon fluxes at the left (panel a) and right (panel b) output port

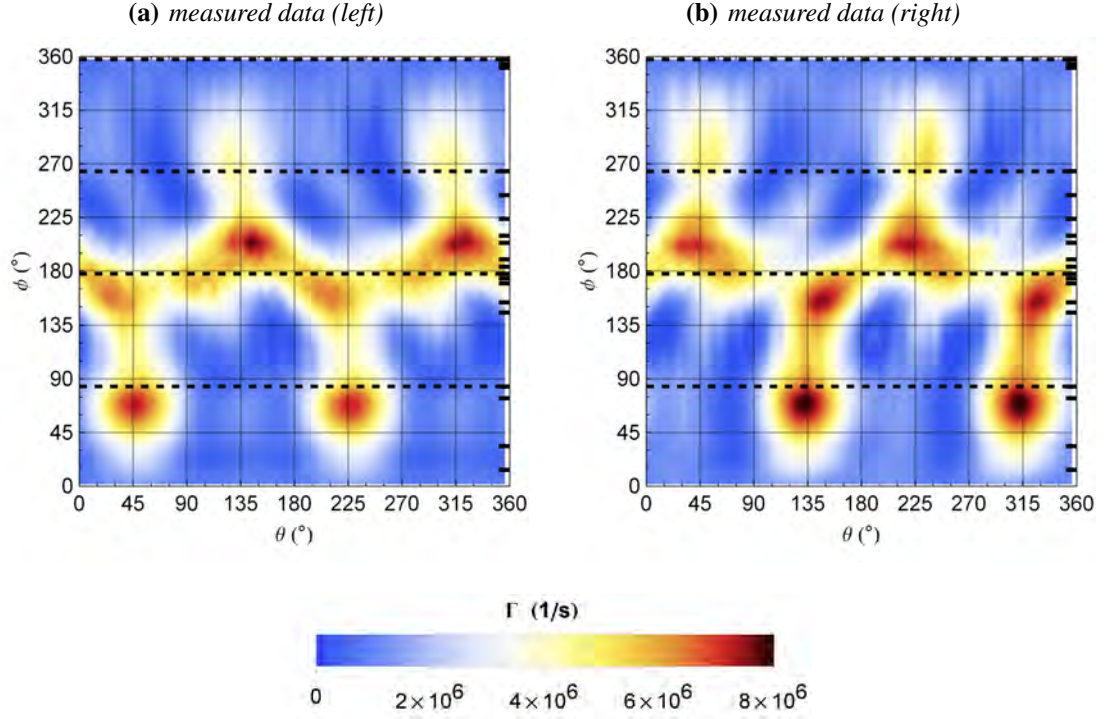


**Figure 5.19: Chiral waveguide coupling - experiment.** (a) and (b) Measured photon flux (raw data, only corrected for the nonlinear response of the SPCMs) of the light scattered into the (a) left and (b) right direction as a function of the azimuthal position of the nanoparticle  $\phi$  and the polarization of the excitation light field set by the angle  $\theta$  of the quarter-wave plate. The ticks on the right mark the azimuthal positions for which data have been acquired with a stepsize of  $\theta = 5^\circ$ . The data are interpolated in between the measured points. The dashed horizontal lines indicate the data sets plotted in Fig. 5.21.

of the fiber. Only for few positions (e.g. all  $\theta$ , where  $\phi = 180^\circ$ ) the photon flux is the same for both directions. Due to the periodicity of the quarter-wave plate, the photon flux data in the range  $0^\circ \leq \theta < 180^\circ$  is repeated for  $180^\circ \leq \theta < 360^\circ$ . The data is symmetric with respect to the point  $(\theta, \phi) = (90^\circ, 180^\circ)$ . The experimental count rates in the range from  $\phi = 270^\circ$  to  $360^\circ$  are much lower than its counterparts in the range from  $\phi = 0^\circ$  to  $90^\circ$  because of a lack of measured data points and a concomitant poor interpolation.

The theoretical predictions calculated according to Eq. (5.17) to the measured photon fluxes are shown in Fig. 5.20a and b under the assumption that the polarization and intensity distribution of the incident light field are not modified by the presence of the optical fiber. We find qualitative agreement between measurement and theoretical prediction. In particular, we observe the expected maximum of the left-right asymmetry for the case of circular input polarization with the particle located at the top or the bottom of the fiber. However, scattering and refraction of the excitation light field by the nanofiber lead to a substantial modification of the polarization and intensity of the field close to the nanofiber surface.

Including these effects in the calculation, one obtains the theoretical predictions shown in panels

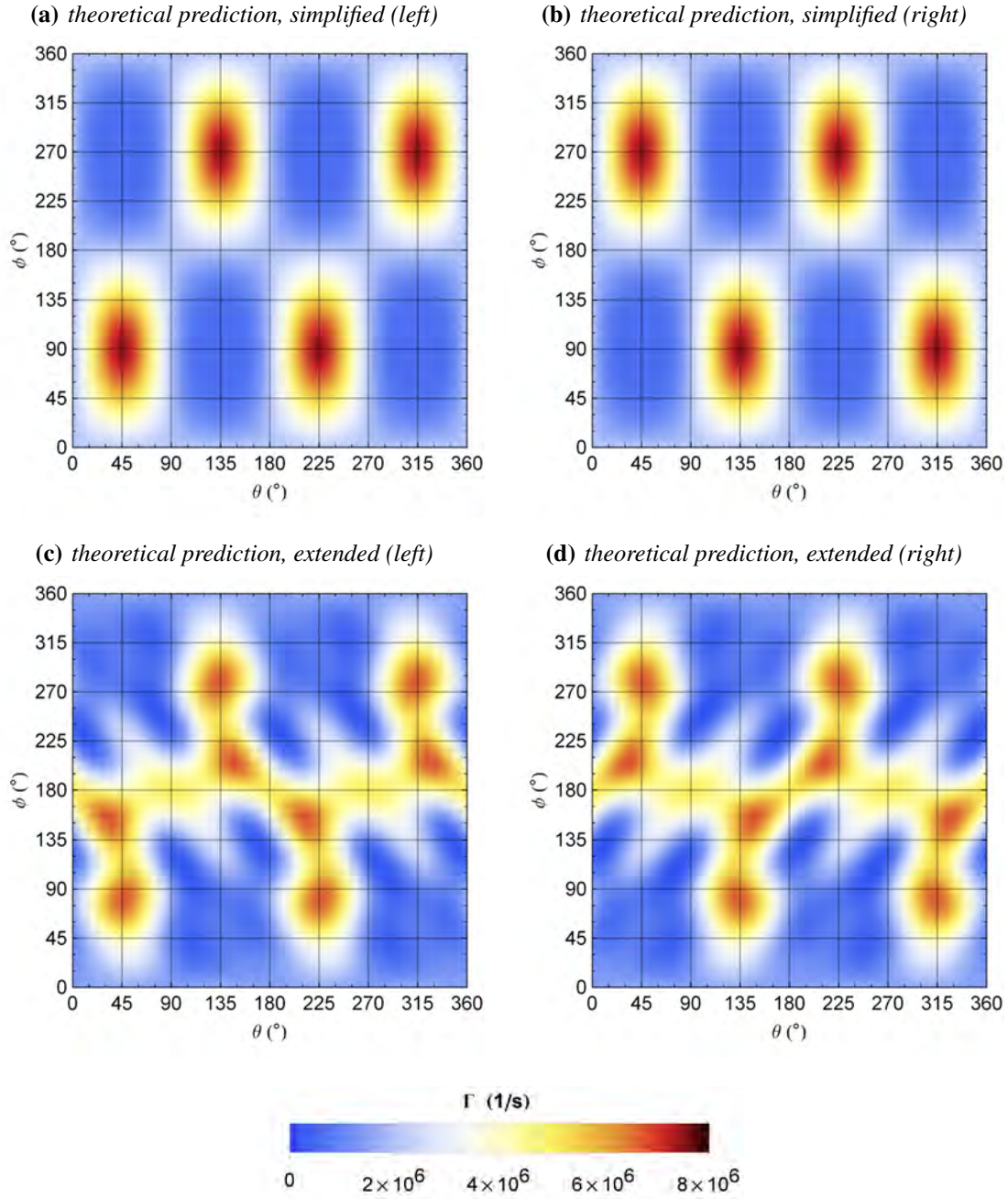


**Figure 5.20: Chiral waveguide coupling - theory.** (a) to (d) Theoretical prediction for the photon fluxes when [(a) and (b)] neglecting and [(c) and (d)] including the effect of the nanofiber on the incident light field. The model uses the angular offset of the nanoparticle and the overall amplitude of the photon flux as free parameters, which are obtained from a fit of (c) and (d) to the data in Fig. 5.19a and b.

**c** and **d**. There, in order to obtain the correct overall scattering rate and nanoparticle position, a least square fit of the model in Eq. (5.17) to the data in panels **a** and **b** was performed using the two fit parameters  $\phi_0$  and  $\kappa_f$ . We obtain  $\phi_0 = (6.3 \pm 0.1)^\circ$  and  $\kappa_f = (21.9 \pm 0.1) \times 10^6/\text{s}$  (goodness of fit: adjusted  $R^2 = 0.91$ ). The parasitic coupling of the excitation light  $c_0 = 22.5 \times 10^3/\text{s}$  was determined before the fit (see Fig. 5.21c). As can be seen, this full model agrees well with the measured data. The main differences to the simple model are an increase of the scattering rate around  $\phi = 180^\circ$  due to the focusing of the incident light field by the fiber and the emergence of a shadow region around  $\phi = 120^\circ$  and  $\phi = 240^\circ$  with a concomitant decrease in the scattering rate (see also Fig. 5.8 for a depiction of the modified intensity distribution due to the presence of the fiber).

For closer comparison, Fig. 5.21a to **d** show the polarization dependence of the measured photon flux in the fiber for selected azimuthal positions of the nanoparticle together with the theoretical prediction. For the cases of the nanoparticle positioned near the top and the bottom of the nanofiber, in Fig. 5.22, we also plot the directionality  $\mathcal{D}$  (see Eq. (5.7)) of the scattering process together with the theoretical prediction. We observe a maximum directionality of  $\mathcal{D} = 0.88$  ( $\mathcal{D} = 0.95$ ) for a particle near the top (bottom) of the fiber which corresponds to a ratio of 16:1 (40:1) between the photon flux scattered to the left and right (right and left).

When the particle is located near the side of the fiber, the overlap of the fiber eigenmodes with any polarization of the excitation light is independent of the propagation direction and zero directionality is expected. In the experiment, we indeed observe only a small variation with the incident polarization, see Fig. 5.21a and **b**. The residual modulation is most probably due to the small angular deviation of the nanoparticle position from the ideal point.

In Fig. 5.21c we can see that the parasitic coupling of the excitation light into the nanofiber without a deposited nanoparticle is 3 to 4 orders of magnitude smaller than the scattering of the nanoparticle (see green and dark yellow data points). Although an oscillatory behavior could be seen,<sup>20</sup> it therefore does not influence the fit if we take the mean photon flux number of all those data points as the fit parameter  $c_0 = 22.5 \times 10^3/\text{s}$ . In Sect. A.3 in the appendix, the photon fluxes for all measured datapoints together with their respective directionalities are presented.

The statistical errors of the presented data originate from the Poissonian distribution of the measured photon count rates. For the measured directionalities, this results in errors below  $\Delta\mathcal{D} < 4 \times 10^{-4}$  which is negligible compared to systematic error sources. To obtain an estimate of the systematic error, we compare measured data points for which we expect approximately the same directionality  $|\mathcal{D}|$ . We obtain  $|\mathcal{D}| = 0.88$ ,  $|\mathcal{D}| = 0.84$  (Fig. 5.21e) and  $|\mathcal{D}| = 0.93$ ,  $|\mathcal{D}| = 0.84$  (Fig. 5.21f) for the positions  $\theta = 67^\circ$  and  $\theta = 112^\circ$ . The variation of these values is significantly larger than the statistical error which indicates the presence of systematic effects. Possible causes include:

- Deviations from the spherical shape of the nanoparticle which would result in a polarization dependent free-space scattering cross section. The SEM pictures suggest that this

---

<sup>20</sup> The oscillatory behavior of the measured photon fluxes when no nanoparticle was deposited on the nanofiber most probably stems from additional scattering sources that show directional coupling to the excitation light field, such as fiber cracks and dust on the nanofiber surface.

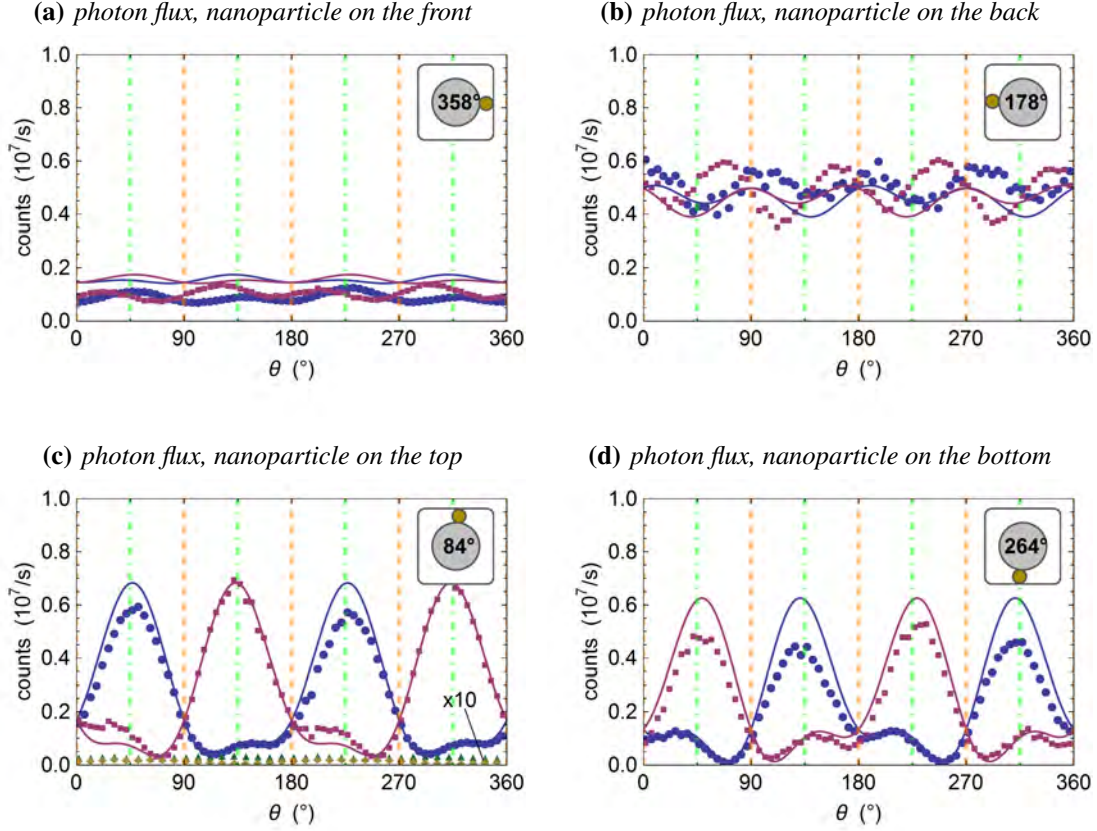


**Figure 5.21: Asymmetry of the scattering process.** (a) to (d) Measured photon fluxes at the left (blue circles) and right (red squares) fiber output port as a function of the angle  $\theta$  of the quarter-wave plate. Here,  $\theta = 0^\circ, 90^\circ, \dots$  corresponds to linear polarization along  $\hat{z}$  (dashed orange lines) and  $\theta = 45^\circ, 225^\circ$  ( $\theta = 135^\circ, 315^\circ$ ) corresponds to  $\sigma^-$  ( $\sigma^+$ ) polarization of the incident light field (both, dash-dotted green lines). (a) to (d) correspond to the azimuthal positions ( $\phi = 358^\circ, 178^\circ, 84^\circ$  and  $264^\circ$ ) of the nanoparticle (green dot) around the fiber (gray disk), as indicated in the insets. The solid lines are the predictions of the full theoretical model. The statistical error bars are too small to be visible in the plot. (c) also shows exemplarily the measured photon fluxes to the left (dark yellow diamonds) and right (green triangles) for the nanofiber without the nanoparticle, scaled up by a factor of 10. This data is used to estimate the photon flux  $c_0$  due to the parasitic coupling of excitation light.



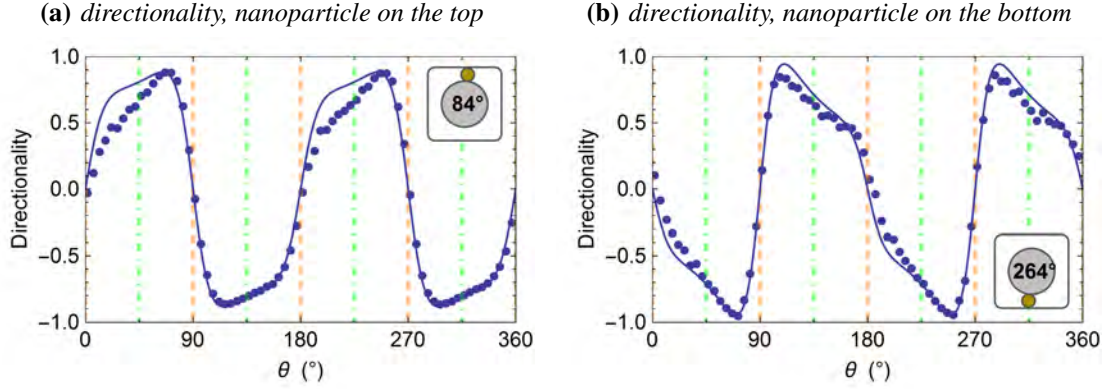


**Figure 5.22: Directionality of the scattering process.** Directionality  $\mathcal{D}$  of the scattering process into the fiber for azimuthal positions of (a)  $\phi = 84^\circ$  and (b)  $264^\circ$  of the nanoparticle (green dot) around the fiber (gray disk), as indicated in the insets. Here,  $\theta = 0^\circ, 90^\circ, \dots$  corresponds to linear polarization along  $\hat{z}$  (dashed orange lines) and  $\theta = 45^\circ, 225^\circ$  ( $\theta = 135^\circ, 315^\circ$ ) corresponds to  $\sigma^-$  ( $\sigma^+$ ) polarization of the incident light field (both, dash-dotted green lines). (a) and (b) correspond to the measured photon fluxes in Fig. 5.21c and d, respectively. The solid lines are the predictions of the full theoretical model. The statistical error bars are too small to be visible in the plot.

should have a minor effect for the sample used in the measurements.

- In the theoretical model, the fields of guided modes and excitation beam are only considered at the center of the nanoparticle. This is, of course, a simplification of the real situation. For the radii obtained with the SEM, the nanoparticle covers a solid angle of about  $25^\circ$  when viewed from the center of the nanofiber. One consequence of this is that the incident light will be preabsorbed by the particle, when it is positioned on the fiber half facing the incident light field. Another consequence of the finite nanoparticle size is that the nanoparticle effectively interacts with the guided modes along a certain azimuthal and longitudinal range.
- Backscattering effects from nanoparticle to nanofiber are not included in the model.
- During the course of a measurement, dust can accumulate on the fiber at different times and locations that are *not* illuminated by the laser beam from the side. This leads to absorption and backscattering of the fiber-guided light and modifies the photon fluxes on each fiber output. To get an idea of the strength of this effect, one set of data points was re-measured at the end of the data acquisition. The mean photon flux was a factor of 1.03 larger than in the previous measurement.
- Between the measurements of the datasets for different angles  $\phi$ , the positioning of the excitation light field on the nanoparticle had to be re-optimized which could result in a

small change ( $< 5\%$ ) of the power of the light incident on the nanoparticle.<sup>21</sup>

Notice, that all mentioned systematic errors that equally affect the photon flux at both SPCMs, will not affect the directionality.

### Absolute scattering into the nanofiber

As a last topic of this section, let us quantitatively relate the measured and theoretically expected scattering cross sections. The scattering cross section  $\sigma_{\text{sca}}$  of a nanoparticle into a given mode is connected to the photon flux  $\gamma = \mathcal{L} \Gamma$  into the mode via

$$\sigma_{\text{sca}} = \frac{\hbar\omega \gamma}{I_{\text{np}}} , \quad (5.18)$$

where  $\mathcal{L}$  incorporates all optical losses after the light was scattered,  $\hbar\omega$  is the photon energy at the excitation wavelength and  $I_{\text{np}}$  is the intensity with which the nanoparticle is excited. In our case, we only measure the *total* amount of photons scattered into one direction of the fiber. Thus, the cross sections into all guided modes propagating along  $+\hat{z}$  or  $-\hat{z}$  have to be considered. The total photon flux is then the sum over the photon fluxes of the four modes  $\mu_{x,y}^{\pm}$ .

We compare these total cross sections into the fiber for three different polarizations of the excitation field, namely  $\sigma^+$ ,  $\sigma^-$  and  $\pi = \hat{x}$ , for the case, where the nanoparticle is positioned at  $\phi = 0^\circ$ .<sup>22</sup> While the calculation of the theoretically expected cross sections is straight forward, some peculiarities have to be considered in the experimental case: The excitation field in the experiment did not cover the cases where the particle is excited by  $\pi$ -polarized light. However, because of the cylindrical symmetry of the nanofiber this case can be associated with the situation where a nanoparticle sits on top of the nanofiber and is illuminated by  $\hat{y}$ -polarized light.<sup>23</sup> This situation can be extracted of the fitted model function.<sup>24</sup> Notice that, the two described situations are only analogous, because the polarization of the incident light field is to a good approximation left unchanged by the fiber for the azimuthal positions  $\phi = 0^\circ$  and  $90^\circ$ . Since the measured nanoparticle positions differ slightly from those two positions, we use the fitted model function to obtain the experimentally observed scattering cross sections. In table 5.1, both, the theoretically expected and experimentally deduced scattering cross sections into the nanofiber are given. They show good agreement. Here, we calculated the theoretical scattering rates as described in Eq. (5.5) and (5.10). In order to estimate the intensity that was present during the measurements for the determined beam parameters (total power,  $P = (260 \pm 5) \mu\text{W}$ ; waist radius at nanofiber,  $w = (150 \pm 10) \mu\text{m}$ ), we take into account that the excitation field is modified due to the presence of the fiber (see 5.8). The loss-factor was assumed to be  $\mathcal{L}_{\text{exp}} = \eta_{\text{SPCM}} \eta_{\text{opt}} = 0.46$  in the experiment and incorporates optical losses after the light has been coupled into the fiber by the nanoparticle ( $\eta_{\text{opt}} = 0.86$ ) as well as the detection efficiency of the SPCMs ( $\eta_{\text{SPCM}} = 0.53$ ).

<sup>21</sup> The excitation light has to be slightly re-positioned onto the nanoparticle for each azimuthal nanoparticle position  $\phi$  because the rotation axis of the rotation mount is not perfectly aligned to the axis of nanofiber.

<sup>22</sup> When considering the total photon flux scattered into the nanofiber, i.e. the fluxes measured at both fiber output ports, the cases for  $\sigma^+$  and  $\sigma^-$  polarized excitation light are identical.

<sup>23</sup> In both cases the polarization is perpendicular to the fiber surface at the position of the nanoparticle.

<sup>24</sup> The total photon flux  $\Gamma_{\hat{y}}$  for  $\hat{y}$  polarized excitation light can be deduced from the photon fluxes  $\Gamma_{\sigma^+}$  and  $\Gamma_{\hat{z}}$  for  $\sigma^+$  and  $\hat{z}$  polarized excitation light, via  $\Gamma_{\hat{y}} = 2\Gamma_{\sigma^+} - \Gamma_{\hat{z}}$ .

Cross section (nm <sup>2</sup> )	$\sigma^{\pm}$	$\pi$
experiment	$1400 \pm 500$	$500 \pm 200$
theory	$1300 \pm 200$	$400 \pm 100$

**Table 5.1: Theoretically and experimentally expected scattering cross sections.** *Experimentally deduced and theoretically expected scattering cross sections into the nanofiber for three cases of the polarization of the excitation light field. Here, the scattering cross sections into all guided modes are given, which means that the cases for  $\sigma^+$  and  $\sigma^-$  polarized light are identical. The error is dominated by the uncertainty of the intensity at the nanoparticle in case of the experimental value and by the uncertainty of the nanoparticle radius in case of the theoretical value.*

### 5.4.3 Conclusion

In this section, it was experimentally shown that the scattering characteristics of a spherical, point-like particle become asymmetric when it is in close proximity to an optical waveguide. The underlying physical mechanism that enables this directional scattering is spin-orbit interaction of light which universally occurs in all kinds of light fields that are transversally confined (e.g. in waveguides, prisms, strongly focused beams, etc.). In particular, this includes the evanescent field of modes in dielectric waveguides of any geometry and material. The effect demonstrated in this chapter is thus very general and we expect it to have important consequences for applications that rely on controlling and manipulating optical signals in waveguides and nanophotonic structures as well as other protocols, such as near-field imaging or optical sensing. The potential of this effect for (quantum) information processing becomes apparent by several very recent publications that propose to use SOI in on-chip realizations based on photonic crystal [43] and silica waveguides [44–46].

Interestingly, for the situation discussed in this chapter, there is no fundamental limit to the directionality: by setting the polarization of the excitation field orthogonal to the polarization of the two fiber eigenmodes  $\mu_x$  and  $\mu_y$  that co-propagate into the left/right direction, unity directionality can in principle always be realized (see Sect. 5.5.1). Moreover, at the inside of the waveguide, the quasi-linearly polarized guided modes of our silica nanofiber exhibit a perfectly circular polarization at two specific positions in the fiber transverse plane. Thus, a particle at such a position that is excited with circularly polarized light will couple light exclusively into one direction of the waveguide. Given the right nanoparticle position, all light that is coupled into the nanofiber can be directed from one fiber output port to the other by simply changing the polarization of the incident side beam – a very small polarizing beam splitter. The high degree of external control and its usability under ambient conditions are important aspects of applicability.

Apart from their usefulness for optical signal processing and routing of light, the findings presented in this section have important consequences for the interaction between light and matter in evanescent fields [162, 163] or strongly focused laser beams. Consequently, they may enable novel nanophotonic sensors that allow one to detect and identify, e.g., scatterers with an intrinsic polarization asymmetry [164], i.e. different free-space emission rates for  $\sigma^+$  and  $\sigma^-$ -polarized light. When exciting them with linearly polarized light close to a nanofiber, this property will lead to different photon fluxes at the two output ports of the fiber.



## 5.5 Towards nanophotonic devices

In the previous section (Sect. 5.4), the general effect of directional coupling of a scatterer to an incident light field in the vicinity of a waveguide could be demonstrated for a nanoparticle-nanofiber system. It seems therefore reasonable, to raise the question of how realistic it is to improve this system to a point where it could be used as a directional coupling device in nanophotonic circuits or similar applications.

In this section, we discuss the most important requirements of such a chiral coupler realized as a nanoparticle-nanofiber system. In terms of incoupling efficiency and directionality there is still room for improvement – the realization presented in the previous section was designed as a proof of principle device. Both the incoupling efficiency and the directionality can be pushed towards higher numbers compared to the ones presented in section 5.4.2 using more sophisticated setups. Besides its potential use as a coupling device, other nanofiber based applications that exploit the spin-orbit interaction of light are thinkable. Here, the concepts of a unidirectional waveguide as well as a unique nanofiber-based sensor are discussed.

### 5.5.1 Chiral Coupler: Optimizing waveguide coupling and directionality

Up to a certain extent, incoupling efficiency and directionality are coupled in case of a waveguide. Both, polarization and field strength of the guided modes depend on the position of the scatterer. Consequently, it is important to realize, that optimizing incoupling efficiency might lead to a decrease of the directionality and vice versa. A priori, a general selection rule is hard to find. It is for that reason, that both terms are discussed individually in the following.

In our realization in section 5.4.2, the fraction of the total scattered power by the nanoparticle that is coupled into the nanofiber is about 10%, depending on the polarization of the excitation field (see Fig. 5.6). There are several ways to increase this coupling efficiency. Taking a look at Eq. (5.10), it is favorable to increase the overlap between guided electric field modes and the dipole moment of the scatterer. This involves several effects that can be optimized individually.

1. The position of the nanoparticle and the fiber radius can be adjusted to increase the amplitude of the guided mode fields at the nanoparticle position. This could also involve embedding the nanoparticle inside the fiber. In general, the guided modes are largest close to the nanofiber center and close to the surface.
2. The position of the nanoparticle and the fiber radius can be adjusted such that the orientation of the dipole moment resembles those of the guided mode fields as much as possible. For example, a dipole circularly polarized in a plane containing the fiber axis scatters more light into the nanofiber than any linearly polarized orientation.

In addition, there are additional possibilities to increase the incoupling efficiency:

3. The refractive index of the waveguide material and thus the numerical aperture of the waveguide can be increased which results in a more strongly confined light field and a larger longitudinal polarization component. Consequently, this increases the collection efficiency as well as the directionality.

4. To increase the scattering cross section into the waveguide, more than just one nanoparticle can be deposited on the nanofiber. Ideally, a periodic array of  $N$  nanoparticles can be placed along the waveguide with an interparticle spacing of  $\lambda/n_{\text{eff}}$ , where  $\lambda$  is the free-space wavelength of the excitation light and  $n_{\text{eff}}$  is the effective refractive index of the waveguide mode. This would increase the total collective scattering cross section into the waveguide mode by a factor of  $N^2$ .

In general, for any position of the nanoparticle, the directionality can always be made to reach the maximum (minimum) value of 1 (-1) if, at the position  $(r, \phi)$  of the particle, the polarization of the excitation field  $\mathbf{E}_0$  is chosen to be orthogonal to both quasi-linearly polarized fiber eigenmodes  $\mathbf{e}_x^-$  and  $\mathbf{e}_y^-$  ( $\mathbf{e}_x^+$  and  $\mathbf{e}_y^+$ ). For the case where the nanoparticle is located at the top of the fiber ( $\phi = 90^\circ$ ), the two profile functions at the particle position are given by

$$\begin{aligned} \mathbf{e}_x^- &\propto (1, 0, 0) \\ \mathbf{e}_y^- &\propto (0, \alpha, \beta), \end{aligned} \quad (5.19)$$

where  $\alpha$  and  $\beta$  are complex amplitudes which depend on the fiber radius and the wavelength of the light (for our system:  $\alpha = 1$ ,  $\beta = i \cdot 0.56$ ). In order to suppress the emission into the  $+\hat{z}$  direction and to obtain unit directionality, the excitation field has to be set to  $\mathbf{E}_0 \propto (0, -\beta^*, \alpha^*)$ . Due to the rotational symmetry of the nanofiber system, this is a general result and, for any particle position, the case of perfect directionality can be derived from this result by a rotation of the field vectors around the nanofiber.

If we consider the case, where a nanosphere positioned on the nanofiber is illuminated by paraxial laser beam from the side, the modification of the excitation light field due to the nanofiber has to be taken into account. Let the polarization of the excitation field again be defined by two parameters  $\alpha$  and  $\beta$ . The excitation field then reads  $\mathbf{E}_0 = E_0(0, \alpha, i\beta)$ , where  $\beta = \sqrt{1 - \alpha^2}$  ( $0 \leq \alpha \leq 1$ ).<sup>25</sup> This way, all counterclockwise circulating elliptical polarizations in the  $yz$ -plane are described via the parameter  $\alpha$ , including the linear polarizations. For clockwise circulation, the directionality simply changes sign. Figure 5.23 shows the dependency of the directionality with respect to the parameter  $\alpha$  and the azimuthal position  $\phi$  of the nanosphere, for the parameters used in our experiment. As expected, the *absolute* directionality has mirror symmetry around the  $\phi = 180^\circ$  axis. The directionality is positive for the case where the nanoparticle is situated on the bottom half of the nanofiber and negative where it is situated on the top half of the nanofiber. For the case, where the nanoparticle sits right in front ( $\phi = 0^\circ$ ) or right at the back ( $\phi = 180^\circ$ ) of the nanofiber with respect to the incident light beam, the directionality is zero. We can see four distinct regions of maximum directionality  $\mathcal{D}(\alpha, \phi)$ . The first two regions can be found in the range from  $0 < \alpha < 0.35$  the other two in the range from  $0.25 < \alpha < 0.7$ . We find four local maxima at  $\mathcal{D}(0.20, 120^\circ) = -0.995$ ,  $\mathcal{D}(0.20, 240^\circ) = 0.995$ ,  $\mathcal{D}(0.46, 77^\circ) = -0.986$  and  $\mathcal{D}(0.46, 283^\circ) = 0.986$  which show a strongly pronounced directionality.<sup>26</sup> The first two maxima correspond to a region, where the nanofiber-modified intensity of the incident light field is very low (see Fig. 5.8) leading to small

<sup>25</sup> At  $\alpha = 1/\sqrt{2}$  the excitation field is circularly polarized.

<sup>26</sup> The unity polarization vectors of the incident light field for the two values  $\alpha = 0.20$  and  $0.46$  are given by  $\hat{\mathbf{E}}_{\alpha=0.2} = (0, 0.2, 0.98i)$  and  $\hat{\mathbf{E}}_{\alpha=0.46} = (0, 0.46, 0.89i)$

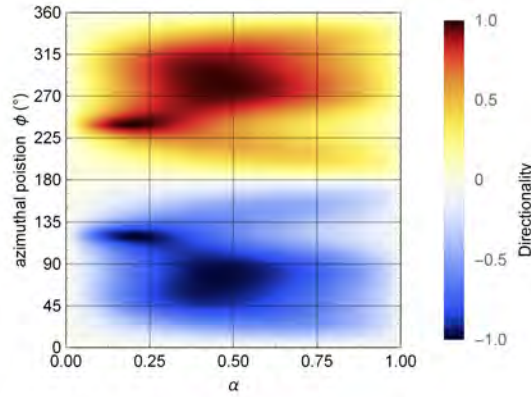


**Figure 5.23: Optimizing directionality.** Directionality as a function of the polarization of the incident light  $\alpha$  and the azimuthal position  $\phi$  of the nanosphere. The parameters used are the ones used in the measurements, i.e. a fiber diameter of  $2a = 315$  nm, a nanosphere diameter of  $2R = 90$  nm and an excitation wavelength  $\lambda = 532$  nm. The largest absolute directionality  $|\mathcal{D}| = 0.995$  can be found at  $(\alpha, \phi) = (0.20, 120^\circ)$  and  $(\alpha, \phi) = (0.20, 240^\circ)$ .

incoupling efficiencies.

It is important to note, that the illustrated behavior of the directionality does not significantly change, when fiber diameter and the radial nanoparticle position are changed. While the positions of maximum directionality slightly shift, the best values remain above  $|\mathcal{D}| > 0.99$ . In contrast to that, the incoupling efficiency depends largely on those two parameters. Although this effect was not studied in this thesis, it could also be interesting, in this context, to investigate the directional behaviour for the case, where the nanoparticle is embedded into the nanofiber.

The nanoparticle-nanofiber system is a suitable system to carry out proof of principle measurements. However, as a realistic device it is too fragile and too susceptible to dust. For realistic applications dielectric integrated surface waveguides are much better candidates. A possible realization is sketched in Fig. 5.24. In such a kind of setup, the excitation light field should be well mode matched to the nanoparticle which leads to higher incoupling efficiencies. Additionally, integrated waveguide structures are much more stable and scalable.

### 5.5.2 Polarization dependent backscattering and unidirectional waveguides

Instead of illuminating the nanoparticle with polarized light from *outside*, the nanoparticle can also be excited via a *guided* light field. Figure 5.25 shows the estimated transmitted and reflected power fractions for the situation, where a nanosphere (diameter,  $2R = 90$  nm), positioned on top of the nanofiber (diameter,  $2a = 315$  nm), is excited by quasi-linearly polarized guided light along  $\varphi_0$  (wavelength,  $\lambda = 532$  nm). As can be seen, the signal at both output ports can be tuned via the incident polarization. The shape of the curves depends on the intensity distributions of the quasi-linear polarization  $\varphi_0$  and the polarization overlap of this mode with the two orthogonal guided modes  $\mu_x$  and  $\mu_y$  at the position of the nanoparticle. For the reflected power, the intensity

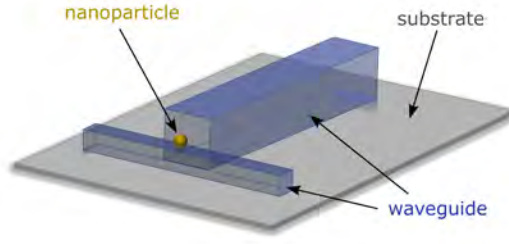


**Figure 5.24: Dielectric surface waveguide as a directional coupler.** Sketch of a possible directional coupling device of two dielectric surface waveguides interfaced by a gold nanoparticle.

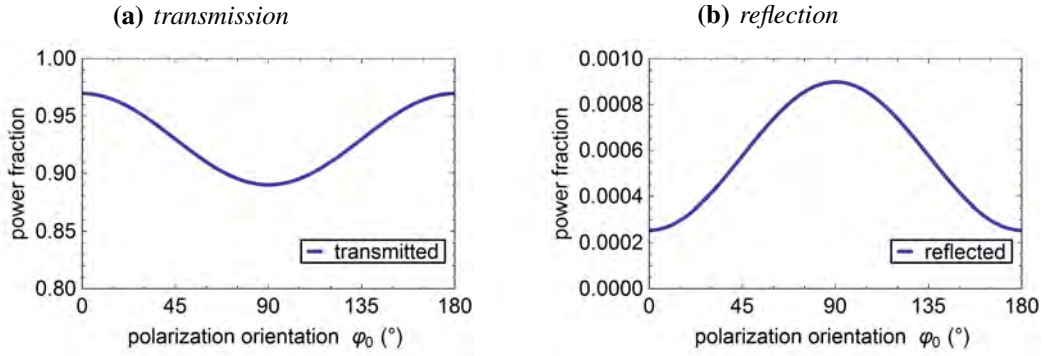


**Figure 5.25: Guided mode interaction.** Fraction of the total guided mode power, quasi-linearly polarized along  $\varphi_0$ , that is (a) transmitted and (b) reflected by the nanofiber-nanoparticle system.

distribution dominates the behavior.<sup>27</sup>

So far, in this chapter, we have only considered polarization maintaining scatterers. If, however, circular scatterers are used, a promising realization seems to be within reach. Here, the term circular scatterers refers to scatterers that have different scattering cross sections for left and right circular polarized light. Examples for such particles are appropriately prepared atoms as well as molecules or quantum dots [165]. In the simplified case, where the scattering cross section for one polarization is much larger than for the other, one of those circular scatterers on top of the nanofiber would already have a *polarization* overlap of more than 0.9 with the guided modes into one propagation direction and less than 0.1 into the other direction. Due to this large discrepancy in the overlaps, the absorbance along one propagation direction can be much larger than along the other. Now, in the case multiple circular scatterers it is possible to suppress the transmittance to almost zero in one direction, while it is still considerable into the other. Such a

<sup>27</sup> This unintuitive behavior stems from the fact that the polarization overlap of the dipole moment with the backward guided mode is four times larger than in free space.

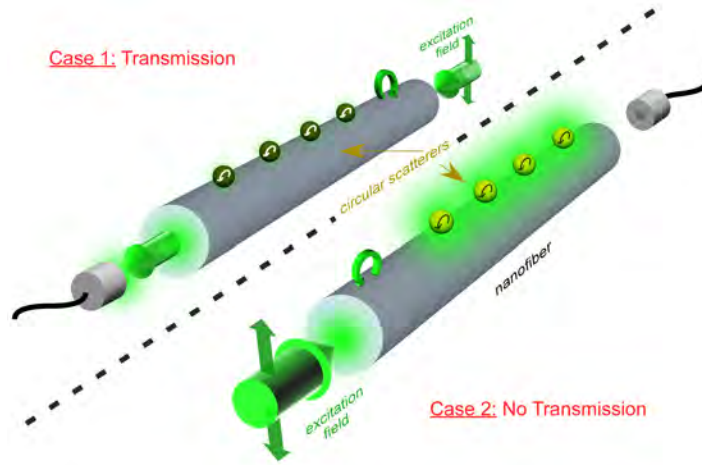


**Figure 5.26: Unidirectional waveguide.** Sketch of the two modes of operation of a unidirectional waveguide. Light, quasi-linearly polarized along  $\hat{y}$ , is sent through the fiber from right to left (case 1) and left to right (case 2). The polarization of the guided light on top of the fiber is denoted by a green, circular arrow on top of the fiber. In both cases, the circular scatterers absorb only light that circulates in counterclockwise direction, which is why a considerably fraction of the light power is transmitted in case 1 and most of the light is absorbed in case 2.

device is also referred to as an optical diode.<sup>28</sup> Figure 5.26 shows an illustration of the idea.

### 5.5.3 Sensing applications

The directional scattering into the waveguide can be exploited for optical sensing applications. In this thesis, it was demonstrated that an asymmetric contribution of  $\sigma^+$  and  $\sigma^-$  polarization in the light scattered by the nanoparticle translates into an unequal photon flux towards the two output ports of the nanofiber. Here, this asymmetry was caused by the elliptical polarization of the excitation beam which was scattered by a polarization-maintaining scatterer (the gold nanoparticle). If, however, the excitation light is linearly polarized, an unequal photon flux can only occur if the scatterer is asymmetric, i.e., if its scattering cross section differs for the two circular polarization components. The ratio of the photon fluxes in the two fiber output ports is thus a direct measure of this polarization asymmetry. This ratio can consequently be used for identifying or characterizing asymmetric scatterers.<sup>29</sup> A demonstration, where the directionality of the scattering depends on different internal states of laser cooled atoms can be found in [164].

<sup>28</sup> It is important to note, that on the bottom of the fiber the circulation is the other way around compared to on top of the fiber for the same propagation direction. Hence, the scatterers must only be situated on one side of the fiber to realize such a unidirectional waveguide.

<sup>29</sup> The appropriate alignment that is needed in order to utilize this effect can be obtained using e.g. a suitable magnetic field to orient the particles correctly.



## Summary and Outlook

This thesis can be divided into two experimental parts that investigated the realization of hybrid quantum architecture. In the first part, the goal was to combine the advantages of tapered optical fibers and trapped ions. Benjamin Ames, the PhD student working at the ion trap setup in Innsbruck, already managed to trap ions down to  $30\text{ }\mu\text{m}$  away from a bare tapered optical fiber (see Fig. 6.1). However, in order to further decrease the distance the tapered optical fiber has to be made electrically conductive up to a certain extent without losing its excellent optical

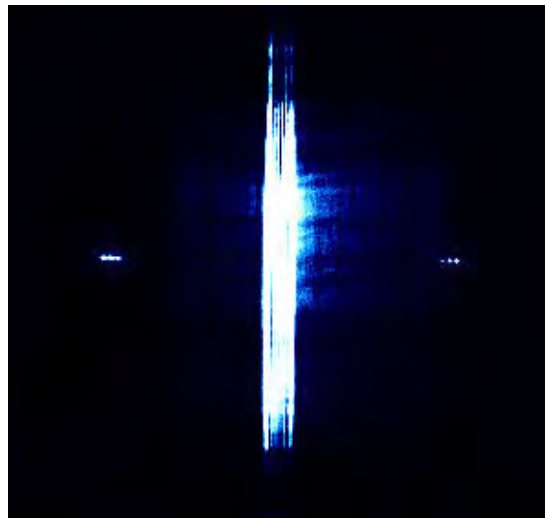


**Figure 6.1: Trapped ions in the vicinity of a tapered optical fiber.** A linear string of six  $^{40}\text{Ca}^+$ -ions split by the presence of a positively charged nanofiber. The ion-fiber separation in this picture is approximately  $150\text{ }\mu\text{m}$ , with the fiber being out of focus and about  $100\text{ }\mu\text{m}$  above the image plane of the ions. The light scattered by the fiber is from the laser beam used for imaging and cooling the  $^{40}\text{Ca}^+$ -ions. (The figure was kindly provided by Benjamin Ames, University of Innsbruck).

properties (i.e. high transmission and strong evanescent field). The technique that was chosen in this thesis to accomplish this goal was physical vapor deposition. Two different coating materials were investigated: silver and chromium. While silver as a deposition material did not yield satisfying results, chromium coating of nanofibers seems to be a promising approach. The chromium coated tapered optical fiber had a resistance significantly below the threshold required to keep it practically charge free. At the same time, still a residual optical transmission through the fiber has been observed.

For their implementations in a realistic experimental setup, however, the transmittance has to be increased which could be realized in different ways: Firstly, in order to have more control over the coating process, the physical vapor deposition setup could be optimized. This way the percolation thickness of the thin coated film should be reducible leading to an increase of the film's transmittance for the same electric properties. Secondly, and more importantly, shortening the the waist section of the tapered optical fiber will increase both the conductance and the transmittance significantly. As the intensity of the guided light that propagates inside the coating reduces exponentially along the thin conductive film, a waist length reduction from 10 mm to 1 mm should already raise the transmittance by at least two orders of magnitude. Additionally, if the fiber pulling process is modified in a way that smaller flame widths than 1 mm are possible, a sharper increase of the fiber radius from the waist to the taper section can be realized. This significantly lowers the losses in the taper section and thus allows for much higher transmissions. Including this optimization, transmittances exceeding a few ten percent with simultaneous electric resistances around  $10^6 \Omega$ , seem to be realistic. As a consequence, the ion trap setup has to be significantly modified to be compatible with shorter fiber waists. Furthermore, chromium oxidizes in ambient conditions. Therefore extraction, transport and integration of the tapered optical fiber will have to be performed in oxygen free conditions. Alternatively, other coating materials that are not prone to oxidization could be used or the coating setup could be included into the vacuum chamber of the ion trap.

In the second part of this thesis, the interaction of individual plasmonic nanoparticles with the evanescent field of the nanofiber was studied: Due to its strong lateral confinement, the guided light field is highly non-paraxial and strong longitudinal electric field components occur. As a consequence, the light can exhibit a local spin that is orthogonal to the propagation direction. Remarkably, this spin changes sign when the propagation direction of the light is reversed. This chiral character of the light has important consequences for the interaction of confined light with matter and has the potential to enable new key devices in an all-optical infrastructure. As a first step towards such devices, this thesis studied the realization of a chiral directional coupler for light, where a single nanoparticle directs an incident field to one or the other output port of the fiber. For this purpose, a method was developed that allows one to deposit individual nanoparticles on a sub-wavelength diameter fiber. Using a pipette, a droplet of gold nanoparticles dispersed in deionized water, was lowered onto the waist section of a tapered optical fiber. In a statistical process, that can be influenced via the nanoparticle density in the droplet and the time nanofiber and droplet touch each other, nanoparticles settle on the nanofiber surface. After the droplet is moved away from the fiber, a clearly measurable increase in the fiber's absorbance can be seen if the deposition was successful. By repeating this process until an increase of ab-



---

sorbance is observed a controlled deposition of individual nanoparticles with a probability of success of close to one is achieved. The positioning accuracy along the nanofiber is currently around 100  $\mu\text{m}$  which could be improved using a smaller pipette tip.

With this technique, we deposit a single nanoparticle on the fiber and make use of the chiral nature of light-matter interaction in the evanescent field of the fiber to realize a directional coupler for light. By illuminating a deposited gold nanoparticle with an external light field, the directionality of the scattering into the fiber could be controlled with the polarization of the incident light. With this setup, up to 94 % of the incoupled light was directed into one or the other direction of the fiber.

In order to turn this proof-of-principle experiment into a miniaturized integrated optical component for commercial devices, chip-based lithographically fabricated waveguides and embedded nanoparticles could be used. In such a setup, the excitation field could be provided by one of those waveguides leading to several orders of magnitude higher incoupling efficiencies than in the demonstrated experiment. Additionally, the efficiency could be further enhanced by increasing the nanoparticle size or number. More advanced techniques in this regard could involve the use of several nanoparticles that are positioned at Bragg condition along the waveguide [166] or using a running wave waveguide-resonator such as, e.g. a whispering gallery-mode resonator, instead of a conventional waveguide [42].

The directional coupler for light is the first demonstration of a novel class of nanophotonic devices that are based on the effect of chiral light-matter interaction. Another possible application involves polarization dependent scatterers whose scattering cross section for right circularly polarized light is different than for left circularly polarized light. This would lead to a nonreciprocal transmission in these structures which directly provides an optical diode where isolation and forward transmission can be adjusted via the number of absorbers coupled to the waveguide. This can for example be realized by coupling atoms or molecules to the evanescent field of the nanofiber [164], where their internal spin leads to the required asymmetry in the scattering rates. For further miniaturized devices, these scatterers could be replaced by plasmonic structures that are subject to a static magnetic field or an external time modulation of their electrical properties.

Ultimately, this work demonstrates the powerful nature of nanofibers when used in conjunction with plasmonic nanoparticles. Devices based on the results of this thesis could be a part of future integrated optical devices and have the potential to replace integrated electronic components. This would potentially path the way towards an all-optical architecture for computing and further advance information processing beyond its current limitations.



# Appendix

## A.1 A nanofiber-based ion trap using a metal nanoparticle and difference frequency generation

In the course of this thesis, an alternative scheme using a nanoparticle-nanofiber system was investigated that could potentially trap ions in close vicinity of the nanofiber surface in order to realize strong light-matter coupling:

Due to the Gaussian law, it is not possible to confine charged particles in three dimensions with electrostatic fields. That is why, for example in the case of the Paul trap, a time modulated electric quadrupole field in addition to a static electric field is employed to realize a stable trapping potential [8, 9, 103]. Following this general principle, one can consider an alternative trapping scheme where a spherical metal nanoparticle is used as a point-like trapping electrode for the generation of a time modulated dipole field. Figure A.1 sketches the two ingredients that have to be combined in order to realize such an ion trap: An oscillating dipole near-field  $\mathbf{E}_{\text{dip}}$  emitted by the nanoparticle and a superposed homogeneous electric field  $\mathbf{E}_{\text{hom}}$  that is oscillating  $\pi$  out of phase to it. More specifically, if the homogeneous field points along the axis of the oscillating dipole an electric field minimum can be realized in the near-field of the dipole (see Eq. (3.17)). In Fig. A.2a and b the resulting fields are shown for the case of a dipole moment of  $\mathbf{d} = d\hat{\mathbf{z}} = 4.5 \times 10^{-23} \text{ C m}$  and a homogeneous field of  $E_{\text{hom}} = E_{\text{hom}}\hat{\mathbf{z}} \simeq 0.8 \text{ MV/m}$ . The fields are cylindrically symmetric and shown for two points in time, i.e.  $\omega t = 0$  (blue) and  $\omega t = \pi$  (red).

The motion of a charged particle of mass  $m$  that is subject to the force  $\mathbf{F} = q\mathbf{E}$  of a field  $\mathbf{E} = \mathbf{E}_0 \sin(\omega t)$  oscillating with high frequency can be described by a time independent pseudopotential [167, 168]

$$U = \frac{q^2 E_0^2}{4 m \omega^2}, \quad (\text{A.1})$$

where  $q$  is the charge of the particle and  $\omega$  the oscillation frequency. It can be seen, that the pseudopotential is independent of the sign of the charge  $q$  and accordingly, that every charged

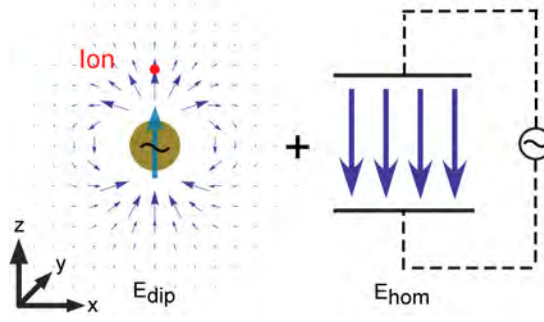


**Figure A.1: Nanoparticle-based ion trap: Schematic.** *Left side: Schematic illustration of a trapping scheme based on a metal nanoparticle. The nanoparticle (dark yellow) is excited such that its dipole moment (shown as a green arrow) oscillates along  $\hat{z}$ . A potentially trapped ion (red) is shown on top of the nanoparticle. The blue arrows depict the electric dipole field  $\mathbf{E}_{\text{dip}}$  at a fixed point in time. Right side: Homogeneous field  $\mathbf{E}_{\text{hom}} = E_{\text{hom}}\hat{z}$  that oscillates  $\pi$  out of phase to the dipole field and that is superposed on it.*

particle is a so-called low-field seeker. In Fig. A.2c we see, that the pseudopotential for a  $^{40}\text{Ca}^+$ -ion ( $m_{\text{Ca}} = 40 \text{ u}$ ) has a trap depth of  $U = 1 \text{ eV}$  for the same values as in panels (a) and (b) and an oscillation frequency of  $\omega = 2\pi 100 \text{ MHz}$ .

Concerning the realization of such an ion trap, the homogeneous field can be provided by applying a high oscillating voltage to two appropriately spaced metal plates in between which the nanoparticle would have to be placed. The oscillating dipole field of the nanoparticle, on the other hand, could in principle be optically induced via difference frequency generation. Indeed, as pointed out by several groups [169–173], beyond dipole approximation, second order nonlinearities can be excited at spherical nanoparticles that in turn would lead to a dipolar emission pattern. A potential realization of a radio frequency dipole field emitted by a spherical nanoparticle can be seen in Fig. A.3. Here, two guided light fields  $\mathbf{E}_i = \mathbf{E}_{0,i} \exp(i[-\omega_i t + k_i z])$  ( $i = 1, 2$ ) are sent through the tapered optical fiber. Because they are detuned by  $\Delta$  with respect to each other they generate a difference frequency dipole field  $\mathbf{E}_{\text{dip}}$  at the spherical nanoparticle that oscillates at a frequency of  $\omega = 2\pi \Delta$ .<sup>1</sup>

In order to estimate the size of the dipole moment  $d_{\text{DFG}}$  generated by difference frequency

<sup>1</sup>In practice, the detuning between the two excitation light fields can, e.g., be provided by an acousto-optic modulator. The local oscillator providing the detuning frequency can also be used as a frequency reference for the oscillating homogeneous field in order to realize a  $\pi$  phase shift between the two fields  $\mathbf{E}_{\text{dip}}$  and  $\mathbf{E}_{\text{hom}}$ .

A.1. A nanofiber-based ion trap using a metal nanoparticle and difference frequency generation

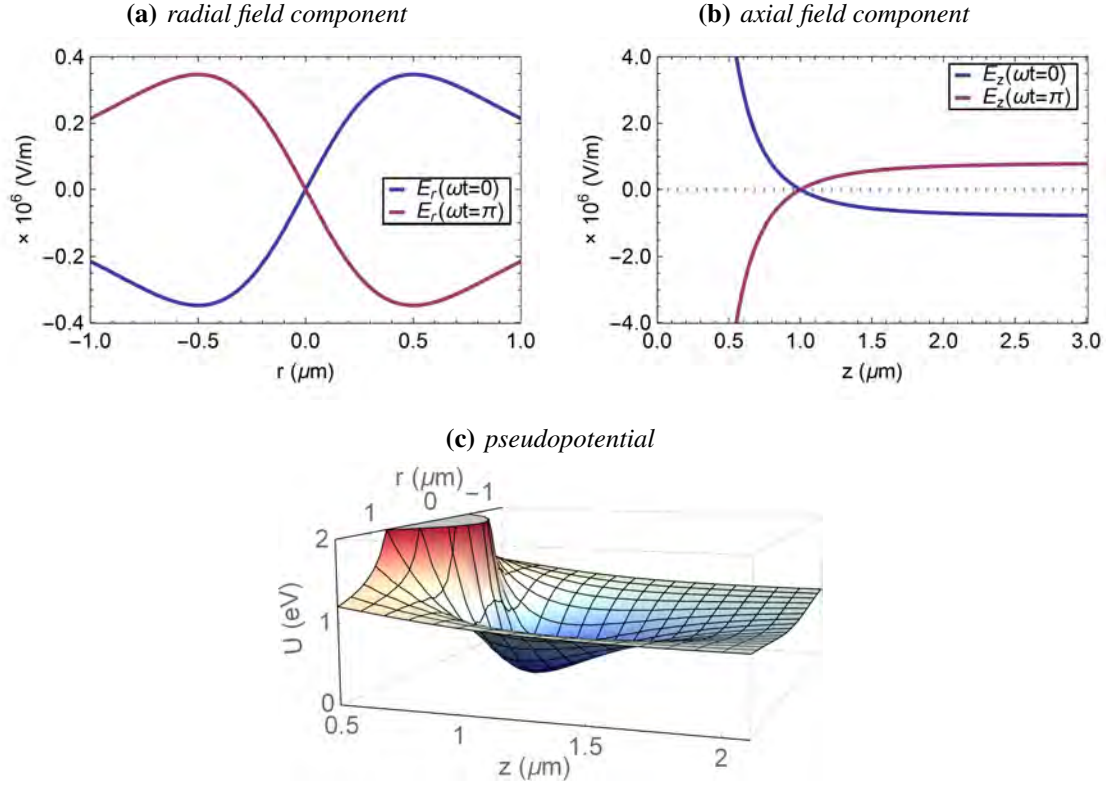


**Figure A.2: Nanoparticle-based ion trap: Fields and potential.** Electric field components along the (a) radial and (b) axial direction for a nanoparticle-generated dipole near-field that is superposed on a homogeneous electric field along the dipole axis. Both fields oscillate  $\pi$  out of phase with respect to each other and interfere destructively at one point in space  $((r, z) = (0, 1 \mu\text{m}))$ . The panels show the situations for  $\omega t = 0$  (blue) and  $\omega t = \pi$  (red). The dipole moment of the nanoparticle is  $\mathbf{d} = d\hat{z} = 4.5 \times 10^{-23} \text{ C m}$  and the strength of the homogeneous field is  $\mathbf{E}_{\text{hom}} = E_{\text{hom}}\hat{z} \simeq 0.8 \text{ MV/m}$ . (c) Pseudopotential for a  $^{40}\text{Ca}^+$ -ion. For the values used in (a) and (b) we find a trap depth of  $0.8 \text{ eV}$ .

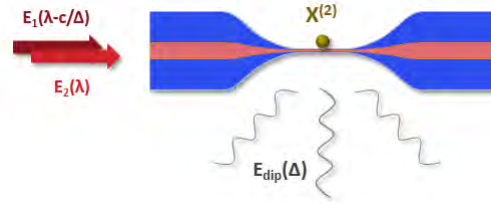


**Figure A.3: Nanoparticle-based ion trap: Difference frequency generation.** Potential setup in order to generate a radio frequency dipole field via difference frequency generation. The difference frequency is generated by sending two guided light fields through a tapered optical nanofiber that are detuned by  $\Delta$ . The nanoparticle is deposited on the waist section of the fiber and radiates a dipole field  $\mathbf{E}_{\text{dip}}$  at the difference frequency  $\omega = 2\pi \Delta$  due to its nonlinear susceptibility  $\chi_s^{(2)}$ .

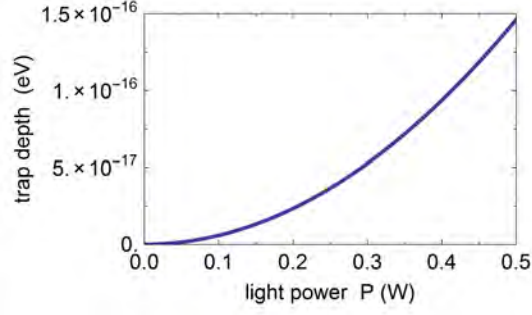


**Figure A.4: Nanoparticle-based ion trap: trap depth.** Potential trap depth  $1 \mu\text{m}$  away from the nanoparticle as a function of the power of each excitation beam.

generation we consult the results in [169–173] and adjust them to the case at hand. We find that<sup>2</sup>

$$\begin{aligned}
 d_{\text{DFG}} &= d_0 \left[ (\hat{e} \cdot \hat{e}) \hat{k} - \kappa (\hat{n} \cdot \hat{e}) \hat{e} \right], \\
 d_0 &= \frac{4\pi \hbar}{15 c} (\omega_1 + \omega_2) R^3 E_1 E_2 \chi_1, \\
 \kappa &= \frac{2 \chi_2}{\chi_1},
 \end{aligned} \tag{A.2}$$

where  $\hat{e} = \hat{e}_1 = \hat{e}_2$  is the unit polarization vector of the excitation fields,  $\hat{k} = \hat{k}_1 \simeq \hat{k}_2$  is the unit wave vector of the excitation fields and  $\hat{n}$  denotes the direction of the scattered light. Note that the formulas are given in Gaussian units.  $\kappa$  is a measure for the quadrupole contribution to the dipole field. In addition, we have introduced the notations

$$\begin{aligned}
 \chi_1 &= \chi_{\perp\perp\perp}^s + \chi_{\perp\parallel\parallel} - 2\chi_{\parallel\perp\parallel} + 5\gamma, \\
 \chi_2 &= \chi_{\perp\perp\perp}^s - \chi_{\perp\parallel\parallel} + 3\chi_{\parallel\perp\parallel}.
 \end{aligned} \tag{A.3}$$

The formulas for the elements  $\chi_{\perp\perp\perp}^s$ ,  $\chi_{\perp\parallel\parallel}$  and  $\chi_{\parallel\perp\parallel}$  of the nonlinear susceptibility tensor  $\chi_s^{\leftrightarrow(2)}$  as well as for  $\gamma$  can be found in [170, 171].

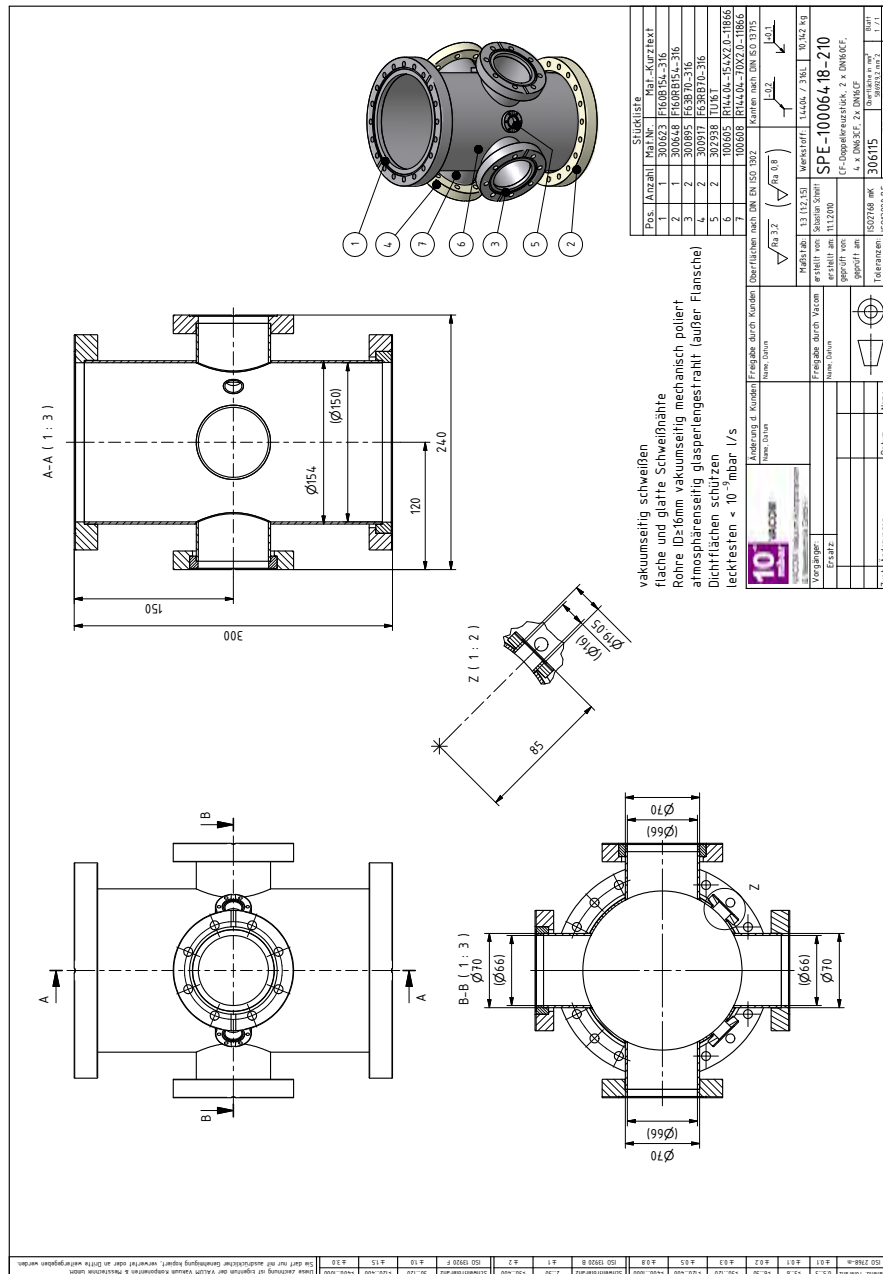
Assuming two 100 mW guided light fields and a nanofiber radius that is optimized to the used wavelength in order to maximize the intensity at the position of the spherical gold nanoparticle ( $R = 40 \text{ nm}$ ), this yields a dipole amplitude of  $d_0 \approx 10^{-32} \text{ C m}$ . As can be seen in Fig. A.4, even for higher optical powers the trap depth is unfortunately far too low to realize an ion trap.<sup>3</sup> Alternative realizations in order to realize a higher dipole moment could be to induce it linearly via external electric fields [174] or by using different plasmonic shapes and materials [175].

---

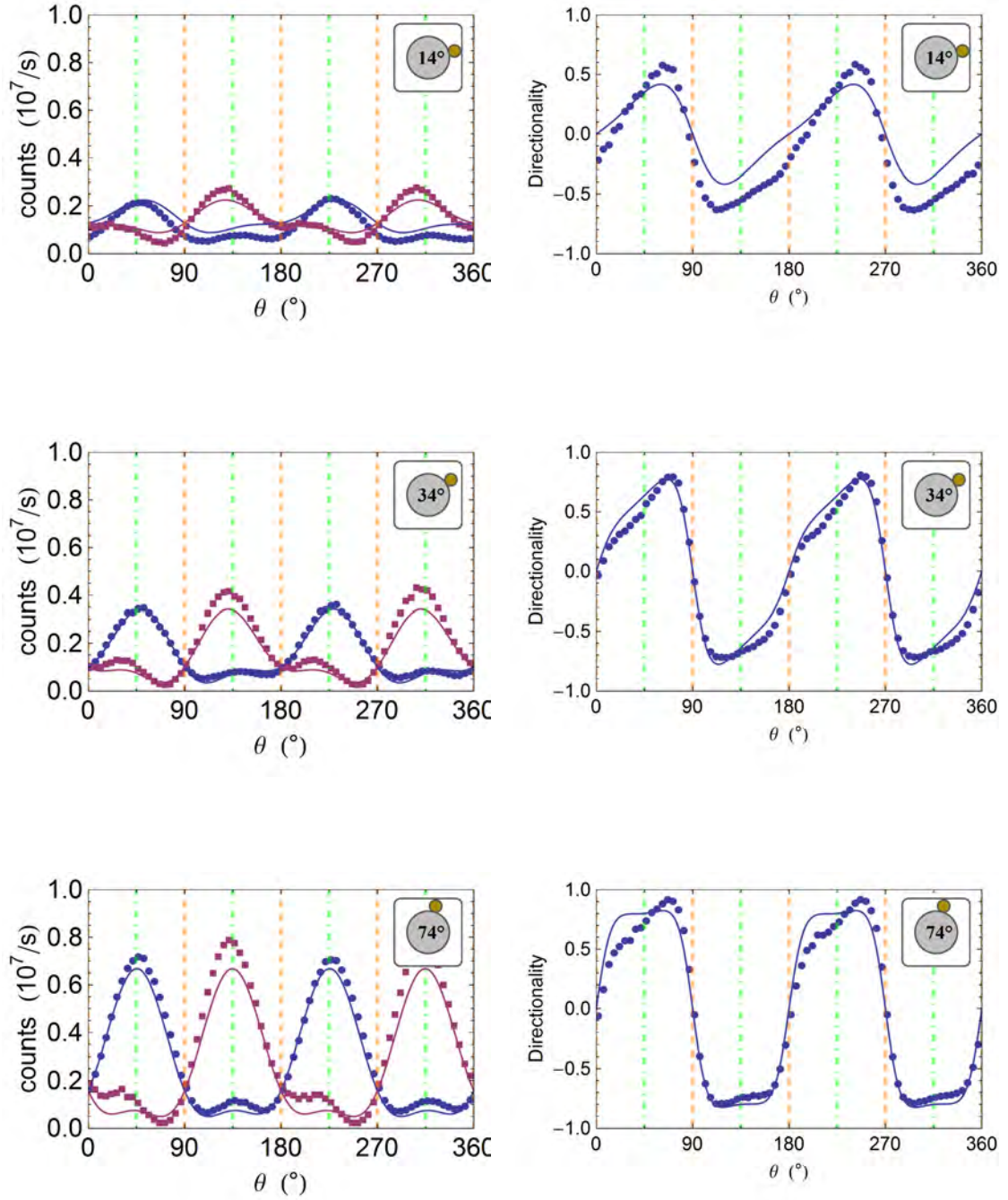
<sup>2</sup>The formulas are kindly provided by Pham Le Kien.

<sup>3</sup> The fact that the nonlinear dipole moment is very small could be confirmed by experiments that were performed during this thesis in order to detect a potential second harmonic generation, another second order nonlinear effect, at a spherical nanoparticle.

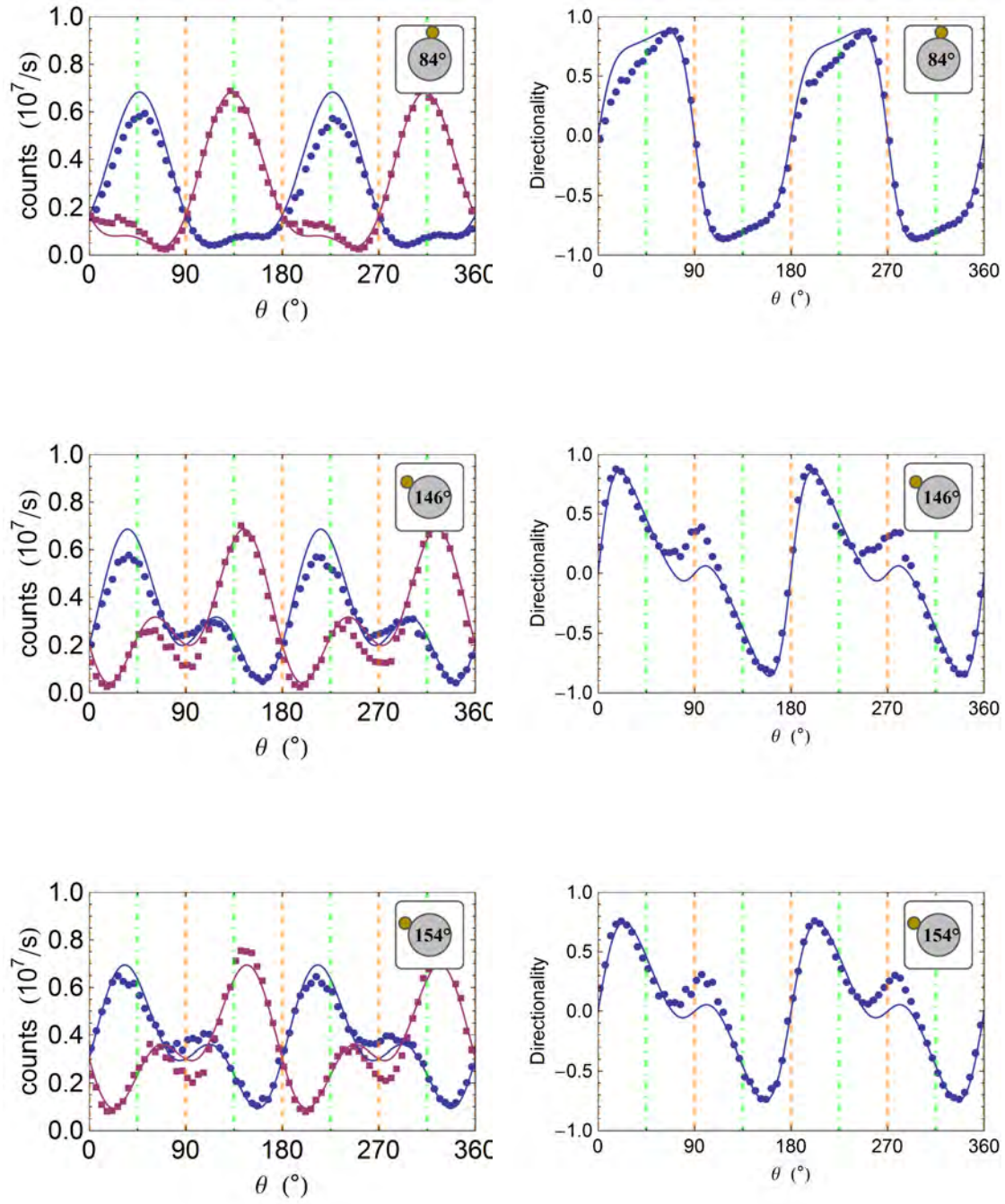
## A.2 Blue print of the PVD vacuum chamber

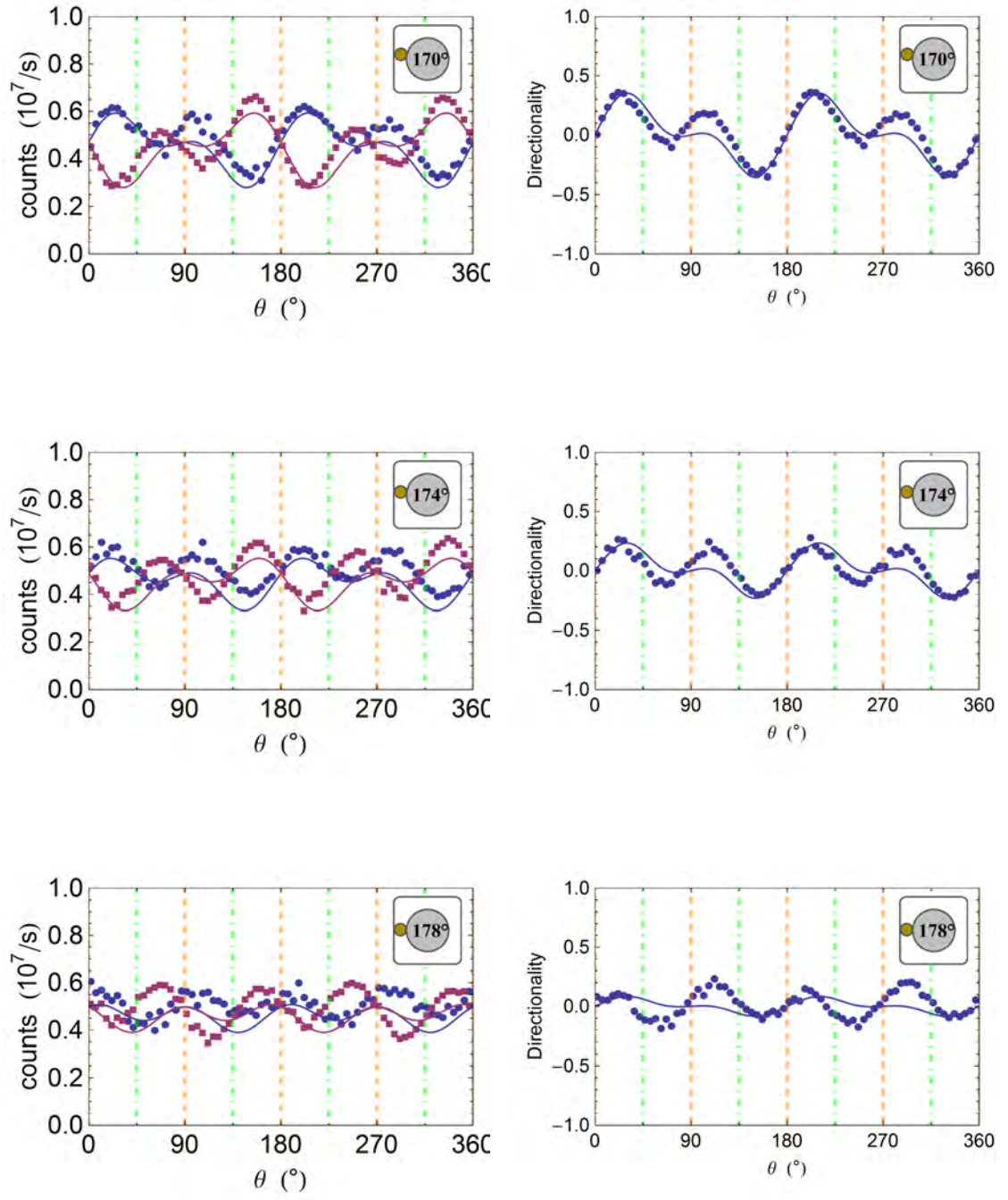


### A.3 A chiral nanophotonic waveguide coupler - Full set of measured datapoints

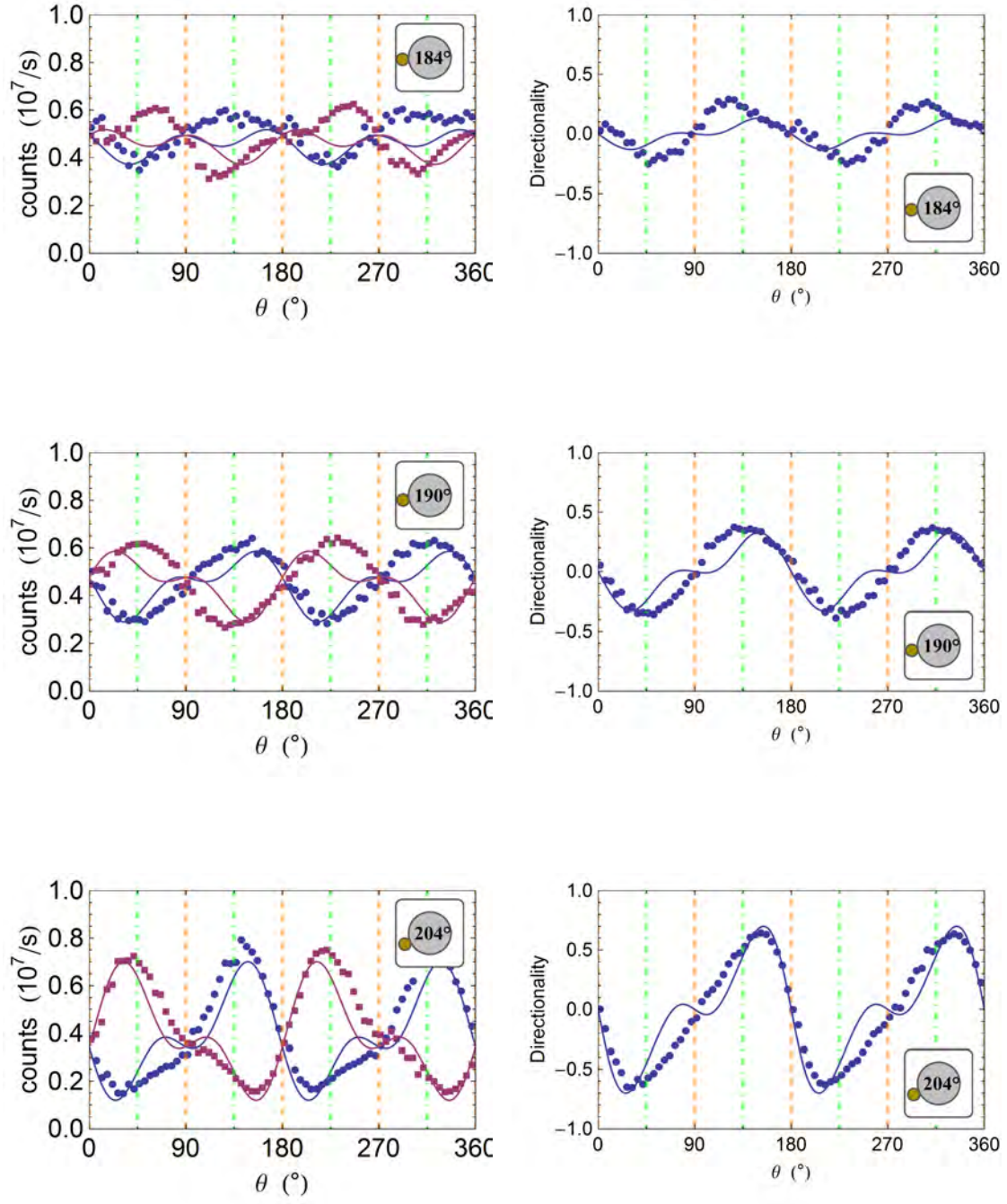




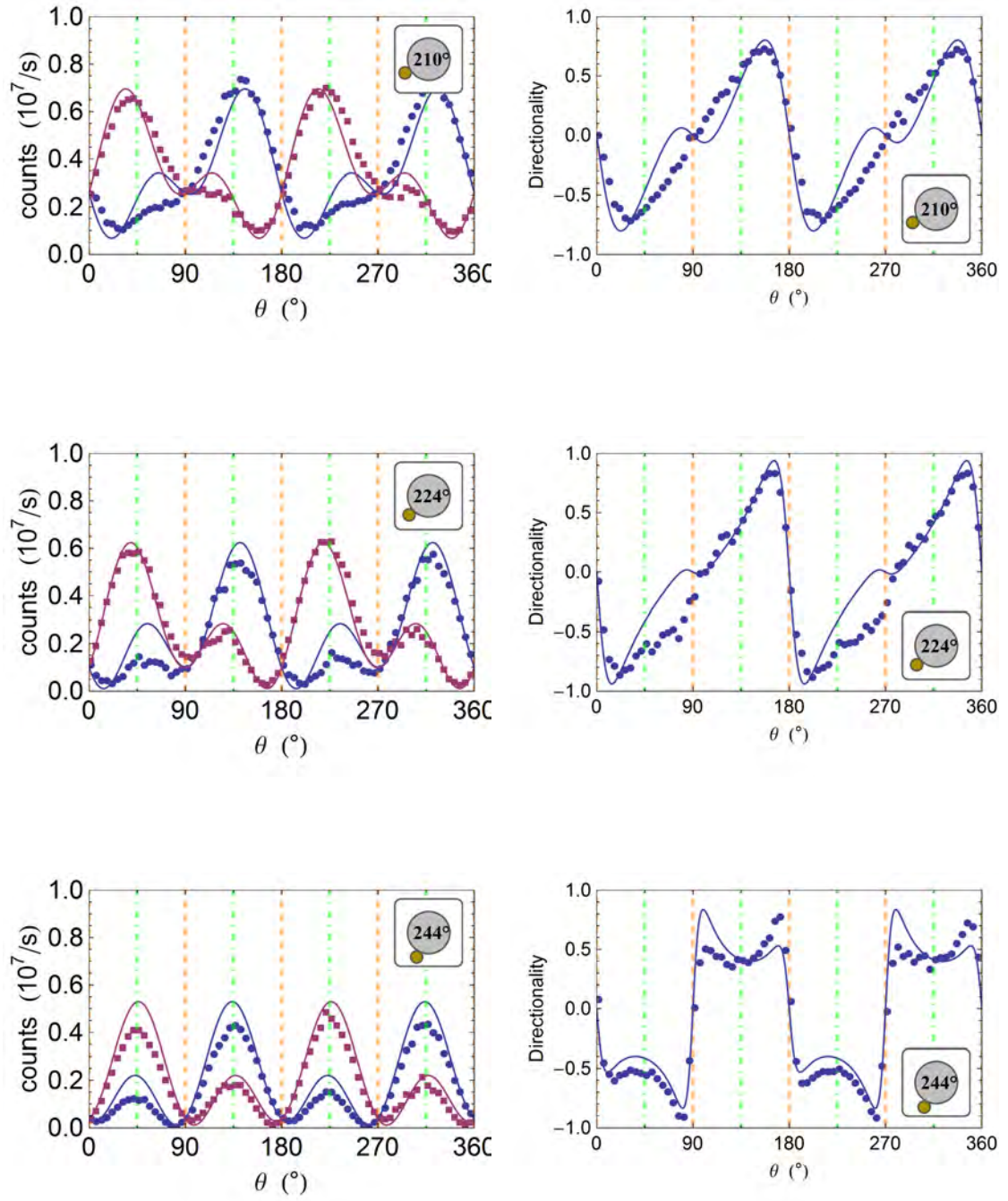




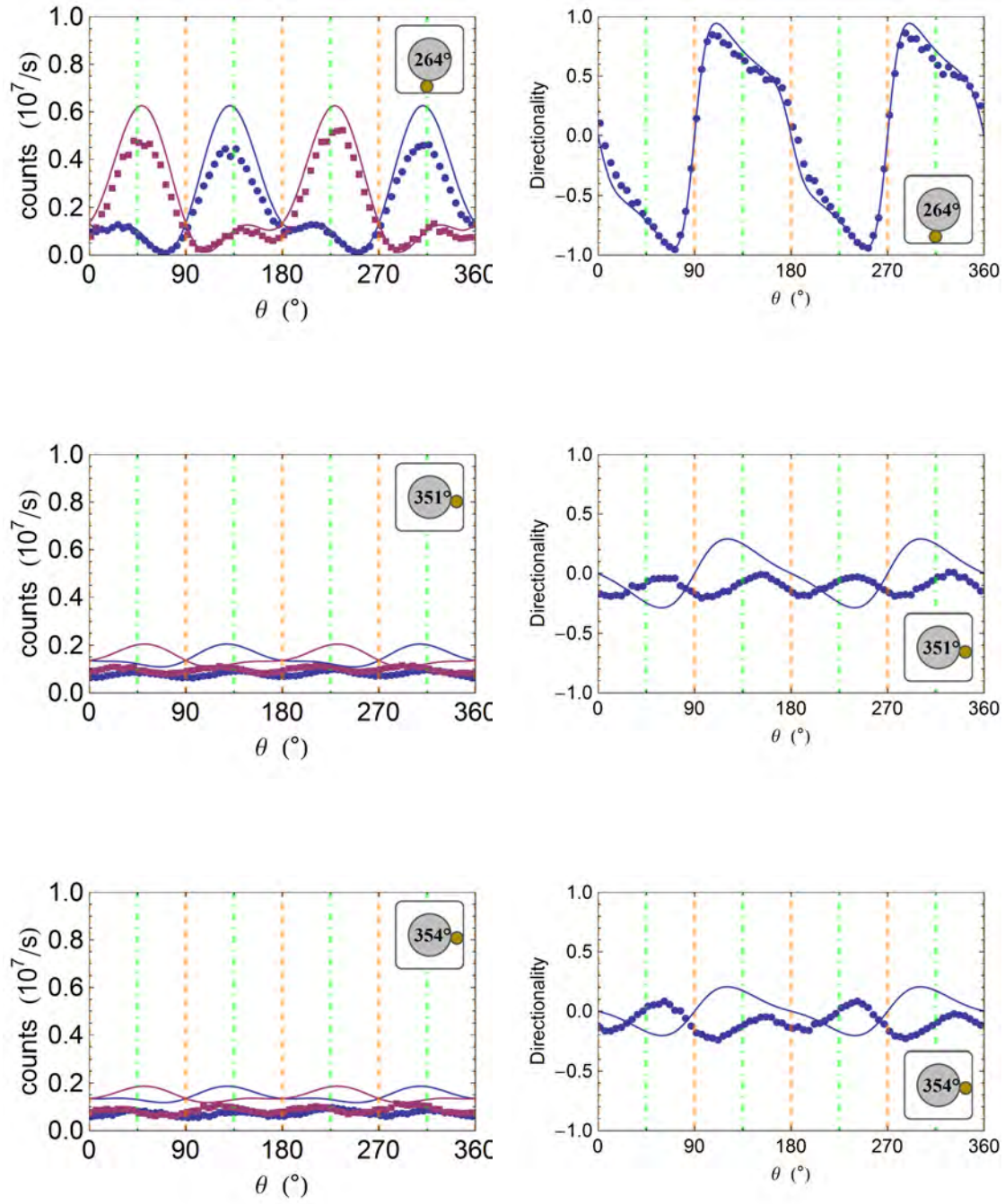
### A.3. A chiral nanophotonic waveguide coupler - Full set of measured datapoints







### A.3. A chiral nanophotonic waveguide coupler - Full set of measured datapoints



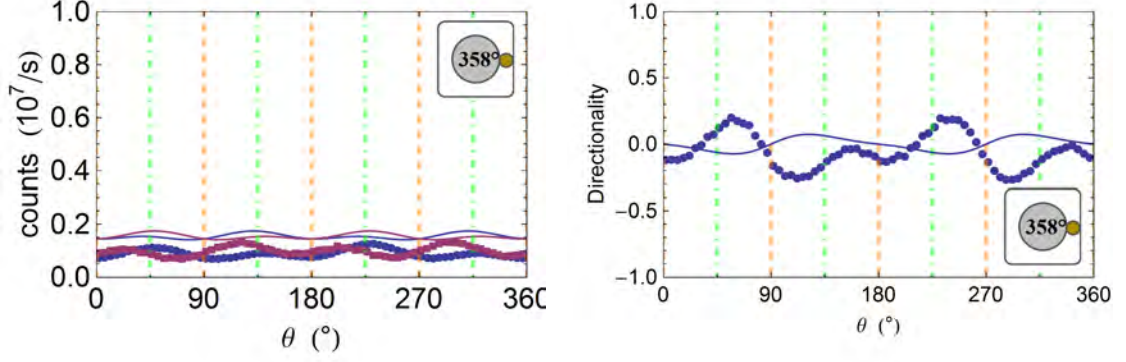


**Figure A.5: Photon flux and directionality – full dataset.** *Left column:* Measured photon fluxes at the left (blue circles) and right (red squares) fiber output port as a function of the angle  $\theta$  of the quarter-wave plate. Here,  $\theta = 0^\circ, 90^\circ, \dots$  corresponds to linear polarization along  $\hat{z}$  (dashed orange lines) and  $\theta = 45^\circ, 225^\circ$  ( $\theta = 135^\circ, 315^\circ$ ) corresponds to  $\sigma^-$  ( $\sigma^+$ ) polarization of the incident light field (dash-dotted green lines). The insets indicate the azimuthal position  $\phi$  of the nanoparticle (green dot) around the fiber (gray disk). The solid lines are the predictions of our theoretical model. The statistical error bars are too small to be visible in the plot. *Right column:* Directionality  $\mathcal{D}$  of the scattering process into the fiber for the data shown in the left column.

# Bibliography

- [1] G. E. Moore. Cramming more components onto integrated circuits. *Electronics*, 38(8):114–117, 1965.
- [2] P. Benioff. Quantum mechanical hamiltonian models of turing machines. *Journal of Statistical Physics*, 29(3):515–546, 1982.
- [3] R. P. Feynman. Simulating physics with computers. *International Journal of Theoretical Physics*, 21(6-7):467–488, 1982.
- [4] R. P. Feynman. Quantum mechanical computers. *Foundations of Physics*, 16(6):507–531, 1986.
- [5] D. P. DiVincenzo. Two-bit gates are universal for quantum computation. *Phys. Rev. A*, 51:1015–1022, Feb 1995.
- [6] P. W. Shor. Algorithms for quantum computation: discrete logarithms and factoring. In *Foundations of Computer Science, 1994 Proceedings., 35th Annual Symposium on*, pages 124–134, Nov 1994.
- [7] L.p K. Grover. Quantum mechanics helps in searching for a needle in a haystack. *Phys. Rev. Lett.*, 79:325–328, Jul 1997.
- [8] W. Paul and H. Steinwedel. Ein neues Massenspektrometer ohne Magnetfeld. *Zeitschrift für Naturforschung A*, 8(7):448–450, 1953.
- [9] W. Paul and H. Steinwedel. Verfahren zur trennung bzw. zum getrennten nachweis von ionen verschiedener spezifischer ladung, June 28 1956. DE Patent 944,900.
- [10] J. Cirac and P. Zoller. Quantum computations with cold trapped ions. *Phys. Rev. Lett.*, 74:4091–4094, May 1995.
- [11] C. Monroe, D. M. Meekhof, B. E. King, W. M. Itano, and D. J. Wineland. Demonstration of a fundamental quantum logic gate. *Phys. Rev. Lett.*, 75:4714–4717, Dec 1995.
- [12] A. Sørensen and K. Mølmer. Quantum computation with ions in thermal motion. *Phys. Rev. Lett.*, 82:1971–1974, Mar 1999.

- [13] J. Benhelm, G. Kirchmair, C. F. Roos, and R. Blatt. Towards fault-tolerant quantum computing with trapped ions. *Nature Physics*, 4:463–466, April 2008.
- [14] T. E. Northup and R. Blatt. Quantum information transfer using photons. *Nature Photonics*, 8(5):356–363, 2014.
- [15] L. Tong, R. R. Gattass, J. B. Ashcom, S. He, J. Lou, M. Shen, I. Maxwell, and E. Mazur. Subwavelength-diameter silica wires for low-loss optical wave guiding. *Nature*, 426(6968):816–819, 2003.
- [16] K. P. Nayak, P. N. Melentiev, M. Morinaga, Fam Le Kien, V. I. Balykin, and K. Hakuta. Optical nanofiber as an efficient tool for manipulating and probing atomicfluorescence. *Opt. Express*, 15(9):5431–5438, Apr 2007.
- [17] G. Sagué, E. Vetsch, W. Alt, D. Meschede, and A. Rauschenbeutel. Cold-atom physics using ultrathin optical fibers: Light-induced dipole forces and surface interactions. *Phys. Rev. Lett.*, 99:163602, Oct 2007.
- [18] Fam Le Kien, J.Q. Liang, K. Hakuta, and V.I. Balykin. Field intensity distributions and polarization orientations in a vacuum-clad subwavelength-diameter optical fiber. *Optics Communications*, 242(4-6):445 – 455, 2004.
- [19] E. Vetsch, D. Reitz, G. Sagué, R. Schmidt, S. T. Dawkins, and A. Rauschenbeutel. Optical interface created by laser-cooled atoms trapped in the evanescent field surrounding an optical nanofiber. *Phys. Rev. Lett.*, 104(20):203603, May 2010.
- [20] A. Stiebeiner, O. Rehband, R. Garcia-Fernandez, and A. Rauschenbeutel. Ultra-sensitive fluorescence spectroscopy of isolated surface-adsorbed molecules using an optical nanofiber. *Opt. Express*, 17(24):21704–21711, Nov 2009.
- [21] L. Liebermeister, F. Petersen, A. v. Münchow, D. Burchardt, J. Hermelbracht, T. Tashima, A. W. Schell, O. Benson, Th. Meinhardt, A. Krueger, A. Stiebeiner, A. Rauschenbeutel, H. Weinfurter, and M. Weber. Tapered fiber coupling of single photons emitted by a deterministically positioned single nitrogen vacancy center. *Applied Physics Letters*, 104(3):–, 2014.
- [22] R. Yalla, K. P. Nayak, and K. Hakuta. Fluorescence photon measurements from single quantum dots on an optical nanofiber. *Opt. Express*, 20(3):2932–2941, Jan 2012.
- [23] M. Harlander, M. Brownnutt, W. Hänsel, and R. Blatt. Trapped-ion probing of light-induced charging effects on dielectrics. *New Journal of Physics*, 12(9):093035, 2010.
- [24] [www-03.ibm.com/press/us/en/pressrelease/39641.wss](http://www-03.ibm.com/press/us/en/pressrelease/39641.wss), December 2012. Accessed 2015-02-01.
- [25] Y. A. Vlasov and W. Haensch. Integrated nanophotonics technology for optical interconnects. In *Frontiers in Optics 2014*, page FM4A.1. Optical Society of America, 2014.



- 
- [26] J. Barhen, C. Kotas, T. S. Humble, P. Mitra, N. Imam, M. A. Buckner, and M. R. Moore. High performance fft on multicore processors. In *Cognitive Radio Oriented Wireless Networks & Communications*, Cognitive Radio Oriented Wireless Networks & Communications (CROWNCOM), pages 1–6, Aug 2010.
- [27] W. Chen, K. M. Beck, R. Bücke, M. Gullans, M. D. Lukin, H. Tanji-Suzuki, and V. Vuletić. All-optical switch and transistor gated by one stored photon. *Science*, 341(6147):768–770, 2013.
- [28] Lucas Novotny and Bert Hecht. *Principles of Nano-Optics*. Cambridge University Press, 2006.
- [29] M. Onoda, S. Murakami, and N. Nagaosa. Hall effect of light. *Phys. Rev. Lett.*, 93:083901, Aug 2004.
- [30] Andrews David and Mohamed Babiker. *The Angular Momentum of Light*. Cambridge University Press, 2012.
- [31] K. Y. Bliokh and F. Nori. Transverse spin of a surface polariton. *Phys. Rev. A*, 85:061801, Jun 2012.
- [32] K. Y. Bliokh, A. Y. Bekshaev, and F. Nori. Extraordinary momentum and spin in evanescent waves. *Nat Commun*, 5:–, March 2014.
- [33] Y. Zhao, J. S. Edgar, G. Jeffries, D. McGloin, and D. T. Chiu. Spin-to-orbital angular momentum conversion in a strongly focused optical beam. *Phys. Rev. Lett.*, 99:073901, Aug 2007.
- [34] J. Korger, A. Aiello, V. Chille, P. Banzer, Ch. Wittmann, N. Lindlein, Ch. Marquardt, and G. Leuchs. Observation of the geometric spin hall effect of light. *Phys. Rev. Lett.*, 112:113902, Mar 2014.
- [35] O. Hosten and P. Kwiat. Observation of the spin hall effect of light via weak measurements. *Science*, 319(5864):787–790, 2008.
- [36] K. Y. Bliokh, A. Niv, V. Kleiner, and E. Hasman. Geometrodynamics of spinning light. *Nat Photon*, 2(12):748–753, December 2008.
- [37] K. Y. Bliokh, Y. Gorodetski, V. Kleiner, and E. Hasman. Coriolis effect in optics: Unified geometric phase and spin-hall effect. *Phys. Rev. Lett.*, 101:030404, Jul 2008.
- [38] Francisco J. Rodríguez-Fortuño, Giuseppe Marino, Pavel Ginzburg, Daniel O’Connor, Alejandro Martínez, Gregory A. Wurtz, and Anatoly V. Zayats. Near-field interference for the unidirectional excitation of electromagnetic guided modes. *Science*, 340(6130):328–330, 2013.
- [39] J. Lin, J. P. Balthasar Mueller, Q. Wang, G. Yuan, N. Antoniou, X.-C. Yuan, and F. Capasso. Polarization-controlled tunable directional coupling of surface plasmon polaritons. *Science*, 340(6130):331–334, 2013.

- [40] D. O'Connor, P. Ginzburg, F. J. Rodríguez-Fortuño, G. A. Wurtz, and A. V. Zayats. Spin-orbit coupling in surface plasmon scattering by nanostructures. *Nature Communications*, 5, 2014.
- [41] P. V. Kapitanova, P. Ginzburg, F. J. Rodríguez-Fortuno, D. S. Filonov, P. M. Voroshilov, P. A. Belov, A. N. Poddubny, Y. S. Kivshar, G. A. Wurtz, and A. V. Zayats. Photonic spin hall effect in hyperbolic metamaterials for polarization-controlled routing of subwavelength modes. *Nat Commun*, 5:–, February 2014.
- [42] Ch. Junge, D. O'Shea, J. Volz, and A. Rauschenbeutel. Strong coupling between single atoms and nontransversal photons. *Phys. Rev. Lett.*, 110:213604, May 2013.
- [43] I. Söllner, S. Mahmoodian, A. Javadi, and P. Lodahl. A chiral spin-photon interface for scalable on-chip quantum-information processing. *arXiv preprint arXiv:1406.4295*, 2014.
- [44] M. Neugebauer, T. Bauer, P. Banzer, and G. Leuchs. Polarization tailored light driven directional optical nanobeacon. *Nano Letters*, 14(5):2546–2551, 2014. PMID: 24724814.
- [45] F. J. Rodríguez-Fortuño, I. Barber-Sanz, D. Puerto, A. Griol, and A. Martínez. Resolving light handedness with an on-chip silicon microdisk. *ACS Photonics*, 1(9):762–767, 2014.
- [46] F. J. Rodríguez-Fortuño, D. Puerto, A. Griol, L. Bellieres, J. Martí, and A. Martínez. Sorting linearly polarized photons with a single scatterer. *Opt. Lett.*, 39(6):1394–1397, Mar 2014.
- [47] [http://www.nobelprize.org/nobel\\_prizes/physics/laureates/2009,2013](http://www.nobelprize.org/nobel_prizes/physics/laureates/2009,2013). Accessed 2013-11-22.
- [48] Amnon Yariv. *Optical Electronics*. Saunders College Publishing, Philadelphia, 1991.
- [49] Dietrich Marcuse, American Telephone, and Telegraph Company. *Theory of Dielectric Optical Waveguides*. Quantum Electronics–Principles & Applications. Academic Press, 1991.
- [50] Fam Le Kien and A. Rauschenbeutel. Anisotropy in scattering of light from an atom into the guided modes of a nanofiber. *Phys. Rev. A*, 90:023805, Aug 2014.
- [51] John D. Jackson. *Classical Electrodynamics*. Wiley, New York, 3 edition, 1999.
- [52] T. Søndergaard and B. Tromborg. General theory for spontaneous emission in active dielectric microstructures: Example of a fiber amplifier. *Phys. Rev. A*, 64:033812, Aug 2001.
- [53] G. Brambilla. Optical fibre nanowires and microwires: a review. *Journal of Optics*, 12(4):043001–, 2010.
- [54] Ariane Stiebeiner. *Nanofiber-based Spectroscopy of Organic Molecules*. Ph.D. thesis, Johannes Gutenberg-Universität Mainz, 2014.

- 
- [55] Florian Arno Warken. *Ultradiünne Glasfasern als Werkzeug zur Kopplung von Licht und Materie*. Ph.D. thesis, Rheinische Friedrich-Wilhelm Universität, Bonn, 2007.
- [56] I. Freestone, N. Meeks, M. Sax, and C. Higgitt. The lycurgus cup – a roman nanotechnology. *Gold Bulletin*, 40(4):270–277, 2007.
- [57] [http://www.nobelprize.org/nobel\\_prizes/chemistry/laureates/1925/](http://www.nobelprize.org/nobel_prizes/chemistry/laureates/1925/), 2014. Accessed 2014-09-17.
- [58] H. A. Atwater. The promise of plasmonics. *Scientific American*, 296(4):56–63, 2007.
- [59] R. Elghanian, J. J. Storhoff, R. C. Mucic, R. L. Letsinger, and C. A. Mirkin. Selective colorimetric detection of polynucleotides based on the distance-dependent optical properties of gold nanoparticles. *Science*, 277(5329):1078–1081, 1997.
- [60] S. J. Oldenburg, C. C. Genick, K. A. Clark, and D. A. Schultz. Base pair mismatch recognition using plasmon resonant particle labels. *Analytical Biochemistry*, 309(1):109 – 116, 2002.
- [61] I. H. El-Sayed, X. Huang, and M. A. El-Sayed. Selective laser photo-thermal therapy of epithelial carcinoma using anti-egfr antibody conjugated gold nanoparticles. *Cancer Letters*, 239(1):129 – 135, 2006.
- [62] P. Fortina, L. J. Kricka, D. J. Graves, J. Park, T. Hyslop, F. Tam, N. Halas, S. Surrey, and S. A. Waldman. Applications of nanoparticles to diagnostics and therapeutics in colorectal cancer. *Trends in Biotechnology*, 25(4):145 – 152, 2007.
- [63] L. K. Bogart, G. Pourroy, C. J. Murphy, V. Puentes, T. Pellegrino, D. Rosenblum, D. Peer, and R. Lévy. Nanoparticles for imaging, sensing, and therapeutic intervention. *ACS Nano*, 8(4):3107–3122, 2014. PMID: 24641589.
- [64] A. J. Haes and R. P. Van Duyne. A nanoscale optical biosensor: Sensitivity and selectivity of an approach based on the localized surface plasmon resonance spectroscopy of triangular silver nanoparticles. *Journal of the American Chemical Society*, 124(35):10596–10604, 2002. PMID: 12197762.
- [65] S. Kühn, U. Håkanson, L. Rogobete, and V. Sandoghdar. Enhancement of single-molecule fluorescence using a gold nanoparticle as an optical nanoantenna. *Phys. Rev. Lett.*, 97:017402, Jul 2006.
- [66] J. N. Anker, W. P. Hall, O. Lyandres, N. C. Shah, J. Zhao, and R. P. Van Duyne. Biosensing with plasmonic nanosensors. *Nature materials*, 7(6):442–453, 2008.
- [67] N. Mauser and A. Hartschuh. Tip-enhanced near-field optical microscopy. *Chem. Soc. Rev.*, 43:1248–1262, 2014.
- [68] J. B. Pendry. Negative refraction makes a perfect lens. *Phys. Rev. Lett.*, 85:3966–3969, Oct 2000.

- [69] H. J. Lezec, J. A. Dionne, and H. A. Atwater. Negative refraction at visible frequencies. *Science*, 316(5823):430–432, 2007.
- [70] N. I. Zheludev. A roadmap for metamaterials. *Opt. Photon. News*, 22(3):30–35, Mar 2011.
- [71] A. R. Tao. Metamaterials: Metamaterials go gattaca. *Nature Photonics*, 8(1):6–8, 2014.
- [72] A. V. Akimov, A. Mukherjee, C. L. Yu, D. E. Chang, A. S. Zibrov, P. R. Hemmer, H. Park, and M. D. Lukin. Generation of single optical plasmons in metallic nanowires coupled to quantum dots. *Nature*, 450(7168):402–406, 2007.
- [73] R. Kolesov, B. Grotz, G. Balasubramanian, R. J. Stöhr, A. Nicolet, P. R. Hemmer, F. Jelezko, and J. Wrachtrup. Wave–particle duality of single surface plasmon polaritons. *Nature Physics*, 5(7):470–474, 2009.
- [74] J. A. Scholl, A. L. Koh, and J. A. Dionne. Quantum plasmon resonances of individual metallic nanoparticles. *Nature*, 483(7390):421–427, 2012.
- [75] J. S. Fakonas, H. Lee, Y. A. Kelaita, and H. A. Atwater. Two-plasmon quantum interference. *Nature Photonics*, 8(4):317–320, 2014.
- [76] B. Lamprecht, J. R. Krenn, G. Schider, H. Ditlbacher, M. Salerno, N. Felidj, A. Leitner, F. R. Aussenegg, and J. C. Weeber. Surface plasmon propagation in microscale metal stripes. *Applied Physics Letters*, 79(1):51–53, 2001.
- [77] S. I. Bozhevolnyi, V. S. Volkov, E. Devaux, J.-Y. Laluet, and T. W. Ebbesen. Channel plasmon subwavelength waveguide components including interferometers and ring resonators. *Nature*, 440(7083):508–511, 2006.
- [78] H. Wei, Z. Wang, X. Tian, M. Käll, and H. Xu. Cascaded logic gates in nanophotonic plasmon networks. *Nature communications*, 2:387, 2011.
- [79] P. Zijlstra, J. W. Chon, and M. Gu. Five-dimensional optical recording mediated by surface plasmons in gold nanorods. *Nature*, 459(7245):410–413, 2009.
- [80] D. M. Koller, A. Hohenau, H. Ditlbacher, N. Galler, F. Reil, F. R. Aussenegg, A. Leitner, E. J. List, and J. R. Krenn. Organic plasmon-emitting diode. *Nature Photonics*, 2(11):684–687, 2008.
- [81] A. L. Falk, F. H. Koppens, L. Y. Chun, K. Kang, N. de Leon Snapp, A. V. Akimov, M.-H. Jo, M. D. Lukin, and H. Park. Near-field electrical detection of optical plasmons and single-plasmon sources. *Nature Physics*, 5(7):475–479, 2009.
- [82] J. M. Luther and J. L. Blackburn. Optoelectronics: Plasmon-enhanced plastic devices. *Nature Photonics*, 7(9):675–677, 2013.

- 
- [83] V. E. Ferry, L. A. Sweatlock, D. Pacifici, and H. A. Atwater. Plasmonic nanostructure design for efficient light coupling into solar cells. *Nano Letters*, 8(12):4391–4397, 2008. PMID: 19367883.
- [84] Y.-H. Su, Y.-F. Ke, S.-L. Cai, and Q.-Y. Yao. Surface plasmon resonance of layer-by-layer gold nanoparticles induced photoelectric current in environmentally-friendly plasmon-sensitized solar cell. *Light: Science & Applications*, 1(6):e14, 2012.
- [85] Craig F. Bohren and Donald R. Huffman. *Classical Theories of Optical Constants*, pages 226–267. Wiley-VCH Verlag GmbH, 2007.
- [86] Stefan A. Maier. *Plasmonics: Fundamentals and Applications*. Springer, 2007.
- [87] Neil W. Ashcroft and N. David Mermin. *Solid State Physics*. Cengage Learning Emea, 1976.
- [88] Uwe Kreibig and Michael Vollmer. *Optical properties of metal clusters*. Springer-Verlag, 1995.
- [89] K.-H. Hellwege, A. M. Hellwege, H. Landolt, R. Börnstein, O. Madelung, and J. H. Callomon. *Landolt-Bornstein: Numerical Data and Functional Relationships in Science and Technology*, volume 15. Springer, 1987.
- [90] A. D. Rakić, A. B. Djurišić, J. M. Elazar, and M. L. Majewski. Optical properties of metallic films for vertical-cavity optoelectronic devices. *Appl. Opt.*, 37(22):5271–5283, Aug 1998.
- [91] G. Mie. Beiträge zur optik trüber medien, speziell kolloidaler metallösungen. *Annalen der Physik*, 330(3):377–445, 1908.
- [92] V. Myroshnychenko, J. Rodriguez-Fernandez, I. Pastoriza-Santos, A. M. Funston, C. Novo, P. Mulvaney, L. M. Liz-Marzan, and F. J. Garcia de Abajo. Modelling the optical response of gold nanoparticles. *Chem. Soc. Rev.*, 37:1792–1805, 2008.
- [93] T. Bauer, S. Orlov, U. Peschel, P. Banzer, and G. Leuchs. Nanointerferometric amplitude and phase reconstruction of tightly focused vector beams. *Nat Photon*, 8(1):23–27, January 2014.
- [94] C.-T. Tai and R.E. Collin. Radiation of a hertzian dipole immersed in a dissipative medium. *Antennas and Propagation, IEEE Transactions on*, 48(10):1501–1506, Oct 2000.
- [95] A. Bellew. <https://www.flickr.com/photos/atb510/6714032603/in/photostream/>, 2012. Photograph of gold nanoparticles.
- [96] Craig F. Bohren and Donald R. Huffman. *Absorption and Scattering of Light by Small Particles*. Wiley, 1983.

- [97] A. Barenco, C. Bennett, R. Cleve, D. DiVincenzo, N. Margolus, P. Shor, T. Sleator, J. Smolin, and H. Weinfurter. Elementary gates for quantum computation. *Phys. Rev. A*, 52:3457–3467, Nov 1995.
- [98] D. P. DiVincenzo. Quantum computation. *Science*, 270(5234):255–261, 1995.
- [99] Eugen Vetsch. *Optical Interface Based on a Nanofiber Atom-Trap*. PhD thesis, Johannes Gutenberg-Universität Mainz, 2010.
- [100] M. Brownnutt, M. Kumph, P. Rabl, and R. Blatt. Ion-trap measurements of electric-field noise near surfaces. *arXiv preprint arXiv:1409.6572*, 2014.
- [101] D. Hite, Y. Colombe, A. Wilson, K. Brown, U. Warring, R. Jördens, J. Jost, K. McKay, D. Pappas, D. Leibfried, and D. Wineland. 100-fold reduction of electric-field noise in an ion trap cleaned with in situ argon-ion-beam bombardment. *Phys. Rev. Lett.*, 109:103001, Sep 2012.
- [102] N.M. Linke, D.T.C. Allcock, D.J. Szwer, C.J. Ballance, T.P. Harty, H.A. Janacek, D.N. Stacey, A.M. Steane, and D.M. Lucas. Background-free detection of trapped ions. *Applied Physics B*, 107(4):1175–1180, 2012.
- [103] Pradip Ghosh. *Ion traps*. Internat. Ser. Mono. Phys. Clarendon Press, Oxford, 1995.
- [104] J. Eschner, G. Morigi, F. Schmidt-Kaler, and R. Blatt. Laser cooling of trapped ions. *J. Opt. Soc. Am. B*, 20(5):1003–1015, May 2003.
- [105] C. Wuttke and A. Rauschenbeutel. Thermalization via heat radiation of an individual object thinner than the thermal wavelength. *Phys. Rev. Lett.*, 111:024301, Jul 2013.
- [106] C. Junge, S. Nickel, D. O’Shea, and A. Rauschenbeutel. Bottle microresonator with actively stabilized evanescent coupling. *Opt. Lett.*, 36(17):3488–3490, Sep 2011.
- [107] D. C. Moore, A. D. Rider, and G. Gratta. Search for millicharged particles using optically levitated microspheres. *Phys. Rev. Lett.*, 113:251801, Dec 2014.
- [108] C. R. Henry. Surface studies of supported model catalysts. *Surface Science Reports*, 31(7-8):231 – 325, 1998.
- [109] M. Bäumer and H.-J. Freund. Metal deposits on well-ordered oxide films. *Progress in Surface Science*, 61(7-8):127 – 198, 1999.
- [110] C. A. Neugebauer and M. B. Webb. Electrical conduction mechanism in ultrathin, evaporated metal films. *Journal of Applied Physics*, 33(1):74–82, 1962.
- [111] R. M. Hill. Electrical conduction in ultra thin metal films. i. theoretical. *Proceedings of the Royal Society of London A: Mathematical, Physical and Engineering Sciences*, 309(1498):377–395, 1969.

- 
- [112] D. S. Herman and T. N. Rhodin. Electrical conduction between metallic microparticles. *Journal of Applied Physics*, 37(4):1594–1602, 1966.
- [113] T. Wenzel, J. Bosbach, F. Stietz, and F. Träger. In situ determination of the shape of supported silver clusters during growth. *Surface Science*, 432(3):257 – 264, 1999.
- [114] N. Kaiser. Review of the fundamentals of thin-film growth. *Appl. Opt.*, 41(16):3053–3060, Jun 2002.
- [115] E. R. Abraham and E. A. Cornell. Teflon feedthrough for coupling optical fibers into ultrahigh vacuum systems. *Appl. Opt.*, 37(10):1762–1763, Apr 1998.
- [116] W. Chen, M. D. Thoreson, S. Ishii, A. V. Kildishev, and V. M. Shalaev. Ultra-thin ultra-smooth and low-loss silver films on a germanium wetting layer. *Opt. Express*, 18(5):5124–5134, Mar 2010.
- [117] Hermann Renner, Günther Schlamp, Klaus Zimmermann, Wolfgang Weise, Peter Tews, Klaus Dermann, Alfons Knödler, Karl-Heinz Schröder, Bernd Kempf, Hans Martin Lüscho, Ralf Drieselmann, Catrin Peter, and Rainer Schiele. *Silver, Silver Compounds, and Silver Alloys*. Wiley-VCH Verlag GmbH & Co. KGaA, 2000.
- [118] Milton Ohring. *Materials science of thin films*. Academic press, 2001.
- [119] R. S. Sennett and G. D. Scott. The structure of evaporated metal films and their optical properties. *J. Opt. Soc. Am.*, 40(4):203–210, Apr 1950.
- [120] Patrick Echlin. *Handbook of Sample Preparation for Scanning Electron Microscopy and X-Ray Microanalysis*. Springer, 2009.
- [121] A.K Kulkarni and L.C Chang. Electrical and structural characteristics of chromium thin films deposited on glass and alumina substrates. *Thin Solid Films*, 301(301):17 – 22, 1997.
- [122] R. Lazzari and J. Jupille. Silver layers on oxide surfaces: morphology and optical properties. *Surface Science*, 482-485, Part 2(0):823 – 828, 2001.
- [123] M. Kariniemi, J. Niinistö, T. Hatanpää, M. Kemell, T. Sajavaara, M. Ritala, and M. Leskelä. Plasma-enhanced atomic layer deposition of silver thin films. *Chemistry of Materials*, 23(11):2901–2907, 2011.
- [124] D. M. Sanders and A. Anders. Review of cathodic arc deposition technology at the start of the new millennium. *Surface and Coatings Technology*, 133-134(0):78 – 90, 2000.
- [125] X. W. Sun, H. C. Huang, and H. S. Kwok. On the initial growth of indium tin oxide on glass. *Applied Physics Letters*, 68(19):2663–2665, 1996.
- [126] R. Bel Hadj Tahar, T. Ban, Y. Ohya, and Y. Takahashi. Tin doped indium oxide thin films: Electrical properties. *Journal of Applied Physics*, 83(5):2631–2645, 1998.

- [127] M.D. Benoy, E.M. Mohammed, M. Suresh Babu, P.J. Binu, and B. Pradeep. Thickness dependence of the properties of indium tin oxide (ITO) FILMS prepared by activated reactive evaporation. *Brazilian Journal of Physics*, 39:629 – 632, 12 2009.
- [128] M. Mazur, D. Kaczmarek, J. Domaradzki, D. Wojcieszak, S. Song, and F. Placido. Influence of thickness on transparency and sheet resistance of ito thin films. In *Advanced Semiconductor Devices Microsystems (ASDAM), 2010 8th International Conference on*, pages 65–68, Oct 2010.
- [129] R. G. Gordon. Criteria for choosing transparent conductors. *MRS Bulletin*, 25:52–57, 8 2000.
- [130] B. P. Anderson and M. A. Kasevich. Loading a vapor-cell magneto-optic trap using light-induced atom desorption. *Phys. Rev. A*, 63:023404, Jan 2001.
- [131] C. Klempt, T. van Zoest, T. Henninger, O. Topic, E. Rasel, W. Ertmer, and J. Arlt. Ultra-violet light-induced atom desorption for large rubidium and potassium magneto-optical traps. *Phys. Rev. A*, 73:013410, Jan 2006.
- [132] A.E. Afanasiev, P.N. Melentiev, and V.I. Balykin. Laser-induced quantum adsorption of atoms on a surface. *JETP Letters*, 86(3):172–177, 2007.
- [133] A. B. Kuzmenko, E. van Heumen, F. Carbone, and D. van der Marel. Universal optical conductance of graphite. *Phys. Rev. Lett.*, 100:117401, Mar 2008.
- [134] Q. Bao, H. Zhang, B. Wang, Z. Ni, C. H. Lim, Y. Wang, D. Y. Tang, and K. P. Loh. Broadband graphene polarizer. *Nature photonics*, 5(7):411–415, 2011.
- [135] J. T. Kim, J. Kim, H. Choi, C.-G. Choi, and S.-Y. Choi. Graphene-based photonic devices for soft hybrid optoelectronic systems. *Nanotechnology*, 23(34):344005, 2012.
- [136] D. E. Chang, A. S. Sørensen, P. R. Hemmer, and M. D. Lukin. Strong coupling of single emitters to surface plasmons. *Phys. Rev. B*, 76:035420, Jul 2007.
- [137] J. Thompson. private communication, 201.
- [138] Andreas W. Schell, Güter Kewes, Tim Schröder, Janik Wolters, Thomas Aichele, and Oliver Benson. A scanning probe-based pick-and-place procedure for assembly of integrated quantum optical hybrid devices. *Review of Scientific Instruments*, 82(7):–, 2011.
- [139] H. Wu, D. Kong, Z. Ruan, P.-C. Hsu, S. Wang, Z. Yu, T. J. Carney, L. Hu, S. Fan, and Y. Cui. A transparent electrode based on a metal nanotrough network. *Nature Nanotechnology*, 8:421–425, June 2013.
- [140] Alexander S. Urban, Andrey A. Lutich, Fenando D. Stefani, and Jochen Feldmann. Laser printing single gold nanoparticles. *Nano Letters*, 10(12):4794–4798, 2010. PMID: 20957994.



- 
- [141] Yu Zhu, Zhengzong Sun, Zheng Yan, Zhong Jin, and James M. Tour. Rational design of hybrid graphene films for high-performance transparent electrodes. *ACS Nano*, 5(8):6472–6479, 2011. PMID: 21774533.
- [142] Johanna Amlacher. Versuche zur herstellung von transmissions- und leitfähigen glasfasern. Bachelor thesis, Technische Universität Wien, 2013.
- [143] Dmitri K. Gramotnev and Sergey I. Bozhevolnyi. Plasmonics beyond the diffraction limit. *Nat Photon*, 4(2):83–91, February 2010.
- [144] O. Benson. Assembly of hybrid photonic architectures from nanophotonic constituents. *Nature*, 480(7376):193–199, 2011.
- [145] L. Tong, F. Zi, X. Guo, and J. Lou. Optical microfibers and nanofibers: A tutorial. *Optics Communications*, 285(23):4641 – 4647, 2012. Special Issue: Optical micro/nanofibers: Challenges and Opportunities.
- [146] M. J. Morrissey, K. Deasy, M. Frawley, R. Kumar, Eu. Prel, L. Russell, V. G. Truong, and S. Nic Chormaic. Spectroscopy, manipulation and trapping of neutral atoms, molecules, and other particles using optical nanofibers: A review. *Sensors*, 13(8):10449–10481, 2013.
- [147] J. Petersen, J. Volz, and A. Rauschenbeutel. Chiral nanophotonic waveguide interface based on spin-orbit interaction of light. *Science*, 346(6205):67–71, 2014.
- [148] D. Axelrod, T.P. Burghardt, and N.L. Thompson. Total internal reflection fluorescence. *Annu. Rev. Biophys. Bio.*, 13(1):247–268, 1984.
- [149] T. Kawalec, L. Józefowski, J. Fiutowski, M.J. Kasprówicz, and T. Dohnalik. Spectroscopic measurements of the evanescent wave polarization state. *Optics Communications*, 274(2):341 – 346, 2007.
- [150] E. M. Purcell, H. C. Torrey, and R. V. Pound. Resonance absorption by nuclear magnetic moments in a solid. *Phys. Rev.*, 69:37–38, Jan 1946.
- [151] Fam Le Kien, S. Dutta Gupta, V. I. Balykin, and K. Hakuta. Spontaneous emission of a cesium atom near a nanofiber: Efficient coupling of light to guided modes. *Phys. Rev. A*, 72:032509, Sep 2005.
- [152] Peter W. Barber and Steven C. Hill. *Light scattering by particles: computational methods*, volume 2. World scientific, 1990.
- [153] H. G. Craighead and G. A. Niklasson. Characterization and optical properties of arrays of small gold particles. *Applied Physics Letters*, 44(12):1134–1136, 1984.
- [154] M. A. van Dijk, A. L. Tchebotareva, M. Orrit, M. Lippitz, S. Berciaud, D. Lasne, L. Cognet, and B. Lounis. Absorption and scattering microscopy of single metal nanoparticles. *Phys. Chem. Chem. Phys.*, 8:3486–3495, 2006.

- [155] E. Betzig and J. K. Trautman. Near-field optics: Microscopy, spectroscopy, and surface modification beyond the diffraction limit. *Science*, 257(5067):189–195, 1992.
- [156] Michael A. Paesler and Patrick J. Moyer. *Near-field optics: theory, instrumentation, and applications*, volume 68. Wiley New York, 1996.
- [157] R. Garcia-Fernandez, W. Alt, F. Bruse, C. Dan, K. Karapetyan, O. Rehband, A. Stiebeiner, U. Wiedemann, D. Meschede, and A. Rauschenbeutel. Optical nanofibers and spectroscopy. *Applied Physics B*, 105(1):3–15, 2011.
- [158] T. Yamaguchi, S. Yoshida, and A. Kinbara. Optical effect of the substrate on the anomalous absorption of aggregated silver films. *Thin Solid Films*, 21(1):173 – 187, 1974.
- [159] O. Benson. Assembly of hybrid photonic architectures from nanophotonic constituents. *Nature*, 480(7376):193–199, 2011.
- [160] T. Junno, K. Deppert, L. Montelius, and L. Samuelson. Controlled manipulation of nanoparticles with an atomic force microscope. *Applied Physics Letters*, 66(26):3627–3629, 1995.
- [161] L. Tong, T. Zhu, and Z. Liu. Atomic force microscope manipulation of gold nanoparticles for controlled raman enhancement. *Applied Physics Letters*, 92(2):–, 2008.
- [162] E. Vetsch, D. Reitz, G. Sagué, R. Schmidt, S. T. Dawkins, and A. Rauschenbeutel. Optical interface created by laser-cooled atoms trapped in the evanescent field surrounding an optical nanofiber. *Phys. Rev. Lett.*, 104:203603, May 2010.
- [163] A. Goban, K. S. Choi, D. J. Alton, D. Ding, C. Lacroûte, M. Pototschnig, T. Thiele, N. P. Stern, and H. J. Kimble. Demonstration of a state-insensitive, compensated nanofiber trap. *Phys. Rev. Lett.*, 109:033603, Jul 2012.
- [164] R. Mitsch, C. Sayrin, B. Albrecht, P. Schneeweiss, and A. Rauschenbeutel. Quantum state-controlled directional spontaneous emission of photons into a nanophotonic waveguide. *Nature communications*, 5, 2014.
- [165] L. Marrucci. Quantum optics: Spin gives direction. *Nature Physics*, 11(1):9–10, 2015.
- [166] S. A. Bosse and N. M. Loening. Using two-dimensional colloidal crystals to understand crystallography. *Journal of Chemical Education*, 85(1):93, 2008.
- [167] Richard J. Cook, Donn G. Shankland, and Ann L. Wells. Quantum theory of particle motion in a rapidly oscillating field. *Phys. Rev. A*, 31:564–567, Feb 1985.
- [168] E. Peik and J. Fletcher. Electrodynamic trapping of charged particles in a monopole field. *Journal of Applied Physics*, 82(11):5283–5286, 1997.
- [169] A. V. Petukhov. Sum-frequency generation on isotropic surfaces: General phenomenology and microscopic theory for jellium surfaces. *Phys. Rev. B*, 52:16901–16911, Dec 1995.

- [170] J. A. Maytorena, B. S. Mendoza, and W. L. Mochán. Theory of surface sum frequency generation spectroscopy. *Phys. Rev. B*, 57:2569–2579, Jan 1998.
- [171] J. A. Maytorena, W. L. Mochán, and B. S. Mendoza. Hydrodynamic model for sum and difference frequency generation at metal surfaces. *Phys. Rev. B*, 57:2580–2585, Jan 1998.
- [172] J. I. Dadap, J. Shan, K. B. Eisenthal, and T. F. Heinz. Second-harmonic rayleigh scattering from a sphere of centrosymmetric material. *Phys. Rev. Lett.*, 83:4045–4048, Nov 1999.
- [173] J. I. Dadap, J. Shan, and T. F. Heinz. Theory of optical second-harmonic generation from a sphere of centrosymmetric material: small-particle limit. *J. Opt. Soc. Am. B*, 21(7):1328–1347, Jul 2004.
- [174] K. P. Tamarov, L. A. Osminkina, S. V. Zinovyev, K. A. Maximova, J. V. Kargina, M. B. Gongalsky, Y. Ryabchikov, A. Al-Kattan, A. P. Sviridov, M. Sentis, A. V. Ivanov, V. N. Nikiforov, A. V. Kabashin, and V. Y. Timoshenko. Radio frequency radiation-induced hyperthermia using si nanoparticle-based sensitizers for mild cancer therapy. *Scientific reports*, 4:7034, 2014.
- [175] M. Kauranen and A. V. Zayats. Nonlinear plasmonics. *Nature Photonics*, 6:737–748, November 2012.



# Acknowledgements / Danksagung

At this point, i want to thank all of those who have contributed to the success of this thesis / An dieser Stelle möchte ich all denjenigen danken, die zum Gelingen dieser Arbeit beigetragen haben:

Mein besonderer Dank gilt Arno Rauschenbeutel für die Betreuung, Ratschläge und das entgegengebrachte Vertrauen. Er gab mir die Gelegenheit an diesem spannenden Projekt arbeiten zu dürfen.

I thank Benjamin Ames and Michael Brownnutt for the fruitful cooperation and friendly atmosphere. Dear Ben, i thank you for your support and friendship as well as your understanding and patience when i had not that much time to work with you. I wish you nothing but the best for the last months of your thesis. At one point we should think about commercializing our infamous 'iGun'.

Ich bedanke mich beim SEM Team am USTEM um Andreas Steiger-Thirsfeld und Karin Whitmore, die mir die Gelegenheit gaben ihre Geräte zu verwenden.

Ich bedanke mich herzlich bei allen Mitgliedern der Arbeitsgruppe. Atmosphäre, Hilfsbereitschaft und Zusammenhalt waren schlichtweg fantastisch. Ich werde die interessanten sowie lustigen Mittagsgespräche sehr vermissen.

Jürgen Volz danke ich für die großartige Unterstützung und Betreuung während der letzten Jahre dieser Arbeit sowie die einerseits erhellenden und andererseits lustigen Gespräche. Ich habe ihm viel zu verdanken.

I want to thank Pham Le Kien for all the time he invested in order to help me when i had questions.

Ich danke der Bachelor Studentin Johanna Amlacher für ihren Beitrag zur Herstellung leitfähiger Glasfasern im Rahmen meiner Doktorarbeit.

My special regards to Danny O'Shea and his whole family. I'll keep all my fingers crossed that these terrible times will soon be over for you.

Christian Wuttke, Rudolf Mitsch und Daniel Reitz möchte ich für ihre Freundschaft, die vielen aufbauenden Gespräche und netten Stunden danken.

Ich bedanke mich sehr bei meinen Freunden in Deutschland. Sie hatten immer ein offenes Ohr für mich, wenn es mir einmal schlechter ging.

I want to thank my hockey coaches Darek and Cedric who have become like a cousin and uncle to me. Their understanding and affection have been really unique.

Auch meinen Hockeymannschaften hier in Wien möchte ich danken. Wie sie mich aufgenommen haben und jede Woche auf's neue zum Lachen bringen ist großartig. Sie sind für mich eine zweite Familie.

Ganz besonders möchte ich mich bei meiner ganzen Familie bedanken. Jeder Einzelne hat mich stets unterstützt und motiviert. Wenn einmal Not am Mann war, konnte ich immer auf sie zählen. Leider kann meine Großmutter diesen Tag nicht mehr miterleben.

Auch wenn er es noch nicht versteht, möchte ich mich bei meinem Sohn Paul bedanken. Die Freude die du verstrahlst hat mich Tag für Tag motiviert, auch in den anstrengenden Tagen zum Schluss, immer weiterzumachen.

Zu guter Letzt danke ich meiner Antje. Bedingungslos hat sie mich tagein tagaus unterstützt wo es nur ging. Dein Beitrag zu dieser Arbeit ist riesig und ich weiß nicht wie diese Zeit ohne dich verlaufen wäre.

# LEBENS LAUF

Jan Petersen  
Castellezgasse 16 / 7  
1020 Wien  
Österreich

## Persönliche Daten

Geburtsdatum: 11. Januar 1983  
Geburtsort: Bad Arolsen  
Staatsangehörigkeit: deutsch

## Ausbildung

seit 05/2009	Technische Universität Wien und Johannes Gutenberg-Universität Mainz Doktorand in Physik
10/2002 – 03/2009	Johannes Gutenberg-Universität Mainz Diplom-Physiker
09/1993 – 06/2002	Max Planck-Gymnasium, Rüsselsehim
08/1988 – 08/1993	Eichgrundschule, Rüsselsheim